



HAL
open science

Investigation of charge transport/transfer and charge storage at mesoporous TiO₂ electrodes in aqueous electrolytes

Yee Seul Kim

► **To cite this version:**

Yee Seul Kim. Investigation of charge transport/transfer and charge storage at mesoporous TiO₂ electrodes in aqueous electrolytes. Other. Université Sorbonne Paris Cité, 2018. English. NNT : 2018USPCC161 . tel-02407183

HAL Id: tel-02407183

<https://theses.hal.science/tel-02407183>

Submitted on 12 Dec 2019

HAL is a multi-disciplinary open access archive for the deposit and dissemination of scientific research documents, whether they are published or not. The documents may come from teaching and research institutions in France or abroad, or from public or private research centers.

L'archive ouverte pluridisciplinaire **HAL**, est destinée au dépôt et à la diffusion de documents scientifiques de niveau recherche, publiés ou non, émanant des établissements d'enseignement et de recherche français ou étrangers, des laboratoires publics ou privés.

DOCTORAT

ELECTROCHIMIE

Yee-Seul KIM

Investigation of charge transport/transfer and charge storage at mesoporous TiO₂ electrodes in aqueous electrolytes

Thèse dirigée par Véronique Balland
et co-encadrée par Benoît Limoges

Soutenue le 08 Novembre 2018

Rapporteurs :	Marie-Noëlle COLLOMB	DR, Université Grenoble Alpes
	Jean-Pierre PEREIRA-RAMOS	DR, Université Paris-Est
Président du jury :	Christel LABERTY-ROBERT	PR, Sorbonne Université
Examineur :	Hyacinthe RANDRIAMAHAZAKA	PR, Université Paris Diderot
Directrice de thèse :	Véronique BALLAND	MCU HDR, Université Paris Diderot
Co-directeur de thèse :	Benoît LIMOGES	DR, Université Paris Diderot

Acknowledgement

Foremost, I would first like to thank my reviewers, Dr. Marie-Noëlle COLLOMB and Dr. Jean-Pierre PEREIRA-RAMOS, of interest in my Ph.D. work and having accepted to evaluate it as well as for reporting and corrections.

I also would like to thank Pr. Christel LABERTY-ROBERT and Pr. Hyacinthe RANDRIAMAHAZAKA, for examining my thesis work.

I want to thank my supervisor, Véronique BALLAND. She has not only taught me the scientific knowledge but also has been supportive with patience and passion to bring me here. I also would like to thank my co-supervisor, Benoît LIMOGES. His kind teaching and deep scientific knowledge were motivational during my Ph.D. work. I deeply appreciate all their contributions of time, efforts and ideas to make my Ph.D. experience productive and stimulating.

I also want to express my gratefulness to Pr. Cyrille COSTENTIN for the modeling study of my experimental results.

I would like to thank to our collaborators who contributed to the achievement of experiments, Dr. Kenneth HARRIS for the preparation of electrodes, Stéphanie LAU for the resonance Raman spectroscopy, and Philippe DECORSE for the XPS experiments.

I am also grateful for the present and former group members that I have(had) met quotidian; Sébastiel KRIEGEL, Charlie, Martin, Heng, Claudio, Khalil, Jérémy, Etienne, Lydia, Célia, Justine, Rabia, Min, Bing, Pan, Hussein, Benjamin, Telmo, Alexis, Geordie, Sihem, Mathieu, François, Nikolina, Julie, who have made my daily life in laboratory much more pleasant.

Finally, a huge thank to my family KIM in Korea and NOLLET in France, my all friends in Korea and France who gave me their dedication and support during these years.

SUMMARY

Abbreviation and notation table.....	5
General introduction.....	9
1. TiO ₂ -based nanostructured mesoporous materials.....	11
2. Description of the electrochemical features of mesoporous semiconductive TiO ₂ films.....	13
2.1. Electronic structure of TiO ₂	13
2.2. Effect of bias.....	14
2.3. Capacitance of nanostructured TiO ₂ electrodes.....	15
2.4. Specificity of aqueous-based electrolytes.....	18
3. Redox reactivity of TiO ₂ electrodes and charge storage.....	20
4. Charge transfer at functionalized mesoporous TiO ₂ electrode.....	22
5. Aim of the present PhD work.....	24
Chapter I. Reactivity of conductive GLAD-ITO and semiconductive GLAD-TiO₂ electrodes functionalized by a manganese porphyrin (Mn-ph).....	31
1. Introduction.....	33
1.1. Aim of work.....	33
1.2. Methodology.....	34
2. Electrode functionalization.....	35
2.1. Description of GLAD-electrodes.....	35
2.2. Chemical surface functionalization of GLAD electrodes by Mn-ph.....	35
3. Interfacial electron transfer at Mn-ph/GLAD-electrodes under degassed condition.....	38
3.1. Mn-ph/GLAD-ITO.....	38
3.2. Mn-ph/GLAD-TiO ₂	42

4. Catalytic reduction of O ₂ at Mn-ph-modified GLAD-ITO and GLAD-TiO ₂ electrodes.....	50
4.1. Mn-ph/GLAD-ITO.....	51
4.2. Mn-ph/GLAD-TiO ₂	55
5. Conclusion.....	60

Chapter II. Introducing molecular functionalities within nanostructured GLAD-ITO electrodes through diazonium electrografting.....65

1. Introduction.....	67
2. Electrografting of diazonium salt on planar ITO and GLAD-ITO electrodes.....	68
3. Spectroscopic characterization of the modified electrodes.....	70
3.1. Spectroelectrochemistry.....	70
3.1.1. UV-visible absorbance spectra.....	70
3.1.2. Extinction coefficient estimation.....	71
3.1.3. Surface concentration of grafted porphyrin.....	73
3.1.4. Ferrocenethanol passivation.....	74
3.1.5. Time-dependent stability in ACN and aqueous solutions.....	76
3.2. resonance Raman (rR) spectroscopy.....	77
3.3. X-ray photoelectron spectroscopy (XPS).....	80
4. Conclusion.....	82

Chapter III. Evidencing fast, massive, and reversible proton insertion in nanostructured GLAD-TiO₂ electrodes at neutral pH.....87

1. Introduction.....	89
2. Description of the GLAD-TiO ₂ films used.....	91
3. Spectroelectrochemical studies in aqueous solution.....	92

4. Description of the intercalation process.....	101
5. Comparative study with lithium insertion.....	105
6. Quantification of the charge stored.....	106
7. Conclusion.....	112

Chapter IV. Investigation of the aqueous electrolyte composition on the proton-coupled electron storage at mesoporous TiO₂ electrodes.....119

1. Introduction.....	121
1.1. Questions about multivalent metallic ion insertion charge storage in aqueous electrolytes.....	121
1.2. Questions about Li ⁺ insertion in basic aqueous electrolytes.....	123
1.3. Presentation of the different GLAD TiO ₂ electrodes used.....	124
2. Elucidating the role of multivalent metallic ions in aqueous electrolytes.....	126
2.1. Evidencing ion insertion charge storage in presence of multivalent metallic ions.....	126
2.2. Mechanistic investigation.....	130
2.3. Conclusion.....	140
3. Optimization of proton insertion charge storage in acetic acid at pH 5.....	142
4. Combined effect of the pH and the weak acid pK _a on the efficiency of charge storage in aqueous solution.....	148
4.1. Evidencing the link between pH and pK _a	148
4.2. Evidencing water as a proton donor.....	151
5. Conclusion.....	155

General conclusions.....	159
Experimental part.....	165
1. Chemicals and Materials.....	167
2. Methodology.....	167
2.1. Electrochemistry (Cyclic voltammetry, Chronoamperometry, Chronopotentiometry)	167
2.2. Real-time UV-visible absorption spectroelectrochemistry (Cyclic-voltabsorptometry, Chronoabsorptometry)	168
2.3. X-ray photoelectron spectroscopy.....	170
2.4. Resonance Raman spectroscopy.....	170
3. GLAD-Electrodes.....	171
3.1. Preparation of mesoporous GLAD-electrode.....	171
3.1.1. GLAD-ITO.....	173
3.1.2. GLAD-TiO ₂	173
3.1.3. GLAD-TiO ₂ /TiO ₂	173
3.1.4. GLAD-TiO ₂ /Ti.....	173
3.2. Electrode cleaning process.....	174
3.3. Surface enhancement.....	174
4. Surface modification.....	175
4.1. Chemisorption of manganese porphyrin (Mn-ph)	175
4.2. Electrografting of diazonium salt.....	176

Abbreviation list

Abs	Absorbance
BET	Brunauer-Emmett-Teller
CB	Conduction Band
CV	Cyclic Voltammogram
CVA	Cyclic VoltAsorptogram
DCVA	Derivative Cyclic VoltAsorptogram
DOS	Density Of States
DSSC (or DSC)	Dye-(S)ensitized Solar Cell
EDL	Electrical Double Layer
EDLC	Electrical Double Layer Capacitance
ESIA	Evaporation Induced Self Assembly
Eq.	Equation
EQCM	Electrochemical Quartz Crystal Microbalance
GLAD	GLancing Angle Deposition
IR	InfraRed
ITO	Indium Tin Oxide
Mn-ph	Manganese porphyrin
NIR	Near InfraRed
SEM	Scanning Electron Microscope
UV	Ultra-Violet
VB	Valence Band
Vis	Visible
XPS	X-Ray Photoelectron Spectroscopy

Notation list

A	Absorbance
ΔA	Absorbance change
C	Concentration
C°	Initial concentration
C_B	Buffer concentration
C_e	Free electron concentration at the interface of semiconductive film/ITO
C_e°	Maximal electron concentration that can be injected in the conduction band of the semiconductive film
CE	Coulombic Efficiency (%)
C_F	Intrinsic capacitance of the film (series capacitance of C_{TiO_2} and C_H)
C_{ITO}	Capacitance at the ITO/electrolyte interface
C_H (or C_{dl})	Double layer capacitance at the electrode/electrolyte interface
C_T	Total capacitance
C_{TiO_2} (or C_{chem})	Chemical capacitance of the TiO_2 electrode
D	Diffusion coefficient
D_{AH} (or $D_{AH,out}$ or $D_{H,out}$)	Diffusion coefficient of proton (donor) in aqueous solution
$D_{H,in}$	Diffusion coefficient of proton within the TiO_2 lattice
D_e	Diffusion coefficient of electron within the TiO_2 lattice
d	Nanorod diameter of GLAD- TiO_2 film
d_f	GLAD-film thickness
E	Potential
E°	Standard potential
$E^{\circ'}$	Apparent standard potential
E°_{CB}	Conduction band potential edge value at pH 0
E_F	Fermi level (Fermi energy)
$E_{cathodic\ cut-off}$	Cathodic cut-off potential in galvanostatic experiments
E_{CB}	Conduction band potential
E_{VB}	Valence band potential
F	Faraday constant ($96485\ C \cdot mol^{-1}$)
k_s	Electron transfer rate constant
l	GLAD-film thickness, penetration length
rR	resonance Raman spectroscopy
i (or I)	Current
I_c	Current arise from capacitive component
I_f	Current arise from faradaic component
i_c (or $i_{f,p}$ or $\phi_{f,p}$)	Cathodic peak current (Cathodic peak of electron flux density)

ϕ	Electron flux density
j (or J)	Current density
n	Number of electron transferred
n_{cb}	Density of free electrons in the TiO ₂
N_C	Density of extended states in the conduction band
N_T	Total trap density in the band gap
n_{trap}	Density of electrons in the band gap
k_B	Boltzmann constant
P	Porosity
R	Gas constant (8.314 J·K ⁻¹ ·mol ⁻¹)
S	Geometric surface area
SA	Surface Area enhancement
S_e	Real surface area (specific electroactive surface area)
Q	Charge density (C·cm ⁻²)
Q	Charge storage capacity (C·g ⁻¹ or mA·h·g ⁻¹)
T	Temperature
t	Time
x	Mole fraction
α	Electron transfer coefficient
δ	Nanorod surface density
ε	Molar extinction coefficient
$\Delta\varepsilon$	Difference of molar extinction coefficient between two different species
Γ^{max}	Maximal surface concentration
Γ	Surface concentration
Γ^0	Initial surface concentration
ϕ	Deposition angle for GLAD method
λ	Wavelength
q	The elementary charge
ν	Scan rate

General introduction

1. TiO₂-based nanostructured mesoporous materials
2. Description of the electrochemical features of mesoporous semiconductive TiO₂ films
 - 2.1. Electronic structure of TiO₂
 - 2.2. Effect of bias
 - 2.3. Capacitance of nanostructured TiO₂ electrodes
 - 2.4. Specificity of aqueous-based electrolytes
3. Redox reactivity of TiO₂ electrodes and charge storage
4. Charge transfer at functionalized mesoporous TiO₂ electrode
5. Aim of the present PhD work

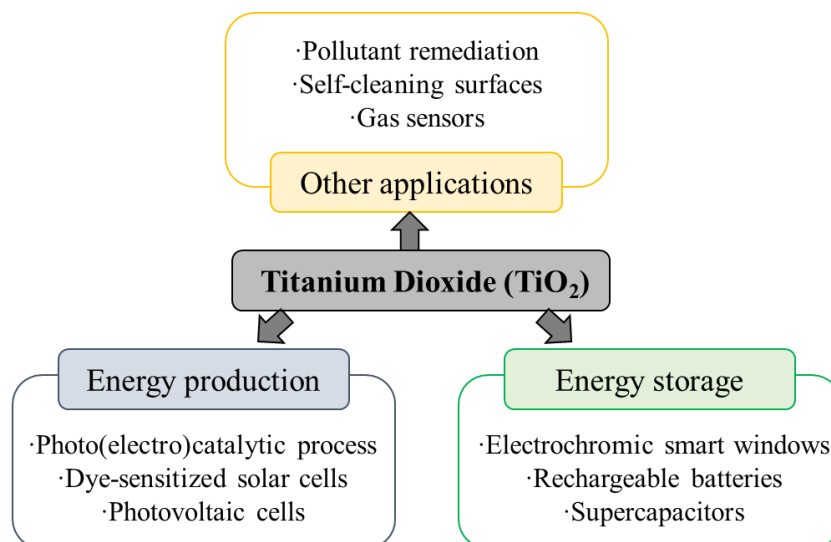
1. TiO₂-based nanostructured mesoporous materials

Due to the constant use of limited resources such as fossil fuels or natural gases and the related emission of greenhouse gases, a number of environmental concerns have been generated in modern societies which requires the development of a sustainable energy production provided by renewable sources. Considerable efforts have been made to produce energy from renewable sources such as solar energy (by using photovoltaic devices) or wind (by turbine) during last few decades, primarily for the electricity.¹⁻² Because of the discontinuity of access to the nature resources, the development of electrical energy storage (*i.e.*, batteries and electrochemical supercapacitors) or conversion (*i.e.*, solar cells) systems has become a major research topic. These technologies are required to satisfy not only the prime characteristics such as high power and high energy or high conversion efficiency, long operating life, and low manufacturing process cost but also the aspect of serious safety concerns over the reliable operating conditions in future electricity supply or conversion systems. Therefore, in order to improve their performances, it is necessary to deeply understand the electrochemical reactivity of materials possibly employed in such energy devices, especially under the eco-friendly operating conditions required to develop sustainable devices.

TiO₂-based mesoporous materials are one of the favorable energy device materials due to their unique electrical, optical and chemical characteristics and have therefore been the subjects of enormous interest since few decades.³ TiO₂ has the great advantages of low-cost, earth-abundance, safety (*i.e.*, low toxicity), excellent chemical/photochemical stability. It allows moreover for easy preparation of high active surface area mesoporous thin films.⁴ TiO₂ is intrinsically a n-type semiconductor, with a band gap around 3 eV, thus making pure TiO₂ active under UV light absorption and transparent in the visible range. One of the earliest use of single crystal rutile TiO₂ was indeed for the photoelectrochemical decomposition of water.⁵ This application relies on a photocatalytic process initiated by UV-light absorption by TiO₂ leading to the formation of electron-hole pairs which can then diffuse through the crystal. Water is then oxidized to dioxygen by the holes photo-generated at the TiO₂ material whereas dihydrogen is produced by reduction of protons at the counter electrode. This reactivity was further exploited for pollutant remediation⁶ or self-cleaning surfaces⁷ that both employs photo-decomposition of organic molecules by TiO₂.⁸⁻⁹

The unique (photo)electrochemical features of TiO₂-based porous materials have also made this material of great interest in the energy field. This concerns both the field of energy

production with by photovoltaic cells¹⁰ such as dye-sensitized solar cells (DSSCs)¹¹⁻¹² for production of electricity or photo(electro)catalytic cells for fuel generation,¹³⁻¹⁵ and the field of energy storage with ion-insertion batteries,¹⁶⁻¹⁷ supercapacitors,¹⁸ and electrochromic smart windows.¹⁹



Scheme 1. Fields of application of TiO₂ nanomaterials that are directly or indirectly related to their (photo)electrochemical properties.²⁰

Currently, a large part of these technologies requires operating in organic aprotic solvents (*e.g.*, DSSC or lithium-ion batteries) which leads to environmental and safety issues. As a result of these considerations, in accordance with the trend for eco-friendly, sustainable, and safe technologies, growing efforts have been recently oriented towards the design of aqueous-based DSSCs or ion-insertion batteries, *i.e.* operating in safe aqueous electrolytes and ideally under non-corrosive conditions.²¹⁻²⁴ These developments require a deep understanding of the reactivity of mesoporous TiO₂ films concerning charge generation, charge transport and charge storage (or accumulation) in aqueous media and our goal is to get better insights into this complex reactivity by developing new quantitative (spectro)electroanalytical methodologies.

2. Description of the electrochemical features of mesoporous semiconductive TiO₂ films

2.1. Electronic structure of TiO₂

The conductivity of a material depends on its electronic band structure and band filling that is temperature-dependent. Conductive materials, such as metals, are indeed characterized by the incomplete filling of the conduction band (CB), leading to the many partially filled and delocalized states near the Fermi level (corresponding to an occupation probability of ½) and easy transportation of electrons within the structure. On the opposite, semiconductors and insulators are characterized by an electronic bandgap between a fully-occupied valence band (VB) and an empty conduction band (at $T = 0$ K), with the Fermi level (E_F) setting in between. As the temperature is increased, their electronic conductivity is increased due to thermal excitation of electrons to conduction band states, leaving holes in the valence band. This increase of conductivity is directly related to the free electron concentration in the conduction band n_{cb} (and symmetrical holes in the valence band) which is determined by the energy difference between the lower edge of the conduction band (E_{CB}) and the Fermi level (E_F) according to the Fermi-Dirac statistics. If this energy difference is much larger than the thermal energy ($E_{CB} - E_F \gg k_B T$), the density of free electrons is given by Eq. 1 assuming a Boltzmann distribution²⁵:

$$n_{cb} = N_C \exp\left(\frac{E_F - E_{CB}}{k_B T}\right) \quad (1)$$

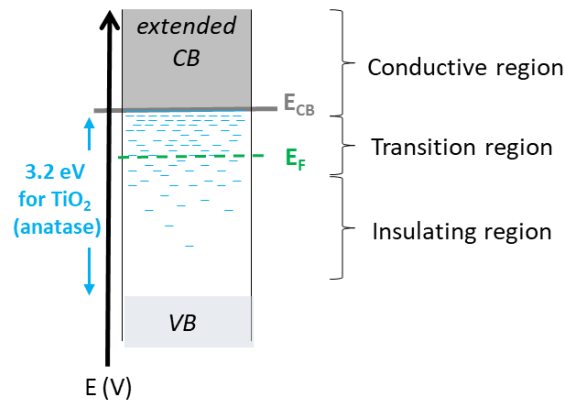
where N_C is the density of extended states in the conduction band ($\sim 10^{17}$ cm⁻³ for undoped anatase TiO₂)²⁶, k_B the Boltzmann constant, E_{CB} the energy level of the lower edge of conduction band of TiO₂ (in eV), and T the temperature (in K).

However, the electronic structure of TiO₂ is not so simple and a high density of localized electronic states (DOS) is located in the bandgap below the conduction band edge. They are attributed notably to oxygen vacancies and interstitial Ti defects, and responsible for n-doping of the material. Based on the seminal work by Nelson for diffusive electron transport, this extra DOS is assumed to follow an exponential distribution in the bandgap, this assumption allowing to properly model the non-ideal electron transport properties of TiO₂.²⁷ Accordingly, the electronic description of TiO₂ includes an exponential distribution of electronic states in the bandgap, located below the conduction band edge and resulting into a shift of the Fermi

level (see Scheme 2). The density of electrons in the bandgap is thus given by the following Eq. 2:

$$n_{trap} = N_T \exp\left(\alpha \frac{E_F - E_{CB}}{k_B T}\right) \quad (2)$$

where N_T is the total trap density in the bandgap ($\sim 4 \cdot 10^{19} \text{ cm}^{-3}$ in TiO_2)²⁸, and α a parameter reflecting the average energy of the trap states distribution below the conduction band.²⁷



Scheme 2. Schematic representation of the electronic structure of n-type semiconductive TiO_2 representing the conduction band as well as the localized DOS in the band gap (in blue). Depending on the applied potential (*i.e.*, Fermi level), TiO_2 behaves as insulating, transition from insulating to conducting, metal-like fully conducting.

2.2. Effect of bias

As the Fermi level corresponds to the chemical potential of electron within the material, it can be tuned upon applying an external potential (or bias) at TiO_2 electrodes (*i.e.*, TiO_2 films deposited onto a conductive substrate) soaked in an electrolyte solution. Under bias, the energy of the Fermi level (in eV) is given by Eq. 3:

$$E_F = -qE \quad (3)$$

where E is the applied potential (in V) and q the elementary charge.

As nanostructured films are highly porous and highly permeable to the electrolyte, the electric field generated within the film by the bias is screened by the electrolyte ions. As a consequence, electron transport occurs by diffusion throughout the TiO_2 lattice allowing to reach thermodynamic equilibrium. This diffusion process is assumed to occur through the

extended states of the conduction band, with the electrons being slowed by a trapping/detrapping mechanism in empty electronic band gap states.²⁹ Moreover, as the size of the TiO₂ nanoparticles (typically 20 nm) is small as compared to the depletion layer (typical width of 10 – 1000 nm), band bending at the nanoparticles/electrolyte interface can be neglected. Finally, homogeneous equilibrium occupancy of bandgap states corresponding to the applied potential can be achieved over the entire nanostructured film.

According to Eq. 1 and Eq. 2, changes in the applied potential will thus induce changes in the electronic occupancy of the electronic states. The conductivity of the film that relies on the density of delocalized electronic states close to the Fermi level, will thus also be tuned under bias. If TiO₂ is biased positively, the Fermi level will lie far from the conduction band and the conductivity will be very low. On the contrary, if the potential is biased negatively, electrons will accumulate in the material by progressively filling the bandgap electronic states. The conductivity of the TiO₂ film will thus increase exponentially up to a maximum value once E_F reaches the conduction band edge³⁰, as demonstrated experimentally. Under such conditions, the TiO₂ film behaves as fully conductive. Accordingly, three potential regions characterized by different conductivities of the TiO₂ film can be defined (see scheme 2).

2.3. Capacitance of nanostructured TiO₂ electrodes

Based on the electronic structure of TiO₂ and the effect of bias on its conductivity, we can now describe the capacitance of a nanostructured TiO₂ electrode soaked into an electrolyte solution. Capacitance is an essential electrical quantity which associates a change in the charge-carrier concentration to a change in potential ($C = dQ/dE$). We will here shortly present the main features of a model initially developed by Bisquert et al. that allows for a good understanding of the unusual cyclic voltammograms (CVs) recorded at TiO₂ electrodes.

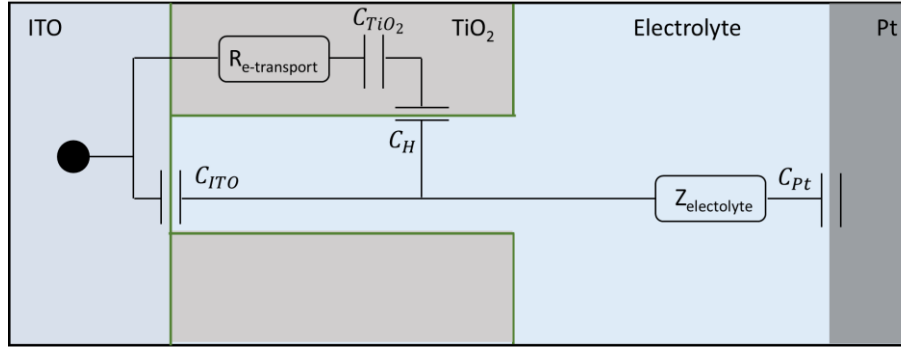
In this model, the TiO₂/electrolyte interface is described by a series connection of two capacitances, combining to define the intrinsic capacitance C_F of the film.²⁹ The first one corresponds to the chemical capacitance of the TiO₂ electrode (C_{TiO_2}) and thus to the progressive filling of the electronic states located in the bandgap as the potential is downshifted toward E_{CB} . It is dominated by the filling of the bandgap states as $N_C \ll N_T$. Accordingly, C_{TiO_2} follows the following exponential law²⁹:

$$C_{TiO_2} = C_e^\circ \exp\left(-\frac{\alpha F}{RT} (E - E_{CB})\right) \quad (4)$$

where C_e° is related to the maximal concentration of electrons that can be injected in the bandgap states, and E_{CB} is expressed in V.

The second capacitance corresponds to the double layer capacitance at the conductive electrode/electrolyte interface (Helmholtz layer, C_H) once TiO_2 is in its conductive state, *i.e.* when E lies close or below E_{CB} . Its value is independent of the applied potential and expected quite high according to the high surface area of the nanostructured film.

Finally, since the nanostructured TiO_2 film is deposited on a fully conductive planar substrate (ITO in the present case), there is also a double layer capacitance at the ITO/electrolyte interface (C_{ITO}). The simplified equivalent electrical circuit characterizing the nanostructured TiO_2 electrode is finally given by scheme 3.



Scheme 3. Equivalent circuit for a semiconductive nanostructured- TiO_2 soaked in an electrolyte. $R_{e\text{-transport}}$ indicates the electron transport resistance. $Z_{\text{electrolyte}}$ is the impedance of diffusion of redox species in the electrolyte. C_{Pt} is the interfacial capacitance at the counter electrode/electrolyte interface.

The total capacitance (C_T) of the electrode is thus given by Eq. 5:

$$C_T = C_{ITO} + C_F \quad (5)$$

where C_F is the series capacitance of C_{TiO_2} and C_H that (see below).

When the applied potential falls in the potential window where TiO_2 behaves as insulator ($E_{VB} \ll E \ll E_{CB}$), the amount of electrons accumulated into the semiconductive film is negligible and only capacitance at the ITO/electrolyte interface (C_{ITO}) remains.

Upon shifting the applied potential toward E_{CB} , electrons are injected (or accumulated) in the TiO_2 film to progressively fill the bandgap electronic states, with both C_{TiO_2} and C_H contributing to the total capacitance according to Eq. 6:

$$\frac{1}{C_F} = \frac{1}{C_{\text{TiO}_2}} + \frac{1}{C_H} \quad (6)$$

Accordingly, the response (*i.e.*, current) of the interface to a change of the electrode potential will depend on the C_H/C_{TiO_2} ratio as evidenced in Figure 1.

For $C_H/C_{\text{TiO}_2} \gg 1$, the capacitance C_F will be governed by C_{TiO_2} . Such a high ratio will be obtained for low C_{TiO_2} values, *i.e.* for potential values remaining far from the conduction band potential. In such a case, and according to Eq. 5, CVs are characterized by an exponential increase of the current as shown in Figure 1A, starting at an onset potential characterizing the accumulation region. As the applied potential gets closer to E_{CB} , the C_H/C_{TiO_2} ratio decreases and the shape of the CV will become more and more rectangular, as evidenced in the simulations of Bisquert et al. reported Figure 1B.

Finally, when the applied potential lies below the conduction band potential (*i.e.*, $E < E_{CB}$), TiO_2 behaves as a fully conductive metal-like electrode and its capacitance is given by the constant Helmholtz capacitance (C_H). In this case, a rectangular shape is expected for the CV as shown in Figure 1C.

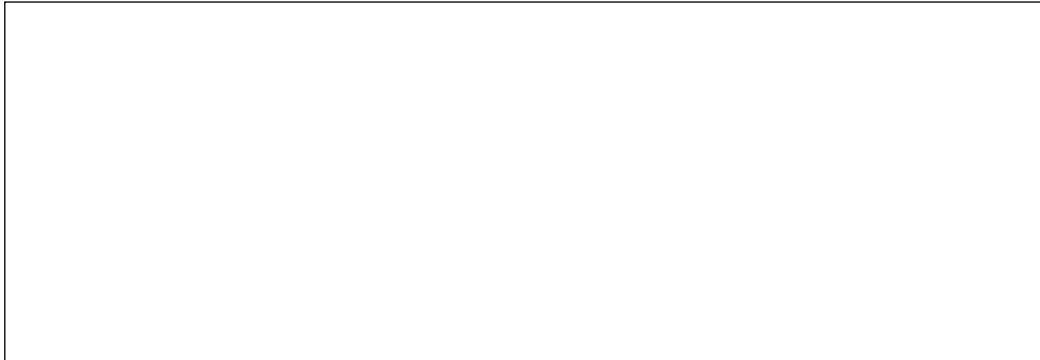


Figure 1. Simulations of cyclic voltammograms for an exponential capacitance with a series of Helmholtz capacitance (C_H) and chemical capacitance (C_{TiO_2}).²⁹ In this simulation, $\alpha = 0.25$ (exponential slope of 240 mV per decade) and $C_H/C_{\text{TiO}_2} = 1000$ for (A), 10 for (B), and 0.1 for (C).

2.4. Specificity of aqueous-based electrolytes

It is well-established that the band positions of semiconductor oxides usually show a strong pH dependence that is generally attributed to acid-base equilibria at the metal oxide surface. This is also the case for TiO₂ as initially demonstrated by Rothenberger et al. using spectroelectrochemical methods.³¹ They evidenced a – 60 mV per pH unit increase dependence of the flatband potential (*i.e.*, the onset potential at which electron starts accumulating within TiO₂) over a pH range from 2 to 12. Further work by Lyon and Hupp demonstrated that the CB edge is indeed controlled by the pH-dependent Ti^{III}/Ti^{IV} couple according to Eq. 7:



A 64 mV shift per log(proton activity) of the E_{CB} value, assumed equal to the flatband potential, was found over ~ 31 pH unit of pH (Figure 2),³² and quantitative uptake of proton upon electrochemical generation of Ti^{III} was moreover supported by EQCM (Electrochemical Quartz Microbalance). According to these two studies, and despite some controversy on the methodology used to determine the flatband and the conduction band potentials in nanostructured TiO₂ electrodes²⁰, the following Eq. 8 is generally used for the pH-dependence of the conduction band potential of nanostructured TiO₂ electrodes³³:

$$E_{CB} = E_{CB}^{\circ} - 0.060 \text{ pH} \quad (8)$$

with E_{CB}° , the value of the conduction band potential edge at pH 0, estimated at *ca.* -0.4 V vs. SCE.

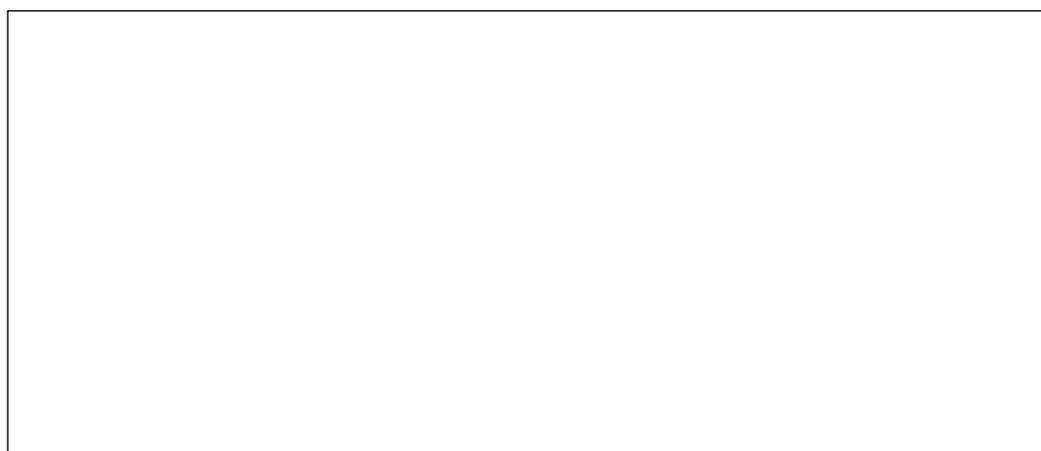


Figure 2. Dependence of reflectance-derived CB edge energy on log(proton activity). (c.s.c.e.: conventional saturated (NaCl) calomel electrode).³²

According to the pH dependence of E_{CB} , the potential window used to investigate nanoparticulate TiO₂ films by cyclic voltammetry has to be adjusted to the pH of the aqueous electrolyte solution, as evidenced in Figure 3.³³ However, the shape of the CV is rather unaffected by the pH change and the capacitive current exhibits the following characteristics, that are fully in line with the model presented in the previous section.

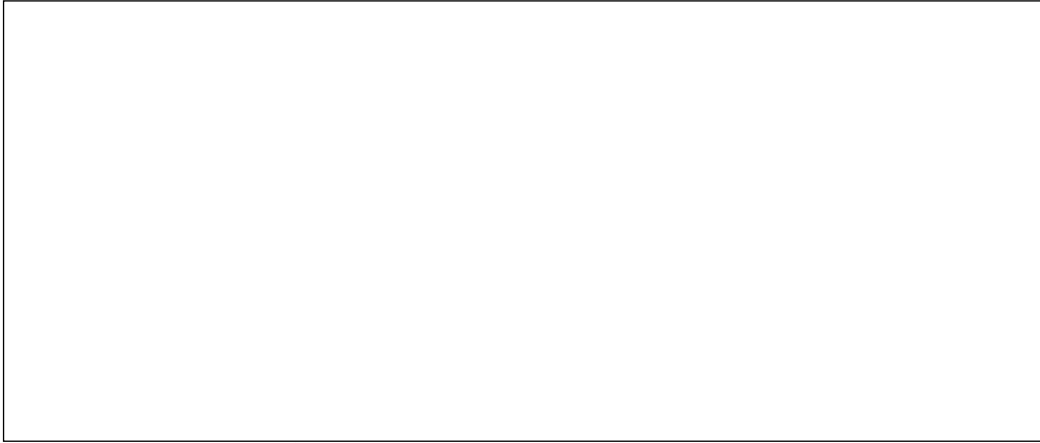


Figure 3. Cyclic voltammograms of a nanoparticulate TiO₂ film soaked in an aqueous solution at (black) pH 3 and (red) pH 11.³⁴ According to Eq. 8, E_{CB} values are estimated to -0.54 and -1.02 V vs. Ag/AgCl for pH 3 and 11, respectively.

Firstly, at potentials $E > 0$ V, the intensity remains low and independent of the applied potential. In this potential window, the TiO₂ film behaves as an insulating porous layer. As long as the applied potential remains much more positive than the conduction band potential of TiO₂, the observed background current only arises from the electrical double-layer charging capacitance of the underlying exposed conductive substrate.

Secondly, exponential increase of the intensity is observed once the applied potential lies below *ca.* -0.1 V and -0.6 V at pH 3 and 11, respectively. At this onset potential, progressive filling of electronic states starts (*i.e.*, the filling of bulk or surface localized states that are distributed in the sub-bandgap region of TiO₂ and filling of extended range of conduction band when the potential is raised close to E_{CB}), allowing for progressive increase of the film conductivity. The current corresponds thus to the chemical capacitive charging current of semiconductive mesoporous TiO₂ film (C_F) and shows exponential increase with the applied potential (when C_F is governed by C_{TiO_2} , *i.e.* when E remains far from E_{CB}).

Finally, as the applied potential reaches the conduction band potential (*i.e.* -0.58 V and -1.06 V at pH 3 and 11, respectively), the semiconductive material is expected to turn out fully degenerate and so to behave as a metal-like conductive film. Under this condition, negative charges are accumulated in TiO₂ by applying cathodic potential, the capacitive background current should become theoretically constant and independent of the potential and just governed by the charging of the double-layer generated at the quasi-metallic TiO₂ film. It is however worth to note that the CV presented here (as most of the CVs available in the literature) do not exactly show the expected rectangular shape expected. This might be due to the occurrence of proton insertion resulting into strong electron accumulation as will be discussed in the next section.

3. Redox reactivity of TiO₂ electrodes and charge storage

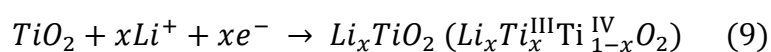
One of the important characteristic of nanostructured porous semiconductive TiO₂ electrode is their ability to massively accumulate electrons, which makes them of prime interest for the development of supercapacitors or batteries.²⁹ In this section, we will thus present the two charge accumulation mechanisms occurring in aqueous electrolytes at conductive nanostructured TiO₂ electrodes, *i.e.* when the applied potential lies below the conduction band potential so that the metal oxide film is in its fully conductive state.

First, once the metal oxide behaves as a conductive material, charge accumulation occurs at the electrode/electrolyte interface through formation of the electrical double layer (EDL). This corresponds to the non-faradaic accumulation of ions from the electrolyte at the metal oxide surface and it is directly proportional to the expanded surface of the material.

Secondly, reversible charge accumulation can also occur by a faradaic redox process associated to the reduction of Ti^{IV} to Ti^{III}. As discussed in the previous section, this reaction can occur at the metal oxide/electrolyte interface and may explain the pH-dependence of E_{CB} observed in aqueous electrolytes. However, it is also expected to occur in the bulk material as long as small cations are present in the electrolyte to insert and locally compensate the charge. As a consequence, massive redox formation of the reduced Ti^{III} ion within the bulk material may occur which is associated to a strong electrochromic effect and blue-black coloration of the film. This ion-insertion faradaic charge storage process has mainly been studied with small

cations such as Li^+ or H^+ , which are capable of insertion and diffusion within the metal oxide lattice.

It is now well established that Li^+ can readily be massively inserted into the TiO_2 lattice. This process was mainly studied in aprotic electrolytes and in presence of highly concentrated electrolytes (typically few molar).³⁵⁻³⁶ Upon Li^+ insertion, charge accumulation within TiO_2 allows for formation of Li_xTiO_2 phases that are exploited as negative electrode in lithium-ion battery. The electrochemical lithiation/delithiation reaction of TiO_2 is described by Eq. 9:^{26,37-38}



with $0 < x < 1$, the mole fraction of inserted Li^+ . This value is greatly affected by the crystallinity of TiO_2 , and a maximal x value of 1 is obtained for (B)- TiO_2 ³⁹, allowing thus to reach the maximal theoretical charge storage capacity of TiO_2 , *i.e.* $335 \text{ mA}\cdot\text{h}\cdot\text{g}^{-1}$. The lithiation/delithiation process remains however slow, which is due to the quite slow diffusion of Li^+ within the TiO_2 lattice, and requires thus very low scan rates to be studied by cyclic voltammetry (typically $< 1 \text{ mV}\cdot\text{s}^{-1}$). In aqueous electrolytes, strong charge accumulation was also observed in presence of a lithium-based electrolyte under basic conditions. This was attributed to Li^+ insertion and thus exploited in the development of rechargeable aqueous alkaline batteries.²³⁻²⁴

Proton insertion within TiO_2 has also been evidenced in aqueous electrolytes, but it is worth to note that this process remains far much less studied than Li^+ insertion. As mentioned in the previous section, Lyon and Hupp have evidenced that the electrochemical reduction of TiO_2 is accompanied by proton uptake over a wide pH range and so assumed that the process occurs within the bulk of the material.³² More recently, Ghicov studied the electrochemical uptake of H^+ in anatase TiO_2 nanotubes.⁴⁰ They observed a high storage capacity together with a strong electrochromic effect upon charge accumulation under strongly acidic conditions (pH 1). By comparing with bulk TiO_2 , they conclude that proton insertion is limited to surface near region and that storage capacity depends on the surface area rather than on the bulk amount of TiO_2 . Accordingly, it is now well-admitted that charge storage within TiO_2 can occur in aqueous solution through proton insertion according to Eq. 10:



Still, many crucial questions concerning proton insertion remains fully open. This concerns notably the source of protons, especially under strong basic conditions where the amount of free protons is negligible, but also the rate and reversibility of the process as well as whether it is a massive process or not. These questions will be addressed in the present study.

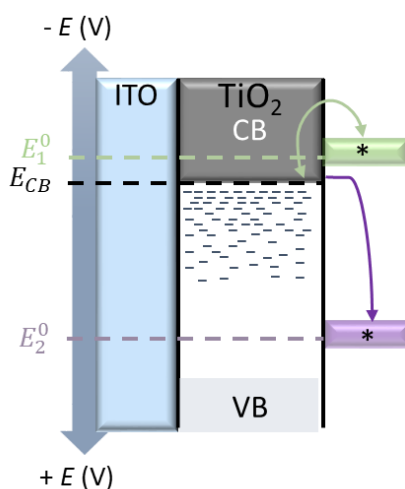
4. Charge transfer at functionalized mesoporous TiO₂ electrode

In the previous sections 2 and 3, we focused on the electrochemical features and charge storage processes at non-functionalized nanostructured TiO₂. Another important field of investigation for semiconductive TiO₂-based materials is when the later are associated to a charge transfer with an immobilized redox active molecule, which is typically the case in photoelectrochemical applications such as DSSCs. In such applications, an electron transfer reaction is generally produced by photoexcitation of an immobilized redox-active chromophore, which once excited leads to the photoinjection of electrons into the conduction band of TiO₂. The efficiency of this process is strongly dependent on the detrimental back electron transfer reaction occurring between the reduced TiO₂ and the oxidized dye.⁴¹ Accordingly, better understanding of electron transfer between the semiconductive electrodes and adsorbed dyes is of crucial importance.

In earlier work in the laboratory, a new UV-visible spectroelectrochemical method was developed to investigate functionalized nanostructured TiO₂ films. Thanks to the large surface area of the nanostructured semiconductive film, large amount of redox-active chromophores can be immobilized, up to a concentration easily detected by spectroscopy. This allows for cross-correlation of absorbance data, arising from the redox-active immobilized chromophore, and electrochemical data associated to the functionalized semiconductive electrode. This methodology allowed notably deciphering between the different modes of charge transport mechanisms that can occur in a mesoporous TiO₂ film loaded with a redox probe (*i.e.*, by physical diffusion of the redox species, by hopping electron transfer mechanism, and by electron diffusion within the TiO₂ material). Also, a model for interfacial electron transfer of TiO₂ functionalized with redox active molecules was successfully developed.²⁸

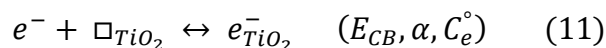
One interesting aspect to note is that the difference of energy position (*i.e.*, potential) between the adsorbed redox active molecule and the TiO₂ conduction band defines not only the thermodynamics of the interfacial electron transfer, but also its reversibility. Indeed,

interfacial electron transfer at the TiO_2 electrode can only occur once the conductivity of the semiconductive film is high enough, *i.e.* once the applied potential is close enough to the conduction band. Accordingly, when the formal potential of the adsorbed redox probe lies much more positive than the conduction band potential (*i.e.*, $E^\circ \gg E_{CB}$), interfacial electron transfer at the TiO_2 interface is irreversible (see scheme 4). In this case, the TiO_2 film shows a diode-like behavior.²⁸ On the contrary, when the formal potential of the adsorbed redox probe lies close (or below, $E^\circ \leq E_{CB}$) to the conduction band potential, the interfacial electron transfer is fully reversible, as recently demonstrated with nanostructured SnO_2 films.⁴²



Scheme 4. Schematic representation of the electronic states involved in the interfacial electron transfer between an EISA- TiO_2 semiconductive film electrode ($\alpha = 1$) and adsorbed redox probes (*) characterized by two different standard redox potentials. In green: if the redox potential lies within the conduction band potential of TiO_2 , electron transfer is expected to be reversible. In violet: interfacial electron transfer will be irreversible if the redox potential of redox active molecule lies far from the conduction band of TiO_2 .

A second interesting aspect concerns the determination of whether localized bandgap electronic states (or trap states) are involved in the interfacial electron transfer or not. In the model developed, fast electron injection from the underlying conductive ITO surface to an exponential distribution of electronic state of TiO_2 (*i.e.*, a Boltzmann distribution of empty conduction band electronic states complemented by an exponential distribution of empty surface states localized in the bandgap) is followed by fast transport of the injected electrons ($e^-_{\text{TiO}_2}$) through a random walk diffusion-like process across the TiO_2 mesoporous network (so fast that it can be assumed not rate limiting).



In this description, C_e° is the maximal concentration of electrons that can be injected at saturation in the TiO_2 material and the parameter α ($0 < \alpha \leq 1$) is a dimensionless factor that characterizes the energy distribution of the localized electronic states involved in the interfacial electron transfer. In the previous work with EISA- TiO_2 electrode²⁸, the α value was found to be 1. This value allowed to conclude that only electrons from the extended conduction band states are involved in the heterogeneous electron transfer reaction. An explanation put forward to interpret this lack of electron transfer communication between the localized traps in TiO_2 and the immobilized redox molecule is that traps are predominantly located into the bulk TiO_2 rather than on the surface of the metal oxide material. This seems to be a specificity of TiO_2 . Indeed, in the case of EISA- SnO_2 electrodes⁴², the α value was founded lower than 1, indicating that the electrons involved in the interfacial electron transfer arise from a larger energy distribution of electronic states, and so the involvement of low energy electronic surface states distributed in the bandgap.

5. Aim of the present PhD work

The aim of the present work is to further investigate charge transfer/transport and charge storage at nanostructured TiO_2 electrodes under aqueous electrolyte conditions, pursuing thus previous work developed at LEM. For such purpose, we will take advantage of highly reproducible mesoporous amorphous TiO_2 electrodes prepared by a one-step vapor deposition method called GLAD (*i.e.*, glancing angle deposition method) from our collaborator in Canada (Dr. Kenneth Harris from the National Institute of Nanotechnology, Edmonton). These electrodes, constituted of TiO_2 -based nanocolumns oriented perpendicular to a conductive underlying substrate, are characterized by a well-opened mesoporosity, a tunable film thickness and a high surface area and, last but not least an excellent reproducibility that allows for quantitative fundamental studies. The detailed electrode preparation and properties are described in the experimental part (section 3).

This manuscript consists of two main parts. Part A (chapters 1 and 2) covers the understanding of charge transport and electron transfer at metal oxide GLAD-electrodes functionalized by a redox active catalytic chromophore. In part B (chapters 3 and 4), we will

focus on charge accumulation within non-functionalized GLAD-TiO₂ electrodes in aqueous solutions.

In chapter 1, we have investigated the non-catalytic and catalytic reactivity of semiconductive GLAD-TiO₂ electrodes functionalized by a manganese porphyrin as redox active chromophore for the catalytic reduction of O₂. A systematic comparison with functionalized GLAD-ITO electrodes was performed in order to unambiguously conclude on the influence of the TiO₂ semiconductive film on the observed reactivity. This work takes advantage of a spectroelectrochemical method developed at LEM, notably by C. Renault, which makes it possible to not only study charge transfer processes at nanostructured semiconductive interfaces functionalized by redox probes that do not possess catalytic activity (briefly described in section 4), but also to investigate the catalytic reactivity of a redox chromophore adsorbed in a nanostructured film of totally conductive metal oxide.^{28,43} In the present study, the redox catalyst, *i.e.* the manganese porphyrin, is chemisorbed at the metal oxide interface thanks to phosphonate functional groups which allows for simplified analysis of charge transport by minimizing desorption of the redox probe and avoiding its interfering physical diffusion throughout the semiconductive film.

Chapter 2 reports on a published study concerning an alternative functionalization protocol developed in order to achieve stable surface functionalization of mesoporous metal oxide films by diazonium electrografting. For such a purpose, planar and high surface fully conductive GLAD-ITO electrodes we modified by a free-base porphyrin diazonium salt through *in-situ* electrodeposition, and then characterized by various analytical methods. This is to our knowledge the first demonstration of high surface ITO electrode functionalized by the diazonium electrografting method. It was initially planned to transpose this process to semiconductive GLAD-TiO₂ electrodes, but unfortunately this could not be done as part of this PhD work due to a lack of time.

Chapter 3 reports on a second published work evidencing that massive, fast, and reversible proton insertion can occur within GLAD-TiO₂ electrodes at neutral pH, *i.e.* in the absence of a significant amount of free protons in solution. In order to emphasize this point, coupled proton-electron storage in GLAD-TiO₂ was investigated by spectroelectrochemistry in either strongly acidic unbuffered aqueous electrolyte (*i.e.*, hydrochloric acid) or buffered aqueous electrolyte at neutral pH 7.0 condition (*i.e.*, Hepes buffer solution). Quantitative analysis of the proton-coupled electron storage reaction was achieved, allowing us to evidence

a process limited by diffusion and to estimate the diffusion coefficient of protons within the bulk TiO₂. On the basis of these experimental results, a model was developed by Pr. C. Costentin to account for cyclic voltammetry modeling of charge storage in conductive materials. This has been the subject of a publication (see annexe).⁴⁴

While chapter 3 is mainly focused on proton insertion at pH 7.0 in the Hepes buffer, in chapter 4, proton-coupled charge accumulation was further investigated from an enlarged point of view in a wide range of aqueous electrolytes. Organic and inorganic weak acid aqueous electrolytes (*i.e.*, with diverse pK_a values) were notably studied under various pH conditions and with advanced types of GLAD-TiO₂ electrodes (see experimental parts) in order to get deeper insights into the crucial parameters of both the electrolyte and the electrode affecting the charge storage performances. These charge/discharge processes have been studied with a view to developing in the medium term a rechargeable aqueous battery based on the reversible insertion of protons, and using a negative electrode consisting of a nanostructured TiO₂ film.

References

- ¹ Lewis, N. S. Toward Cost-Effective Solar Energy. *Science*. **2007**, 315, 798-801.
- ² Armaroli, N.; Balzani, V. Solar Electricity and Solar Fuels: Status and Perspectives in the Context of the Energy Transition. *Chem. Eur. J.* **2016**, 22, 32-57.
- ³ Chen, X.; Mao, S. S. Titanium Dioxide Nanomaterials: Synthesis, Properties, Modifications, and Applications. *Chem. Rev.* **2007**, 107, 2891-2959.
- ⁴ Wang, H. -H.; Su, C.; Chen, H. -S.; Liu, Y. -C.; Hsu, Y. -W.; Hsu, N. -M.; Li, W. -R. Preparation of Nanoporous TiO₂ Electrodes for Dye-Sensitized Solar Cells. *J. Nanomater.* **2011**, 1-7.
- ⁵ Fujihira, A.; Honda, K. Electrochemical Photolysis of Water at a Semiconductor Electrode. *Nature*. **1972**, 238, 37-38.
- ⁶ Zhang, Y.; Xiong, X.; Han, Y.; Zhang, X.; Shen, F.; Deng, S.; Xiao, H.; Yang, X.; Yang, G.; Peng, H. Photoelectrocatalytic degradation of recalcitrant organic pollutants using TiO₂ film electrodes: An overview. *Chemosphere*. **2012**, 88, 145-154.
- ⁷ Watanabe, T.; Nakajima, A.; Wang, R.; Minabe, M.; Koizumi, S.; Fujishima, A.; Hashimoto, K. Photocatalytic activity and photoinduced hydrophilicity of titanium dioxide coated glass. *Thin Solid Films*. **1999**, 351, 260-263.
- ⁸ Kraeutler, B.; Bard, A. J. Heterogeneous Photocatalytic Decomposition of Saturated Carboxylic Acids on TiO₂ Powder. Decarboxylative Route to Alkanes. *J. Am. Chem. Soc.* **1978**, 100, 5985-5992.
- ⁹ Gaya, U. I.; Abdullah, A. H.; Heterogeneous photocatalytic degradation of organic contaminants over titanium dioxide: A review of fundamentals, progress and problems. *J. Photochem. Photobiol. C*. **2008**, 9, 1-12.
- ¹⁰ Grätzel, M. Sol-Gel Processed TiO₂ Films for Photovoltaic Applications. *JSST*, **2001**, 22, 7-13.
- ¹¹ Chen, D.; Huang, F.; Cheng, Y. -B.; Caruso, R. A. Mesoporous Anatase TiO₂ Beads with High Surface Areas and Controllable Pore Sizes: A Superior Candidate for High-Performance Dye-Sensitized Solar Cells. *Adv. Mater.* **2009**, 21, 2206-2210.
- ¹² Koo, H. -J.; Kim, Y. J.; Lee, Y. H.; Lee, W. I.; Kim, K.; Park, N. -G. Nano-embossed Hollow Spherical TiO₂ as Bifunctional Material for High-Efficiency Dye-Sensitized Solar Cells. *Adv. Mater.* **2008**, 20, 195-199.
- ¹³ Ashford, D. L.; Gish, M. K.; Vannucci, A. K.; Brennaman, M. K.; Templeton, J. L.; Papanikolas, J. M.; Meyer, T. J. Molecular Chromophore-Catalyst Assemblies for Solar Fuel Applications. *Chem. Rev.* **2015**, 115, 13006-13049.
- ¹⁴ Ma, Y.; Wang, X. L.; Jia, Y. S.; Chen, X. B.; Han, H. X.; Li, C. Titanium Dioxide-Based Nanomaterials for Photocatalytic Fuel Generations. *Chem. Rev.* **2014**, 114, 9987-10043.
- ¹⁵ Kitano, M.; Matsuoka, M.; Ueshima, M.; Anpo, M. Recent developments in titanium oxide-based photocatalysts. *Applied Catalysis, A. General*, **2007**, 1, 325.

- ¹⁶ Zhonghe Bi, Z.; Paranthaman, M. P.; MENCHHOFFER, P. A.; Dehoff, R. R.; Bridges, C. A.; Chi, M.; Guo, B.; Sun, X. -G.; Dai, S. Self-organized amorphous TiO₂ nanotube arrays on porous Ti foam for rechargeable lithium and sodium ion batteries. *J. Power Sources*. **2013**, 222, 461-466.
- ¹⁷ Armstrong, G.; Armstrong, A. R.; Canales, J.; Bruce, P. G. TiO₂ (B) Nanotubes as Negative Electrodes for Rechargeable Lithium Batteries. *ECS Solid State Lett.* **2006**, 9, A139-A143.
- ¹⁸ Lu, X.; Wang, G.; Zhai, T.; Yu, M.; Gan, J.; Tong, Y.; Li, Y. Hydrogenated TiO₂ Nanotube Arrays for Supercapacitors. *Nano Lett.*, **2012**, 12, 1690-1696.
- ¹⁹ Nang Dinh, N.; Minh Quyen, N.; Chung, D. N.; Zikova, M.; Truong, V. Van Highly-efficient electrochromic performance of nanostructured TiO₂ films made by doctor blade technique. *Sol. Energy Mater. Sol. Cells* **2011**, 95, 618-623.
- ²⁰ Berger, T.; Monllor-Satoca, D.; Jankulovska, M.; Lana-Villarreal, T.; Gomez, R. The Electrochemistry of Nanostructured Titanium Dioxide Electrodes. *ChemPhysChem*. **2012**, 13, 2824 – 2875.
- ²¹ Bella, F.; Gerbaldi, C.; Barolo, C.; Grätzel, M. Aqueous dyesensitized solar cells. *Chem. Soc. Rev.* **2015**, 44, 3431-3473.
- ²² Bella, F.; Galliano, S.; Falco, M.; Viscardi, G.; Barolo, C.; Grätzel, M.; Gerbaldi, C. Unveiling iodine-based electrolytes chemistry in aqueous dye-sensitized solar cells. *Chem. Sci.* **2016**, 7, 4880-4890.
- ²³ Liu, S.; Pan, G. L.; Yan, N. F.; Gao, X. P. Aqueous TiO₂/ Ni(OH)₂ rechargeable battery with a high voltage based on proton and lithium insertion/extraction reactions. *Energy Environ. Sci.* **2010**, 3, 1732.
- ²⁴ Liu, J.; Wang, J.; Ku, Z.; Wang, H.; Chen, S.; Zhang, L.; Lin, J.; Shen, Z. X. Aqueous Rechargeable Alkaline Co_xNi_{2-x}S₂/TiO₂ Battery. *ACS Nano*. **2016**, 10, 1007-1016.
- ²⁵ Bisquert, J. Physical electrochemistry of nanostructured devices. *PhysChemChemPhys* **2008**, 10, 49
- ²⁶ Boschloo, G.; Fitzmaurice, D. Electron Accumulation in Nanostructured TiO₂ (Anatase) Electrodes. *J. Phys. Chem. B* **1999**, 103, 7860-7868.
- ²⁷ Nelson, J. Continuous-time random-walk model of electron transport in nanocrystalline TiO₂ electrodes. *Phys. Rev. B*. **1999**, 59, 15374 – 15380.
- ²⁸ Renault, C.; Nicole, L.; Sanchez, C.; Costentin, C.; Balland, V.; Limoges, B. Unraveling the Charge Transfer/Electron Transport in Mesoporous Semiconductive TiO₂ Films by Voltabsorptometry. *Phys. Chem. Chem. Phys.* **2015**, 17, 10592-10607.
- ²⁹ Fabregat-Santigato, F.; Mora-Sero, I.; Garcia-Belmonte, G.; Bisquert, J. Cyclic Voltammetry Studies of Nanoporous Semiconductors. Capacitive and Reactive Properties of Nanocrystalline TiO₂ Electrodes in Aqueous Electrolyte. *J. Phys. Chem. B*. **2003**, 107, 758-768.

- ³⁰ Abayev, I.; Zaban, A.; Fabregat-Santiago, F.; Bisquert, J. Electronic conductivity in nanostructured TiO₂ films permeated with electrolyte. *J. Phys. Stat. Sol. (a)* **2003**, 196, 1, R4–R6.
- ³¹ Rothenberger, G.; Fitzmaurice, D.; Grätzel, M. Spectroscopy of Conduction Band Electrons in Transparent Metal Oxide Semiconductor Films: Optical Determination of the Flatband Potential of Colloidal Titanium Dioxide Films. *J. Phys. Chem.* **1992**, 96, 5983-5986.
- ³² Hupp, J. T.; Lyon, L. A. Energetics of the Nanocrystalline Titanium Dioxide/Aqueous Solution Interface: Approximate Conduction Band Edge Variations between H₀ = -10 and H. = +26. *Phys. Chem. B.* **1999**, 103, 4623-4628.
- ³³ Hagfeldt A.; Grätzel, M. Light-induced redox reactions in nanocrystalline systems. *Chem. Rev.* **1995**, 95, 49-68.
- ³⁴ Bisquert, J.; Fabregat-Santigato, F.; Mora-Sero, I.; Garcia-Belmonte, G.; Barea, E. M.; Palomares, E. A review of recent results on electrochemical determination of the density of electronic states of nanostructured metal-oxide semiconductors and organic hole conductors. *Inorg. Chim. Acta.* **2008**, 361,684–698.
- ³⁵ Henrik Lindström, H., Södergren, S.; Solbrand, A.; Rensmo, H.; Hjelm, J.; Hagfeldt, A.; Lindquist, S. –E. Li⁺ Ion Insertion in TiO₂ (Anatase). 2. Voltammetry on Nanoporous Films. *J. Phys. Chem B.* **1997**, 101, 7717-7722.
- ³⁶ Henrik Lindström, H., Södergren, S.; Solbrand, A.; Rensmo, H.; Hjelm, J.; Hagfeldt, A.; Lindquist, S. –E. Li⁺ Ion Insertion in TiO₂ (Anatase). 1. Chronoamperometry on CVD Films and Nanoporous Films. *J. Phys. Chem B.* **1997**, 101, 7710-7716.
- ³⁷ Wu, M. –S.; Wang, M. –J.; Jow, J. –J.; Yang, W. –D.; Hsieh, C. –Y.; Tsai, H. –M. Electrochemical fabrication of anatase TiO₂ nanostructure as an anode material for aqueous lithium-ion batteries. *J. Power Sources.* **2008**, 185, 1420-1424.
- ³⁸ Reinman, K. H.; Brace, K. M.; Gordon-Smith, T. J.; Nandhakumar, I.; Attard, G. S.; Owen, J. R. Lithium insertion into TiO₂ from aqueous solution – Facilitated by nanostructure. *Electrochem Commun.* **2006**, 8, 517–522.
- ³⁹ Dylla, A. G.; Henkelman, G.; Stevenson, K. J. Lithium Insertion in Nanostructured TiO₂(B) Architectures. *Acc. Chem. Res.* **2013**, 46, 1104-1112.
- ⁴⁰ Ghicov, A.; Tsuchiya, H.; Hahn, R.; Macak, J. M.; Muñoz, A. G.; Schmuki, P. TiO₂ nanotubes: H⁺insertion and strong electrochromic effects. *Electrochem Commun.* **2006**, 8, 528-532.
- ⁴¹ Ko, K. H.; Lee, Y. C.; Jung, Y. J. Enhanced efficiency of dye-sensitized TiO₂ solar cells (DSSC) by doping of metal ions. *J Colloid Interface Sci.* **2005**, 283, 482–487.
- ⁴² Hamd, W.; Laberty-Robert, C.; Lambert, F.; Costentin, C.; Limoges, B.; Balland, V. Investigating Charge Transfer in Functionalized Mesoporous EISA-SnO₂ Films. *J. Phys. Chem. C.* **2017**, 121, 23207-23217.

⁴³ Renault, C.; Andrieux, C. P.; Tucker, R. T.; Brett, M. J.; Balland, V.; Limoges, B. Unraveling the Mechanism of Catalytic Reduction of O₂ by Microperoxidase-11 Adsorbed within a Transparent 3D-Nanoporous ITO Film. *J. Am. Chem. Soc.*, **2012**, 134, 6834–6845.

⁴⁴ Kim, Y. S.; Balland, V.; Limoges, B.; Costentin, C. Cyclic voltammetry modeling of proton transport effects on redox charge storage in conductive materials: application to a TiO₂ mesoporous film. *Phys. Chem. Chem. Phys.*, **2017**, 19, 17944-17951.

**Chapter I. Reactivity of conductive GLAD-ITO and
semiconductive GLAD-TiO₂ electrodes
functionalized by a manganese porphyrin (Mn-ph)**

1. Introduction

1.1. Aim of work

1.2. Methodology

2. Electrode functionalization

2.1. Description of GLAD-electrodes

2.2. Chemical surface functionalization of GLAD electrodes by Mn-ph

3. Interfacial electron transfer at Mn-ph/GLAD-electrodes under degassed condition

3.1. Mn-ph/GLAD-ITO

3.2. Mn-ph/GLAD-TiO₂

4. Catalytic reduction of O₂ at Mn-ph-modified GLAD-ITO and GLAD-TiO₂ electrodes

4.1. Mn-ph/GLAD-ITO

4.2. Mn-ph/GLAD-TiO₂

5. Conclusion

1. Introduction

1.1. Aim of work

In this chapter, the main objective was to study and characterize the dynamics of charge transfer and electron transport within a transparent mesoporous semiconductor metal oxide film of TiO₂ coupled to the catalytic reactivity of a redox-active molecular catalyst immobilized within this porous film. Qualitative and quantitative analysis were carried out to interpret and elicit the crucial information on the heterogeneous charge transfer occurring between the adsorbed redox species and the semiconductive mesoporous TiO₂ film. Another objective of this study is to complement the knowledge acquired through a series of works previously carried out in the laboratory and that have allowed a better understanding of the charge transport/electron transfer within mesoporous TiO₂ and SnO₂ films functionalized with redox active porphyrins.¹⁻² In these previous works, through the modeling of interfacial charge transfer between the adsorbed redox species and the porous semiconductor, the electron transport by different modes (*i.e.*, through physical diffusion, electron hopping, or conduction band) was unraveled.

In the present work, with the aim to go a step further in the understanding of the electron transfer and charge transport properties within a mesoporous semiconductive material, the reactivity of a redox-active porphyrin immobilized within a nanostructured mesoporous TiO₂ film has been investigated under catalytic turnover conditions (*i.e.*, under the catalytic reduction of molecular oxygen). The aim here is to address some unsolved fundamental questions concerning the influence of the semiconductor network on the catalytic reactivity of a molecular catalyst immobilized on its surface. Moreover, in order to observe unique features of the semiconductive TiO₂ films, fully conductive ITO films were investigated as well to compare those two films with different conductive characteristics.

This fundamental work is linked to the field of energy conversion technologies such as dye-sensitized solar cells or photoelectrocatalytic cells for the reason that many of these applications are conceptually based on the immobilization of molecular redox-active catalyst or dye within a conductive or semiconductive mesoporous metal oxide films.³⁻⁶ Consequently, in order to better understand and optimize these systems, there is a need to investigate the fundamental aspects of electron transport and charge transfer processes that take place within these functionalized mesoporous semiconductive films.

1.2. Methodology

The important role of metalloporphyrins plays in vital biological processes, in particular photosynthesis (chlorophyll), oxygen transport (hemoglobin), oxygen activation (cytochrome).⁷ Interest in metalloporphyrins are not confined only in the biological field as these compounds are well-known dyes for photocatalysis and efficient molecular redox catalysts in the presence of O₂, H₂O₂, or other oxidants.⁸⁻¹¹ Among the various available metalloporphyrins, we have selected and synthesized the manganese porphyrin (Mn-ph) which is an ideal one-electron redox porphyrin with intense absorption band around 466 nm (Soret band, will discuss later), a redox-active molecular chromophore known to efficiently catalyze the reduction of molecular O₂.¹⁰⁻¹³ This manganese porphyrin (see experimental part, page 46 for a chemical structure) is functionalized with a phosphonate group in such a way to allow its anchoring on the surface of a metal oxide material through stable chemisorption.¹⁴⁻¹⁵

The mesoporous ITO and TiO₂ films were prepared by GLAD, a physical vapor deposition method that allows producing relatively thick mesoporous films of TiO₂ with a high degree of control in the porosity and morphology as well as in the film reproducibility (see experimental part). In previous works in the laboratory, the mesoporous TiO₂ electrodes were prepared by a sol-gel process called evaporation-induced self-assembly (EISA), but, despite the possibility to reach a much higher specific surface area than with the GLAD technique, the batch-to-batch reproducibility was not as good.¹⁴

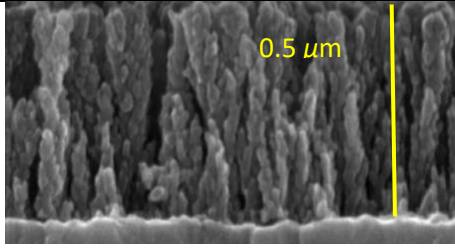
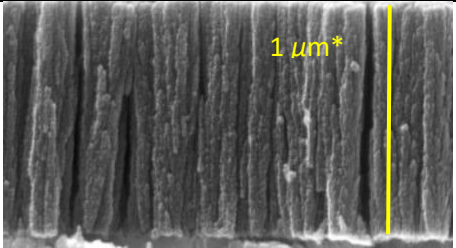
GLAD-ITO and -TiO₂ mesoporous films also offer a good transparency in the visible range, which is important for quantitatively investigating by real-time spectroelectrochemistry the reactivity of Mn-ph functionalized metal oxide electrodes (*i.e.*, Mn-ph/GLAD-ITO and Mn-ph/GLAD-TiO₂). This methodology allows to simultaneously follow absorbance changes of the immobilized chromophore and transparent semiconductive electrode at specific wavelengths respectively during an electrochemical experiment. Thus, establish the cyclic voltabsorptograms (CVAs) at various specific wavelengths depending on the purpose of focusing on each electron transfer reaction. CVAs and derivative cyclic voltabsorptograms (DCVAs) lead to a particularly accurate monitoring of faradaic electron transfer reactions at immobilized redox chromophores without the capacitive contribution from the high surface area electrode.¹⁶⁻¹⁷

2. Electrode functionalization

2.1. Description of GLAD-electrodes

In this chapter, GLAD-ITO and -TiO₂ films grown on ITO-coated glass slides were used. The structural information for each type of GLAD electrodes is gathered in Table 1.

Table 1. Structural information of the GLAD-ITO and -TiO₂ electrodes used in this chapter.

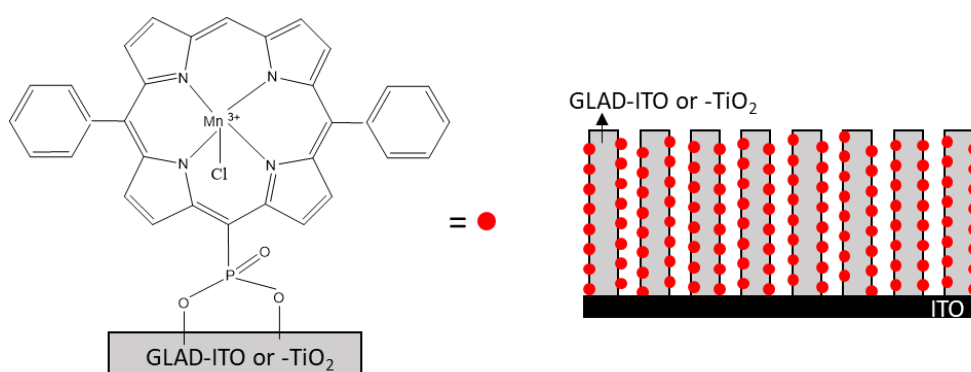
GLAD electrode type	ITO	TiO ₂
Film thickness (d _f , μm) that used in this chapter	0.5	0.55
deposition angle (°)	80	72
Surface enhancement ¹⁸ by BET	65	300
Surface enhancement ¹⁸ by electrochemistry	30	not determined
Porosity ¹⁸	0.54	0.35
SEM image (side view)		

* No SEM image for 0.55 μm film thickness GLAD-TiO₂.

2.2. Chemical surface functionalization of GLAD electrodes by Mn-ph

Functionalization of mesoporous GLAD-electrodes films was achieved by immersing them in a solution of manganese porphyrin (~ 25 μM of Mn-ph in a 1:9 mixture of DMSO and water adjusted to pH 4-5 with HCl) during overnight. Mn-ph was synthesized by our collaborator (Dr. Alla Lemeune) from Université de Bourgogne.¹⁹ Exact concentration of Mn-ph in solution was determined from the Soret band in UV-visible spectroscopy. Absorbance of Mn-ph solution was 0.5 at 466 nm in a 2 mm cuvette. The concentration of Mn-ph, therefore, was estimated to be 25 μM, assuming a molar extinction coefficient of 10⁵ M⁻¹

$l \cdot \text{cm}^{-1}$ at Soret band.²⁰ Mn-ph was immobilized through chemisorption of the phosphonate anchoring group onto the mesoporous metal oxide surfaces (Scheme 1). Thereafter, the Mn-ph-functionalized GLAD electrodes (*i.e.*, Mn-ph/GLAD-ITO or Mn-ph/GLAD-TiO₂) were rinsed with Milli-Q water and immersed in an aqueous buffer solution (*i.e.*, a 0.1 M HEPES buffer with 0.05 M Na₂SO₄, pH 7.0) at least for ~20 min prior to the experiments.



Scheme 1. Schematic representation of chemisorbed Mn-ph onto three-dimensional GLAD-ITO or -TiO₂ electrodes.

The resulting Mn-ph/GLAD-electrodes were characterized by UV-visible absorbance spectroscopy (Figure 1). The UV-visible spectra of the Mn-ph-modified GLAD electrodes were systematically corrected from blank contribution of the unmodified porous metal oxide film. The Soret band of Mn-ph/GLAD-ITO and Mn-ph/GLAD-TiO₂ were both observed at 466 nm, whereas the Soret band of the Mn-ph in solution is located at 462 nm. Once normalized to the real surface area (~35-fold surface area enhancement for the 500 nm GLAD-ITO *vs.* ~300-fold for the 550 nm GLAD-TiO₂), the magnitude of absorbance (representing the surface concentration of Mn-ph immobilized within the metal oxide film) was observed much lower at the Mn-ph/GLAD-TiO₂ than at the Mn-ph/GLAD-ITO. This might be attributed to various other factors such as isoelectric point, binding affinity, porosity, and density of electrodes.

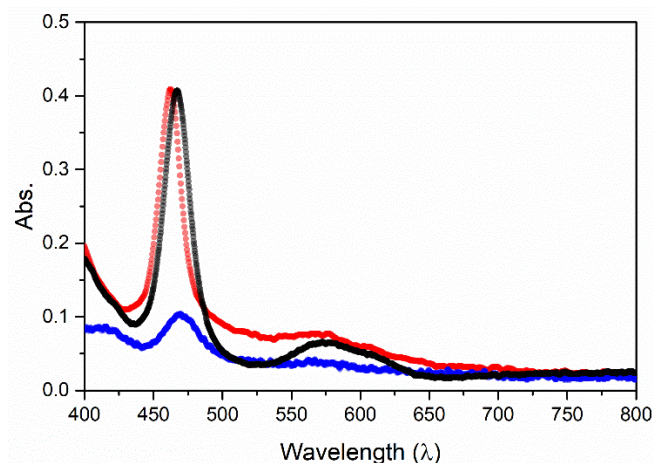


Figure 1. UV-visible spectra of (red) Mn-ph (25 μ M) DMSO and water solution (1:9, v/v), (blue) Mn-ph/GLAD-ITO and (black) Mn-ph/GLAD-TiO₂ in Milli-Q water. The UV-visible spectra of Mn-ph/GLAD-ITO and -TiO₂ were compensated by subtract of contribution of each porous metal oxide film, respectively.

It is well known that the intense Soret band absorption in most porphyrins is attributed to the electron dipole movement that allows a π - π^* transition of $S_0 \rightarrow S_2$ (*i.e.*, ground state to second excited state), while for the Q-band(s) it arises from the $S_0 \rightarrow S_1$ transition (*i.e.*, ground state to first excited state).²⁰ For the immobilized porphyrin, Q-bands at 560 nm are not very well-defined. This is attributed to the fact that the Q-bands has a weak intensity as compare to Soret band due to the weak transition, splitting to several peaks, resulting the ratio of Soret band and Q-band intensities even to be 50:1.²²

In order to identify the wavelength that should be appropriate to monitor in spectroelectrochemistry, the Mn-ph/GLAD-ITO and Mn-ph/GLAD-TiO₂ electrodes were characterized by UV-visible spectroscopy as a function of different applied potentials. Before to apply a cathodic potential, the Soret band located at 466 nm corresponds to the oxidized state of Mn-ph (*i.e.*, Mn^{III}-ph) either at the GLAD-ITO or the GLAD-TiO₂ electrode. After polarizing the electrode at a negative potential of -0.8 V (*vs.* Ag/AgCl), a nearly instantaneous shift of the Soret band at 432 nm is observed, characteristic of the reduced Mn^{II}-ph (Figure 2). These results demonstrate that all immobilized Mn-ph is electroactive.

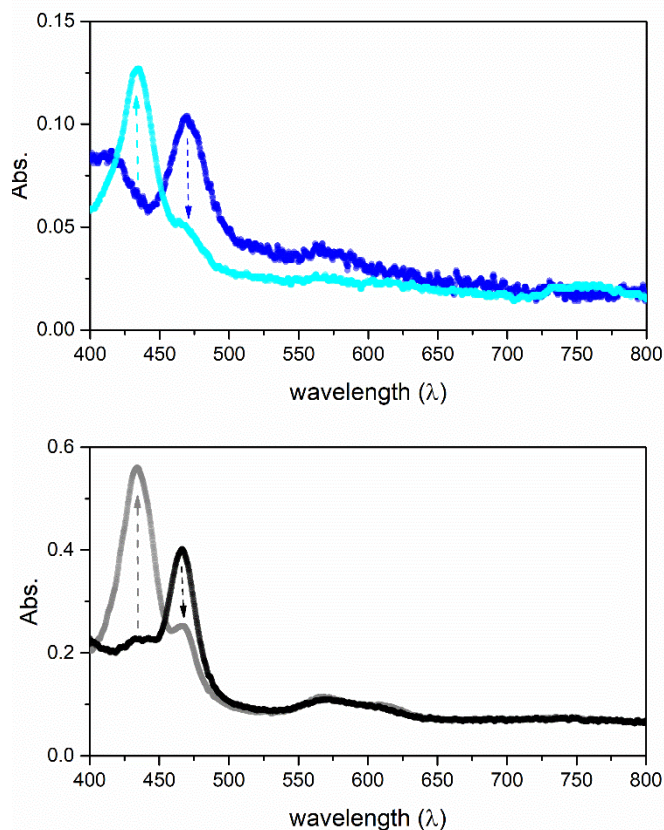


Figure 2. UV-visible spectra of (top) Mn-ph/GLAD-ITO and (bottom) Mn-ph/GLAD-TiO₂ recorded at (blue and black) +0.5 V (vs. Ag/AgCl) and (cyan and grey) -0.8 V (vs. Ag/AgCl). UV-visible spectra were all corrected from the UV-vis blank spectra recorded in the absence of Mn-ph.

3. Interfacial electron transfer at Mn-ph/GLAD-electrodes under degassed condition

The electrochemical reactivity of Mn-ph/GLAD-electrodes under degassed condition was first investigated. Degassed condition was achieved by thoroughly bubbling Argon gas into the electrochemical cell.

3.1. Mn-ph/GLAD-ITO

Mn-ph/GLAD-ITO electrodes were investigated using the combined technique of cyclic voltammetry and UV-visible spectroscopy (*i.e.*, by monitoring the absorbance change at 432 nm during a CV scan). The resulting cyclic voltammograms (CVs) (the current is here normalized to the geometric electrode area, the Faraday constant and the scan rate ν), cyclic voltabsorptograms (CVAs, where the y-axis represents the absorbance change monitored at 432 nm), and the corresponding derivative cyclic voltabsorptograms (DCVAs) are shown in Figure 3.

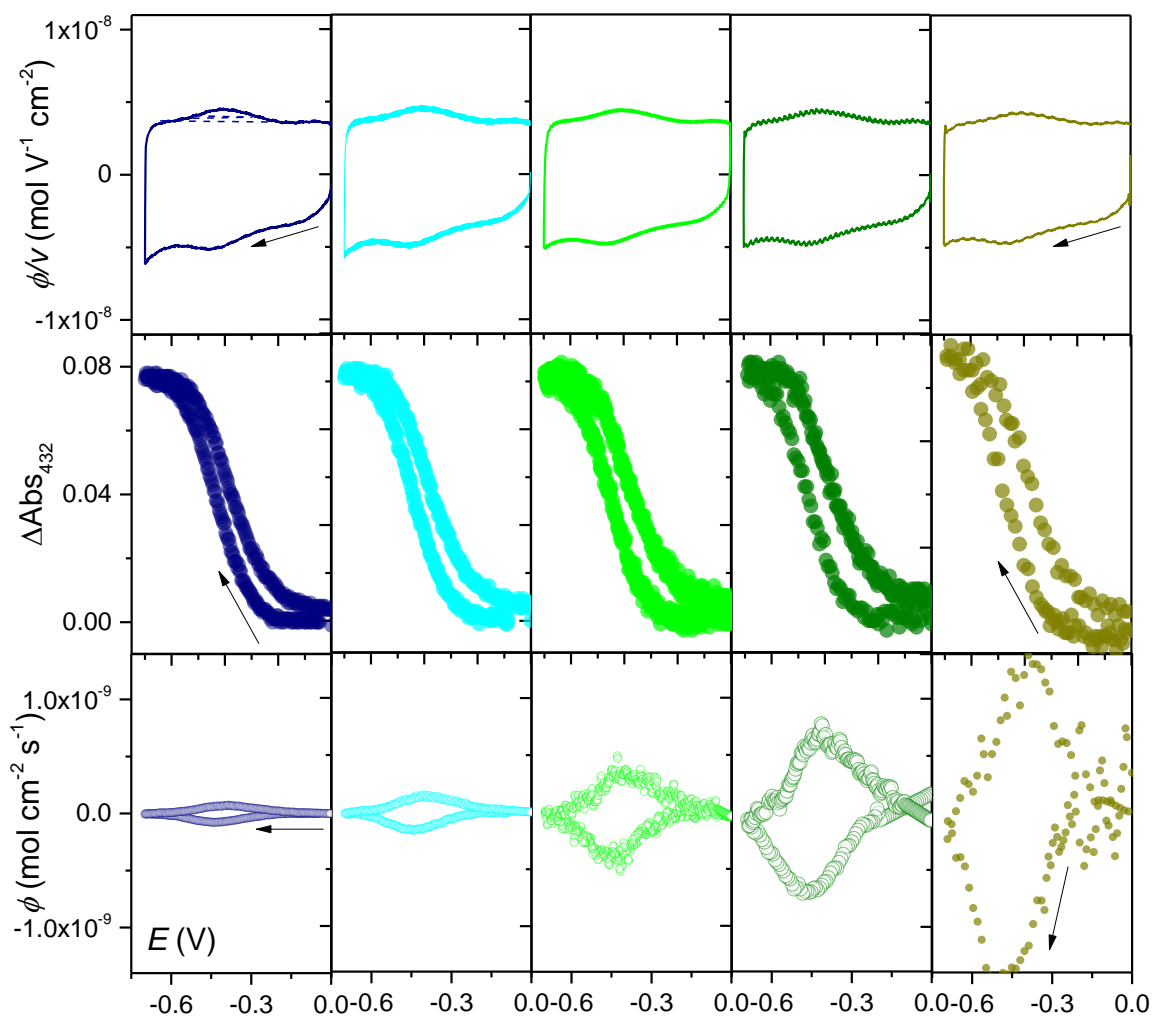


Figure 3. (Top) CVs, (middle) CVAs monitored at 432 nm, and (bottom) corresponding DCVAs recorded at a Mn-ph/GLAD-ITO electrode at a scan rate ν of (navy) $0.1 \text{ V}\cdot\text{s}^{-1}$, (cyan) $0.2 \text{ V}\cdot\text{s}^{-1}$, (green) $0.5 \text{ V}\cdot\text{s}^{-1}$, (olive) $1 \text{ V}\cdot\text{s}^{-1}$, (dark yellow) $2 \text{ V}\cdot\text{s}^{-1}$. Electrolyte is 0.1 M Hepes buffer solution with 50 mM Na_2SO_4 (pH 7.0).

The relationship between CVs and DCVAs is given by the following equation (expressed in electron flux density ϕ , *i.e.*, in $\text{mol}\cdot\text{cm}^{-2}\cdot\text{s}^{-1}$):

$$\phi = \frac{\Delta A_\lambda}{\Delta \varepsilon_\lambda dt} = \frac{i}{nFS} \quad (1)$$

where F is the Faraday constant ($96500 \text{ C}\cdot\text{mol}^{-1}$), n the number of electrons involved in the redox reaction ($n = 1$ for $\text{Mn}^{\text{III}}/\text{Mn}^{\text{II}}$ couple), S is the projected geometric electrode area (cm^2), i current (A), ΔA_λ the absorbance change at a specific wavelength (here at 432 nm), and $\Delta \varepsilon_\lambda$ the extinction coefficient difference between the reduced and oxidized states of Mn-ph (*i.e.*,

Mn^{III}/Mn^{II}). The extinction coefficient difference $\Delta\epsilon_{432}$ is determined from the Beer-Lambert law given by Eq. 2:

$$\Delta A_{432} = \Delta\epsilon_{432} * \Delta\Gamma_{Mn^{II}} \quad (2)$$

From integration of the faradaic peak in CV (dashed line in Figure 3, navy color), the amount of reduced porphyrin ($\Delta\Gamma_{Mn^{II}}$) was estimated to 1.7×10^{-10} mol·cm⁻². From the absorbance change in CVA ($\Delta A_{432} = 0.065$), a $\Delta\epsilon_{432}$ value of 380 000 M⁻¹·cm⁻¹ is obtained.

CVs are characterized by a large rectangular shaped capacitance contribution over the entire potential window, arising from the high surface area conductive GLAD-ITO film. On the top of the capacitive current, a well-defined pair of reversible faradaic peaks centered on a formal potential of -0.42 V vs. Ag/AgCl is observed. It is attributed to the Mn^{III}/Mn^{II} reversible one-electron redox couple process, as confirmed from absorbance variation at 432 nm. It is clearly seen that the total current density (*i.e.*, the sum of capacitive and faradaic current) is proportional to the scan rate, at least within the range of scan rates that were investigated (from 0.1 to 2 V·s⁻¹) (Figures 3 and 4).

It is interesting to note that the absorbance variation on the CVAs shows a full reversibility with a low hysteresis between the forward and backward scans. Also, the absorbance change remains constant and independent of ν up to 2 V·s⁻¹, whereas the faradaic peaks of Mn^{III}/Mn^{II} in CVs and DCVAs (will discuss later) shows a linear relationship with scan rate ν (Figure 4). This result attests of a surface-confined redox process involving a fast interfacial electron transfer. This indicates that all Mn-ph molecules within the film are rapidly and reversibly converted into their reduced and oxidized states within the time scale of the experiment. The surface concentration of Mn-ph can also be estimated from the linear relationship between the electron flux density and the scan rate, using the following expression which assumes a fast Nernstian electron transfer reaction:

$$\phi = \frac{i}{nFS} = \frac{nF}{4RT} \nu \Gamma \quad (3)$$

where ν is the scan rate (in V·s⁻¹), T the temperature (25°C, 298 K), F the Faraday constant (96500 C·mol⁻¹), R the gas constant (8.314 J·K⁻¹·mol⁻¹), n the number of electrons involved in the redox reaction (here $n = 1$), S is the projected geometric electrode surface area, and Γ the surface concentration of the oxidized form of immobilized Mn-ph at the TiO₂ interface (in

mol·cm⁻²). Using Eq. 3, the surface concentration (Γ) was estimated as 1.0×10^{-10} mol·cm⁻², a value which is close to the one estimated from integration of the faradaic peak in CVs (*i.e.*, 1.7×10^{-10} mol·cm⁻²).

Finally, similarly to CVs, DCVAs show a well-defined pair of reversible symmetrical peaks at a formal potential of $E^0 = -0.42$ V that can be attributed to the Mn^{III}-ph/Mn^{II}-ph couple (Figure 3). In contrast to CVs, DCVAs are not affected by a capacitive contribution, allowing thus to better and more accurately discern the redox conversion of Mn-ph. The cathodic and anodic electron flux densities as well as the cathodic and anodic peak potentials of Mn^{III}-ph/Mn^{II}-ph redox process are plotted as a function of ν in Figure 4. Electron flux density is proportional to ν whereas the absorbance changes monitored at 432 nm are independent of ν , a result which is also a characteristic of a thin-layer redox process.

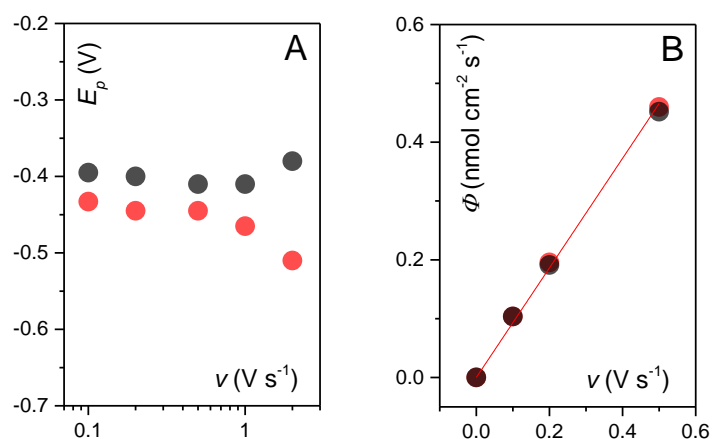
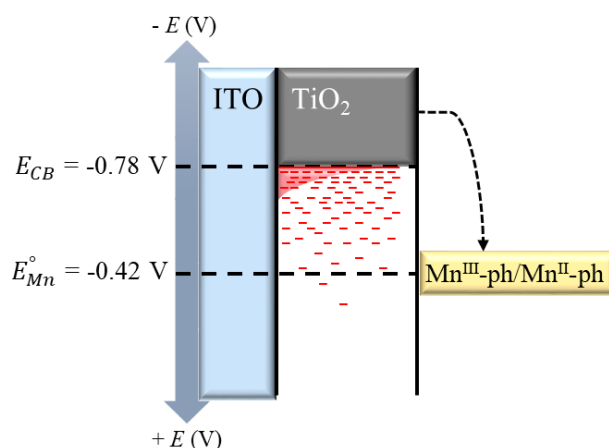


Figure 4. Variation of (A) peak potential and (B) electron flux density of the (red) cathodic and (black) anodic DCVAs peaks as a function of ν .

The kinetics of electron transfer can be inferred by measuring the peak potential separation between the anodic and cathodic waves of DCVAs as a function of ν . Upon raising ν up to $1 \text{ V}\cdot\text{s}^{-1}$, no significant hysteresis (*i.e.*, no large peak separation) is observed on the DCVAs, indicating that the heterogeneous electron transfer is fast and not rate-limiting. At a scan rate higher than $2 \text{ V}\cdot\text{s}^{-1}$, however, an increasing hysteresis is progressively observed. The small peak potential difference observed between the anodic and cathodic peaks up to $1 \text{ V}\cdot\text{s}^{-1}$ (*i.e.*, $\Delta E_p \sim 40$ mV) demonstrates that the reversible reduction of the chemisorbed Mn-ph is fast and thus occurs under thermodynamic equilibrium.

3.2. Mn-ph/GLAD-TiO₂

In section 3.1, the Mn^{III}-ph/Mn^{II}-ph redox potential was observed at -0.42 V using a fully conductive GLAD-ITO electrode. As mentioned in the general introduction, the conductivity of TiO₂ is progressively increased upon applying an increasingly more negative potential, passing thus progressively from an insulating to a conductive state at cathodic potential (onset potential at -0.5 V vs. Ag/AgCl at pH 7.0). When the applied potential is raised towards to the conduction band potential of TiO₂ ($E_{CB} = -0.78$ V at pH 7.0), the occupancy of electrons in the electronic states of the band gap (trapped electrons) and of the extended conduction band edge is increased (see general introduction). Therefore, compared to the fully conductive Mn-ph/GLAD-ITO electrode so far investigated, the electrochemical behavior of the Mn-ph/GLAD-TiO₂ electrode is expected to be different owing to its unique semiconductive properties (scheme 2).



Scheme 2. Schematic representation of distributed electronic states in band gap below the conduction band of TiO₂ and the interfacial electron transfer between TiO₂ and the chemisorbed Mn-ph.

To investigate this specific behavior, unmodified and Mn-ph-modified GLAD-TiO₂ electrodes were investigated by spectroelectrochemistry using the same coupled technique of cyclic voltabsorptometry than the one used for studying the Mn-ph-modified GLAD ITO electrode. The CVs, CVAs and DCVAs for the two different electrodes are shown in Figure 5.

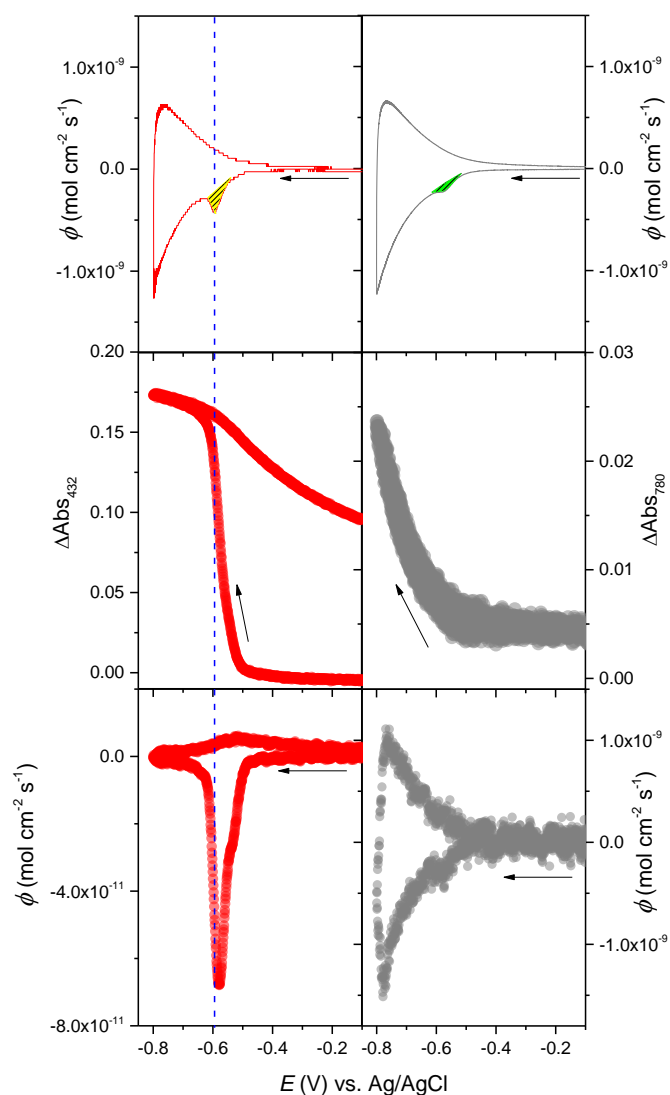


Figure 5. (Top) CVs, (middle) CVAs, and (bottom) corresponding DCVAs of (left column) Mn-ph/GLAD-TiO₂ and (right column) unmodified GLAD-TiO₂ recorded in 100 mM Hepes buffer solution with 50 mM Na₂SO₄ (pH 7.0) in degassed condition. $\nu = 10 \text{ mV} \cdot \text{s}^{-1}$. $\Delta\epsilon_{432} = 380\,000 \text{ M}^{-1} \cdot \text{cm}^{-1}$ and $\Delta\epsilon_{780} = 1200 \text{ M}^{-1} \cdot \text{cm}^{-1}$ (see text).

The CV of the Mn-ph/GLAD-TiO₂ electrode shows a characteristic irreversible faradaic reduction peak of Mn^{III}-ph localized at -0.6 V (yellow dashed peak in Figure 5), which is more negative than the formal potential of the Mn-ph (*i.e.*, -0.42 V). This behavior is characteristic of the semiconductive properties of TiO₂, the latter starting to be conductive at potential more negative than -0.5 V as evidenced for the CV of the unmodified GLAD-TiO₂ (the exponential rise of the current starts at potential < -0.5 V). At potentials where the redox process of Mn^{III}-ph/Mn^{II}-ph is expected to occur, the GLAD-TiO₂ film behaves as an insulator and so the electron transfer reaction through the mesoporous TiO₂ film cannot proceed. This is only when

the applied potential reaches values that render the film increasingly conductive that the reduction of the Mn^{III}-ph can happen.

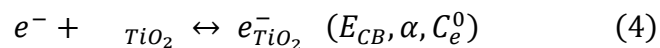
It is worth to note that on the CV of the unmodified GLAD-TiO₂ electrode, a smaller irreversible peak is also observed at a potential of -0.55 V (green dashed in Figure 5), at a potential value that is slightly more positive than the one observed in the presence of Mn-ph. Even though there are some controversy in the literature about the exact nature of this irreversible peak,²³ it is generally assumed to be related to a narrow distribution of localized electronic states in the band gap of TiO₂ (see the general introduction). In order to determine the surface concentration of redox-active Mn-ph entrapped within the mesoporous film, it is thus necessary to subtract the CV obtained with the Mn-ph-modified GLAD-TiO₂ to the one recorded in the absence of Mn-ph. The resulting difference allows thus to recover the faradaic response only due to the reduction of Mn^{III}-ph into Mn^{II}-ph. Integration of this faradaic response allowed us to estimate a Mn-ph surface concentration of 4.7×10^{-10} mol·cm⁻².

The CVAs in Figure 5 show a nearly irreversible absorbance change at 432 nm for the Mn-ph/GLAD-TiO₂ electrode, characteristic of an irreversible conversion of Mn^{III}-ph into Mn^{II}-ph, whereas at the unmodified GLAD-TiO₂ electrode no absorbance change is observed (data not shown). This absorbance change moreover coincides with the irreversible peak on the CV, which both are thus located at a potential much more negative than the formal reduction potential of Mn^{III}-ph/Mn^{II}-ph (*i.e.*, -0.42 V). Again this demonstrates that the interfacial electron transfer between TiO₂ and immobilized Mn-ph should only proceeds once the applied potential to the TiO₂ film is sufficiently negative (*i.e.*, for $E < -0.5$ V at pH 7, scheme 2). This process is also expected to be fully irreversible because when Mn-ph is reoxidisable (at potentials > -0.42 V), the TiO₂ film returned to its insulating state. Nevertheless, spontaneous slow re-oxidation of Mn-ph was observed to occur even under open circuit potential. This is the reason why, on the CVA, the absorbance during the backward scan is slightly decreased. One possible explanation is that the Mn^{II}-ph is chemically reoxidized by residual traces of molecular oxygen that are difficult to completely removed by Argon bubbling. The corresponding DCVA, as expected, shows an irreversible reduction peak of Mn^{III}-ph. In addition, the $\Delta\epsilon_{432}$ value was estimated to 380 000 M⁻¹·cm⁻¹ from the absorbance change ($\Delta A_{432} = 0.18$). This $\Delta\epsilon_{432}$ for Mn^{III}/Mn^{II} within GLAD-TiO₂ has good agreement with that of Mn-ph/GLAD-ITO in section 3.1.

On the other hand, electrons accumulation within a semiconductive TiO₂ electrode can be characterized from the growth of absorption in the wavelength range 700-1000 nm, allowing thus to directly measure the accumulated charges from (see general introduction). We have thus decided to follow the change of absorbance at 780 nm during CV scans. Consequently, by monitoring CVAs at 432 nm and 780 nm, it becomes possible to simultaneously get quantitative information on the amount of Mn-ph that is electrochemically converted during a scan and, at the same time, on the amount of electrons that are accumulated within the nanostructured TiO₂ film. The absorbance variation at 780 nm at GLAD-TiO₂ and Mn-ph/GLAD-TiO₂ were observed almost the same (data not shown), indicating that charge accumulated in the nanostructured GLAD-TiO₂ is not significantly affected by the presence of Mn-ph.

The extinction coefficient of electrons that are injected at 780 nm (*i.e.*, ϵ_{780}) in the nanostructured GLAD-TiO₂ was estimated from cross-correlating the current response in CV to the absorbance change measured by DCVA at a same unmodified GLAD-TiO₂ electrode. Direct comparison of CVs and DCVAs can be made possible by representing the flux (ϕ) of electron collected per unit of time and electrode area (see Eq. 1). Using an extinction coefficient value of 1200 M⁻¹·cm⁻¹ for the GLAD-TiO₂ electrode at 780 nm, the electron surface concentration ($\Delta\Gamma_{e^-}$) accumulated in the TiO₂ film can be estimated as being 3.13×10^{-8} mol·cm⁻², while from the absorbance change at 432 nm ($\Delta A_{432} = 0.18$) the surface concentration of Mn-ph adsorbed on the surface of GLAD-TiO₂ can be estimated to be 4.7×10^{-10} mol·cm⁻² using an extinction coefficient difference of $\Delta\epsilon_{432} = 380\,000$ M⁻¹·cm⁻¹. This indicates that the total amount of electrons accumulated within the GLAD-TiO₂ film is much higher (~ 67-fold) than the amount of electrons required for the Mn-ph reduction.

In order to get deeper insight into the heterogeneous electron transfer between TiO₂ and the chemisorbed Mn-ph redox probe, the irreversible reduction peak was analyzed according to the same theoretical framework as it was previously achieved at the laboratory using EISA-TiO₂ electrodes¹ and assuming the following electron transfer mechanism:



Reaction 4 is related to the fast reversible injection of electrons from the underlying conductive ITO surface into the exponential distribution of electronic states of the GLAD TiO₂ film (*i.e.*, into a Boltzman distribution of empty conduction band electronic states and also possibly into an exponential distribution of empty localized states or traps within the bandgap), followed by fast transport of the injected electrons ($e_{TiO_2}^-$) through a random walk diffusion-like process across the TiO₂ mesoporous network (sufficiently fast for these processes being assumed never rate limiting). Under these conditions, reaction 4 can be simply quantitatively described by the following key parameters: C_e^0 the maximal volumetric concentration of electrons that can be injected within the TiO₂ material, α the dimensionless factor that characterizes the energy distribution of electronic states involved in the interfacial electron transfer, and E_{CB} the conduction band edge potential of TiO₂. Reaction 5 is related to the irreversible reduction of chemisorbed Mn-ph at the TiO₂ interface. It is characterized by an interfacial electron transfer rate k_s .

Determination of interfacial electron transfer rate at a Mn-ph-modified GLAD-TiO₂ electrode under Ar condition can be achieved from the analysis of either the CV or DCVA plots recorded as a function of different scan rates. In CV, the cathodic current is the sum of a faradaic component (I_f) related to the irreversible redox transformation of the Mn-ph molecules chemisorbed on the surface of the GLAD-TiO₂ and of a capacitive component (I_C) related to the exponential increase of electrons injected into the extended states of TiO₂, but also, when the film is becoming fully degenerated (*i.e.*, fully conductive), to the charging of the double layer. In DCVA, only the faradaic component (I_f) has to be considered owing to the fact that the monitored absorbance change is exclusively focused on the redox state of the active species absorbed within the GLAD-TiO₂ film. This faradaic component (I_f) can furthermore be subdivided in two components, *i.e.* $I_{f,1}$ associated to the reduction of the redox active species directly at the TiO₂ interface and $I_{f,2}$ arising from the fraction of redox probe in the film that can directly electrochemically reacts at the uncovered underlying ITO electrode. In this work, we assumed that accordingly to the strong binding of the immobilized redox active chromophore to the TiO₂ interface, the faradaic component $I_{f,2}$ is negligible (in other words, Mn-ph is assumed so strongly anchored to TiO₂ that it cannot physically move by slow diffusion up to the underlying uncovered ITO electrode). Also, in the potential window that we have investigated (*i.e.*, < -0.5 V where TiO₂ is becoming increasingly metal-like conductive), only the faradaic component associated to the direct reduction of the redox active species at

the TiO₂ interface need to be taken into account ($I_{f,2} \rightarrow 0, I_f = I_{f,1}$). If we assumed that, once injected, the rate of electron mass transport across the TiO₂ film is very fast and never rate limiting, it is possible to describe the irreversible peak of reduction by the following analytical expression:¹

$$\phi_f = kC_e^0 \Gamma \exp \left[-\frac{F}{RT} (E - E_{CB}) \right] \times \exp \left\{ -\frac{RT}{Fv} kC_e^0 \exp \left[-\frac{F}{RT} (E - E_{CB}) \right] \right\} \quad (6)$$

where E_{CB} is the conduction band edge potential of TiO₂ (*i.e.*, -0.78 V at pH 7.0), E is the applied potential (in V), T the temperature (in K), F the Faraday constant (in C·mol⁻¹), R the gas constant (in J·K⁻¹·mol⁻¹), v the scan rate (in V·s⁻¹), Γ the surface coverage of the oxidized form of the adsorbed redox chromophore (in mol·cm⁻²), and kC_e^0 (in s⁻¹) a parameter characterizing the interfacial electron transfer rate between the immobilized redox active molecule and the semiconductive film. This expression is only valid when there is no localized state within the bandgap of TiO₂. In case where electrons are also trapped in localized states in the bandgap of the semiconductor and where the latter could contribute to the interfacial electron transfer, the following alternative theoretical expression can be used:¹

$$\phi_f = kC_e^0 \Gamma \exp \left[-\alpha \frac{F}{RT} (E - E_{CB}) \right] \times \exp \left\{ -\frac{RT}{\alpha Fv} kC_e^0 \exp \left[-\alpha \frac{F}{RT} (E - E_{CB}) \right] \right\} \quad (7)$$

wherein the additional parameter α reflects the distribution of localized states (or traps) within the bandgap of the semiconductor. This analytical expression can thus be used to fit the irreversible peaks in the experimental DCVAs, allowing thus from the best fitting to extract the unknown parameters kC_e^0 and α if knowing the parameters E_{CB} , Γ and v . This is typically what it has been done in Figure 6.

In order to take into account the slow desorption of Mn-ph from the GLAD TiO₂ film during the time course of the experiment (and so the progressive change of the Γ value), the surface concentration was systematically reevaluated for each experiment performed at a different scan rate (the experiments were performed starting with the fastest scan rate of 0.1 V·s⁻¹ and decreasing to the slower scan rates down to 1 mV·s⁻¹). The values of Γ determined at each scan rate from the maximal absorbance change in CVAs at reported in Table 2.

Table 2. Surface concentration Γ (nmol·cm⁻²) determined from the absorbance change in CVAs at different scan rates.

ν (V·s ⁻¹)	Γ (nmol·cm ⁻²)
0.001	0.38
0.005	0.37
0.01	0.47
0.05	0.53
0.1	0.61

Using these Γ values, the theoretical Eq. 7 was thus fitted to the experimental data in Figure 6 by adjusting kC_e^0 and α (for E_{CB} a value of -0.78 V vs. Ag/AgCl at pH 7.0 was used). From the best fits, the following values of $\alpha = 0.9$ and $kC_e^0 = 272$ s⁻¹ were finally obtained.

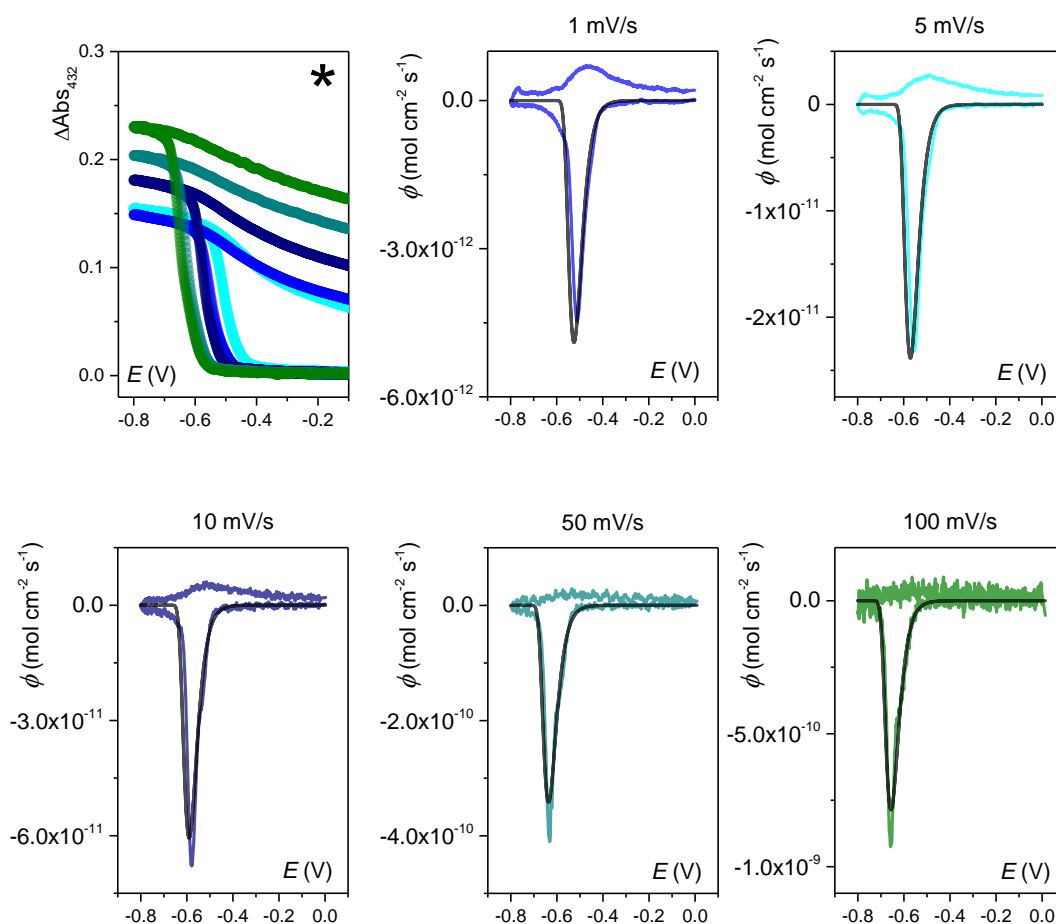


Figure 6. (*) CVAs monitored at 432 nm of Mn-ph/GLAD-TiO₂ with scan rate ν of (blue) 1, (cyan) 5, (navy) 10, (dark cyan) 50, (olive) 100 mV·s⁻¹ in a deaerated 0.1 M Hepes buffer solution with 50 mM Na₂SO₄ (pH 7.0). (Rest) Corresponding DCVAs (the code color is the same than in *). The black solid lines are the best fits of Eq. 5 to the experimental data. The Γ values used for the fits are reported in Table 2. The value of E_{CB} was set at -0.78 V vs. Ag/AgCl (pH 7.0). The overall fits were adjusted with a single set of parameters $\alpha = 0.9$ and $kC_e^0 = 272$ s⁻¹.

From Eq. 7, it can be mathematically demonstrated that the peak potential position of the irreversible peak is a function of α and kC_e^0 according to the following expression:¹

$$E_p = E_{CB} + \frac{RT}{\alpha F} \ln\left(\frac{RT}{\alpha F v} kC_e^0\right) \quad (8)$$

while the maximum peak, $\phi_{f,p}$ is linearly proportional to v and Γ according to Eq. 9:

$$\phi_{f,p} = \frac{I_{f,p}}{F} = \frac{F\alpha}{RT} v \Gamma \quad (9)$$

According to Eq. 8, the peak potential determined for the DCVAs was plotted as a function of $\ln\left(\frac{1}{v}\right)$ (Figure 7). From the linear fit, α and kC_e^0 can be again estimated, assuming $E_{CB} = -0.78$ V at pH 7.0. From the best fit of Eq. 8 to the experimental data in Figure 7, $\alpha = 0.9$ and $kC_e^0 = 272$ s⁻¹ were inferred.

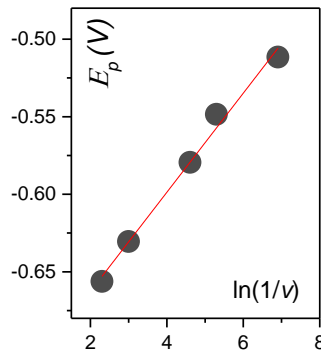


Figure 7. The linear relation between peak potential and $\ln(1/v)$. From the linear regression fit of Eq. 8 to the experimental data (red straight line), the values of kC_e^0 and α were determined to be 0.9 and 272 s⁻¹.

In previous work done in the lab with EISA-TiO₂, the α value was founded to 1, suggesting a heterogeneous electron transfer reaction that exclusively involves the extended conduction band states with no contribution from electrons trapped at lower energy states. This would also mean that, in this case, trapped electrons can only be indirectly involved through an equilibrated bulk trapping-detrapping mechanism with the extended conduction band states.²³ In the case of GLAD-TiO₂ the α value is lower than 1 (*i.e.*, $\alpha = 0.9$), which indicates a somewhat contribution of trapped electrons to the interfacial electron transfer. In another recent paper of the lab,² an α value of 0.71 has been found for EISA-SnO₂ electrode, which is much lower than at GLAD-TiO₂. This suggests that a significantly higher number of surface traps are involved in the interfacial electron transfer at EISA-SnO₂ films, contributing thus to an

enlargement of the irreversible reduction peak in CV or DCVA.² The small difference between EISA-TiO₂ and GLAD-TiO₂ is difficult to explain and need further investigation. However, it is interesting to note that the degree of TiO₂ crystallinity deposited by EISA and GLAD methods are significantly different (the EISA TiO₂ being a crystalline anatase structure while the GLAD TiO₂ being totally amorphous) and the immobilized redox active molecules are not same (iron porphyrin vs. Mn-ph). Table 3 gathers the values of α that were determined by cyclic voltabsorptometry at different mesoporous semiconductive electrodes modified with different redox probes.

Table 3. Diverse experimental conditions and its characteristics of EISA-TiO₂, GLAD-TiO₂, and EISA-SnO₂.

Electrodes	E_{CB} at pH 7.0 (V)	redox molecules	E^0_{molecule} (V)	crystallinity	l (nm)	α	ref
EISA-TiO ₂	-0.78	FeTMPyP, MP-11	-0.16, -0.38	anatase	220	1	¹
EISA-SnO ₂	-0.39	FMN, OsP	-0.4, +0.6	nanocrystalline	250	0.71	²
GLAD-TiO ₂	-0.78	Mn-ph	-0.42	amorphous	550	0.9	This work

In this section, interfacial electron transfers at Mn-ph/GLAD-ITO and Mn-ph/GLAD-TiO₂ electrodes were successfully investigated under Ar condition.

4. Catalytic reduction of O₂ at Mn-ph-modified GLAD-ITO and GLAD-TiO₂ electrodes

In a previous work at the laboratory, the catalytic reduction of O₂ by microperoxidase-11 (MP-11) adsorbed within a GLAD-ITO electrode (MP-11/GLAD-ITO) was investigated by spectroelectrochemistry.²⁴ In this work, cross-correlation of the simultaneously recorded CV and CVA under catalytic turnover was shown very useful for characterizing the catalytic reaction mechanism as well as for determining some of kinetics rate constants. On the basis of this previous work, it was thus interesting to investigate the catalytic reduction of O₂ with another porphyrin catalyst such as the Mn-ph molecule chemisorbed within not only a GLAD-ITO electrode, as previously, but also chemisorbed within a GLAD-TiO₂ electrode which semiconductive properties are expected to significantly alters the catalytic response compared with a fully conductive GLAD-ITO electrode.

4.1. Mn-ph/GLAD-ITO

A typical set of CVs and DCVAs (derivatives of CVAs monitored at 432 nm) recorded at a Mn-ph/GLAD-ITO electrode under saturated Ar and O₂ conditions in a 0.1 M HEPES buffer solution with 50 mM Na₂SO₄ (pH 7.0) is shown in Figure 8 (scan rate 0.1 V·s⁻¹).

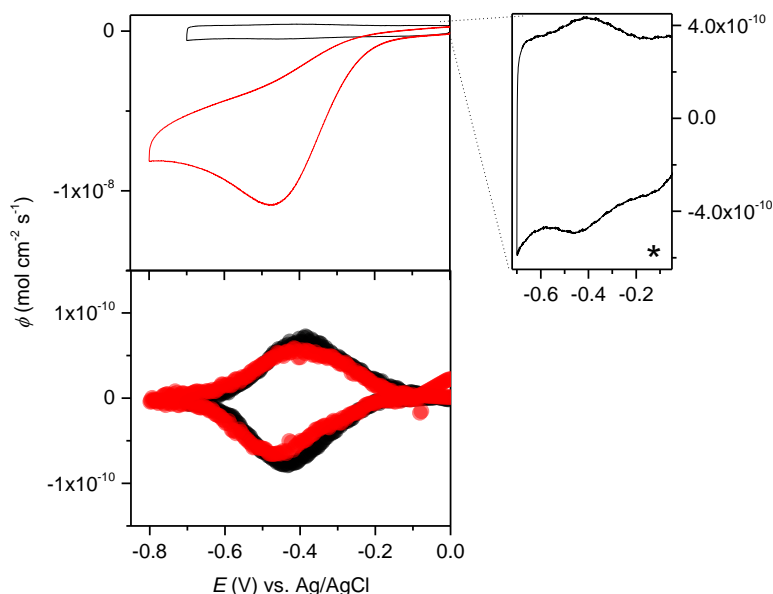


Figure 8. (Top) CVs and (bottom) DCVAs (432 nm) recorded at a Mn-ph/GLAD-ITO electrode under (black) a saturated Argon and (red) O₂ atmosphere. Electrolyte is 0.1 M HEPES buffer solution with 50 mM Na₂SO₄. $\nu = 0.1$ V·s⁻¹. *: enlarged CV graph of a Mn-ph/GLAD-ITO electrode under saturated Argon, showing well-defined reversible wave centered at $E^{0'} = -0.42$ V.

Compared to the very low reversible faradaic wave on the CV under Ar (characteristic of the reversible one electron transfer reaction of the Mn-ph), in the presence of O₂ a huge irreversible cathodic wave is observed at -0.45 V, characteristic of a redox-mediated catalytic current response. Because of the catalytic process, the electron flux flowing through the electrode is greatly increased, resulting in an amplified current response in CV (centered on the formal potential of the redox couple Mn^{III}-ph/Mn^{II}-ph, *i.e.* $E^{0'} = -0.42$ V) compared to that obtained in the absence of O₂. In marked contrast to the CVs, a very small change is observed on the DCVAs, showing a nearly identical symmetric reversible wave centered on the formal potential of the redox couple Mn^{III}/Mn^{II}, whether there is O₂ or not. This behavior is characteristic a fast catalytic reaction that strongly consume O₂ within the diffusion layer at the electrode interface (so that the local O₂ concentration within the GLAD-ITO film is close to zero), allowing thus the accumulation of Mn^{II}-ph during the cathodic scan (leading thus to a

cathodic peak in DCVA that is not significantly different from the one recorded in the absence of O₂). The rapidity of the catalytic process is also supported by the fact that in CV the catalytic wave is peak shaped and not plateau shaped, which indicates that the consumption of O₂ within the diffusion layer is fast and so that the catalytic current is rapidly rate-limited by the mass transport of O₂ from the solution to the electrode interface.

In order to decrease the consumption of O₂ and to attempt to reach conditions that are no more limited by the mass transport of substrate to the electrode but instead by the rate of the catalytic reaction, CVs and CVAs (monitored at 432 nm) were recorded at different scan rates ν (Figure 9). Indeed, increasing the scan rate allows shortening the time window of the experiment and thereby reducing the consumption of O₂.

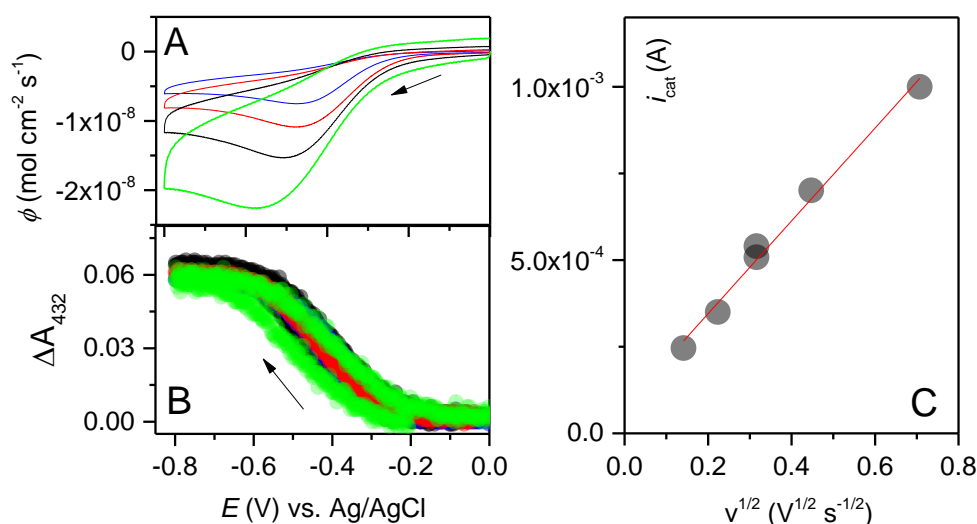


Figure 9. (A) CVs and (B) CVAs (monitored at 432 nm) simultaneously recorded at a Mn-ph/GLAD-ITO electrode (the surface concentration of Mn-ph is ~ 0.16 nmol·cm⁻²) in a saturated O₂ solution of 0.1 M HEPES buffer and 50 mM Na₂SO₄ and for different scan rates ν of: (blue) 0.05 V·s⁻¹, (red) 0.1 V·s⁻¹, (black) 0.2 V·s⁻¹, and (green) 0.5 V·s⁻¹. (C) Catalytic peak current in CV (after being subtracted from the capacitive current) as a function of the square root of scan rate. The straight red line is the linear regression fit to the data.

As seen in Figure 9, the catalytic cathodic peak current derived from CVs (*i.e.*, subtracted from the GLAD-ITO capacitive contribution) is increased proportionally to the square root of ν . This clearly demonstrates that the catalytic reduction of O₂ is rate-limited by diffusion of O₂ in solution and never limited by the reaction of O₂ with Mn^{II}-ph. From the linear relationship of the catalytic cathodic peak current as a function of $\sqrt{\nu}$, it is thus only possible to recover information from the mass transport rate of O₂. Assuming we are under the limiting

case of total catalysis (*vide infra*) and that the heterogeneous electron transfer between Mn-ph and ITO is fast (*i.e.*, Nernstian behavior), we can use the following theoretical Eq. 10 to fit the data:²⁵

$$i_p = 0.496 nFAC_{O_2} \left(\sqrt{\frac{nFvD_{O_2}}{RT}} \right) \quad (10)$$

where n is the number of electron involved in the redox process, F the Faraday constant, A the geometric surface area of ITO film, v the scan rate, T the temperature, C_{O_2} the O_2 concentration in solution, $R = 8.314 \text{ J}\cdot\text{K}^{-1}\cdot\text{mol}^{-1}$, and D_{O_2} the diffusion coefficient of O_2 in solution ($\text{cm}\cdot\text{s}^{-1}$). According to the literature,²⁶ the number of electron involved in the catalytic reduction of O_2 by Mn-ph is assumed to be 2. Knowing that the concentration of molecular oxygen is 1.4 mM in an aqueous solution at 1 atm,²¹ the diffusion coefficient of O_2 could thus be estimated from the linear regression fit in Figure 9C. A value of $D_{O_2} = 9.6 \times 10^{-6} \text{ cm}^2\cdot\text{s}^{-1}$ is obtained, which is not so far from the value reported in literature (*i.e.*, $\sim 2 \times 10^{-5} \text{ cm}^2\cdot\text{s}^{-1}$ at 25°C).^{21,27} It is worth to note that we have not considered here a possible favorable partitioning of O_2 from the solution into the mesoporous ITO film, an effect that was previously taken into account in the former study with MP-11-modified GLAD-ITO electrode.²⁴ Also, in contrast to the previous study with MP-11,²⁴ no hysteresis effect was observed between the forward and backward scans on the CVAs (leading to a near identical shape of the CVAs in the presence of O_2 than in its absence, at least within the range of scan rate explored here). This lack of hysteresis clearly indicates no delay in the accumulation of Mn^{II} -ph, even at the highest scan rate of $0.5 \text{ V}\cdot\text{s}^{-1}$, a behavior that clearly results from the too fast catalytic reaction between O_2 and Mn^{II} -ph which thus induces a systematic strong depletion of O_2 concentration at the electrode interface and so a process always rate-limited by the mass transport of O_2 , impeding thus finally an access to the intrinsic kinetics of the reaction.

In an attempt to slow-down the consumption rate of O_2 within the mesoporous film and thus to be more rate-controlled by the catalytic reaction rather than by the O_2 mass transport, the surface concentration of the Mn-ph catalyst was decreased from 0.2 to $0.1 \text{ nmol}\cdot\text{cm}^{-2}$. The resulting CVs in Figure 10 show an only $\sim 20\%$ decrease of the catalytic peak current while $\Gamma_{\text{Mn-ph}}$ is 2-fold decreased, suggesting that consumption of O_2 continue to rate-limiting process despite a lower catalyst surface coverage. Further decreasing the surface concentration of Mn-ph is thus required if one want to reach conditions where the mass transport is definitely no

more rate limiting. It is nevertheless interesting to note that the catalytic current recorded at the lowest Mn-ph surface concentration is significantly less peak shaped with a tendency to reach a more steady-state catalytic current response than at higher catalyst coverage.

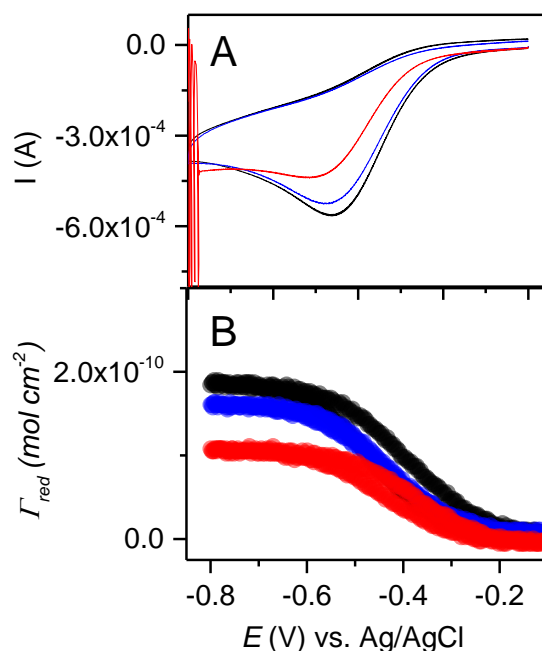
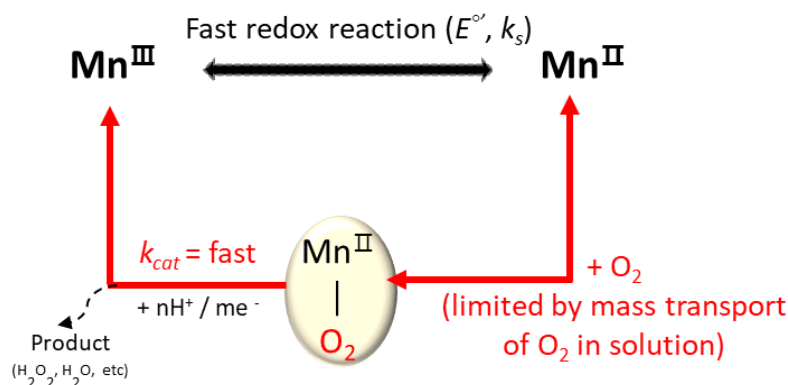


Figure 10. (A) CVs and (B) Mn-ph surface concentration derived from CVAs monitored at 432 nm at Mn-ph/GLAD-ITO electrode. Electrolyte is O_2 saturated 100 mM Hepes buffer solution with 50 mM Na_2SO_4 . $\nu = 0.1 \text{ V} \cdot \text{s}^{-1}$.

The catalytic behavior we observed here at Mn-ph/GLAD-ITO is clearly faster than the one that was previously investigated at MP-11/GLAD-ITO.²⁴ This can be attributed to the more negative formal potential of Mn-ph ($E^{0'} = -0.42 \text{ V}$) compared to MP-11 ($E^{0'} = -0.36 \text{ V}$),²⁴ leading thus to more favorable driving force for O_2 reduction that thus enhances the rate of the catalytic reaction.

All of these results agree with the reaction scheme depicted in Scheme 3 where the heterogeneous electron transfer reaction between the $\text{Mn}^{\text{III}}\text{-ph}/\text{Mn}^{\text{II}}\text{-ph}$ couple is reversible and fast and the catalytic reduction of O_2 by the immobilized Mn-ph is efficient and fast, so fast that it is always, under our experimental conditions, rate-limited by the mass transport of O_2 in solution.



Scheme 3. Schematic representation of the reaction of Mn-ph immobilized within GLAD-ITO under either argon or O_2 conditions.

4.2. Mn-ph/GLAD-TiO₂

As for Mn-ph/GLAD-ITO electrodes, Mn-ph/GLAD-TiO₂ electrodes were similarly investigated by CVs and CVAs in a deaerated or saturated O_2 aqueous buffer solution (pH 7.0). In CVA, in addition to the monitoring of the Mn^{III}-ph Soret band at 432 nm, the absorbance of electrons injected into the TiO₂ was followed at 780 nm.

A typical set of CV and CVA experiments are shown in Figure 11 either at unmodified or Mn-ph-modified GLAD-TiO₂ electrode, and also in the presence or absence of O_2 .

At the Mn-ph-free GLAD-TiO₂ electrode, the direct reduction of O_2 at TiO₂ is slow, leading in CV to an ill-defined broad cathodic wave at $E < -0.6$ V when the metal oxide film is becoming increasingly conductive. Under same conditions, the CVA monitored at 780 nm show an identical absorbance change either there is O_2 or not in solution, showing that the amount of accumulated electrons in the bulk TiO₂ remains unaffected by the reduction of O_2 at the TiO₂ interface.

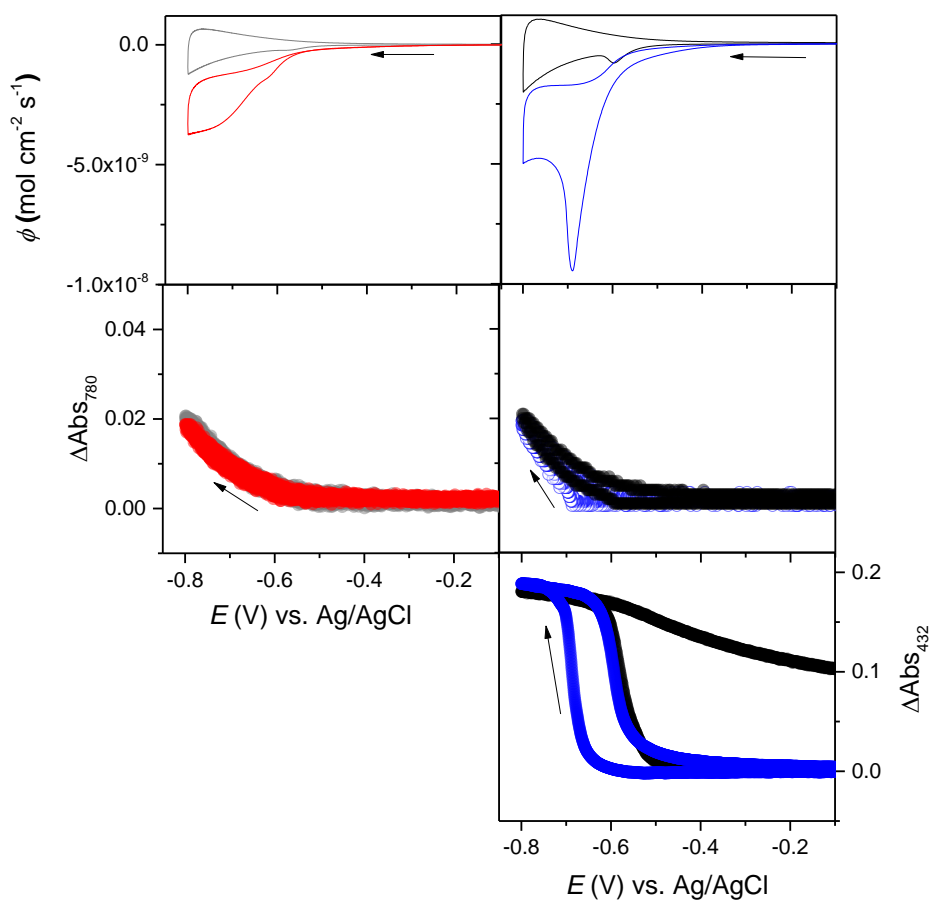


Figure 11. (top) CVs, (middle) CVAs (monitored at 780 nm), and (bottom) CVAs (monitored at 432 nm) simultaneously recorded at a (left) GLAD-TiO₂ and (right) Mn-ph/GLAD-TiO₂ electrode. All grey and black curves were obtained under deaerated conditions, while all red and blue curves were obtained under saturated O₂ conditions. The electrolyte was a 0.1 M HEPES buffer solution with 50 mM Na₂SO₄. $\nu = 10 \text{ mV} \cdot \text{s}^{-1}$.

In the presence of Mn-ph within the GLAD-TiO₂ and O₂ in solution, the CV shows a strong and sharp irreversible cathodic peak at -0.69 V, much more intense than in the absence of Mn-ph, characteristic of a redox-mediated catalytic reduction of O₂ with strong consumption of the substrate (blue CV in Figure 11), while in the absence of O₂, the CV shows, as previously, a much smaller irreversible peak (located at -0.60 V) characteristic of the irreversible reduction of Mn^{II}-ph at TiO₂ (black CV in Figure 11).

Compared to the results above obtained at GLAD-ITO, it is interesting to note that the peak current for the catalytic reduction of O₂ at Mn-ph/GLAD-TiO₂ is localized at a potential much more negative (*i.e.*, -0.69 V at 0.01 V·s⁻¹) than at Mn-ph/GLAD-ITO (*i.e.*, -0.45 V at 0.05 V·s⁻¹, see section 4.1). This well-illustrates the contrasting behavior that arises from the

semiconductive properties of TiO₂. With TiO₂, the catalytic current can only start to rise when the semiconductive material is switched sufficiently conductive. It can thus only happen when the applied potential is sufficiently negative (*i.e.*, at $E < -0.5$ V which is more negative than the formal reduction potential of Mn-ph).

As discussed in section 3.2, the absorbance change at 432 nm represents the appearance of Mn^{II}-ph by reduction of Mn^{III}-ph at Mn-ph/GLAD-TiO₂. As shown on the CVA monitored at 432 nm in Figure 11, this reduction is irreversible in the absence of O₂, but in the presence of O₂, it becomes fully reversible. This is explained by the fast recovery of Mn^{II}-ph into Mn^{III}-ph through the catalytic re-oxidation by O₂. One could also notice that, during the forward cathodic scan, the rise of absorbance at 432 nm occurs at a more negative potential than in absence of O₂, a potential that nearly coincide to the maximum of the catalytic peak current in CV. This delay in the rise of absorbance results from the need to nearly fully consumed O₂ at the electrode interface before Mn^{II}-ph starts to accumulate within the film.

Concerning the CVAs recorded at 780 nm, a surprising small shift of the onset absorbance change at negative potentials (~ 110 mV) is observed for the Mn-ph/GLAD-TiO₂ electrode under saturated O₂. This behavior suggests that the accumulation of electrons in bulk TiO₂ is delayed. This might be possibly due to the fact that as soon as electrons are injected into the bulk of TiO₂ most of them are nearly instantaneously consumed by the catalytic reduction of O₂, therefore delaying their accumulation into the semiconductive material. This would also suggest that the apparent rate of mass transport of electrons across the nanostructured TiO₂ film is not so fast and may be rate-limiting.

Additionally, a series of CVs and CVAs were recorded at various scan rates up to 0.1 V·s⁻¹ in the presence of saturated O₂ in solution (Figure 12).

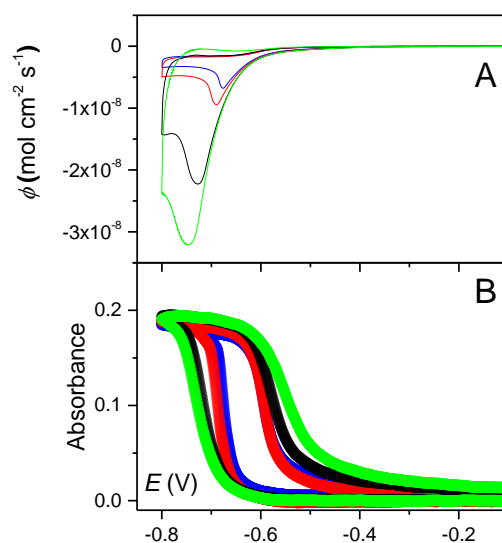


Figure 12. (A) CVs and (B) CVAs monitored at a Mn-ph/GLAD-TiO₂ electrode in a saturated O₂ solution with scan rate of (blue) 5 mV·s⁻¹, (red) 10 mV·s⁻¹, (black) 50 mV·s⁻¹ and (green) 100 mV·s⁻¹. Electrolyte is 100 mM Hepes buffer solution with 50 mM Na₂SO₄.

The resulting CVs show a catalytic cathodic peak current that increase as a function of the square root of the scan rate, suggesting a catalytic response governed by the diffusion rate of O₂ to the electrode interface whatever the scan rate (a behavior that is similar to the one we have observed at Mn-ph-modified GLAD-ITO electrode). The catalytic peak potentials were also downshifted with the increase of scan rate, a behavior that is corroborated by the negative shift of the onset absorbance change at 432 nm on the CVAs. Upon increasing the scan rate, an increasing hysteresis between the forward and backward scan is also observed on CVAs, a behavior which translates on the DCVAs in an increased separation between the anodic and cathodic peak potentials (Figure 13).

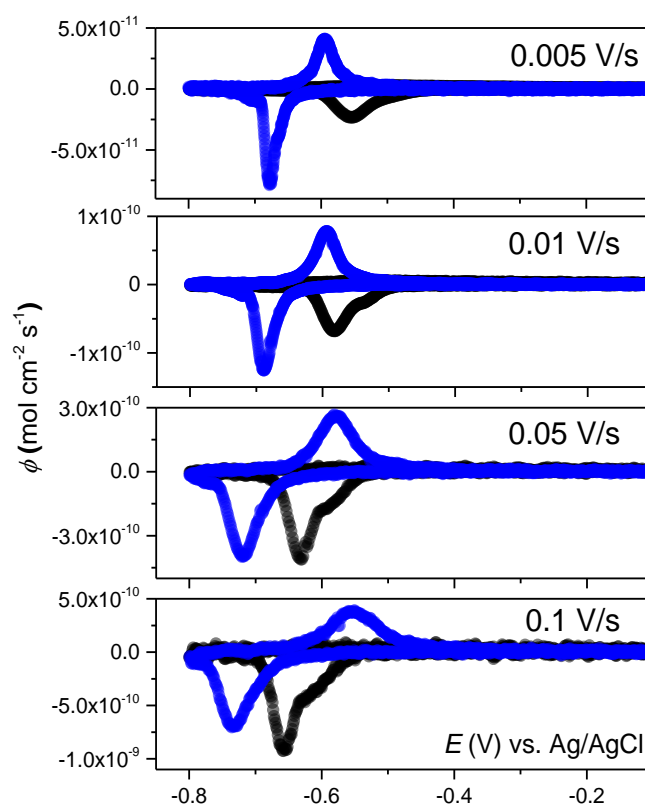
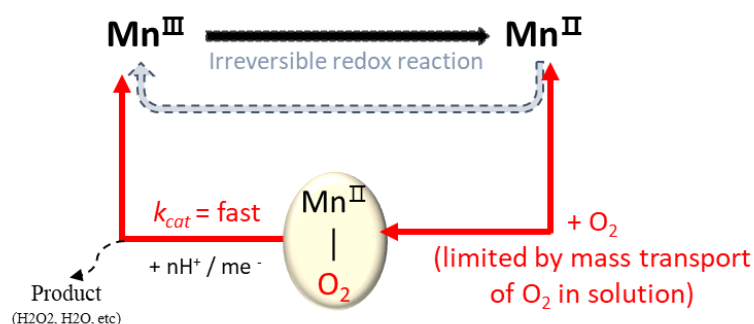


Figure 13. DCVAs (monitored at 432 nm) of Mn-ph/GLAD-TiO₂ under (blue) saturated O₂ condition and (black) deaerated condition at 5, 10, 50, and 100 mV·s⁻¹. In the absence of O₂ (black curves), the value of Γ_{Mn-ph} estimated from maximal amplitude of absorbance change in CVAs was observed to slightly decrease upon successively recording the experiments from fast to slow scan rate, resulting thus in the following surface coverages (bottom to top): 0.61, 0.53, 0.41, and 0.37 nmol·cm⁻². This decrease of Γ_{Mn-ph} is attributed to the slow desorption of Mn-ph from the porous film, as it was previously discussed. In contrast, under O₂, the value of Γ_{Mn-ph} was observed to remain more stable, leading to a nearly constant value of 0.51 nmol·cm⁻² whatever the scan rate.

For comparative purpose, the DCVAs recorded in the absence of O₂ are also reported in Figure 13. As previously observed and discussed, the cathodic peak corresponding to the reductive accumulation of Mn^{II} under O₂ is shifted at a more negative potential than under Ar because of the delay required to fully catalytically deplete O₂ at the electrode interface before Mn^{II} starts to rise. This is here observed whatever the scan rate, which suggests that even for the highest scan rate (*i.e.*, 0.1 V·s⁻¹) the catalytic reaction cannot be kinetically limiting.

All of the above results allowed us to propose the reaction scheme depicted in Scheme 4, in which the reduction of Mn^{III}-ph at GLAD-TiO₂ proceeds through an irreversible electron transfer reaction at a potential more negative than the formal redox potential of Mn^{III}-ph/Mn^{II}-

ph because of the semiconductive properties of TiO₂. On account of the high driving force between the redox potential of Mn^{III}-ph/Mn^{II}-ph ($E^{0'} = -0.42$ V at pH 7.0) and the conduction band potential of TiO₂ ($E_{CB} = -0.78$ V at pH 7.0), this heterogeneous electron transfer reaction is fast. In the presence of O₂, the re-oxidation of Mn-ph is rapidly achieved chemically through a fast catalytic reduction of O₂ into probably H₂O₂.



Scheme 4. Schematic representation of electron transfer of Mn-ph within GLAD-TiO₂ under argon or O₂.

5. Conclusion

In this chapter, we have successfully investigated by spectroelectrochemistry the interfacial electron transfer and catalytic activity of a small redox-active dye (Mn-ph) chemisorbed within a transparent mesoporous electrode made of a conductive or a semiconductive mesoporous metal oxide material (*i.e.*, GLAD-ITO and semiconductive TiO₂).

The comparative study of CVAs and DCVAs recorded at both Mn-ph/GLAD-ITO or Mn-ph/GLAD-TiO₂ has allowed us to better highlight the main differences taking place between the conductive and semiconductive material. In contrast to Mn-ph/GLAD-ITO, an irreversible interfacial electron transfer process located at a cathodic potential significantly lower than the formal potential of Mn^{III}-ph/Mn^{II}-ph was observed at Mn-ph/GLAD-TiO₂, a behavior that is consistent with that previously found in the lab for other redox-active compound whose formal potentials lies within the potential window where the semiconductor material behaves insulating.¹ From the shape and position of this irreversible peak, it was possible to recover the interfacial electron transfer rate as well as the extent of surface localized states involved in the heterogeneous electron transfer reaction. From the value of $a = 0.9$ we have obtained, we were able to conclude that the contribution of localized states into the interfacial electron transfer between Mn^{II}-ph and GLAD-TiO₂ is low, finally being close to the

value of 1 that was previously found at EISA-TiO₂ using MP-11 as a redox-active chromophore.¹

The redox-mediated catalytic reduction of O₂ at a Mn-ph/GLAD-TiO₂ electrode was also shown to behave completely different to that at a Mn-ph/GLAD-ITO. The contrasted behavior is again due to the semiconductive properties of TiO₂, which prevents the catalytic reaction to take place until TiO₂ is becoming enough conductive, delaying thus the reaction at more cathodic potential. It is thus only when the applied cathodic potential has reached a value close to the conduction band of TiO₂ that suddenly the fast catalytic reduction of O₂ occurs. On account of the rate of the catalytic reaction that is fast, it was not possible to have an access to some details on the mechanism of the reaction, the CVs or CVAs being always rate-limited by the mass transport of O₂ in solution.

References

- ¹ Renault, C.; Nicole, L.; Sanchez, C.; Costentin, C.; Balland, V.; Limoges, B. Unraveling the Charge Transfer/Electron Transport in Mesoporous Semiconductive TiO₂ Films by Voltabsorptometry. *Phys. Chem. Chem. Phys.* **2015**, *17*, 10592–10607.
- ² Hamd, W.; Laberty-Robert, C.; Lambert, F.; Costentin, C.; Limoges, B.; Balland, V. Investigating Charge Transfer in Functionalized Mesoporous EISA-SnO₂ Films. *J. Phys. Chem. C* **2017**, *121*, 23207-23217.
- ³ Cracknell, J. A.; Vincent, K. A.; Armstrong, F. A. Enzymes as Working or Inspirational Electrocatalysts for Fuel Cells and Electrolysis. *Chem. Rev.* **2008**, *108*, 2439–2461.
- ⁴ Fukuzumi, S.; Kishi, T.; Kotani, H.; Lee, Y-M.; Nam, W. Highly efficient photocatalytic oxygenation reactions using water as an oxygen source. *Nat. Chem.* **2011**, *3*, 38–41.
- ⁵ Hagfeldt, A.; Gratzel, M. Light-induced redox reactions in nanocrystalline systems. *Chem. Rev.* **1995**, *95*, 49–68.
- ⁶ Gratzel, M. Photoelectrochemical Cells. *Nature*, **2001**, *414*, 338– 344.
- ⁷ Chandra, R.; Tiwari, M.; Kaur, P.; Sharma, M.; Jain, R. ; Dass, S. Metalloporphyrins-Applications and clinical significance. *Indian J Clin Biochem.* **2000**, *15*, 189-199.
- ⁸ Zhou, X. –T.; Ji, H. –B.; Huang, X. –J. Photocatalytic Degradation of Methyl Orange over Metalloporphyrins Supported on TiO₂ Degussa P25. *Molecules* **2012**, *17*, 1149-1158.
- ⁹ Groves, J. T. Reactivity and mechanisms of metalloporphyrincatalyzed oxidations. *J. Porphyrins Phthalocyanines* **2000**, *4*, 350–352.
- ¹⁰ Masa, J.; Ozoemena, K.; Schuhmann, W.; Zagal, J. –H. Oxygen reduction reaction using N₄-metallomacrocyclic catalysts: fundamentals on rational catalyst design. *J. Porphyr. Phthalocyanines.* **2012**. *16*, 761–784.
- ¹¹ Costentin, C.; Dridi, H.; Saveant, J. –M. Molecular Catalysis of O₂ Reduction by Iron Porphyrins in Water: Heterogeneous versus Homogeneous Pathways. *J. Am. Chem. Soc.* **2015**, *137*, 13535–13544.
- ¹² Pecoraro, V. L.; Baldwin, M. J.; Gelasco, A. Interaction of Manganese with Dioxygen and Its Reduced Derivatives. *Chem. Rev.* **1994**, *94*, 807-826.
- ¹³ Kadish, K. M.; Fremond, L.; Burdet, F.; Barbe, J. –M.; Gros, C. P.; Guillard, R. Cobalt(IV) corroles as catalysts for the electroreduction of O₂: Reactions of heterobimetallic dyads containing a face-to-face linked Fe(III) or Mn(III) porphyrin. *J Inorg Biochem.* **2006**, *100*, 858–868.
- ¹⁴ Forget, A.; Limoges, B.; Balland, V. Efficient Chemisorption of Organophosphorous Redox Probes on Indium Tin Oxide Surfaces under Mild Conditions. *Langmuir*, **2015**, *31*, 1931–1940.
- ¹⁵ Guerrero, G.; Mutin, P. H.; Vioux, A. Mixed Nonhydrolytic/Hydrolytic Sol–Gel Routes to Novel Metal Oxide/Phosphonate Hybrids. *Chem. Mater.*, **2000**, *12*, 1268–1272.

- ¹⁶ Bancroft, E. E.; Sidwell, J. S.; Blount, H. N. Derivative Linear Sweep and Derivative Cyclic Voltabsorptometry. *Anal. Chem.* **1981**, 53, 1390–1394.
- ¹⁷ Renault, C.; Balland, V.; Limoges, B.; Costentin, C. Chronoabsorptometry To Investigate Conduction-Band-Mediated Electron Transfer in Mesoporous TiO₂ Thin Films. *J. Phys. Chem. C.* **2015**, 119, 14929-14937.
- ¹⁸ Krause, K. M.; Taschuk, M. T.; Harris, K. D.; Rider, D. A.; Wakefield, N. G.; Sit, J. C.; Buriak, J. M.; Thommes, M.; Brett, M. J. Surface Area Characterization of Obliquely Deposited Metal Oxide Nanostructured Thin Films. *Langmuir*, **2010**, 26, 4368–4376.
- ¹⁹ Enakieva, Y. Y.; Michalak, J.; Absulaeva, I. A.; Volostnykh, M. V.; Stern, C.; Guillard, R.; Gessmertnykh-Lemeune, A. G.; Gorbunova, Y. G.; Tsivadze, A. Y.; Kadish, K. M. General and Scalable Approach to A2B- and A2BC-Type Porphyrin Phosphonate Diesters. *Eur. J. Org. Chem.* **2016**, 4881-4892.
- ²⁰ Giovannetti, R. The Use of Spectrophotometry UV-Vis for the Study of Porphyrins. *Macro to Nano Spectroscopy, Dr. Jamal Uddin (Ed.)*, **2012**, 87-108.
- ²¹ CRC. Handbook of Chemistry and Physics; 88th ed.; *CRC Press*: Boca Raton, FL, **2008**.
- ²² Makarska, M.; Radzki, S. Water-soluble porphyrins and their metal complexes. *ANNALES UNIVERSITATIS MARIAE CURIE-SKŁODOWSKA LUBLIN-POLONIA*, **2002**, VOL. LVII, 17 SECTIO AA, 332-363.
- ²³ Berger, T.; Anta, J. A.; Morales-Florez, V. Electrons in the band gap: Spectroscopic characterization of anatase TiO₂ nanocrystal electrodes under fermi level control. *J. Phys. Chem. C* **2012**, 116, 11444–11455.
- ²⁴ Renault, C.; Andrieux, C. P.; Tucker, R. T.; Brett, M. J.; Balland, V.; Limoges, B. Unraveling the Mechanism of Catalytic Reduction of O₂ by Microperoxidase-11 Adsorbed within a Transparent 3D-Nanoporous ITO Film. *J. Am. Chem. Soc.*, **2012**, 134, 6834–6845.
- ²⁵ Bard, A. J.; Faulkner, L. R. *Electrochemical Methods: Fundamentals and Applications*. *New York: Wiley*, **2001**.
- ²⁶ Pegis, M. L.; Wise, C. F.; Martin, D. J.; Mayer, J. M. Oxygen Reduction by Homogeneous Molecular Catalysts and Electrocatalysts. *Chem. Rev.* **2018**, 118, 2340-2391.
- ²⁷ Ferrell, R. T.; Himmelblau, D. M. Diffusion Coefficients of Nitrogen and Oxygen in Water. *J Chem Eng Data.* **1967**, 12, 111-115.

Chapter II. Introducing molecular functionalities within nanostructured GLAD-ITO electrodes through diazonium electrografting

Adapted from

Kim, Y. -S.; Fournier, S.; Lau-Truong, S.; Decorse, P.; Devillers, C. H.; Lucas, D.; Harris, K. D.; Limoges, B.; Balland, V. *ChemElectroChem*, **2018**, 5(13), 1625–1630.

1. Introduction
2. Electrografting of diazonium salt on planar ITO and GLAD-ITO electrodes
3. Spectroscopic characterization of the modified electrodes
 - 3.1. Spectroelectrochemistry
 - 3.1.1. UV-visible absorbance spectra
 - 3.1.2. Extinction coefficient estimation
 - 3.1.3. Surface concentration of grafted porphyrin
 - 3.1.4. Ferrocenethanol passivation
 - 3.1.5. Time-dependent stability in ACN and aqueous solutions
 - 3.2. resonance Raman (rR) spectroscopy
 - 3.3. X-ray photoelectron spectroscopy (XPS)
4. Conclusion

1. Introduction

Indium-tin oxide (ITO) is one of the wide band gap metal oxides combining interesting characteristics of both high electronic conductivity and good transmission in the visible region. As degenerate *n*-type semiconductors,¹ nanostructured films of ITO can be used either as photoanodes or photocathodes, depending on the type of dye-sensitizers or light excitation.¹⁻⁶

One of the crucial issues for efficient and stable dye-sensitized photoelectrodes is the degree of electronic coupling and stability with which the molecular sensitizer is chemically anchored onto the metal oxide surface. Indeed, it has to be strong enough to withstand the hydrolytic conditions generally required for sustainable and eco-friendly devices,⁷ and at the same time, it must lead to an efficient electronic coupling between the dye and the metal oxide to allow fast interfacial electron transfer reactions.

The most commonly used method for dye sensitization of metal oxide surfaces is by chemisorption of carboxylate or phosphonate anchoring groups present on the dye molecule.⁸ This chemical surface functionalization strategy has been notably used for the sensitization of metal oxide surfaces with a wide range of porphyrins, which are attractive for their advantageous light harvesting properties and also for their easily adjustable photophysicochemical properties through the introduction of appropriate metal ions and substituents.^{2,8} The resulting porphyrin-modified electrodes however suffer from poor stability due to a progressive loss of dye from the surface by hydrolytic cleavage of the anchoring bond, especially under basic aqueous conditions.⁹

Therefore, there is a need to develop alternative surface functionalization methods in order to obtain more stable dye-modified mesoporous metal oxide surfaces with high coverage, and with easy to implement techniques. One method that can potentially meet these criteria is the electrochemical functionalization of conductive surfaces through the reduction of aryl diazonium salts. With this methodology, electrochemically-generated aryl radicals form covalent bonds with the electrode surface, and fairly good control over the quantity of grafted molecules can be obtained via adjustment of the applied potential, appropriate selection of the grafting time and variation of the diazonium salt concentration in solution.¹⁰ This strategy has been widely used for the covalent modification of planar electrodes of different conductive materials,¹¹ including metal oxide surfaces such as ITO,¹²⁻¹⁸ but it has never been explored for

the modification of 3D transparent mesoporous metal oxide films and in particular 3D mesoporous films of ITO.

The purpose of the present work is to fill this gap by investigating the electrochemical grafting of high surface area nanostructured ITO electrodes by an in-situ generated meso-triaryl free-base porphyrin diazonium salt [$\text{H}_2(\text{PDTP})\text{-N}_2^+$], a surface functionalization strategy that was previously validated at standard planar electrodes.¹⁷ As a redox-active chromophore, the grafted porphyrin has the merit of allowing quantitative analysis of the modified 3D electrodes not only by electrochemistry but also using various complementary spectroscopic techniques. The nanostructured ITO electrodes used in the present study were prepared by glancing angle deposition (GLAD), a one-step vapor deposition method allowing well-defined and reproducible fabrication of mesoporous ITO films. 500 nm-thick nanocolumnar GLAD-ITO films were deposited on flat conductive ITO substrates (Figure 1), with the open porosity beneficial for fast diffusion of chemical species throughout the void volume of the film.¹⁹⁻²⁰ The films are characterized by a porosity of 47 % and an electroactive surface area enhancement of 35 (see Experimental Section).

2. Electrografting of diazonium salt on planar ITO and GLAD-ITO electrodes

The surface functionalization by electrochemical grafting of diazonium salt on planar ITO and GLAD-ITO electrodes was achieved by multiple reductive cyclic voltammetry (CV) scans of the free-base porphyrin diazonium salt (generated in situ beforehand by addition of NaNO_2 and trifluoroacetic acid to 1 mM $\text{H}_2(\text{PDTP})\text{-NH}_2$, see Experimental part for detail) in acetonitrile solution without or with forced convection (Figure 1).¹⁷

In the absence of forced convection, reductive cycling results in non-uniformly modified GLAD-ITO electrodes as clearly evidenced in Figure 2 (electrode B). This was attributed to a mass transport limitation of the diazonium salt into the porous film. The huge surface area of the GLAD electrode and relatively low diazonium salt concentration (~1 mM) is expected to lead to a strong concentration polarization at the electrode interface during the electrochemical grafting. To better regulate the mass transport both in solution and within the porous electrode, the electrografting was performed under a moderate flow of argon bubbles near the working electrode surface. Under this forced convection, the $\text{H}_2(\text{PDTP})$ -modified

electrodes are darker and much more uniform (Figure 2, electrodes C and D), characteristic of an improved grafting homogeneity.

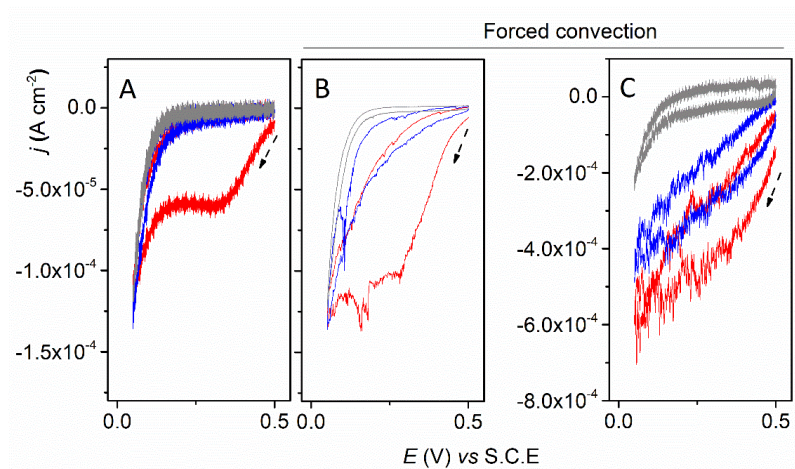


Figure 1. (—) 1st, (—) 2^d and (—) 10th cyclic voltammograms recorded during the electrografting of H₂(PDTP-N₂⁺) (~1 mM of the *in-situ* generated diazonium salt in 0.1 M TBAPF₆/ACN solution) at (A,B) planar and (C) GLAD-ITO electrodes ($v = 50 \text{ mV}\cdot\text{s}^{-1}$, $T = 20^\circ\text{C}$). In B and C, the solution was stirred during electrografting by continuously bubbling argon.

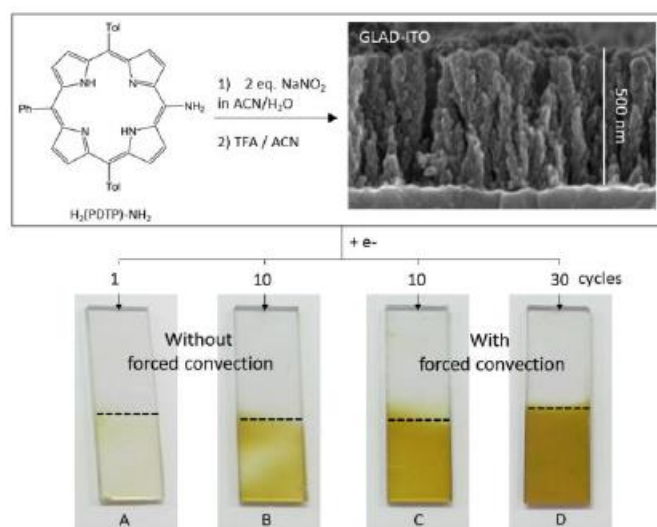


Figure 2. *In-situ* generation of the free-base meso-triaryl porphyrin diazonium ion followed by its electrochemical reduction at 500-nm-thick nanostructured GLAD-ITO electrodes (side-view of the GLAD electrode obtained by SEM). Electrodes A and B were obtained without forced convection in solution after 1 or 10 CV electrodeposition cycles, respectively. Electrodes C and D were obtained with forced convection in solution after 10 and 30 CV electrodeposition cycles, respectively.

3. Spectroscopic characterization of the modified electrodes

3.1. Spectroelectrochemistry

Detailed set-up is reported in experimental section. Briefly, UV-visible absorption spectroscopy was performed on a TORUS UV-visible spectrophotometer (Ocean Optics) with optical fibers and a balanced deuterium tungsten source (Micropack) in a thermostated cell (25 °C). The ITO electrode was inserted in a classical 1-cm cuvette filled with solution, and detection was performed in transmittance. Electrochemical experiments were carried out with an Autolab potentiostat (PGSTAT-12) linked to GPES software.

3.1.1. UV-visible absorbance spectra

The resulting modified 3D GLAD-ITO electrodes (and controls) were characterized by UV-visible absorption spectroscopy in acetonitrile (Figure 3). All modified electrodes share common spectroscopic features, showing a large and intense Soret band centered at 420 nm, analogous to that obtained for H₂(PDTP)-NH₂ in homogenous solution, and a shoulder at 405 nm that might arise from H-aggregates. In contrast, the free-base porphyrin Q bands pattern (500—750 nm) is strongly affected by the grafting, suggesting modification of the porphyrin symmetry.²¹ It is indeed striking to note that the UV-visible spectrum of the grafted porphyrin is strongly analogous to that of fully symmetrical tetraphenylporphyrins either in solution or once grafted on surfaces,^{15,22} which raises questions about the nature of the meso substituents of porphyrin once grafted (*vide infra*).

Additionally, the metalation of H₂(PDTP)-modified GLAD-ITO was further investigated by soaking the modified electrode in a saturated zinc acetate solution (see experimental part). Metalation of the grafted porphyrins is confirmed by the typical bathochromic shift of the Soret band from 420 to 426 nm as well as Q band pattern change from four Q bands positioned at 521, 555, 595, 654 nm to two Q bands at 562, 602 nm. Interestingly, metalation was successfully performed upon moderate heating of the electrode (50 °C for 15 minutes) without significant loss of the grafted porphyrin which confirms the particularly good stability of the modified electrode (see below).

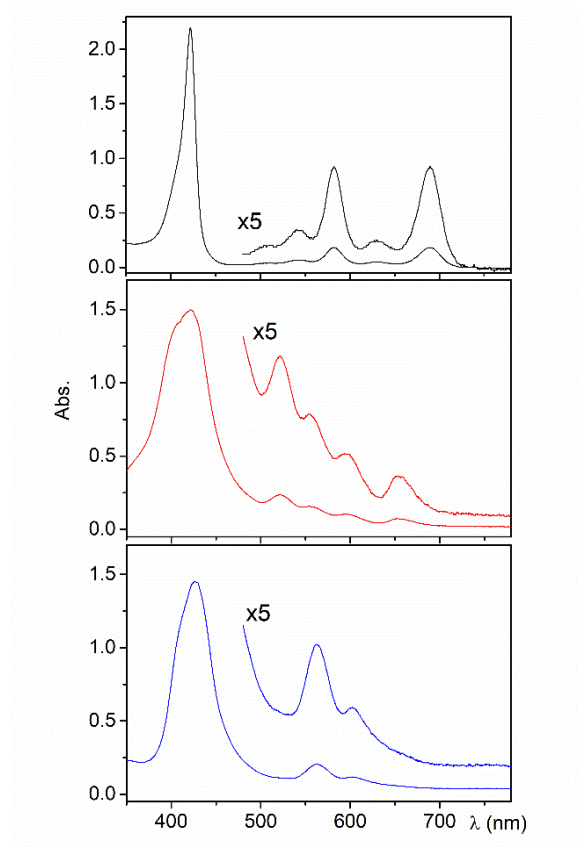


Figure 3. UV-visible spectra recorded for (black) $\text{H}_2(\text{PDTP})\text{-NH}_2$ in solution and $\text{H}_2(\text{PDTP})\text{-GLAD-ITO}$ (red) prior to and (blue) after metallization by Zn^{2+} . The spectra of $\text{H}_2(\text{PDTP})\text{-NH}_2$ was recorded in acetonitrile. All UV-visible absorption spectra are subtracted from GLAD-ITO contribution.

3.1.2. Extinction coefficient estimation

In order to soundly estimate the extinction coefficient of the grafted porphyrin, $\text{H}_2(\text{PDTP})\text{-modified}$ GLAD-ITO electrodes prepared from 30 electrodeposition cycles were further characterized by spectroelectrochemistry in acetonitrile by monitoring the absorbance change of the grafted film during a reductive CV scan down to $-1.5 \text{ V vs. Ag/AgCl}$ (Figure 4). A reversible cathodic wave is clearly visible at -1.24 V and attributed to the one-electron reduction of the porphyrin core into a porphyrin radical anion. This redox process is accompanied by strong extinction of the Soret until it completely vanishes at the slowest scan rates. This behavior is in agreement with that previously reported for porphyrin radical anions.²³⁻²⁴ Redox process is also reasonably chemically reversible as revealed by the nearly complete recovery of the Soret band intensity upon scanning back to the initial anodic potential. It is however worth noting that on account of the intrinsically poor stability of the porphyrin

radical anion (especially in the presence of trace water), on the time scale of the CV experiment a small fraction is converted to an unknown compound that oxidizes at -0.4 V during the backward scan.²⁵ The fact that all grafted porphyrins can be electrochemically reduced demonstrates that they are all electrically wired to the underlying conductive ITO surface, even those that are somewhat remote from the surface due to the oligomerisation process (see below). The reduction rate of the grafted porphyrin however remains slow as attested by the rapid lowering of the fraction of reduced porphyrin by increasing scan rates. Only 75 % of the grafted porphyrins are reduced at $100 \text{ mV}\cdot\text{s}^{-1}$ comparing to 100 % at $10 \text{ mV}\cdot\text{s}^{-1}$. Such an observation is consistent with a multimeric porphyrin film leading to slow, long-range electron transport.

Finally, by correlating the integrated charge recovered from the cathodic peak in CV with the intensity decrease of the Soret band absorbance, it becomes possible to properly estimate the ϵ value of the Soret band for the grafted free-base porphyrin on GLAD-ITO. From the integration of the CV cathodic peak recorded at $100 \text{ mV}\cdot\text{s}^{-1}$ (right graph, integration corresponds to the dashed area obtained after subtraction of the capacitive current contribution), the amount of reduced porphyrin was estimated as being $6 \text{ nmol}\cdot\text{cm}^{-2}$. According to the corresponding Soret band decrease on the left graph (passage from the grey plot to the black one), it is assumed to correspond to $\sim 75 \%$ reduction of the grafted porphyrin (total disappearance of the Soret band can be achieved at slower scan rates, see for instance the spectra recorded at $10 \text{ mV}\cdot\text{s}^{-1}$, or by applying a constant cathodic potential of -1.5 V for a few seconds). This result finally allows us to calculate an epsilon value of *ca.* $175\,000 \text{ M}^{-1}\cdot\text{cm}^{-1}$ for the non-reduced porphyrin at 420 nm.

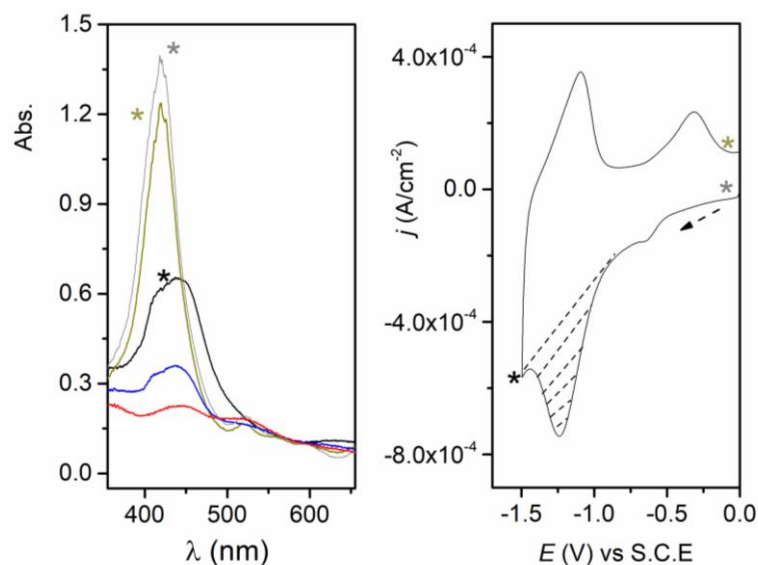


Figure 4. (Left) UV-visible absorbance spectra recorded at a H₂(PDTP)-functionalized GLAD-ITO electrode (obtained from 30 electrografting cycles) during the time course of a CV scan (in 0.1 M TBAPF₆ in ACN). The spectra were recorded at (grey and dark yellow) 0 V (corresponding both to the starting and final applied potential in CV, respectively), and -1.5 V for different scan rates: (black) 100, (blue) 20 and (red) 10 mV·s⁻¹. All spectra are corrected from the bare GLAD-ITO absorbance, and especially in the red spectra some residual contribution from light diffraction at the mesoporous film is visible and responsible for the large bands detected. (Right) Corresponding CV recorded at 100 mV·s⁻¹ (in 0.1M TBAPF₆ in ACN) showing a fairly good reversibility of the one-electron reduction process centered at $E^\circ = -1.17$ V.

3.1.3. Surface concentration of grafted porphyrin

Quantification of the amount of grafted porphyrins is simply achieved from the magnitude of the Soret band absorbance assuming an extinction coefficient of $\epsilon_{420} = 175\,000$ M⁻¹cm⁻¹ inferred from spectroelectrochemistry (see section 3.1.2). The surface coverage of grafted porphyrins exhibits a strong dependence over the number of CV electrodeposition cycles until it reaches a maximal value after *ca.* 30 electrodeposition cycles (Figure 5). Maximal surface concentration Γ^{\max} of 1.2 ± 0.3 and 9.9 ± 1.5 nmol·cm⁻² were obtained at planar and GLAD-ITO electrodes, respectively, after normalized to the geometric electrode area. The low relative standard deviation on Γ^{\max} (*i.e.*, 15 % from 10 independent experiments) at GLAD-ITO electrodes attests to high uniformity of the nanostructured GLAD-ITO electrodes as well as good control over the electrodeposition process. The much larger surface concentration obtained with GLAD-ITO electrodes is also consistent with the higher specific surface area of these electrodes as compared with planar ITO. The Γ^{\max} value at planar ITO

electrodes is ~ 4 times larger than that theoretically expected for a closed-packed monolayer of porphyrin (a theoretical value of $\Gamma^{\text{sat}} = 0.3 \text{ nmol}\cdot\text{cm}^{-2}$ can be calculated for a stacked-monolayer of porphyrins oriented perpendicular to a flat solid surface).²⁶ This result suggests the formation of porphyrin multilayers via coupling reactions between electrochemically-generated radical porphyrins and surface-grafted porphyrins, a behavior commonly encountered with electrodeposition of diazonium salts.¹¹ The growth of multilayers is however rapidly self-limited by the very poor conductivity of the oligomeric film on the surface which will be discussed on next section.

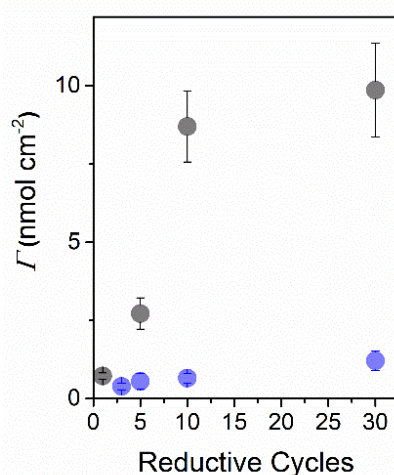


Figure 5. Porphyrin surface coverage deduced from the Soret band absorbance as a function of the number of electrodeposition cycles on (●) 2D- and (●) 3D-GLAD ITO electrodes. The standard deviation was calculated from at least 3 independent electrodes.

3.1.4. Passivation effect of electron transfer

The electron transfer blocking properties of the dense multilayer films generated at planar ITO electrodes were indirectly confirmed in CV by the strong decrease in the magnitude of the reversible faradaic current response of the soluble redox probe $[\text{Fe}(\text{CN})_6]^{3-}$ (Figure 6, Left) and by the change in the shape of the reversible wave to a more S-shaped steady-state voltammogram rather than a semi-infinite linear diffusion voltammogram.

Such behavior is characteristic of an imperfect insulating layer of blocking electron transfer on the electrode surface which indicates partial conductive pinholes of uncovered ITO through the grafted film. This can then be described as a randomly distributed array of

independent microelectrodes wherein the mass transport of the soluble redox probe occurs by hemispherical diffusion.²⁷

In contrast to that of planar ITO electrodes, CVs recorded at GLAD-ITO electrodes in the presence of the $[\text{Fe}(\text{CN})_6]^{3-}$ (Figure 6, right) shows a less passivation effect of electron transfer through the grafted porphyrin layer. This is supported by the fact that the faradaic current response is less diminished and the reduction wave remains quite reversible compared to planar ITO electrode. Such behavior also indicates that a large fraction of ITO remains uncovered and that the resulting randomly distributed conducting sites act as an array of microelectrodes wherein diffusion layers from individual sites overlap and merge.²⁷ Another outcome to consider (that certainly occurs there) is a change in the redox probe partitioning to the mesoporous GLAD-ITO film once the surface is chemically modified. This should contribute to decrease the faradaic current response. These statements are consistent with the porphyrin surface coverage determined at GLAD-ITO film by UV-visible. Dividing the maximal surface concentration (9.9 nmol per cm^2 of geometric electrode area) by the surface enhancement (35 for a 500 nm thick GLAD-ITO film) leads to a coverage value of 0.28 ± 0.04 nmol· cm^{-2} . This is comparable to the theoretical coverage calculated for a saturated monolayer (*i.e.*, 0.3 nmol· cm^{-2}), but much less than that obtained at planar ITO electrodes (see above). These overall observations finally indicate formation of a less compact porphyrin layer at GLAD-ITO, wherein the layer arrangement is much closer to a loosely packed layer of porphyrin oligomers than a close-packed monolayer. This also means that the GLAD-ITO film nanostructure and mesoporosity has a non-negligible impact on the homogeneity of the grafted layer. This may be due to the difficulty of accessing in the same way the entire porosity of the film. It can also be the consequence of different concentration gradients that develop across the high surface GLAD-ITO film during electrochemical grafting.

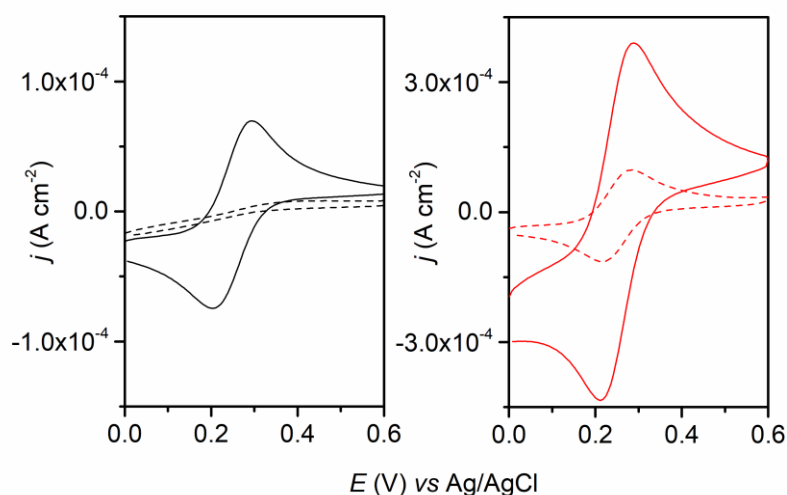


Figure 6. Cyclic voltammograms of a 1 mM $\text{K}_3\text{Fe}(\text{CN})_6$ aqueous solution (50 mM Hepes, 0.3 M KCl, pH 7) recorded on (Left) planar ITO and (Right) nanostructured GLAD-ITO in the absence (solid line) and presence of grafted porphyrins (dashed line, 30 electrodeposition cycles). $\nu = 0.1 \text{ V}\cdot\text{s}^{-1}$, $T = 20^\circ\text{C}$.

It is worth to note that the Faradaic current responses of the redox probe $\text{Fe}(\text{CN})_6^{3-}$ at the porous GLAD-ITO electrode is not proportional to the real electrode area. This result can be predicted by the fact that at the CV scan rate used in this experiment, the diffusion layer has a thickness of several micrometers. Such a value is significantly larger than the $0.5 \mu\text{m}$ film thickness of the mesoporous GLAD-ITO film. Therefore, on the scale of the diffusion layer, the GLAD-ITO electrode appears as flat electrode and the area of the diffusion field is probably not far from the geometric electrode area. That the faradaic currents are finally higher by a factor 5-6 at the GLAD-ITO electrode than at the planar ITO electrode can be explained by a favorable partitioning of the soluble redox active compound to the mesoporous GLAD-ITO film, therefore locally increasing the concentration of the redox actives molecules and thus the current response.

3.1.5. Time-dependent stability in ACN and aqueous solutions

The long term time-dependent stability of the $\text{H}_2(\text{PDTP})$ -functionalized GLAD-ITO electrodes, particularly regarding desorption and/or hydrolysis from the surface, was investigated under various experimental conditions. As reported in Figure 7, the modified electrodes are very stable in organic as well as neutral aqueous solutions, showing less than 30 % decrease of surface coverage after 2 weeks and *ca.* 50 % decrease after 7 weeks (data not

shown). These observations strongly suggest that porphyrins are chemically anchored to the ITO surface through the formation of stable covalent bonds (formed either at the ITO surface or within the porphyrin oligomers). The stability of the modified electrode is however dependent on the pH, tending toward much less stability under extreme pH conditions, *i.e.* pH 2 and 12. Such a pH effect might be indicative of a metal-O-carbon bond sensitive to acid/base catalysed hydrolysis and that is assumed to be formed from the coupling reaction between the electrochemically generated porphyrin radical and the oxygen atoms present at the ITO interface. One should however note that the desorption/hydrolysis here occurs at a much slower rate than in the case of redox-active molecules chemisorbed on ITO electrode surfaces through phosphonate or phosphate anchoring groups (we previously reported a 30 % surface coverage decrease within 7 days at pH 7 for a chemisorbed flavin mononucleotide, as well as an immediate massive desorption at pH > 9).²⁸

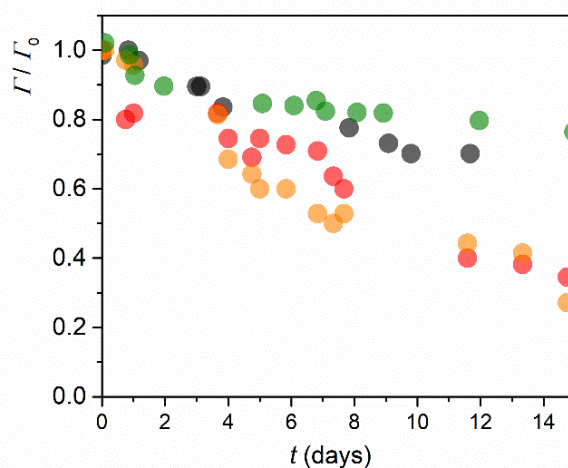


Figure 7. Evolution of the surface coverage with time upon soaking H₂(PDTP)-GLAD-ITO electrodes (obtained after 30 electrodeposition cycles) in (●) acetonitrile and aqueous solutions at pH (●) 2, (●) 7, and (●) 12.

3.2. resonance Raman (rR) spectroscopy

In order to get deeper insights into the chemical structure of the grafted porphyrin, the modified electrodes were characterized by resonance Raman (rR) spectroscopy and the spectra then compared to that obtained for H₂(PDTP)-NH₂ in homogeneous solution (Figure 8). The rR spectra are dominated by the vibronic modes of the porphyrin and show almost no difference between the initial and grafted porphyrin, except for the $\nu_{(\text{C}_{\text{meso}}-\text{C}_{\text{phenyl}})}$ vibrational mode (ν_I)

linked to the phenyl meso-substituents (see Table 1 for band assignment). A unique vibrational mode is indeed observed at 1237 cm^{-1} for the grafted porphyrin while this mode is split into two separate components (at 1228 and 1250 cm^{-1}) for the $\text{H}_2(\text{PDTP})\text{-NH}_2$ compound (which is expected for an asymmetric triphenylporphyrin).²⁹⁻³⁰ This particularity in the rR spectrum of the grafted porphyrin combined with the Q-bands shape in the UV-visible absorption spectrum (see section 3.1.1) strongly supports the assumption that highly symmetric porphyrins dominate in the grafted layers. We can thus assume that porphyrin oligomers are formed by direct reactions between the electrogenerated porphyrin radicals and surface grafted porphyrins. It has to be mentioned here that the meso phenyl substituent (located anti to the diazonium functionality) is assumed to be much more prone to chemical coupling with the electrochemically-generated $\text{H}_2(\text{PDTP})\bullet$ radical *via* its para position than the meso tolyl substituents, leading predominantly to grafting of linear chains of porphyrin oligomers on the ITO surface.

Full metalation of the grafted porphyrin upon soaking in a saturated zinc acetate solution is further confirmed by rR, with complete disappearance of several vibrational modes characteristic of the free base porphyrins (notably at 964 , 1292 and 1237 cm^{-1}). Moreover, the rR spectra of $\text{Zn}(\text{PDTP})$ -modified GLAD-ITO exhibits specific vibrational modes such as the intense ν_4 mode at 1355 cm^{-1} .

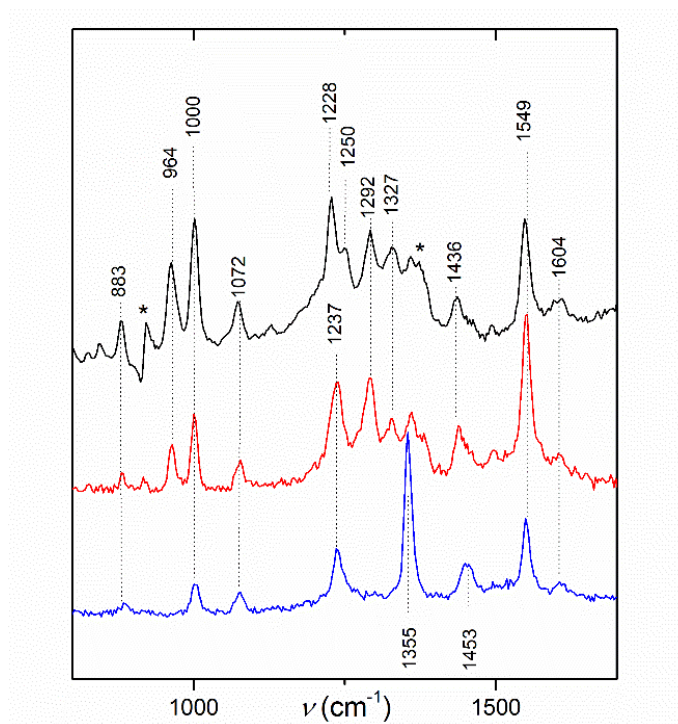


Figure 8. resonance Raman spectra ($l_{\text{exc}} = 405 \text{ nm}$) recorded for (black) $\text{H}_2(\text{PDTP})\text{-NH}_2$ in solution and $\text{H}_2(\text{PDTP})\text{-GLAD-ITO}$ (red) prior to and (blue) after metallization by Zn^{2+} . The spectra of $\text{H}_2(\text{PDTP})\text{-NH}_2$ was recorded in acetonitrile and the rR spectrum was subtracted from contributions of acetonitrile (remaining contributions are highlighted by *).

Table 1. Resonance Raman peak assignment. Frequencies are given in cm^{-1} . Band assignment was realized according to the literature.³¹⁻³³

	$\text{H}_2(\text{PDTP})\text{-NH}_2$	$\text{H}_2(\text{PDTP})\text{-GLAD-ITO}$	$\text{Zn}(\text{PDTP})\text{-GLAD-ITO}^*$
$\delta(\text{pyr}) + \nu_{10}$	1604	1604	1604
$\nu_{\text{C}\beta\text{-C}\beta} (\nu_2)$	1549	1549	1549
$\nu_{\text{C}\alpha\text{-C}\beta}$	1436	1436	1453
$\nu_{\text{C}\alpha\text{-N}} (\nu_4)$	1361	1361	1355
$\delta(\text{pyr})$	1292	1292	
$\nu_{\text{C}\alpha\text{-CPh}} (\nu_1)$	1250	1237	1237
	1228		
$\delta_{\text{C}\beta\text{-H}}$	1072	1072	1072
Phenyl	1000	1000	1000

* only A_{1g} modes are expected to be active in Raman which is expected for a D_{4h} metallated porphyrin.

3.3. X-ray photoelectron spectroscopy (XPS)

To get more information on the chemical bonds formed at the ITO interface, planar modified ITO electrodes were investigated by XPS. After electrografting, the presence of the porphyrinic film on the ITO substrate is attested by the appearance of a signal specific to N_{1s} (absent in the bare ITO), as well as a large increase of the signal relative to C_{1s} and a large decrease in the intensity of the In_{3d} signal (Figure 9). Both the N/In and C/In ratios (see Table 2) are larger for planar ITO electrodes as compared to GLAD ITO electrodes, which further confirm that the grafted porphyrin layer is denser at planar electrodes. Aside from the decreased intensity, the In and Sn peaks remain unaffected by the grafting (data not shown), which indicates that the metal sites are not directly involved in the chemical bond formed between the metal oxide interface and the grafted porphyrin. These observations are in line with previous data obtained at ITO.¹²

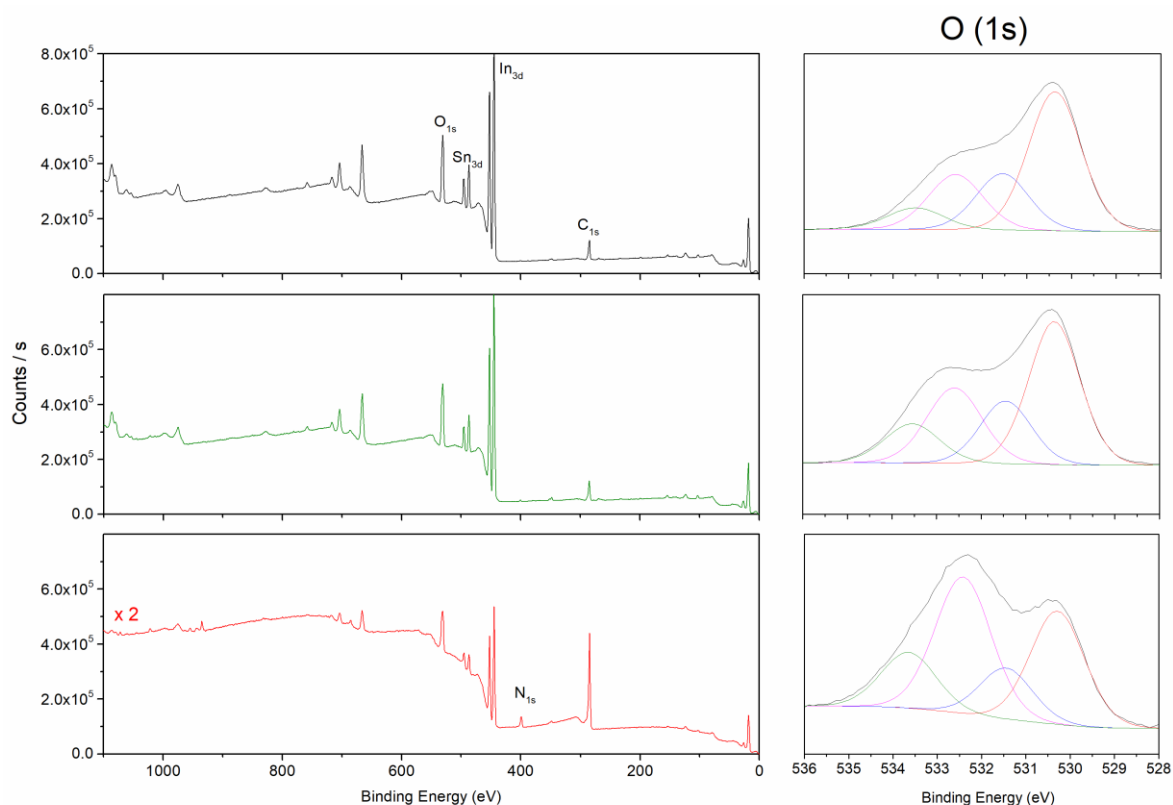


Figure 9. (Left) XPS survey spectra obtained at planar ITO electrodes (top, black) prior to cyclic voltammetry, (bottom, red) after electrografting and (middle, green) after cyclic voltammetric experiments identical to that for electrografting but in the absence of $H_2(PDTP)-NH_2$ in solution. (Right) Corresponding $O(1s)$ spectra with individual components (see Table 2).

Table 2. XPS binding energy (in eV) and atomic composition obtained for the survey spectra recorded at planar and GLAD ITO electrodes. The ITO and GLAD-ITO columns correspond to the data collected at the as received planar and GLAD ITO electrodes respectively, while ITO-CV corresponds to the data collected at a planar ITO electrode after the electrode has been scanned by CV for 30 cycles in the H₂PDTP-NH₂-free electrografting electrolyte solution. The H₂PDTP-ITO and H₂PDTP-GLAD-ITO columns correspond to the data collected at planar and GLAD ITO electrodes after they were scanned by CV for 30 cycles in the electrografting electrolyte solution containing 1 mM of the diazonium salt of H₂PDTP-NH₂. The relative atomic composition of the C(1s), N(1s) and O(1s) contribution were averaged from at least three different independent measurements.

	ITO	ITO-CV	H ₂ (PDTP)-ITO	GLAD-ITO	H ₂ (PDTP)- GLAD-ITO
C(1s)	285.3 (23.6 %)	283.3 (26.8 %)	284.9 (71 %)	285.2 (36 %)	285.1 (61.3 %)
N(1s)*	400.3 (< 1%)	400.5 (1.2 %)	400.1 (2.3 %) 398.9 (3%)	400.1 (1%)	400.4 (3%) 398.9 (3 %)
In(3d)	444.7 (27.7 %)	444.7 (23.2 %)	444.7 (6.8 %)	444.7 (21 %)	444.7 (9.3 %)
Sn(3d)	486.7 (4.1 %)	486.8 (3.7 %)	486.7 (1%)	486.8 (2 %)	486.9 (0.9 %)
O(1s)	530.3 (43.8 %)	530.7 (45%)	532 eV (15.2 %)	530.5 (36.6 %)	531 eV (21 %)
Sn(3d)/In(3d)	0.15	0.16	0.15	0.10	0.10
C(1s)/In(3d)	1.2 ± 0.3	1.2 ± 0.2	12.1 ± 2.3	1.7 ± 0.3	6.6 ± 1.2
N(1s)/In(3d)	-	0.05 ± 0.02	0.78 ± 0.05	1.7 ± 0.02	0.65 ± 0.05
O(1s)/In(3d)	1.7 ± 0.1	2.0 ± 0.2	2.6 ± 0.3	1.7 ± 0.3	2.3 ± 0.3

*The N_{1s} signal exhibits two main components as expected for free base porphyrins.³⁴

We thus focused on the O_{1s} peak as metal-O-carbon bonds are expected to be present at *ca.* 533 eV.^{16,35-37} Our analysis evidences first that the relative amount of oxygen atoms detected at the surface (*i.e.*, the O/In ratio, Table 2) increases upon electrochemical grafting, despite the fact that the grafted porphyrin is free of oxygen atoms.

Second, we notice that the shape of the O_{1s} peak is strongly modified upon electrografting, with an increase in the relative intensity of the component at 532.6 eV and, to a lower extent, the component at 533.5 eV (Figure 10, Table 3). These observations suggest that the mechanism of aryl radical grafting is related to significant hydroxylation of the ITO surface. Decisive assignment of metal-O-carbon bond to one of the high binding energy components of the O_{1s} peak still remains difficult as these components are present in all samples and are generally attributed to surface hydroxyl groups for the component at 532.6 eV, whereas the component at 533.5 eV is required for proper fitting and may arise from adsorbed

water molecules.³⁸⁻³⁹ We can however not rule out that metal-O-carbon bonds combine with one of these components according to their high binding energy. Representative metal-O-carbon bonds at GLAD-ITO is described in Figure 10.

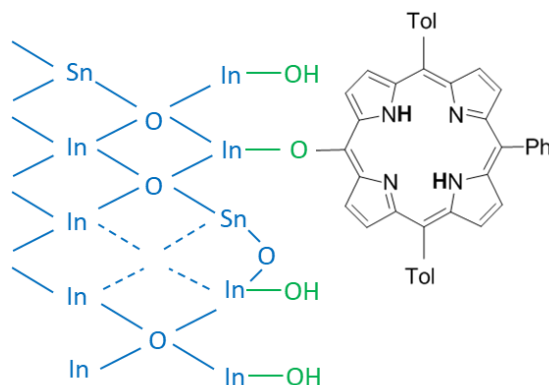


Figure 10. Representation of metal-O-carbon bonds on H₂PDTP-GLAD-ITO.

Table 3. Individual components of the O(1s) spectra recorded at planar ITO electrodes. The O_A and O_B components are attributed to bulk oxygen and adjacent vacancy oxygen of the ITO lattice, respectively. The O_C component is attributed to surface hydroxyls, and the O_D component is required for proper fitting but not precisely attributed.³⁸⁻³⁹

	O _A	O _B	O _C	O _D	O _B /O _A	O _C /(O _A + O _B)
E (eV)	530.3	531.4	532.6	533.5		
ITO	50.5	20.5	20	8.5	0.41	0.28
ITO-CV	43.5	19.1	24.7	12.7	0.44	0.39
H ₂ (PDTP)-ITO	31.3	13.8	39.3	15.6	0.44	0.87

4. Conclusion

In the present work, we demonstrate that efficient and homogeneous functionalization of 3D nanostructured transparent GLAD-ITO electrodes was successfully achieved by electrochemical reduction of in-situ generated free-base porphyrin diazonium salts with a high degree of control over the homogeneity, surface coverage and reproducibility. The resulting modified electrodes were characterized by cyclic voltammetry, UV-visible absorption, resonance Raman and XPS. The overall results strongly support the formation of covalently linked electroactive porphyrin oligomers on the ITO surface through an underlying metal-O-

carbon bond. This leads to highly stable toward desorption or hydrolysis in organic as well as mild hydrolytic conditions, and allowing quantitative post-metalation by zinc ions of the grafted free-base porphyrins. The present study opens thus new opportunities for the preparation of more stable dye-sensitized or molecular catalyst-functionalized high-surface area photoelectrodes by functionalization of nanostructured transparent metal oxide-based electrodes with a wide range of adjustable molecular properties.

References

- ¹ Kim, H.; Gilmore, C. M. Electrical, optical, and structural properties of indium–tin–oxide thin films for organic light-emitting devices. *J. Appl. Phys.* **1999**, *86*, 6451–6461.
- ² Furmansky, Y.; Sasson, H.; Liddell, P.; Gust, D.; Ashkenasy, N.; Visoly-Fisher, I. Porphyrins as ITO photosensitizers: substituents control photo-induced electron transfer direction. *J. Mater. Chem.* **2012**, *22*, 20334.
- ³ Huang, Z.; He, M.; Yu, M.; Click, K.; Beauchamp, D.; Wu, Y. Dye-Controlled Interfacial Electron Transfer for High-Current Indium Tin Oxide Photocathodes. *Angew. Chemie - Int. Ed.* **2015**, 6857–6861.
- ⁴ Yu, Z.; Perera, I. R.; Daeneke, T.; Makuta, S.; Tachibana, Y.; Jasieniak, J. J.; Mishra, A.; Bäuerle, P.; Spiccia, L.; Bach, U. Indium tin oxide as a semiconductor material in efficient p-type dye-sensitized solar cells. *NPG Asia Mater.* **2016**, *8*, e305.
- ⁵ Farnum, B. H.; Wee, K. R.; Meyer, T. J. Self-assembled molecular p/n junctions for applications in dye-sensitized solar energy conversion. *Nat. Chem.* **2016**, *8*, 845–852.
- ⁶ Kato, M.; Cardona, T.; Rutherford, A.W.; Photoelectrochemical Water Oxidation with Photosystem II Integrated in a Mesoporous Indium–Tin Oxide Electrode. Reisner, E. *J. Am. Chem. Soc.* **2012**, 8332–8335.
- ⁷ Bella, F.; Gerbaldi, C.; Barolo, C.; Grätzel, M. Aqueous dye-sensitized solar cells. *Chem. Soc. Rev.*, **2015**, *44*, 3431-3473.
- ⁸ Nayak, A.; Roy, S.; Sherman, B. D.; Alibabaei, L.; Lapidés, A. M.; Brennaman, M. K.; Wee, K. R.; Meyer, T. J. Phosphonate-derivatized porphyrins for photoelectrochemical applications. *ACS Appl. Mater. Interfaces* **2016**, *8*, 3853–3860.
- ⁹ Brennan, B. J.; Llansola Portolés, M. J.; Liddell, P. A.; Moore, T. A.; Moore, A. L.; Gust, D. Comparison of silatrane, phosphonic acid, and carboxylic acid functional groups for attachment of porphyrin sensitizers to TiO₂ in photoelectrochemical cells. *Phys. Chem. Chem. Phys.* **2013**, *15*, 16605.
- ¹⁰ Pinson, J.; Podvorica, F. Attachment of organic layers to conductive or semiconductive surfaces by reduction of diazonium salts. *Chem. Soc. Rev.* **2005**, *34*, 429–39.
- ¹¹ A. Berisha, A.; Chehimi, M. M.; Pinson, J.; Podvorica, F.I. Electrode surface modification using diazonium salts. *Electroanal. Chem.*, CRC Press, **2015**, 115–224.
- ¹² Maldonado, S.; Smith, T. J.; Williams, R. D.; Morin, S.; Barton, E.; Stevenson, K. J. Surface Modification of Indium Tin Oxide via Electrochemical Reduction of Aryldiazonium Cations. *Langmuir* **2006**, *22*, 2884–2891.
- ¹³ Chen, X.; Chockalingam, M.; Liu, G.; Luais, E.; Gui, A. L.; Gooding, J. J. A Molecule with Dual Functionality 4-Aminophenylmethylphosphonic Acid: A Comparison Between Layers Formed on Indium Tin Oxide by In Situ Generation of an Aryl Diazonium Salt or by Self-Assembly of the Phosphonic Acid. *Electroanalysis* **2011**, *23*, 2633–2642.

- ¹⁴ Gross, A. J.; Bucher, C.; Coche-Guerente, L.; Labbé, P.; Downard, A. J.; Moutet, J. C. Nickel (II) tetraphenylporphyrin modified surfaces via electrografting of an aryldiazonium salt. *Electrochem. commun.* **2011**, *13*, 1236–1239.
- ¹⁵ Picot, M.; Nicolas, I.; Poriel, C.; Rault-Berthelot, J.; Barrière, F. On the nature of the electrode surface modification by cathodic reduction of tetraarylporphyrin diazonium salts in aqueous media. *Electrochem. commun.* **2012**, *20*, 167–170.
- ¹⁶ Samanta, S.; Bakas, I.; Singh, A.; Aswal, D. K.; Chehimi, M. M. In situ diazonium-modified flexible ITO-coated PEN substrates for the deposition of adherent silver–polypyrrole nanocomposite films. *Langmuir* **2014**, *30*, 9397–9406.
- ¹⁷ Hebié, S.; Devillers, C. H.; Fournier, S.; Lucas, D. Direct Grafting of Free-Base meso-Triarylporphyrins on Electrode Materials through Diazonium Reduction: Reversible Zinc(II) Metallation of the Resulting Materials. *ChemElectroChem* **2016**, *3*, 45–50.
- ¹⁸ Cao, L.; Fang, G.; Wang, Y. Electroreduction of Viologen Phenyl Diazonium Salts as a Strategy To Control Viologen Coverage on Electrodes. *Langmuir* **2017**, *33*, 980–987.
- ¹⁹ Krause, K. M.; Taschuk, M. T.; Harris, K. D.; Rider, D. A.; Wakefield, N. G.; Sit, J. C.; Buriak, J. M.; Thommes, M.; Brett, M. J. Surface area characterization of obliquely deposited metal oxide nanostructured thin films. *Langmuir* **2010**, *26*, 4368–76.
- ²⁰ Renault, C.; Andrieux, C. P.; Tucker, R. T.; Brett, M. J. Balland, V.; Limoges, B. Unraveling the Mechanism of Catalytic Reduction of O₂ by Microperoxidase-11 Adsorbed within a Transparent 3D-Nanoporous ITO Film. *J. Am. Chem. Soc.* **2012**, *134*, 6834–45.
- ²¹ Giovannetti, R. in *Macro to Nano Spectrosc.* (Ed.: J. Dr. Uddin). The use of spectrophotometry UV-Vis for the study of porphyrins. *InTech*, **2012**, 87–109.
- ²² Paul-Roth, C.; Rault-Berthelot, J.; Simonneaux, G.; Poriel, C.; Abdalilah, M.; Letessier, J. Electroactive films of poly (tetraphenylporphyrins) with reduced bandgap. *Electroanal. Chem.* **2006**, *597*, 19–27.
- ²³ Fang, Y.; Bhyrappa, P.; Ou, Z.; Kadish, K. M. Planar and Nonplanar Free-Base Tetraarylporphyrins: β -Pyrrole Substituents and Geometric Effects on Electrochemistry, Spectroelectrochemistry, and Protonation/Deprotonation Reactions in Nonaqueous Media. *Chem. Eur. J.* **2014**, *20*, 524 – 532.
- ²⁴ Merhi, A.; Zhang, X.; Yao, D.; Drouet, S.; Mongin, O.; Paul, F.; Williams, J. A. G.; Fox, M. A.; Paul-Roth, C. O.; New donor–acceptor conjugates based on a trifluorenylporphyrin linked to a redox–switchable ruthenium unit. *Dalton. Trans.* **2015**, *44*, 9470–9485.
- ²⁵ Kalyanasundaram, K.; Neumann-Spallart, M. Photophysical and redox properties of water-soluble porphyrins in aqueous media. *J. Phys. Chem.* **1982**, *413*, 5163–5169.

- ²⁶ Bramblett, A. L.; Boeckl, M. S.; Hauch, K. D.; Ratner, B. D.; Sasaki, T. Determination of surface coverage for tetraphenylporphyrin monolayers using ultraviolet visible absorption and x-ray photoelectron spectroscopies. *Surf. Interface Anal.* **2002**, 33, 506–515.
- ²⁷ Amatore, C.; Savéant, J. M.; Tessier, D. Charge transfer at partially blocked surfaces: a model for the case of microscopic active and inactive sites. *J. Electroanal. Chem.* **1983**, 147, 39–51.
- ²⁸ Forget, A.; Tucker, R. T.; Brett, M. J.; Limoges, B.; Balland, V. Tuning the reactivity of nanostructured indium tin oxide electrodes toward chemisorption. *Chem. Commun.* **2015**, 51, 6944–6947.
- ²⁹ Zhang, Y. H.; Zhao, W.; Jiang, P.; Zhang, L. J.; Zhang, T.; Wang, J. Structural parameters and vibrational spectra of a series of zinc meso-phenylporphyrins: A DFT and experimental study. *Spectrochim. Acta - Part A Mol. Biomol. Spectrosc.* **2010**, 75, 880–890.
- ³⁰ Andersson, L. A.; Loehr, T. M.; Thompson, R. G.; Strauss, S. H. Influence of symmetry on the vibrational spectra of Zn (TPP), Zn (TPC), and Zn (TPiBC). *Inorg. Chem.* **1990**, 29, 2142–2147.
- ³¹ Blom, N.; Odo, J.; Nakamoto K.; Strommen, D. P. Resonance Raman studies of metal tetrakis (4-N-methylpyridyl) porphine: band assignments, structure-sensitive bands, and species equilibria. *J. Phys. Chem.*, **1986**, 90, 2847-2852.
- ³² Zhang, Y. -H.; Zhao, W.; Jiang, P.; Zhang, L. -J.; Wang, J. Structural parameters and vibrational spectra of a series of zinc meso-phenylporphyrins: A DFT and experimental study. *Spectroc. Acta A*, **2010**, 75, 880-890.
- ³³ Aydin, M. DFT and Raman spectroscopy of porphyrin derivatives: Tetraphenylporphine (TPP). *Vib. Spectrosc.* **2013**, 68, 141-152.
- ³⁴ Gassman, P.G.; Ghosh, A.; Almlöf, J. Electronic effects of peripheral substituents in porphyrins: x-ray photoelectron spectroscopy and ab initio self-consistent field calculations. *J. Am. Chem. Soc.*, **1992**, 114, 9990-10000.
- ³⁵ Hurley, B. L.; McCreery, R. L. Covalent bonding of organic molecules to Cu and Al alloy 2024 T3 surfaces via diazonium ion reduction. *J. Electrochem. Soc.* **2004**, 151, B252.
- ³⁶ Bell, K. J.; Brooksby, P. A.; Polson, M. I. J.; Downard, A. J. Evidence for covalent bonding of aryl groups to MnO₂ nanorods from diazonium-based grafting. *Chem. Commun.* **2014**, 50, 13687–90.
- ³⁷ Charlton, M. R.; Suhr, K. J.; Holliday, B. J.; Stevenson, K. J. Electrochemical modification of indium tin oxide using di (4-nitrophenyl) iodonium tetrafluoroborate. *Langmuir* **2015**, 31, 695–702.
- ³⁸ Donley, C.; Dunphy, D.; Paine, D.; Carter, C. Characterization of Indium–Tin Oxide Interfaces Using X-ray Photoelectron Spectroscopy and Redox Processes of a Chemisorbed Probe Molecule: Effect of Surface Pretreatment Conditions. *Langmuir* **2002**, 18, 450–457.
- ³⁹ Forget, A.; Limoges, B.; Balland, V. Efficient chemisorption of organophosphorous redox probes on indium tin oxide surfaces under mild conditions. *Langmuir* **2015**, 31, 1931–1940.

Chapter III. Evidencing fast, massive, and reversible proton insertion in nanostructured GLAD-TiO₂ electrodes at neutral pH

Adapted from

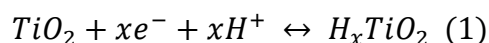
Kim, Y. -S.; Kriegel, S.; Harris, K. D.; Costentin, C.; Limoges, B.; Balland, V. Evidencing Fast, Massive, and Reversible H⁺ Insertion in Nanostructured TiO₂ Electrodes at Neutral pH. Where Do Protons Come From? *J. Phys. Chem. C.* **2017**, 121, 10325–10335.

1. Introduction
2. Description of the GLAD-TiO₂ films used
3. Spectroelectrochemical studies in aqueous solution
4. Description of the intercalation process
5. Comparative study with lithium insertion
6. Quantification of the charge stored
7. Conclusion

1. Introduction

TiO₂-based mesoporous semiconductive electrodes have attracted in the past decades due to its unique electrical, optical, and chemical properties (including low-cost, high availability, low toxicity, and excellent chemical/photochemical stability). This implies that the TiO₂ can be a prime candidate in large-scale fabrication of transparent high-surface area electrodes and also enable an increasing range of applications in which mesoporous TiO₂ electrodes play a central role.^{1,2} Due to the issues for the environment and safety and in some cases for long-term stability arise from the dry, aprotic organic solvents operating conditions of most applicable fields with TiO₂-based mesoporous semiconductive electrodes³⁻¹¹, growing efforts to meet the demand for eco-friendly and sustainable technologies have been made recently toward the design of TiO₂-based aqueous DSSCs^{12,13} and aqueous ion-insertion batteries^{14,15} but also the development of TiO₂-based photoelectrocatalytic aqueous cells for water splitting,⁹ CO₂ reduction,¹⁰ biocatalysis,¹⁶ and biosensing.¹⁷

Significantly, many of the above applications incorporate complex processes of charge carrier generation, separation, transport, and recombination in the metal oxide films which are currently not fully understood and predictable. This is particularly true for mesoporous TiO₂ electrodes operating in aqueous media, wherein the complex interplay between electron and proton transfer/transport strongly influences the material's behavior. It is indeed well-admitted that upon applying negative bias to a TiO₂ electrode in strongly acidic conditions (pH < 2) protons have the ability to not only adsorb at the TiO₂/solution interface but also intercalate within the metal oxide lattice according to reaction 1.



where x is the maximal mole fraction of protons that can be inserted in the metal oxide lattice.

This process is also often referred to as electrochemical doping of the semiconductor. It has been reported over a wide range of TiO₂ film morphologies and crystallinities, mostly anatase nanocrystalline films¹⁸ or nanotube arrays,¹⁹⁻²¹ but also rutile,²² mixed anatase–rutile,^{23,24} nanostructured films, and amorphous TiO₂ nanotube arrays.²¹ Accordingly, proton insertion/intercalation appears as a general feature of mesoporous TiO₂ films.

By analogy to Li⁺ insertion in TiO₂, proton insertion is assumed to result from local compensation of the loss of charge that is generated during the formal reduction of Ti^{IV} sites

into Ti^{III} in the bulk material,²⁴ a process associated with a strong electrochromic effect for which interpretation is still a matter of debate.^{18,22,24–26} Proton insertion can thus be expected, similarly to Li^+ , to lead to a strong increase of the electron storage capacity of TiO_2 under accumulation conditions.^{27,28} In contrast to Li^+ insertion in TiO_2 that has been the subject of intense research due to its fundamental role in Li^+ insertion batteries,⁵ H^+ insertion in TiO_2 has been much less investigated, and many questions remain unanswered. For instance, the insertion speed, reversibility, and long-term cyclability have not been determined. It is moreover not clear which parameters influence the extent of proton insertion, at which potential it occurs, and if strongly acidic condition is a necessary prerequisite.

The purpose of this chapter is to answer these questions by investigating the electrochemical reductive protonation of nanostructured films of amorphous TiO_2 prepared by glancing angle deposition (GLAD) on planar ITO conductive substrates in aqueous solution in the presence of either a strong acid (HCl) in an unbuffered solution or a weak acid in a neutral buffered solution (HEPES buffer).²⁹⁻³⁰

As will be shown in the present work, we were able to clearly distinguish between two charge storage mechanisms. The first is purely capacitive and related to charging of the electrical double-layer capacitance (EDLC) when the electrode is converted to its fully conductive state at negative bias potentials. The second storage mechanism occurs at a well-defined formal potential, negative with respect to the conduction band, and corresponds to a faradaic process associated with reductive proton insertion in the solid phase of TiO_2 . We demonstrate that this faradaic electron storage process is fast, electrochemically reversible, and diffusion controlled and occurs extensively at a well-defined potential not only under unbuffered strong acidic conditions but also, more remarkably, under neutral pH conditions in a buffered solution.

Furthermore, models describing ion insertion processes associated with charge storage have been described in the attached article (see annexe) focusing on (i) ion diffusion exclusively inside the materials and (ii) phase transformation electrodes but (iii) without interference of diffusion outside the materials. The purpose of this modeling is to study of the effect of proton transport interplay inside and outside the materials on the cyclic voltammetry response, considering that proton transport in aqueous electrolytes near the electrode surface is provided by buffer diffusion. The formulation of the problem through introduction of dimensionless variables will allow defining the minimum number of parameters that govern the cyclic

voltammetry response considering a simple description of the system geometry. This approach will then be illustrated by the analysis of proton insertion in a mesoporous TiO₂ film.

2. Description of the GLAD-TiO₂ films used

All experiments were carried out with 1 μm thick amorphous TiO₂ mesoporous films deposited by glancing angle deposition (deposition angle of 72°) on flat conductive ITO surfaces (Figure 1). Nanostructured GLAD TiO₂ films exhibit a high density of vertically aligned nanosized columnar structures, with a well-opened mesoporosity and controlled film thickness. From the volumetric mass density of the film (*i.e.*, 2.5 g·cm⁻³) and the bulk density of compact amorphous GLAD-TiO₂ film (3.8 g·cm⁻³ for a TiO₂ film prepared with a 0° deposition angle),²⁹ a film porosity P of 0.34 can be estimated. A film surface area enhancement (SA) of 540 per μm of film thickness was deduced from BET krypton gas adsorption isotherms.²⁹ It has been previously established that SA increases linearly with film thickness,^{29,31} while nanorod diameter and intercolumn spacing follow power-law growth patterns.³² In order to estimate the mean nanorod diameter (that is difficult to infer from Figure 1), we have considered a simplified geometrical representation of the GLAD films by assuming an array of uniform cylindrical nanorods homogeneously distributed perpendicular to the underlying flat ITO surface. According to this simplified picture, the mean nanorod diameter d and nanorod surface density δ were roughly estimated from both P and SA by solving the following set of two linear equations: $SA = \pi d(10^{-4} + d/4)\delta$ and $1 - P = \pi d^2 \delta/4$. Using the experimentally determined values of P and SA , the mean nanorod diameter and number density of 5 nm and $3.3 \times 10^{12} \text{ cm}^{-2}$ were calculated, respectively.

Experimental reproducibility is attested by the good overlap of cyclic voltammograms recorded under identical experimental conditions for different GLAD-TiO₂ electrodes arising from different GLAD deposition batches (Figure 2, relative standard deviation RSD < 5%, $N = 7$). The reproducibility of the corresponding cyclic voltabsorptograms was not as good (RSD < 40%), suggesting a higher sensitivity of the absorbance measurement to batch-to-batch variations in the GLAD-TiO₂ samples.

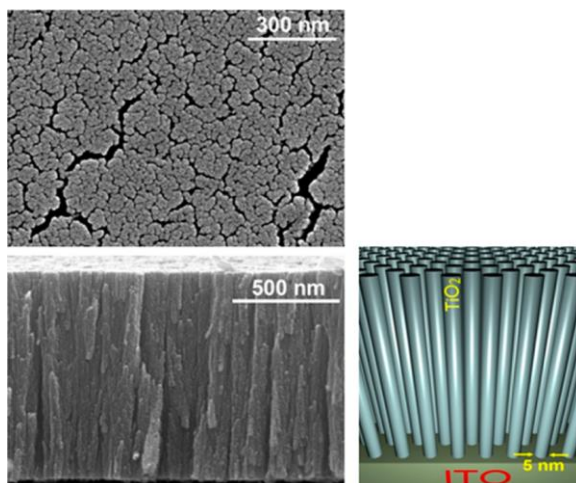


Figure 1. SEM images (top and side views) of the 1 μm GLAD-TiO₂ films. The right cartoon is a schematic representation of the film consisting of an array of homogeneously distributed cylindrical nanorods. The indicated diameter (5 nm) was calculated based on BET measurements of surface area and characterizes the high surface area fine structure internal to TiO₂ columns grown by GLAD.

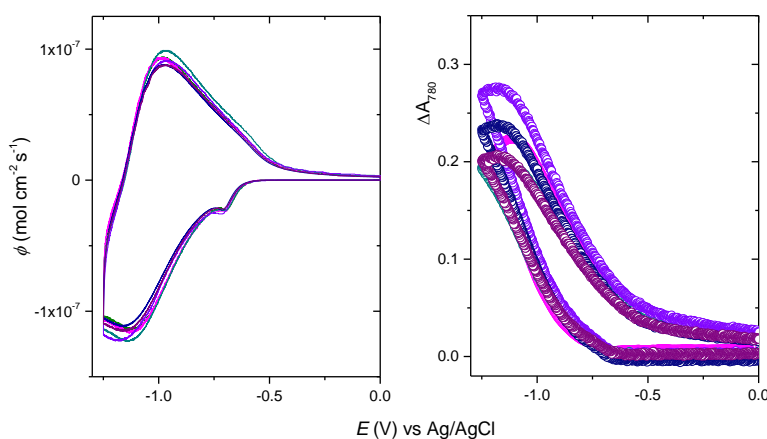


Figure 2. (Left) CVs and (right) CVAs ($\lambda = 780$ nm) recorded at 7 different 1 μm -thick GLAD-TiO₂ electrodes (arising from 2 different GLAD deposition batches) in 0.1 M HEPES (pH 7.0) and 0.3 M KCl. Each color denotes a simultaneously recorded CV/CVA pair. Scan rate: 0.1 V·s⁻¹. $T = 25^\circ\text{C}$.

3. Spectroelectrochemical studies in aqueous solution

GLAD-TiO₂ electrodes were investigated by the coupled techniques of cyclic voltammetry and cyclic voltabsorptometry, which allow simultaneous monitoring of electrical current and optical absorbance changes for TiO₂ electrodes during cyclic potential scans at the semiconductive films.³⁰ Experiments were conducted in aqueous solutions containing a fixed concentration of KCl (0.3 M) as a supporting electrolyte.³³ The influence of different

concentrations of two soluble proton donors was studied, either (i) free protons (*i.e.*, H_3O^+) resulting from the addition of HCl in water (pH values ranging from 7 to 1.85, equivalent thus to $[\text{H}_3\text{O}^+]$ concentrations ranging from 10^{-7} to 0.014 M) or (ii) the acidic AH form of the HEPES buffer at pH 7 (the concentration of which was altered by changing the buffer concentration C_B from 0 to 0.86 M with $[\text{AH}] = C_B/1.3$ at pH 7). The simultaneously recorded cyclic voltammograms (CVs) and cyclic voltabsorptograms (CVAs, monitored at 780 nm) under different proton donor concentrations and pHs are reported in Figures 3, 4, and 5. Cyclic scans were systematically initiated at anodic potentials where the semiconductive TiO_2 films were insulating. The potential was then increased to sufficiently cathodic potentials where TiO_2 was fully converted into a metal-like conductive film, and then the potential sweep was reversed to recover the initial insulating state. During the charging process (forward scan), all CVs and CVAs share some common features (Figures 3, 4, and 5). First of all, the current recorded at the beginning of the forward cathodic scan is very small and nearly constant, engendering no significant absorbance change at 780 nm. These observations indicate that TiO_2 behaves as an insulator within this potential window and that the small recorded current on the CVs only arises from the double-layer charging capacitance of the underlying exposed ITO surface. At negative potentials to -0.60 V at pH 7.0 (or -0.30 V at pH 1.85), the exponential increase of current in CVs reflects both the progressive filling of electronic states that are localized in traps distributed in the band gap of TiO_2 and the filling of extended conduction band states when the applied potential becomes sufficiently negative (*i.e.*, when it is raised close to the TiO_2 conduction band edge potential of $E_{CB} \sim -0.75$ V *vs.* Ag/AgCl at pH 7.0 or -0.45 V *vs.* Ag/AgCl at pH 1.85).²⁵ This transition thus characterizes the increase of the Fermi level of electrons in the TiO_2 film and also the transition from an insulating to a conductive state by increasing the chemical capacitance (C_{chem}) of the semiconductive material. (To preserve the electrical neutrality, negative charges accumulated in TiO_2 are assumed to be compensated by electrosorption of cations at the metal–oxide interface).^{1,34} This process is associated with a simultaneous increase of the TiO_2 film absorbance monitored at 780 nm. Accumulated electrons can thus be quantitatively analyzed in CVs through the exponential increase of current occurring from an onset potential less negative than E_{CB} but also in CVAs through absorbance increase in the near-IR region from the same onset potential (an increase which linearly scales with the amount of electrons accumulated in the semiconductive material).^{18,26} As attested by complete restoration of the initial metal oxide transparency upon scanning the potential back in the anodic direction, the charging/discharging process is fully

reversible under the present experimental conditions, indicating complete removal of all injected charges. The onset potential at which both current and absorbance start to increase is pH dependent, showing a 60 mV anodic shift per unit of pH decrease, fully consistent with the reported Nernstian pH dependence of the TiO_2 conduction band edge.^{35,36} The potential at which the amorphous GLAD- TiO_2 electrode becomes fully degenerate at pH 7.0 (*i.e.*, at $E < -0.75$ V vs Ag/AgCl, corresponding also to the transition from the exponential growth of the current to a constant double-layer capacitive current) is also consistent with the E_{CB} reported for sintered nanoparticulate films of anatase at the same pH (-0.8 V vs SCE).²⁵ One may however notice that the onset potential at which the film transitions from an insulating to a conductive state is steadily downshifted as the scan rate is increased, suggesting a transition process which does not occur at thermodynamic equilibrium within the range of scan rates explored (0.05 to 0.5 $\text{V}\cdot\text{s}^{-1}$). It seems thus that there is a kinetic barrier in the delivery of electrons to the semiconductive material that for the moment we cannot clearly interpret and which is beyond the scope of this work. Once the applied potential lies within the potential window corresponding to the fully conductive state of TiO_2 , shapes and magnitudes of both CVs and CVAs exhibit strong differences and changes as a function of the proton donor concentration (Figures 3, 4, and 5). Two distinct behaviors can be clearly identified as detailed below.

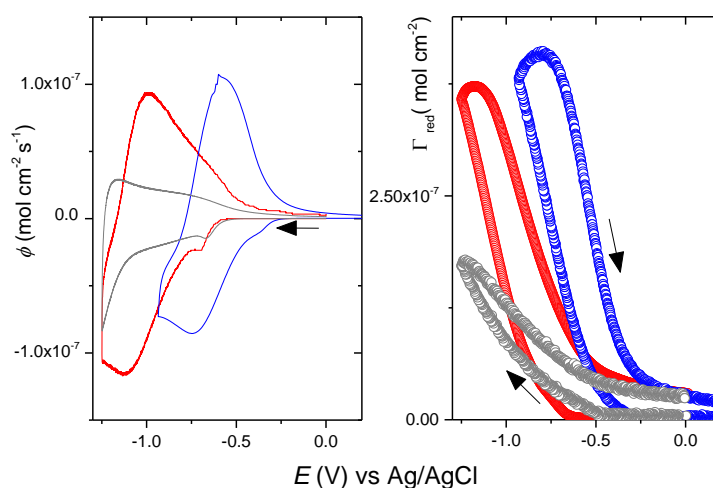


Figure 3. (Left) CVs and (right) CVAs (monitored at 780 nm) recorded simultaneously at a 1 μm thick GLAD- TiO_2 electrode in an aqueous solution of (blue) 14 mM HCl (pH 1.85) or buffered solutions (pH 7.0) of (black) 1 mM HEPES or (red) 100 mM HEPES. All solutions also contained 0.3 M KCl as supporting electrolyte. Electrodes were scanned from 0 to -1.25 V at pH 7 and from 0 to -0.96 V at pH 1.85. CVs are expressed in flux density and CVAs in surface concentrations (*i.e.*, $\Delta A_{780}/(1000 \cdot \epsilon_{780})$). Scan rate: 0.1 $\text{V}\cdot\text{s}^{-1}$. $T = 25^\circ\text{C}$.

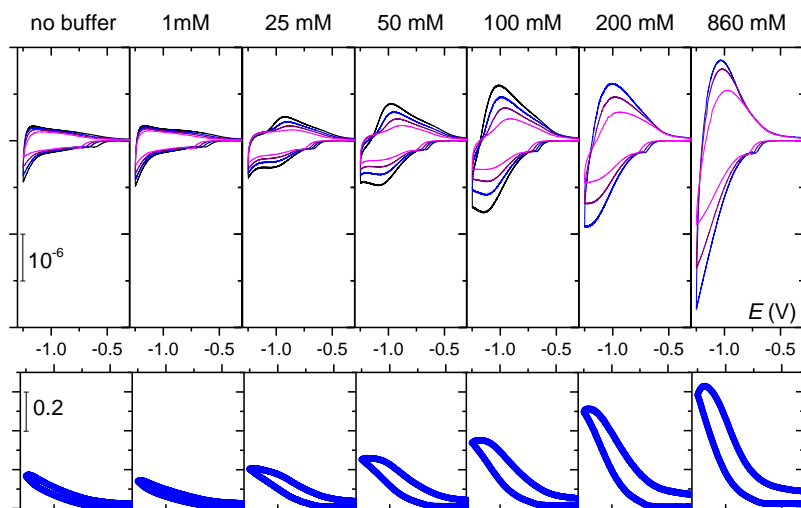


Figure 4. Top: CVs recorded at 1 μm -thick GLAD-TiO₂ electrodes in aqueous solutions of 0.3 M KCl complemented with increasing concentration of HEPES buffer (pH 7.0). Buffer concentrations (C_B) are reported on top of the graphs, and currents are converted to electron flux density normalized to the scan rate. The ordinate is $\phi/v = i/FSv$ with units $\text{mol}\cdot\text{V}^{-1}\cdot\text{cm}^{-2}$. Scan rates: 0.05 $\text{V}\cdot\text{s}^{-1}$ (black), 0.1 $\text{V}\cdot\text{s}^{-1}$ (blue), 0.2 $\text{V}\cdot\text{s}^{-1}$ (purple) and 0.5 $\text{V}\cdot\text{s}^{-1}$ (magenta). Bottom: CVAs ($\lambda = 780\text{ nm}$) recorded during the 0.1 $\text{V}\cdot\text{s}^{-1}$ CV scans. The ordinate is in absorbance units. The abscissa for both the CVs and CVAs are potential (V) with respect to the Ag/AgCl (3 M KCl) reference electrode. $T = 25^\circ\text{C}$.

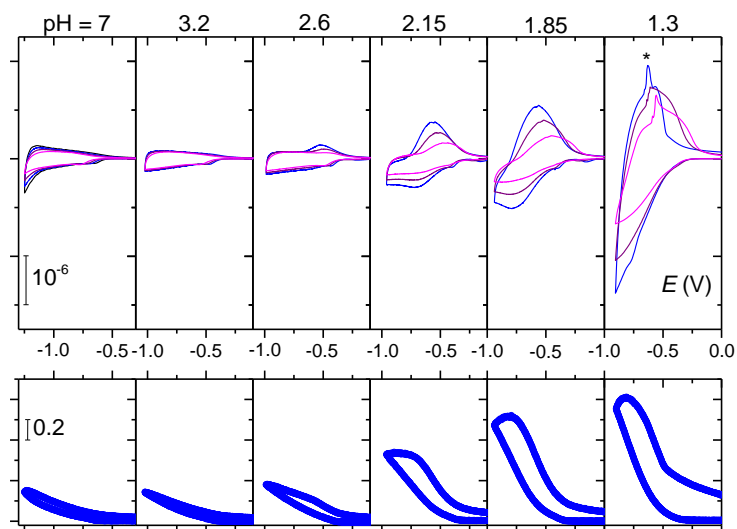


Figure 5. Top: CVs recorded at 1 μm -thick GLAD-TiO₂ electrodes immersed in increasingly acidic aqueous solutions (pHs are reported above the graphs). Currents are converted to electron flux density normalized to the scan rate. The ordinate is $\phi/v = i/FSv$ with units $\text{mol}\cdot\text{V}^{-1}\cdot\text{cm}^{-2}$. Scan rates: 0.05 $\text{V}\cdot\text{s}^{-1}$ (black), 0.1 $\text{V}\cdot\text{s}^{-1}$ (blue), 0.2 $\text{V}\cdot\text{s}^{-1}$ (purple) and 0.5 $\text{V}\cdot\text{s}^{-1}$ (magenta). Bottom: CVAs ($\lambda = 780\text{ nm}$) recorded simultaneously to the CVs (only experiments conducted at 0.1 $\text{V}\cdot\text{s}^{-1}$ are shown). The ordinate is in absorbance units. The abscissa for both the CVs and CVAs are potential (V) with respect to the Ag/AgCl (3 M KCl) reference electrode. $T = 25^\circ\text{C}$.

Low Proton Donor Concentrations (Unbuffered Aqueous Solutions of pH > 3.5 or Poorly Buffered Aqueous Solutions with [AH] < 5 mM).

For very low acid concentrations and for potentials more negative than the conduction band edge of TiO₂, CVs display a rectangular-shaped current response almost independent of the applied potential and scaling linearly with the scan rate ν (Figures 3 and also Figures 4 and 5 wherein CVs are normalized to the scan rate). This behavior is typical of the double-layer capacitive charging current that can be recorded at a high surface area electrode immersed in an inert supporting electrolyte (differing from the chemical capacitive charging current by its independence from the applied potential). This is corroborated in CVAs by the near overlap of absorbance change between the forward and backward potential scans at 0.1 V·s⁻¹ (absence of significant hysteresis), a behavior that is reminiscent of a fast charging/discharging of a double-layer capacitive current. Since the double-layer capacitance (C_{dl}) is connected in series with the chemical capacitance, it can only be assessed when $C_{chem} \gg C_{dl}$ (*i.e.*, at potentials more negative than the E_{CB} of TiO₂).^{30,34} It is worth mentioning that CVs normalized to ν at neutral pH (Figure 4) do not all completely overlap in the lowest range of negative potentials; under -1.1 V, a small rise of current is observed and accompanied by a concomitant increase in absorbance at 780 nm. We assume that this arises not from the hydrogen evolution reaction (HER) as often assumed but from the reductive coloration of the underlying ITO substrate, a phenomenon that was recently ascribed to the reductive formation of metallic nanoparticles of indium and tin at the ITO surface and which strongly depends on the electrolyte composition and pH.^{37,38} Control CV experiments were thus performed at bare ITO electrodes under the same experimental conditions as those for GLAD-TiO₂ electrodes, and the same increases in current and absorbance were observed at potentials more negative than -1.0 V (not shown). The above results allowed us to conclude that when the applied potential is more negative than E_{CB} and when there is no significant concentration of free protons or weak acid in solution the GLAD-TiO₂ electrode behaves like a high surface area electrical capacitor. Assuming that at low proton donor concentration the CV current is purely capacitive at pH 7.0 in the potential window -0.7 to -1.1 V, an average electrical capacitance density of 18 ± 2 mF·cm⁻² (*i.e.*, normalized to the geometric electrode area) can be inferred (which also corresponds to a specific double-layer capacitance of 72 F·g⁻¹), which is far more than expected for a standard flat conductive electrode in an electrolyte solution (10–40 μ F·cm⁻²).^{39,40} The value is, however, consistent with the large specific surface area generated by the quasi-metallic GLAD-TiO₂ films at these potentials. Once corrected for film surface area enhancement (*i.e.*, 540 μ m⁻¹), an

intrinsic capacitance density of $33 \mu\text{F}\cdot\text{cm}^{-2}$ was found for the degenerate semiconductive film, a value that is close to the theoretical one ($10\text{--}20 \mu\text{F}\cdot\text{cm}^{-2}$) calculated for a flat conductive surface in an aqueous electrolyte solution.⁴¹ The measured capacitance density, however, is in the lower end of values previously reported for nanocrystalline films of TiO_2 in aprotic solvents ($30\text{--}120 \mu\text{F}\cdot\text{cm}^{-2}$),⁴²⁻⁴⁴ which is unsurprising in light of the fact that all of the previously reported intrinsic capacitances were determined in the presence of lithium cations. These cations complicate the accurate estimation of the true capacitive contribution on account of their intercalating faradaic contribution to the current. Another factor that can also significantly affect a reliable evaluation of the intrinsic capacitance density is the extent of correlation between the inner surface area of the nanostructured electrode (*i.e.*, measured using the BET measurement, see experimental section) and the effective electroactive surface area.

High Proton Donor Concentrations (Unbuffered Aqueous Solutions with $\text{pH} < 3.5$ or Buffered Aqueous Solutions with $[\text{AH}] > 5 \text{ mM}$).

Upon either increasing the buffer concentration (up to 860 mM at pH 7) or decreasing the pH below pH 3, the shapes and magnitudes of current/ absorbance changes in CVs/CVAs are strongly modified and increased for cathodic potentials wherein TiO_2 is conductive (Figures 3, 4, and 5). The strong increase in current is linked to the growth of a broad reversible wave on top of the capacitive current. Depending on the pH, this reversible wave is centered on formal potentials (E^0) of -1.06 V vs Ag/AgCl at pH 7.0 (0.1 M HEPES) and -0.68 V vs Ag/AgCl at pH 1.85 (Figure 3 and Table 1), exhibiting thus a shift of -74 mV per unit of pH, which is again reminiscent of the -60 mV pH dependence of the E_{CB} of TiO_2 .^{1,36}

Table 1. Features of CVs and CVAs shown in Figure 3.

pH	1.85	7	7
$[\text{H}_3\text{O}^+]$ (mM)	14	~ 0	~ 0
$[\text{AH}]$ (mM)	-	0	77
E_{onset} (V) ^a	-0.30	-0.60	-0.60
E^0 (V) ^b	-0.68	-	-1.06
ΔE_p (mV)	220	-	120
$\Delta A_{780}^{\text{max}}$	0.51	0.15	0.34
ϵ_{780} ($\text{M}^{-1} \text{ cm}^{-1}$)	1200	800	800

^a Potential that characterize the onset increase of absorbance measured at 780 nm.

^b Formal potential obtained from the average of cathodic and anodic peak potentials at the slowest scan rate.

The current of this reversible wave is clearly not proportional to the scan rate as shown from CVs normalized to v in Figures 4 and 5. In order to further analyze this wave, CVs recorded at different proton donor concentrations were systematically corrected for the electrochemical double-layer capacitance contribution by subtracting the CVs obtained under negligible proton donor concentration (*i.e.*, by subtracting the CVs in 0.3 M KCl). Once corrected for capacitive current and normalized to $v^{1/2}$, the resulting CVs gathered in Figure 6 show good overlap, especially in terms of magnitudes of cathodic and anodic peaks. These results clearly demonstrate that the reversible wave is proportional to $v^{1/2}$ over the entire range of buffer concentrations and pHs investigated in this work (Figure 7), a behavior that strongly supports the occurrence of a reversible faradaic process rate-limited by a diffusion-controlled mass transport. On account of its $E^{0'}$ position, strong dependence on proton donor concentration, and also diffusion-controlled response, the reversible wave can be reasonably ascribed to the reversible faradaic reduction of Ti^{IV} sites in the metal oxide lattice coupled with proton uptake for local charge compensation. Depending on the experimental conditions, this proton-coupled electron transfer reaction, when fast, can be assumed to be rate-limited either by the solid-state diffusion of protons inserted within the TiO_2 lattice or by the solution diffusion of proton donors in the bulk electrolyte. This process is formally equivalent to the Li^+ -coupled electron transfer reaction occurring in insertion metal oxide materials, a process that has been and continues to be widely studied based on its great importance in the field of Li-ion batteries.^{4,5} Compared to the CVs reported in the literature for Li^+ insertion in nanocrystalline TiO_2 films, it is remarkable here to note the rather high electrochemical reversibility of proton insertion (characterized by a small potential separation between the anodic and cathodic peaks, *i.e.*, $\Delta E_p < 0.23$ at $0.1 \text{ V}\cdot\text{s}^{-1}$, see Table 1), as compared to corresponding reports for Li^+ -insertion in nanocrystalline TiO_2 films ($\Delta E_p > 0.4 \text{ V}$ at CV scan rates $< 10 \text{ mV}\cdot\text{s}^{-1}$).⁴³⁻⁴⁵ The poor reversibility of lithium-ion insertion is often associated with crystallographic phase changes during the faradaic process, so the good electrochemical reversibility we observed here for H^+ insertion suggests that crystallographic variations may not be a major issue. The disordered structure and defects in amorphous TiO_2 may also contribute to facilitate the interfacial proton-coupled electron transfer reaction.

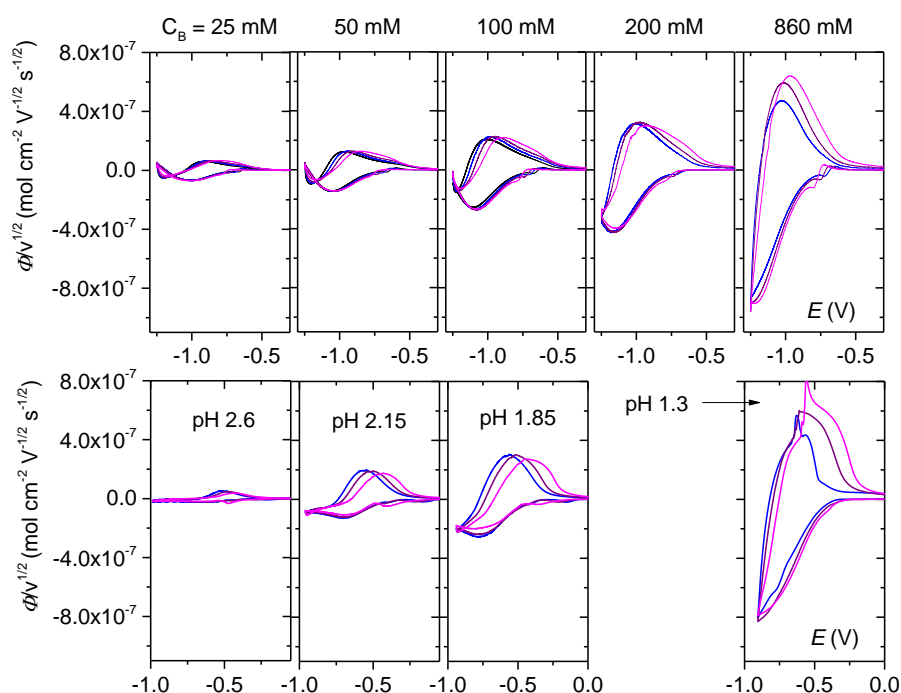


Figure 6. Top: CVs previously presented in Figure 4 with correction to remove the capacitive contribution to the total current (*i.e.*, by subtracting the CVs recorded in 0.3 M KCl without buffer). Bottom: CVs previously presented in Figure 5 with correction to remove the capacitive contribution to the total current (*i.e.*, by subtracting the CVs recorded in 0.3 M KCl). Currents were all converted to electron flux density normalized to the square root of scan rate. Scan rates: 0.05 V·s⁻¹ (black), 0.1 V·s⁻¹ (blue), 0.2 V·s⁻¹ (purple) and 0.5 V·s⁻¹ (magenta). The abscissa are potential (V) with respect to the Ag/AgCl (3 M KCl) reference electrode. $T = 25^{\circ}\text{C}$.

In order to get deeper insights into the diffusion-limited faradaic charge storage process, the electron flux density of the cathodic peak $\phi_{f,p}$, normalized to $v^{1/2}$, was plotted as a function of the proton donor concentration (Figure 7). Provided that the proton donor concentration in solution remains low, the data clearly show a linear relationship which is indicative of a process rate-controlled by the diffusional mass transport of proton donors in the electrolyte. Upon further increasing the proton donor concentration (*i.e.*, >100 mM), a progressive deviation from linearity with a tendency to asymptotically reach a maximal value at high buffer concentrations is well-discerned at pH 7.0. That the diffusion-controlled cathodic peak current is independent of the proton donor concentration at high buffer concentrations, but still proportional to $v^{1/2}$, allows us to conclude that the faradaic process is now rate-controlled by the solid-state diffusion of protons within the TiO₂ lattice, rather than by the mass transport of proton donor in solution (the latter being sufficiently fast to support the redox process at the interface under these conditions). Such a transition from one limiting case to the other was unfortunately not

observable under acidic pH conditions for the reason that we were unable to perform CV experiments at $\text{pH} < 1.0$ without generating an irreversible loss of the electrical properties of TiO_2 together with a concomitant and permanent coloration of the metal oxide film. (This blue/black coloration was observed after exceeding a certain charge accumulation threshold or upon scanning the potential into excessively negative values.) Such an abrupt alteration of the physicochemical properties of TiO_2 might be related to a significant structural/ morphological change of the metal oxide lattice, which under strong electron/ proton accumulation may lead to delamination or breakage/ collapse of the GLAD- TiO_2 film.

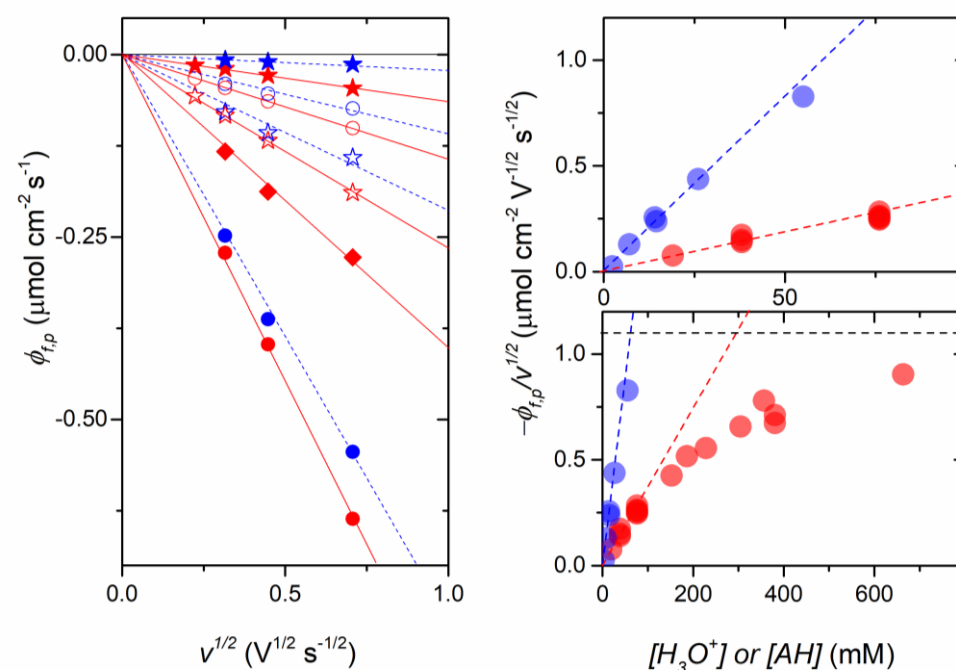
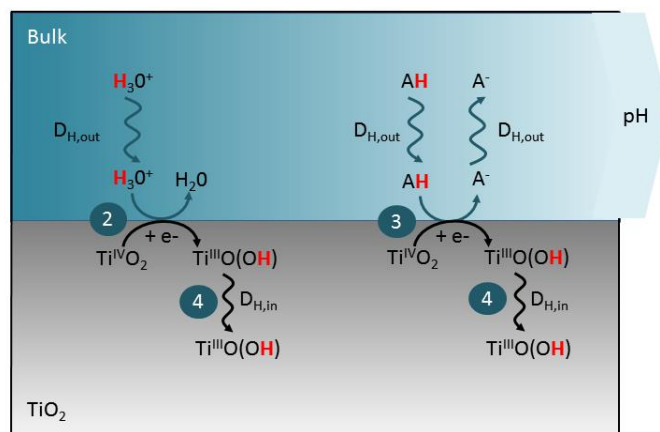


Figure 7. (Left) Cathodic peak electron flux density in CV as a function of $v^{1/2}$ (for scan rates ranging from 0.05 to $0.5 \text{ V}\cdot\text{s}^{-1}$) and for different concentrations of (blue data) free protons, *i.e.*, $[\text{H}_3\text{O}^+]$ = (solid blue star) 2.5, (blue open circle) 7, (open blue star) 14, and 50 (solid blue circle) mM or (red data) the acidic form of HEPES buffer, *i.e.*, $[\text{AH}]$ = (solid red star) 19, (red open circle) 38, (red open star) 77, (red solid diamond) 153, and (red solid circle) 656 mM. (Right) Cathodic peak electron flux density normalized to $v^{1/2}$ and plotted as a function of proton donor concentration: (blue) free protons and (red) the acidic form of HEPES buffer. Dashed lines correspond to the linear regression fits of Eq. 5 to the data determined at low proton donor concentrations. The horizontal dotted black line corresponds to the extrapolated limiting value of $\phi_{f,p}/v^{1/2}$.

From the above experimental observations, it can be concluded that the charging/discharging process related to the reversible proton-coupled reduction of Ti^{IV} ions can, depending on the experimental conditions, be rate-limited by any of (i) the mass transport

of proton donor in solution, (ii) the solid-state diffusion of protons in the TiO_2 lattice, (iii) the interfacial proton-coupled electron transfer, or (iv) a mixed control of these different processes (Scheme 1).

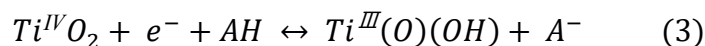
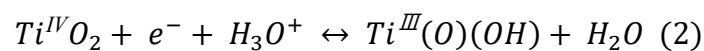


Scheme 1. Schematic Representation of the Faradaic Charging Processes Occurring at the TiO_2 Mesoporous Electrodes Involving Proton–Coupled Electron Transfer to Solvent-Accessible Ti^{IV} Ions According to the Interfacial Reactions 2 or 3, Depending on the Proton Provider, Followed by Coupled Electron/Proton Diffusion Within the TiO_2 Lattice According to Reaction 4.

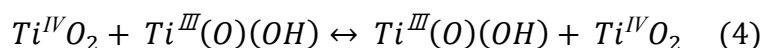
Another important finding from the above results is that the aqueous solvent is an ineffective proton donor in comparison to the acidic form of HEPES or H_3O^+ . This might be explained by the very low acidity of water ($\text{pK}_a = 14$ which is 6.5 orders of magnitude higher than the pK_a of the HEPES buffer), which would suggest that the thermodynamic ease with which the proton donor can deliver a proton to the metal oxide is a key factor in the proton insertion mechanism.

4. Description of the insertion process

The proton-coupled reduction of Ti^{IV} is assumed to be induced at the metal oxide/electrolyte interface. It thus involves the soluble proton donor locally available at this interface, which according to the experimental conditions can be either free protons in solution or the acidic form [AH] of the buffer (in the present case, the zwitterionic protonated form of HEPES). We can thus write the following electron transfer reactions at the metal oxide interface for each proton donor as following Eq. 2 and Eq. 3:



These reactions are expected to occur more favorably at grain boundaries where interfacial Ti^{IV} sites are more accessible and solvent exposed.⁴⁶ According to the high specific surface area of GLAD-TiO₂ electrodes and the high surface concentration of Ti^{IV} ions, these reactions are assumed to provoke massive consumption of the proton donor present at the metal oxide/ electrolyte interface (*i.e.*, in the void volume of the porous film). Under these circumstances, consumption is sufficient to rapidly induce rate limitation by the mass transport of proton donor from the bulk solution. This is especially true when the working concentration of the proton donor is low, thus leading to a current response of the diffusion-controlled reversible wave linearly dependent on the soluble proton donor concentration. Once surface Ti^{IV} sites are reduced and charge compensated by protonation, we can assume that the paired electron/proton couple (e^-/H^+) can be transferred between adjacent titanium ions localized in the subsurface region of the amorphous TiO₂ material, formally according to the following electron–proton transfer reaction:



This mechanism of charge transfer propagation throughout the metal oxide lattice can be assumed to be equivalent to a diffusion-like process considering an isotropic random walk of e^-/H^+ throughout the TiO₂ lattice. (It is worth noting that in this process electrons may not originate from hopping electron transfer reactions between adjacent titanium ions but rather from transfer with electrons accumulated in the delocalized states of the conduction band. Therefore, during this e^-/H^+ migration, only protons can truly be considered to hop between adjacent titanium sites.) To determine the rate of this solid-state diffusion-like process, it is essential to ensure that the mass transport of proton donor in solution does not play a role. Such a situation is encountered in Figure 7 when the magnitude of the reversible wave is nearly independent of the proton donor concentration.

The linear relationship observed between $\phi_{f,p}/v^{1/2}$ and the soluble proton donor concentration, [H], at low and intermediate concentrations in Figure 7 (*i.e.*, <100 mM) is typically associated with the first situation where the diffusion-controlled reversible current response is limited by mass transport of the proton donor. If we assume a Nernstian interfacial

reaction (*i.e.*, a fast reversible proton-coupled electron transfer reaction), the following Randles–Sevcik equation can be applied for both reactions 2 and 3 at low proton donor concentrations^{40,47}

$$\frac{\phi_{f,p}}{\nu^{1/2}} = \frac{i_{f,p}}{FS\nu^{1/2}} = 0.4463 \sqrt{\frac{F}{RT}} \sqrt{D_{H,out}} [H] \quad (5)$$

where $\phi_{f,p}$ and $i_{f,p}$ are the faradaic peak flux density ($\text{C}\cdot\text{mol}^{-1}\cdot\text{cm}^{-2}$) and peak current (A), respectively; ν is the scan rate ($\text{V}\cdot\text{s}^{-1}$); S is the delimited geometric electrode area (or projected electrode area, cm^2); $D_{H,out}$ is the diffusion coefficient of proton donor in the bulk aqueous solution ($\text{cm}^2\cdot\text{s}^{-1}$); and $[H]$ is the concentration of proton donor in solution ($\text{mol}\cdot\text{cm}^{-3}$). The geometric electrode area is utilized in this equation due to the fact that the diffusion layer thickness of the soluble proton donor is much larger than the 1 μm film thickness of GLAD-TiO₂ within the range of scan rates used in the present study. From the linear regression fit of Eq. 5 to the linear part of experimental plots in Figure 7, it becomes possible to determine the diffusion coefficient $D_{H,out}$ of each proton donor we have investigated. Diffusion coefficients of $3 \times 10^{-5} \text{ cm}^2\cdot\text{s}^{-1}$ and $1.5 \times 10^{-6} \text{ cm}^2\cdot\text{s}^{-1}$ were found for H_3O^+ and the protonated form of HEPES, respectively. These values are in good agreement with the diffusion coefficient values reported in the literature (*i.e.*, $2.3 \times 10^{-5} \text{ cm}^2\cdot\text{s}^{-1}$ for H_3O^+ ^{48,49} and $6.2 \times 10^{-6} \text{ cm}^2\cdot\text{s}^{-1}$ for HEPES,⁵⁰ both at 25 °C).

In highly concentrated solutions of proton donor it was not possible to definitely reach the limiting case where $\phi_{f,p}$ is uniquely rate-controlled by the apparent diffusion of H^+ in TiO₂; however, the apparent diffusion coefficient of protons within the metal oxide lattice could be estimated from the maximal electron flux density that was extrapolated at high buffer concentrations in Figure 7 (dotted black line). Under this limiting case, Eq. 5 no longer applies and must be modified to consider reaction 4 as the rate-limiting diffusion-like process. On account of the small solid-state diffusion coefficients reported for cations in TiO₂ (10^{-13} – $10^{-17} \text{ cm}^2\cdot\text{s}^{-1}$),^{42–44,51–55} the diffusion length of H^+ within the bulk metal oxide is expected to be much smaller than the smallest dimension of nanorods (5 nm diameter) such that the proton gradient can be considered as a semi-infinite linear diffusion-like process occurring normal to the metal oxide interface (*i.e.*, normal to the vertical walls of the nanorods). Under these conditions, the following Randles–Sevcik equation can be used (assuming again a Nernstian redox reaction)

$$\frac{\phi_{f,p}}{v^{1/2}} = \frac{i_{f,p}}{FSv^{1/2}} = 0.4463 \sqrt{\frac{F}{RT}} \frac{S_e}{S} \sqrt{D_{H,in}} x C_{Ti}^0 \quad (6)$$

where S_e (in cm^2) is here the specific electroactive surface area of the mesoporous electrode; $D_{H,in}$ (in $\text{cm}^2 \cdot \text{s}^{-1}$) is the apparent diffusion coefficient of H^+ within the metal oxide lattice; C_{Ti}^0 ($0.048 \text{ mol} \cdot \text{cm}^{-3}$) is the maximal concentration of titanium ions in amorphous TiO_2 ; and x is the maximal mole fraction of protons that can be inserted in the fully reduced phase H_xTiO_2 . This equation can thus be used to calculate the diffusion coefficient of H^+ within the TiO_2 lattice using the limiting value of $\phi_{f,p}/v^{1/2}$ extrapolated in Figure 7 (dotted black line, $\phi_{f,p}/v^{1/2} = 1.1 \times 10^{-6} \text{ mol} \cdot \text{cm}^{-2} \cdot \text{s}^{-1/2} \cdot \text{V}^{-1/2}$). Two issues must, however, be considered. First, an appropriate estimate of the maximal value of x must be available. Unfortunately, we were experimentally unable to reach full reduction of TiO_2 before permanent failure of the GLAD- TiO_2 electrode. The second issue is related to the difficulty of reliably evaluating the true specific electroactive surface area, S_e , through which the proton-coupled charge transfer occurs, an area which does not necessarily correspond to that determined by BET. This is indeed supported by the idea that ion insertion may not occur homogeneously at the electrolyte/metal oxide interface but preferentially via percolation channels within single grains, as has been recently demonstrated by nanoscale imaging of a lithium titanate surface at various states of Li^+ insertion.⁵⁶ Consequently, the diffusion coefficient for ion insertion determined from Eq. 6 is an apparent value (one can finally hardly deconvolute the two parameters contained in the $S_e \times D_{H,in}^{1/2}$ product). Assuming $S_e/S = SA = 540$ (estimated from BET) for the $1 \mu\text{m}$ thick GLAD- TiO_2 film and a mole fraction $x = 0.5$ by analogy to that usually reported for Li^+ in anatase,^{5,52} an apparent solid-state proton diffusion coefficient of $D_{H,in} = 10^{-15} \text{ cm}^2 \cdot \text{s}^{-1}$ is obtained. From such a value, the penetration length, l , of protons within the metal oxide lattice during the time course of a typical CV experiment can be estimated using Eq. 7, where t is the charging time of the experiment.

$$l = \sqrt{\pi D_{H,in} t} \quad (7)$$

At the slowest scan rate ($0.1 \text{ V} \cdot \text{s}^{-1}$) we have used, and for the highest buffer concentration (860 mM HEPES at pH 7), a proton penetration length l of 1.25 nm was calculated. This diffusion length is less than the smallest dimension of GLAD- TiO_2 nanorods ($\sim 5 \text{ nm}$) we have roughly estimated from our simple model in Figure 1, a result which therefore justifies *a posteriori* the validity of Eq. 6 and, therefore, the assumption of 1D semi-infinite

linear diffusion. It also suggests that for the strongest accumulation conditions we were able to reach, the concentration gradient layer of reduced Ti^{IV} extends from the TiO_2 nanorod walls up to $\sim 40\%$ of the total metal oxide volume.

5. Comparative Study with Lithium Insertion

With the aim of directly comparing proton-ion versus lithium-ion insertion in a $1\ \mu\text{m}$ thick amorphous GLAD- TiO_2 film, a series of CV and CVA experiments were performed in aqueous electrolytes containing either $76\ \text{mM Li}^+$ ($\text{pH} \sim 6.5$) or $76\ \text{mM}$ acid form of HEPES ($\text{pH} 7.0$) for a set of scan rates (Figure 8). The marked differences between the shapes of CVs (and also CVAs) recorded in the presence of a proton ion donor and those recorded in the presence of lithium ion suggest that Li^+ insertion does not proceed as fast as proton insertion under the selected conditions. One may argue that at the low Li^+ concentration used the lack of discernible lithium insertion within GLAD- TiO_2 films would result from a slow diffusion rate of Li^+ in the bulk of solution, leading thus to a low faradaic current response according to Eq. 5. This is however unlikely because the diffusion coefficient of Li^+ in aqueous solution is quite high ($\sim 10^{-5}\ \text{cm}^2 \cdot \text{s}^{-1}$),⁵⁷ and so its diffusion rate in water is even faster than the AH form of HEPES. Still, an additional CV experiment was performed at a much higher concentration of Li^+ ($1\ \text{M}$) (Figure 8), but again the small increase of current compared with that obtained with a proton donor such as the protonated form of HEPES at $0.66\ \text{M}$ de finitely indicates the much slower insertion of Li^+ than H^+ in the amorphous film of GLAD- TiO_2 . One should note that the broad and small reversible waves we observed here for Li^+ insertion in amorphous GLAD- TiO_2 are in line with previous reports of Li^+ insertion in other types of amorphous mesoporous TiO_2 films in aprotic solvents, exhibiting a similar broad and small reversible wave in CV, much smaller and less well-defined than for Li^+ insertion in mesoscopic films of pure anatase.^{51,58} All of these observations allow us to conclude that, under our conditions, proton ion insertion occurs in amorphous mesoporous GLAD- TiO_2 films through a remarkably faster and more favorable process than lithium-ion insertion.

On account of the above observations, it is interesting to return to the value we have determined for the solid-state diffusion coefficient of protons in GLAD- TiO_2 ($D_{\text{H,in}} = 10^{-15}\ \text{cm}^2 \cdot \text{s}^{-1}$) because it is the key parameter governing the proton charge storage dynamics in TiO_2 relative to lithium. Analyzing in detail the solid-state diffusion coefficients of Li^+ reported in the literature (in particular those obtained at nanoporous TiO_2 films made of $7\text{--}8\ \text{nm}$ anatase

particles) allows us to identify consistent values in the range of 1×10^{-17} to 6×10^{-17} $\text{cm}^2 \cdot \text{s}^{-1}$.^{42,43,51} Assuming these data as the most relevant for direct comparison to the present value of $D_{H,in}$ in GLAD-TiO₂, we can conclude that protons diffuse 20- to 100-fold faster in amorphous TiO₂ than Li⁺ in anatase. This strong difference may explain the obvious contrast we observe between proton and lithium-ion insertion in amorphous GLAD-TiO₂ electrodes.

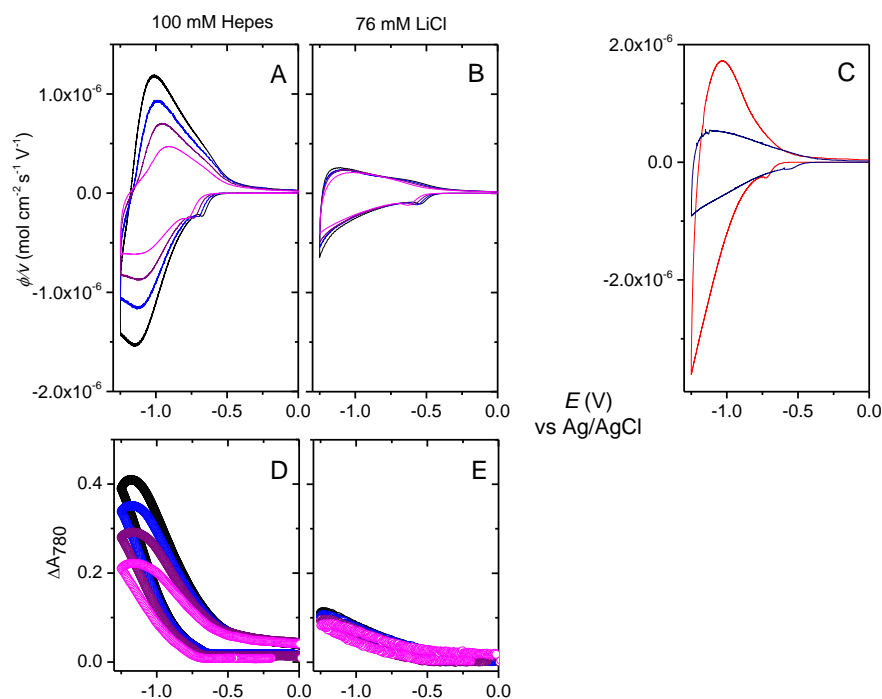


Figure 8. (A,B) CVs recorded at 1 μm -thick GLAD-TiO₂ electrodes immersed in aqueous solutions containing 0.3 M KCl and (A) 76 mM acidic form of HEPES (*i.e.* 0.1 M HEPES buffer, pH 7.0) and (B) 76 mM LiCl. Scan rates: 0.05 $\text{V} \cdot \text{s}^{-1}$ (black), 0.1 $\text{V} \cdot \text{s}^{-1}$ (blue), 0.2 $\text{V} \cdot \text{s}^{-1}$ (purple) and 0.5 $\text{V} \cdot \text{s}^{-1}$ (magenta). (C) Same as (A,B) but with 0.3 M KCl and (red) 0.66 M acidic form of HEPES (0.66 M AH in 0.86 M HEPES, pH 7.0) or (dark blue) 1 M LiCl, both recorded at a scan rate of 0.1 $\text{V} \cdot \text{s}^{-1}$. (D,E) CVAs ($\lambda = 780$ nm) recorded during the corresponding CV scans in (A,B). $T = 25^\circ\text{C}$.

6. Quantification of the charge stored

One great advantage of cyclic voltabsorptometry lies in the correlation that can be done between electrochemical and spectroscopic data. In the present study, it allows for real-time analysis of the spectroscopic features of TiO₂ films during the electrochemical charging process. Assuming that all injected electrons give rise to absorbance at 780 nm, cyclic voltabsorptograms can be converted to derivative cyclic voltabsorptograms (DCVA) according

to Eq. 8 (where both current and absorbance are expressed in flux density ϕ in $\text{mol}\cdot\text{cm}^{-2}\cdot\text{s}^{-1}$) and directly compared to each other.

$$\phi = \frac{1}{1000\epsilon_{780}} \frac{dA_{780}}{dt} = \frac{i}{FS} \quad (8)$$

where A_{780} is the absorbance monitored at 780 nm and ϵ_{780} in $\text{M}^{-1}\cdot\text{cm}^{-1}$ is the extinction coefficient of the stored electron.

As shown in Figure 9, when using an extinction coefficient value of 800 or 1200 $\text{M}^{-1}\cdot\text{cm}^{-1}$ at 780 nm, depending on the electrode batch, a perfect overlap of the DCVAs and CVs is obtained over the entire potential window, regardless of the pHs and buffer concentrations. The independence of ϵ_{780} from both the applied potential as well as the proton provider is *a priori* surprising since it indicates that all electrons stored within the material share common spectroscopic features in the visible range, regardless of their origin or nature (*i.e.*, either the electrons are associated with the filling of electronic states in the band gap and/or conduction band, or stored in the double-layer capacitance at the TiO_2 -electrolyte interface, or associated with the faradaic charging process leading to the reductive protonation of Ti^{IV} ions within the TiO_2 lattice). Such an observation seems to contradict a previous report in the literature suggesting that electrons associated with lithium-ion insertion in TiO_2 have a marked increase in average extinction coefficient (in the near-IR range) with respect to electrons accumulated in the conduction band.³⁵ This previous report, however, was performed under strong accumulation conditions, which are known to lead to a long lasting coloration of the metal oxide film. In the present study, such strong accumulation conditions are not encountered. The extinction coefficient values used in the present study, $900 \pm 300 \text{ M}^{-1}\cdot\text{cm}^{-1}$, are in good agreement with those previously found under different experimental conditions and for different types of mesoporous TiO_2 films.^{18,25,35}

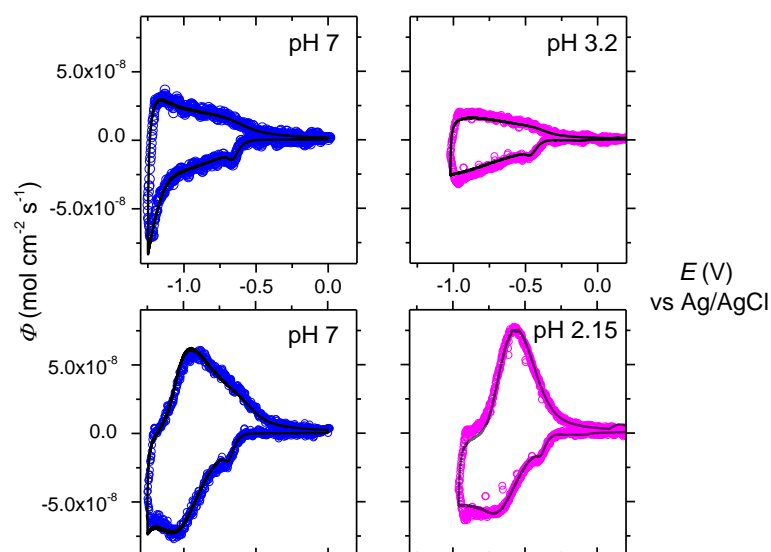


Figure 9. CVs (black line) and DCVAs (circles) expressed in flux density and recorded at (left) neutral pH in the presence of (top) 1 mM or (bottom) 50 mM HEPES, or (right) acidic pHs. The optimized overlay of DCVAs and CVs was obtained by adjusting the ϵ_{780} value to (blue) $800 \text{ M}^{-1}\cdot\text{cm}^{-1}$ and (magenta) $1200 \text{ M}^{-1}\cdot\text{cm}^{-1}$. All experiments were conducted in the presence of 0.3 M KCl at a scan rate of $0.1 \text{ V}\cdot\text{s}^{-1}$. $T = 25^\circ\text{C}$.

The charge density Q (in $\text{C}\cdot\text{cm}^{-2}$) stored in the $1 \mu\text{m}$ thick GLAD-TiO₂ film can be easily determined for each electrode either from the maximum absorbance change monitored at 780 nm or from integration of the charging/discharging current in CV, using Eq. 9:

$$Q = F \frac{\Delta A_{780}}{1000 \epsilon_{780}} F \int \frac{i}{S} dt \quad (9)$$

This equation was used to estimate the total charge stored at the highest tested concentration of proton donor (0.66 M AH in 0.86 M HEPES buffer, pH 7) and $0.1 \text{ V}\cdot\text{s}^{-1}$ (Figure 10). A value of $78 \text{ mC}\cdot\text{cm}^{-2}$ was obtained, corresponding thus to a total charge capacity of $310 \text{ C}\cdot\text{g}^{-1}$. This total stored charge results from the combined contributions of charges stored from faradaic reduction of TiO₂ and charges accumulated at the double-layer interface of the nanostructured metal oxide. The charge fraction associated with the faradaic contribution can be determined by subtraction of charge accumulated in the absence of significant proton insertion (corresponding to the double-layer capacitance charge) from the total charge. From the magnitude of absorbance changes recorded at the lowest concentration of proton donor, a capacitive charge density of $18 \text{ mC}\cdot\text{cm}^{-2}$ (or $72 \text{ C}\cdot\text{g}^{-1}$) could be recovered. This implies that 23 % of the total stored charge results from the double-layer capacitance of the nanoporous

TiO₂ film, while the remaining 77 % (*i.e.*, 60 mC·cm⁻² or 240 C·g⁻¹ or 66 mA·h·g⁻¹) arises from the proton-coupled electron transfer reaction within the metal-oxide network (Table 2). This latter value is equivalent to 0.6 μmol·cm⁻² of intercalated protons and thus corresponds to the reductive protonation of ~20 % of the total titanium ions in the lattice (equivalent to a x value of 0.2). As the charging process is diffusion-limited under the experimental conditions, the maximal mole fraction x is manifestly not reached. It could theoretically be attained experimentally by either decreasing the scan rate or prolonging the time the electrode is biased at negative potentials ($<E^{0'}$). However, the scan rate could not be decreased below 0.05 V·s⁻¹ in the present study without the strong charge accumulation condition inducing a sudden irreversible failure of the GLAD-TiO₂ electrodes (see above).

Despite the inability to reach the maximum mole fraction, it is still possible to compare the total e⁻/H⁺ charges that could be reversibly stored in the 1 μm thick GLAD-TiO₂ electrode against previous reports for Li⁺ storage in various mesoporous anatase films (in aprotic solvents) (Table 2). It is remarkable to note in Table 2 that under our experimental conditions proton ion insertion within amorphous GLAD-TiO₂ films occurs nearly as extensively as lithium-ion insertion in mesoporous crystalline films of anatase. Moreover, this extensive proton insertion is achieved much more rapidly than reported for lithium-ion insertion (the 0.2 mole fraction was attained here at a scan rate of 100 mV·s⁻¹, while for Li⁺, the 0.15 to 0.31 mole fractions were obtained at 0.5 mV·s⁻¹; see Table 1). Interestingly, in spite of completely different experimental conditions, a similarly extensive reductive protonation of TiO₂ (~16 %) was obtained by prolonged UV-irradiation in toluene of amorphous nanoparticles capped with organic ligands.⁵⁹

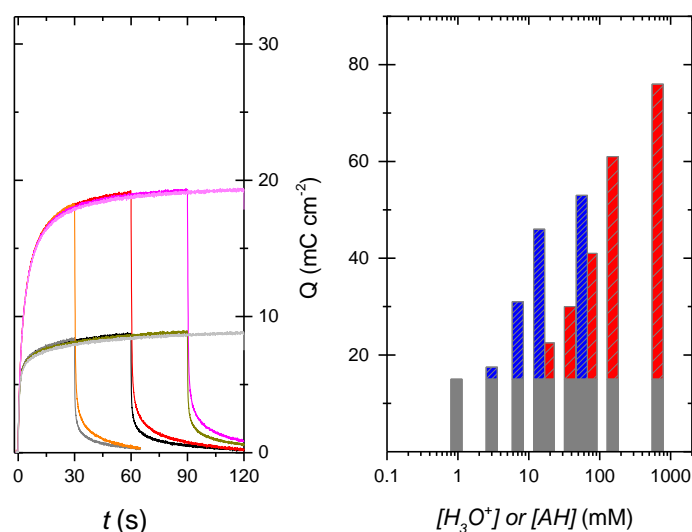


Figure 10. (Left) Double potential step chronoabsorptometric responses (the absorbance has been converted into charge per unit of geometric electrode area using Eq. 9) monitored at 780 nm in a 0.3 M KCl aqueous solution containing (black and gray lines) 1 mM or (orange, red, magenta, pink lines) 100 mM HEPES at pH 7. The potential was stepped from 0.0 to -1.0 V and then back to 0.0 V (vs Ag/AgCl). The double potential step experiment was repeated several times by progressively increasing both the cathodic and anodic polarization time from 30 to 120 s. (Right) Charge contributions of the (gray) double-layer charging and (blue and red) faradaic proton insertion to the total charge stored in a GLAD-TiO₂ film during a CV performed at $0.1 \text{ V}\cdot\text{s}^{-1}$. Bars in blue are for free protons, while those in red are for the acidic form, AH, of the HEPES buffer.

Table 2. Structural Characteristics and Charge Storage Properties of the Present GLAD-TiO₂ Films Compared to Those Previously Established for Other Mesoporous TiO₂ Films.

	GLAD film	nanopartical films			sol-gel film
TiO ₂ crystallinity	amorphous	anatase	anatase	anatase	anatase
BET surface area ($\text{m}^2\cdot\text{g}^{-1}$)	220	220	150	350-400	180-200
nanoparticle diameter (nm)	$\sim 5^a$	7	10	4-5	nd
intercalating ion	H ⁺	Li ⁺	Li ⁺	Li ⁺	Li ⁺
scan rate ($\text{mV}\cdot\text{s}^{-1}$)	100	0.5	0.5	0.5	0.5
total charge stored ($\text{C}\cdot\text{g}^{-1}$)	310	490	460	200	340
electrical capacitive contribution (%)	23	55	35	50	40
ion insertion capacity ($\text{mA}\cdot\text{h}\cdot\text{g}^{-1}$)	66	61	83	28	57
mole fraction of inserted cation	0.2	0.15	nd ^b	0.18	0.31
ref	Present work	44	44	45	45

^aEstimated from geometrical consideration (see text). ^bNot determined.

To better characterize the long-term stability, reversibility, and speed of e^-/H^+ charge/discharge in GLAD-TiO₂, mesoporous films were investigated by double potential step chronoabsorptometric experiments in HEPES buffer at two different proton donor concentrations (*i.e.*, 0.77 and 77 mM AH). To avoid excessive charge accumulation, the forward potential was stepped from 0.0 to -1.0 V, a moderate cathodic potential only slightly more positive than the formal potential ($E^{0'} = -1.06$ V) of the reversible proton insertion/disinsertion wave. In the absence of significant proton donor in solution, the time-course absorbance change in Figure 4 grows rapidly until it reaches a steady state value of 8.7 mC·cm² (in less than 30 s). This fast absorbance increase is representative of the electrode capacitive charging rate (*i.e.*, the charging of both the chemical and double-layer capacitances) when there is no significant contribution of proton insertion to charge storage. At an appreciable proton donor concentration of 77 mM (0.1 M HEPES), a significantly higher limiting charge storage value of 19.3 mC·cm² (an increase of 120 %) is reached after only slightly longer accumulation time (*ca.* 60 s). This result confirms the remarkably fast reductive protonation of GLAD-TiO₂ and allows for easy estimation of the additional stored charges resulting from the faradaic proton insertion at the selected applied potential. The stationary charge accumulated after 1 min of electrode polarization at -1.0 V also points to thermodynamic control of the accumulated charge (*i.e.*, in equilibrium with the Fermi level of -1.0 V applied to the metal oxide film), which is here assumed governed by the Nernst's law. (This is a reasonable assumption when one considers the good electrochemical reversibility of the proton insertion/disinsertion waves on the CVs.) From the maximal faradaic charge density extracted in Figure 10 (*i.e.*, $Q = 11$ mC·cm⁻² after subtraction of the capacitive charge density), it can be calculated that 4 % of the total Ti ions present in the metal oxide film are electrochemically reduced after only 1 min of electrode polarization at -1.0 V. Inserting this ratio into the Nernst equation and assuming the law remains valid regardless of the amount of charge injected into TiO₂ allows us to estimate an x value of 0.45 (using $E^{0'} = -1.06$ V and $E = -1.0$ V). This maximum insertion ratio is close to the mole fraction of 0.5 found for lithiated anatase (Li_{0.5}TiO₂) wherein lithium ions are randomly distributed over half of the available interstitial octahedral sites.⁶⁰ It also validates a posteriori the x value of 0.5 used in Eq. 6 for the calculation of $D_{H,in}$. Another important merit of the chronoabsorptometric experiments in Figure 10 is to clearly highlight the high-rate electrochemical charging and discharging processes as well as their high reversibility and cyclability as attested by the perfect overlay of the multiple double potential-step experiments repetitively recorded.

7. Conclusion

In the present work, we demonstrate that the charge storage capacity of amorphous GLAD-TiO₂ electrodes can be strongly enhanced upon reductive protonation of lattice Ti^{IV} ions. This process is characterized by a reversible and fast faradaic proton-coupled electron transfer reaction centered at a well-defined formal potential (*i.e.*, a well-defined localized state), energetically positioned at a value negative to the conduction band potential of TiO₂ (*i.e.*, at a potential where TiO₂ is fully degenerate), and that we can reasonably attribute to the Ti^{IV}O₂/Ti^{III}O(OH) redox couple. This reversible process can however only be revealed by the presence of a sufficiently large concentration of an appropriate proton donor in solution, *i.e.*, free protons or a much weaker acid such as the acidic form of the buffer. We demonstrate moreover that reductive doping of amorphous mesoporous TiO₂ in aqueous solution is highly specific for protons and that Li⁺ insertion does not compete with proton insertion under the present experimental conditions, most likely because of the short time window used. Despite this, the total charge stored in the GLAD-TiO₂ electrode upon proton insertion falls within the range of values reported for mesoporous TiO₂ electrodes upon lithium insertion in aprotic solvent. The present study is of special interest for the development of devices operating under mildly aqueous conditions as it demonstrates that electron/proton accumulation within mesoporous TiO₂ films can occur massively and rapidly at neutral pH conditions. This, in turn, indicates that high rate and high power could be achieved for reversible proton charge/discharge storage within the material. It provides moreover an easy methodology to distinguish the faradaic current density related to proton insertion from that associated with the classical electrical capacitance by modifying the concentration of the weak acid.

References

- ¹ Berger, T.; Monllor-Satoca, D.; Jankulovska, M.; Lana-Villarreal, T.; Gomez, R. The electrochemistry of nanostructured titanium dioxide electrodes. *ChemPhysChem* **2012**, 13, 2824–2875.
- ² Li, W.; Wu, Z.; Wang, J.; Elzatahry, A. A.; Zhao, D. A Perspective on Mesoporous TiO₂ Materials. *Chem. Mater.* **2014**, 26, 287–298.
- ³ Hagfeldt, A.; Boschloo, G.; Sun, L.; Kloo, L.; Pettersson, H. Dyesensitized Solar Cells. *Chem. Rev.* **2010**, 110, 6595–6663.
- ⁴ Reddy, M. V.; Subba Rao, G. V.; Chowdari, B. V. Metal oxides and oxysalts as anode materials for Li ion batteries. *Chem. Rev.* **2013**, 113, 5364–5457.
- ⁵ Dylla, A. G.; Henkelman, G.; Stevenson, K. J. Lithium Insertion in Nanostructured TiO₂ (B) Architectures. *Acc. Chem. Res.* **2013**, 46, 1104–1112.
- ⁶ Bai, J.; Zhou, B. Titanium dioxide nanomaterials for sensor applications. *Chem. Rev.* **2014**, 114, 10131–10176.
- ⁷ Nang Dinh, N.; Minh Quyen, N.; Chung, D. N.; Zikova, M.; Truong, V. Van Highly-efficient electrochromic performance of nanostructured TiO₂ films made by doctor blade technique. *Sol. Energy Mater. Sol. Cells* **2011**, 95, 618–623.
- ⁸ Watanabe, T.; Nakajima, A.; Wang, R.; Minabe, M.; Koizumi, S.; Fujishima, A.; Hashimoto, K. Photocatalytic activity and photoinduced hydrophilicity of titanium dioxide coated glass. *Thin Solid Films* **1999**, 351, 260–263.
- ⁹ Ashford, D. L.; Gish, M. K.; Vannucci, A. K.; Brennaman, M. K.; Templeton, J. L.; Papanikolas, J. M.; Meyer, T. J. Molecular Chromophore-Catalyst Assemblies for Solar Fuel Applications. *Chem. Rev.* **2015**, 115, 13006–13049.
- ¹⁰ Ma, Y.; Wang, X. L.; Jia, Y. S.; Chen, X. B.; Han, H. X.; Li, C. Titanium Dioxide-Based Nanomaterials for Photocatalytic Fuel Generations. *Chem. Rev.* **2014**, 114, 9987–10043.
- ¹¹ Zhang, Y.; Xiong, X.; Han, Y.; Zhang, X.; Shen, F.; Deng, S.; Xiao, H.; Yang, X.; Yang, G.; Peng, H. Photoelectrocatalytic degradation of recalcitrant organic pollutants using TiO₂ film electrodes: *An overview*. *Chemosphere* **2012**, 88, 145–154.
- ¹² Bella, F.; Gerbaldi, C.; Barolo, C.; Grätzel, M. Aqueous dyesensitized solar cells. *Chem. Soc. Rev.* **2015**, 44, 3431–3473.
- ¹³ Bella, F.; Galliano, S.; Falco, M.; Viscardi, G.; Barolo, C.; Grätzel, M.; Gerbaldi, C. Unveiling iodine-based electrolytes chemistry in aqueous dye-sensitized solar cells. *Chem. Sci.* **2016**, 7, 4880–4890.
- ¹⁴ Liu, S.; Pan, G. L.; Yan, N. F.; Gao, X. P. Aqueous TiO₂/Ni(OH)₂ rechargeable battery with a high voltage based on proton and lithium insertion/extraction reactions. *Energy Environ. Sci.* **2010**, 3, 1732.

- ¹⁵ Liu, J.; Wang, J.; Ku, Z.; Wang, H.; Chen, S.; Zhang, L.; Lin, J.; Shen, Z. X. Aqueous Rechargeable Alkaline Cox Ni₂ S_{2-x}/TiO₂ Battery. *ACS Nano* **2016**, 10, 1007–1016.
- ¹⁶ Hambourger, M.; Gust, D.; Hambourger, M.; Kodis, G.; Moore, A.; Moore, G. F. Solar energy conversion in a photoelectrochemical biofuel cell. *Dalton Trans.* **2009**, 9979–9989.
- ¹⁷ Zhao, W.-W.; Xu, J.-J.; Chen, H.-Y. Photoelectrochemical bioanalysis: the state of the art. *Chem. Soc. Rev.* **2015**, 44, 729–741.
- ¹⁸ Berger, T.; Anta, J. A.; Morales-Florez, V. Electrons in the band gap: Spectroscopic characterization of anatase TiO₂ nanocrystal electrodes under fermi level control. *J. Phys. Chem. C* **2012**, 116, 11444–11455.
- ¹⁹ Fabregat-Santiago, F.; Barea, E. M.; Bisquert, J.; Mor, G. K.; Shankar, K.; Grimes, C. A. High carrier density and capacitance in TiO₂ nanotube arrays induced by electrochemical doping. *J. Am. Chem. Soc.* **2008**, 130, 11312–11316.
- ²⁰ Meekins, B. H.; Kamat, P. V. Got TiO₂ Nanotubes? Lithium Ion Intercalation can Boost Their Photoelectrochemical Performance Supporting Information. *ACS Nano* **2009**, 3, 3437–3446.
- ²¹ Ghicov, A.; Tsuchiya, H.; Hahn, R.; MacAk, J. M.; Munoz, A. G.; Schmuki, P. TiO₂ nanotubes: H⁺insertion and strong electrochromic effects. *Electrochem. Commun.* **2006**, 8, 528–532.
- ²² Berger, T.; Anta, J. A.; Morales-Flórez, V. Spectroscopic properties of electrochemically populated electronic states in nanostructured TiO₂ films: anatase versus rutile. *Phys. Chem. Chem. Phys.* **2013**, 15, 13790–5.
- ²³ Idigoras, J.; Berger, T.; Anta, J. A. Modification of mesoporous TiO₂ films by electrochemical doping: Impact on photoelectrocatalytic and photovoltaic performance. *J. Phys. Chem. C* **2013**, 117, 1561–1570.
- ²⁴ Cao, F.; Oskam, G.; Searson, P. C.; Stipkala, J. M.; Heimer, T. A.; Farzad, F.; Meyer, G. J. Electrical and optical properties of porous nanocrystalline TiO₂ films. *J. Phys. Chem.* **1995**, 99, 11974–11980.
- ²⁵ Rothenberger, G.; Fitzmaurice, D.; Graetzel, M. Spectroscopy of conduction band electrons in transparent metal oxide semiconductor films: optical determination of the flatband potential of colloidal titanium dioxide films. *J. Phys. Chem.* **1992**, 96, 5983–5986.
- ²⁶ Mandal, D.; Hamann, T. W. Band energies of nanoparticle semiconductor electrodes determined by spectroelectrochemical measurements of free electrons. *Phys. Chem. Chem. Phys.* **2015**, 17, 11156–11160.
- ²⁷ Simon, P.; Gogotsi, Y.; Dunn, B. Where Do Batteries End and Supercapacitors Begin? *Science* **2014**, 343, 1210–1211.
- ²⁸ Augustyn, V.; Simon, P.; Dunn, B. Pseudocapacitive oxide materials for high-rate electrochemical energy storage. *Energy Environ. Sci.* **2014**, 7, 1597.
- ²⁹ Krause, K. M.; Taschuk, M. T.; Harris, K. D.; Rider, D. A.; Wakefield, N. G.; Sit, J. C.; Buriak, J. M.; Thommes, M.; Brett, M. J. Surface area characterization of obliquely deposited metal oxide nanostructured thin films. *Langmuir* **2010**, 26, 4368–76.

- ³⁰ Renault, C.; Nicole, L.; Sanchez, C.; Costentin, C.; Balland, V.; Limoges, B. Unraveling the charge transfer/electron transport in mesoporous semiconductive TiO₂ films by voltabsorptometry. *Phys. Chem. Chem. Phys.* **2015**, *17*, 10592–10607.
- ³¹ Renault, C.; Andrieux, C. P.; Tucker, R. T.; Brett, M. J.; Balland, V.; Limoges, B. Unraveling the mechanism of catalytic reduction of O₂ by microperoxidase-11 adsorbed within a transparent 3D-nanoporous ITO film. *J. Am. Chem. Soc.* **2012**, *134*, 6834–45.
- ³² Krause, K. M.; Vick, D. W.; Malac, M.; Brett, M. J. Taking a Little off the Top: Nanorod Array Morphology and Growth Studied by Focused Ion Beam Tomography. *Langmuir* **2010**, *26*, 17558–17567.
- ³³ One should note that the K⁺ cation present in the supporting electrolyte has not been considered as a potentially intercalating ion because of its too large size and the absence of effect on the CVs upon changing the KCl concentration.
- ³⁴ Fabregat-Santiago, F.; Mora-Seró, I.; Garcia-Belmonte, G.; Bisquert, J. Cyclic Voltammetry Studies of Nanoporous Semiconductors. Capacitive and Reactive Properties of Nanocrystalline TiO₂ Electrodes in Aqueous Electrolyte. *J. Phys. Chem. B* **2003**, *107*, 758–768.
- ³⁵ Boschloo, G.; Fitzmaurice, D. Electron Accumulation in Nanostructured TiO₂ (Anatase) Electrodes. *J. Phys. Chem. B* **1999**, *103*, 7860–7868.
- ³⁶ Lyon, L. A.; Hupp, J. T. Energetics of the Nanocrystalline Titanium Dioxide/Aqueous Solution Interface: Approximate Conduction Band Edge Variations between H₀ = - 10 and H⁻ = + 26. *J. Phys. Chem. B* **1999**, *103*, 4623–4628.
- ³⁷ Zúkalová, M.; Bousa, M.; Bastl, Z.; Jirka, I.; Kavan, L. Electrochemical Doping of Compact TiO₂ Thin Layers. *J. Phys. Chem. C* **2014**, *118*, 25970–25977.
- ³⁸ Liu, L.; Yellinek, S.; Valdinger, I.; Donval, A.; Mandler, D. Important Implications of the Electrochemical Reduction of ITO. *Electrochim. Acta* **2015**, *176*, 1374–1381.
- ³⁹ Zhang, Y.; Feng, H.; Wu, X.; Wang, L.; Zhang, A.; Xia, T.; Dong, H.; Li, X.; Zhang, L. Progress of electrochemical capacitor electrode materials: A review. *Int. J. Hydrogen Energy* **2009**, *34*, 4889–4899.
- ⁴⁰ Bard, A. J.; Faulkner, L. R. *Electrochemical Methods: Fundamentals and Applications*; Wiley, **2000**.
- ⁴¹ Kötzt, R.; Carlen, M. Principles and applications of electrochemical capacitors. *Electrochim. Acta* **2000**, *45*, 2483–2498.
- ⁴² Lindström, H.; Södergren, S.; Solbrand, A.; Rensmo, H.; Hjelm, J.; Hagfeldt, A.; Lindquist, S.-E. Li⁺ Ion Insertion in TiO₂ (Anatase). 1. Chronoamperometry on CVD Films and Nanoporous Films. *J. Phys. Chem. B* **1997**, *101*, 7710–7716.
- ⁴³ Lindström, H.; Södergren, S.; Solbrand, A.; Rensmo, H.; Hjelm, J.; Hagfeldt, A.; Lindquist, S.-E. Li⁺ Ion Insertion in TiO₂ (Anatase). 2. Voltammetry on Nanoporous Films. *J. Phys. Chem. B* **1997**, *101*, 7717–7722.

- ⁴⁴ Wang, J.; Polleux, J.; Lim, J.; Dunn, B. Pseudocapacitive Contributions to Electrochemical Energy Storage in TiO₂ (Anatase) Nanoparticles. *J. Phys. Chem. C* **2007**, 111, 14925–14931.
- ⁴⁵ Brezesinski, T.; Wang, J.; Polleux, J.; Dunn, B.; Tolbert, S. H. Templated Nanocrystal-Based Porous TiO₂ Films for Next-Generation Electrochemical Capacitors. *J. Am. Chem. Soc.* **2009**, 131, 1802–1809.
- ⁴⁶ Rahman, M. M.; Wang, J. Z.; Hassan, M. F.; Wexler, D.; Liu, H. K. Amorphous carbon coated high grain boundary density dual phase Li₄Ti₅O₁₂-TiO₂: A nanocomposite anode material for li-ion batteries. *Adv. Energy Mater.* **2011**, 1, 212–220.
- ⁴⁷ Note: it is also possible to consider the case of a slow or irreversible electrochemical reaction by analyzing the peak current using the following expression $i_{fp}/FSv^{1/2} = 0.4958\sqrt{F/RT}\alpha D_{H,oul}[H]$, where α is the transfer coefficient. If we assume $\alpha = 0.5$, it would mean that the constant 0.4463 in eq 1 is replaced by 0.3506 for an irreversible electrochemical reaction.
- ⁴⁸ Wang, J. H.; Robinson, C. V.; Edelman, I. S. Self-diffusion and Structure of Liquid Water. III. Measurement of the Self-diffusion of Liquid Water with H₂, H₃ and O₁₈ as Tracers. *J. Am. Chem. Soc.* **1953**, 75, 466–470.
- ⁴⁹ Lee, S. H.; Rasaiah, J. C. Proton transfer and the mobilities of the H⁺ and OH⁻ ions from studies of a dissociating model for water. *J. Chem. Phys.* **2011**, 135, 124505.
- ⁵⁰ <http://www.bio.umass.edu/biology/kunkel/probe/buffers/> (accessed December **2016**).
- ⁵¹ Kavan, L.; Rathouský, J.; Grätzel, M.; Shklover, V.; Zukal, A. Surfactant-Templated TiO₂ (Anatase): Characteristic Features of Lithium Insertion Electrochemistry in Organized Nanostructures. *J. Phys. Chem. B* **2000**, 104, 12012–12020.
- ⁵² Van De Krol, R.; Goossens, A.; Schoonman, J. Spatial Extent of Lithium Intercalation in Anatase TiO₂. *J. Phys. Chem. B* **1999**, 103, 7151–7159.
- ⁵³ Kanamura, K.; Yuasa, K.; Takehara, Z. Diffusion of lithium in the TiO₂ cathode of a lithium battery. *J. Power Sources* **1987**, 20, 127–134.
- ⁵⁴ Wu, M.-S.; Wang, M.-J.; Jow, J.-J.; Yang, W.-D.; Hsieh, C.-Y.; Tsai, H.-M. Electrochemical fabrication of anatase TiO₂ nanostructure as an anode material for aqueous lithium-ion batteries. *J. Power Sources* **2008**, 185, 1420–1424.
- ⁵⁵ Van der Ven, A.; Bhattacharya, J.; Belak, A. A. Understanding Li Diffusion in Li-Intercalation Compounds. *Acc. Chem. Res.* **2013**, 46, 1216–1225.
- ⁵⁶ Verde, M. G.; Baggetto, L.; Balke, N.; Veith, G. M.; Seo, J. K.; Wang, Z.; Meng, Y. S. Elucidating the Phase Transformation of Li₄Ti₅O₁₂ Lithiation at the Nanoscale. *ACS Nano* **2016**, 10, 4312–4321.
- ⁵⁷ Braun, B. M.; Weingaertner, H. Accurate self-diffusion coefficients of lithium⁺, sodium⁺, and cesium⁺ ions in aqueous alkali metal halide solutions from NMR spin-echo experiments. *J. Phys. Chem.* **1988**, 92, 1342–1346.

- ⁵⁸ Huang, S.; Zhang, L.; Lu, X.; Liu, L.; Liu, L.; Sun, X.; Yin, Y.; Oswald, S.; Zou, Z.; Ding, F.; Schmidt, O. G. Tunable Pseudocapacitance in 3D TiO₂- δ Nanomembranes Enabling Superior Lithium Storage Performance. *ACS Nano* **2017**, 11, 821–830.
- ⁵⁹ Schrauben, J. N.; Hayoun, R.; Valdez, C. N.; Braten, M.; Fridley, L.; Mayer, J. M. Titanium and Zinc Oxide Nanoparticles Are Proton-Coupled Electron Transfer Agents. *Science* **2012**, 336, 1298–1301.
- ⁶⁰ Cava, R. J.; Murphy, D. W.; Zahurak, S.; Santoro, A.; Roth, R. S. The crystal structures of the lithium-inserted metal oxides Li_{0.5}TiO₂ anatase, LiTi₂O₄ spinel, and Li₂Ti₂O₄. *J. Solid State Chem.* **1984**, 53, 64–75.

**Chapter IV. Investigation of the aqueous electrolyte
composition on the proton-coupled electron storage
at mesoporous TiO₂ electrodes**

1. Introduction

1.1. Questions about multivalent metallic ion insertion charge storage in aqueous electrolytes

1.2. Questions about Li^+ insertion in basic aqueous electrolytes

1.3. Presentation of the different GLAD TiO_2 electrodes used

2. Elucidating the role of multivalent metallic ions in aqueous electrolytes

2.1. Evidencing ion insertion charge storage in presence of multivalent metallic ions

2.2. Mechanistic investigation

2.3. Conclusion

3. Optimization of proton insertion charge storage in acetic acid at pH 5

4. Combined effect of the pH and the weak acid pK_a on the efficiency of charge storage in aqueous solution

4.1. Evidencing the link between pH and pK_a

4.2. Evidencing water as a proton donor

5. Conclusion

1. Introduction

There have been many efforts directed toward ion insertion charge storage in metal oxide materials using aqueous electrolytes, in order to improve production issues such as low cost, long lasting and safety that can potentially contribute to large-scale energy storage applications.¹ This concept is inspired by the currently used Li⁺-ion batteries, but replacing harmful organic solvents by aqueous-based electrolytes and Li⁺ by more earth-abundant cations whose natural occurrence is well distributed over the planet. This will allow ion insertion rechargeable batteries to be manufactured with low cost (with abundant cations in aqueous solution) and higher ionic conductivity.

As the previous study described in chapter 3 was performed at pH 7 with a weak acid (Hepes) of pK_a 7.5, further investigation of the proton-coupled charge storage at mesoporous TiO₂ electrodes was achieved by a modification of the electrolyte composition (*i.e.*, pH, chemical features of the weak acid). This is the objective of the current chapter.

1.1. Questions about multivalent metallic ion insertion charge storage in aqueous electrolytes

One of the main subjects addressed in this chapter concerns the ability of multivalent metallic cations to insert within TiO₂. Recently, several studies evidenced competitive charge storage capacity values (~ few hundreds mA·h·g⁻¹) at metal oxide-based electrodes soaked into an aqueous-based electrolytes in the presence of multivalent metal cations such as Al³⁺ or Zn²⁺.²⁻⁷ In studies focusing on anode electrodes, significant increase of the charge storage capacity in TiO₂-based electrodes was thus evidenced in presence of Al³⁺-based electrolyte solutions.^{2-3,8} The results obtained in these recent studies are summarized in Table 1.

In these studies, the benefit of adding multivalent metal ions to the aqueous electrolyte in order to increase the charging capacity of metal oxide-based electrodes is undeniable and clearly related to a redox process occurring at the metal oxide electrode. This has been through the existence of well-defined reversible waves in cyclic voltammetry and also plateaus in charging/discharging galvanostatic experiments.^{2-3,8}

Table 1. Recent studies on charge storage capacity achieved at TiO₂-based electrodes in various aqueous electrolytes.

Anode materials	Putative inserted ion	Charge storage capacity (mA·h·g ⁻¹) at optimized experimental condition	Electrolyte Acidity (pH value, electrolyte composition)	Ref.
TiO ₂	Al ³⁺	75	nd (nd, 1 M AlCl ₃)	2
TiO ₂ -NTA	Al ³⁺ /H ⁺	nd	acidic (pH 1.0 ~ 2.5, AlCl ₃ or Al ₂ (SO ₄) ₃ up to 0.5 M)	8
TiO ₂	Al ³⁺	278	nd (1 M Al(NO ₃) ₃)	3
TiO ₂	Li ⁺	69	basic (nd, 1.5 M LiOH + 4 M KOH)	9
TiO ₂	Li ⁺	135	basic (pH 10, 3.5 M LiCl + 0.25 M Li ₂ SO ₄)	10
TiO ₂	Li ⁺	nd	basic (nd, 1 M LiOH)	12
TiO ₂	Li ⁺	52	basic (nd, 2 M LiOH + 4 M KOH)	13

nd = not determined.

By analogy to Li⁺-ion batteries, this increased charge storage capacity is assumed to be related to insertion-desinsertion of the multivalent metallic cations within the metal oxide structure to locally compensate the negative charge arising from the reduction of metal oxide. Because of its small ionic radius (0.053 nm)¹⁴, it is indeed considered that Al³⁺ can be inserted within the TiO₂ structure and locally compensate the reduced Ti^{IV}. However, the exact molecular mechanism related to bulk metal oxide reduction/re-oxidation and concomitant ion insertion-desinsertion for local charge compensation occurring at the electrode remains unclear and still a matter of debate. Indeed, it is worth to note here that dissolution of aluminum salts such as AlCl₃ in aqueous solutions results into strong acidification of the solution. Accordingly, depending on the aluminum salt concentration, competitive proton insertion can occur. Co-insertion of Al³⁺ and H⁺ within TiO₂-based electrodes was thus proposed under the acidic conditions induced by dissolution of aluminum salts at molar concentrations (pH < 3).⁸

In addition, it should be noted that the small diameter reported for the Al³⁺ ion corresponds to the dehydrated ion. In aqueous solution, it seems more reasonable to consider the [Al(H₂O)₆]³⁺ hexa-aquo-complex. This later is characterized by a quite large molecular size (diameter > 0.38 nm) according to the Al-O internuclear distance of 0.19 nm.¹⁵ Insertion of Al³⁺ within TiO₂ would thus require most likely ion desolvation prior insertion, which is a highly energetic process. Moreover, the [Al(H₂O)₆]³⁺ complex is a weak acid characterized by

a pK_a value of 4.97 (see Table 2).¹⁶ Based on the results presented in the previous chapter, a fundamental question that is raised about Al^{3+} is can it play the role of a proton provider rather than being an insertion cation.

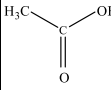
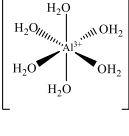
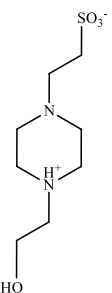
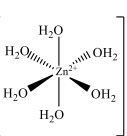
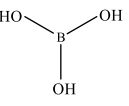
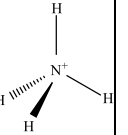
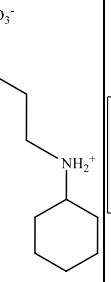
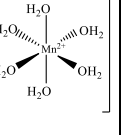
The first part of the chapter will focus on the analysis of charge storage at mesoporous TiO_2 electrodes soaked in aqueous electrolytes in the presence of multivalent metallic ions. We will more specifically focus on Al^{3+} -based electrolytes, taking special care to the pH to avoid competitive proton insertion from free protons. We have carried out systematic comparison with acetic acid-based electrolytes, *i.e.*, containing an organic weak acid characterized by a pK_a value of 4.76 (close to that of $[Al(H_2O)_6]^{3+}$, see Table 2), in such a way to unambiguously highlight the role of Al^{3+} ions.

1.2. Questions about Li^+ insertion in basic aqueous electrolytes

In our previous study (chapter 3), we demonstrated that Li^+ -insertion was rather inefficient as compared to proton-insertion at mesoporous TiO_2 electrodes. This observation was made in an aqueous electrolyte stabilized at pH 6.5 ~ 7.0. This result is quite surprising as in several studies, TiO_2 electrodes are used as negative electrodes for batteries operating in aqueous electrolytes containing Li^+ ions.⁹⁻¹⁰ In such studies, charge storage at the TiO_2 electrode is believed to occur through concomitant Li^+ -insertion. It is however worth to note that all of these studies (summarized in Table 1) are performed under strongly basic conditions which are quite different from the one tested by us (in chapter 3).

In the second part of this chapter, we investigate the effect of electrolyte pH on the charge storage through proton insertion in mesoporous TiO_2 films. The objective of this study is to evidence if proton insertion can indeed occur in the entire pH window, and especially under strongly basic conditions, and to define the proton provider required under these conditions. For such a purpose, the chemical composition of the electrolyte, *i.e.* the nature of the weak acid, was adjusted to the pH in order to keep a significant amount of proton provider. We thus investigated a large panel of weak acids characterized by different pK_a values (see Table 2).

Table 2. Information on the diverse electrolytes used in the present studies.

Chemical name	Acetic acid	Aluminum chloride	Hepes	Zinc chloride	Boric acid	Ammonium chloride	Caps	Manganese chloride
Chemical formula of salts	CH ₃ CO ₂ H	AlCl ₃	C ₈ H ₁₈ N ₂ O ₄ S	ZnCl ₂	B(OH) ₃	NH ₄ Cl	C ₉ H ₁₉ NO ₃ S	MnCl ₂
Structural formula of salts in aqueous solution (acidic form)								
pK _a	4.76	5.00 ¹⁶	7.5	9.0 ¹⁶	9.24	9.25	10.4	10.6 ¹⁶

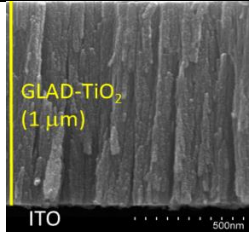
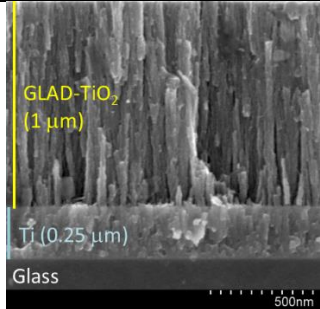
1.3. Presentation of the different GLAD-TiO₂ electrodes used

In chapter 3, electrode failure was observed when using the classical GLAD-TiO₂ electrodes under strong charge accumulation conditions (*i.e.*, upon applying a potential < -1.25 V vs. Ag/AgCl at pH 7.0 for a certain time or upon scanning the potential at a slow scan rate < 50 mV·s⁻¹). This was attributed to instability of the underlying ITO material at too negative potentials. Therefore, it was necessary to find a strategy for increasing the electrode stability in order to improve the charge storage performances. For such purpose, two types of new electrodes were prepared by our collaborator (Dr. Kenneth Harris from the National Institute of Nanotechnology, Edmonton in Canada).²² The deposition condition of the mesoporous TiO₂ film was not modified (*i.e.*, 1 μm film thickness with 72° deposition angle), but the film was deposited on different underlying thin films to avoid direct exposure of ITO to the electrolyte solution. Two types of underlying dense layers were used, either a 15-nm thick film of bulk TiO₂ deposited on top of the ITO substrate as a protective layer (*i.e.*, first type, GLAD-TiO₂/TiO₂) or a 0.25-μm thick metallic film of Ti deposited on top of a glass substrate allowing thus to completely avoid ITO (*i.e.*, second type, GLAD-TiO₂/Ti).

The SEM images and few structural properties of these new mesoporous electrodes are given in Table 3. It is worth to mention that the GLAD-TiO₂/TiO₂ is still transparent, allowing

studies by spectroelectrochemistry, whereas the GLAD-TiO₂/Ti is not transparent, and was thus investigated only by electrochemistry.

Table 3. Main characteristics of the three types of GLAD-TiO₂ electrodes used in this work.

	Chapter 3	Chapter 4	Chapter 4
GLAD electrode type	TiO ₂	TiO ₂ /TiO ₂	TiO ₂ /Ti
Film thickness (μm)	1	1/0.015	1/0.25
Underlying substrate	ITO	ITO	Glass
deposition angle (°)	72	72/0	72/0
SEM image (side view)		no data	
transparency	Yes	Yes	No
photo		no data (Transparency is similar to GLAD-TiO ₂)	

Electrochemical characterization of the different types of GLAD-TiO₂ electrodes was carried out by CVs in 0.3 M KCl electrolyte at pH 3, *i.e.* in conditions where the concentration of free protons in solution is negligible (Figure 1). One might notice a small onset potential difference (~ 24 mV, which is equivalent to pH difference of 0.4) among the different CVs of Figure 1, which might be due to some pH variation in the unbuffered electrolyte solutions used (*e.g.*, pH value for 7 falls in the range of 6.8 ~ 7.3).

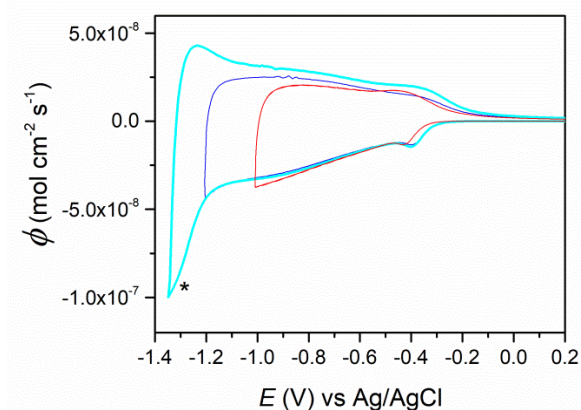


Figure 1. CVs of various types of GLAD-TiO₂ electrodes used in this work (red) GLAD-TiO₂/TiO₂, and (blue and cyan) GLAD-TiO₂/Ti in 0.3 M KCl electrolyte at pH 3. $\nu = 0.1 \text{ V} \cdot \text{s}^{-1}$. * Intensity increase attributed to proton reduction (*i.e.*, hydrogen evolution reaction).

As will be discussed later, despite increased charge storage achieved with the GLAD-TiO₂/TiO₂ electrodes as compared to the previously used GLAD-TiO₂ electrodes, electrode failure still occurred under strong accumulation conditions (data not shown). The best performances were finally obtained with the GLAD-TiO₂/Ti electrodes, allowed to reach more negative potential values for long polarization times without electrode failure (Figure 1). Under these highly cathodic conditions, competitive hydrogen evolution reaction (HER) was observed with sudden increase of the electron flux density (start symbol, Figure 1). HER was confirmed by the observation of bubbles formed at the TiO₂ electrode surface.

Consequently, optimization of the charge storage capacity was performed at GLAD-TiO₂/Ti electrodes, whereas transparent GLAD-TiO₂/TiO₂ electrodes were used for preliminary studies by spectroelectrochemistry.

2. Elucidating the role of multivalent metallic ions in aqueous electrolytes

2.1. Evidencing ion insertion charge storage

In order to evidence the increase of charge storage capacity in the presence of multivalent metallic ions in solution, we investigated the electrochemical features of GLAD-TiO₂/TiO₂ (1 μm /15 nm) electrodes soaked in aqueous solution containing 0.25 M of one of the following salt: AlCl₃, ZnCl₂, or MnCl₂. Under such experimental conditions, multivalent

metal ions (*i.e.*, Al^{3+} , Zn^{2+} , Mn^{2+}) predominantly exists in aqueous solution as metal aquo complex (*i.e.*, general stoichiometry $[\text{M}(\text{H}_2\text{O})_n]^{z+}$). It is thus more relevant to express Al^{3+} , Zn^{2+} , Mn^{2+} as $[\text{Al}(\text{H}_2\text{O})_6]^{3+}$, $[\text{Zn}(\text{H}_2\text{O})_6]^{2+}$, and $[\text{Mn}(\text{H}_2\text{O})_6]^{2+}$, which are characterized by pK_a value of 4.97, 9.0 and 10.6, respectively.¹⁶

The corresponding CVs and CVAs (monitored at 780 nm) at pH 3 are shown in Figure 2. Cyclic scans were initiated at anodic potentials where the semiconductive TiO_2 films behave as an insulator. The potential was then increased to sufficiently cathodic values to fully convert TiO_2 into a metal-like conductive film, and then the potential sweep was reversed to recover the initial insulating state. Charging process is occurring during the forward scan and associated to the blue-black coloration of the GLAD- $\text{TiO}_2/\text{TiO}_2$ transparent films, whereas the discharging process is occurring during the reverse scan. During the discharging process, the initial GLAD- $\text{TiO}_2/\text{TiO}_2$ transparency is completely recovered indicating a fully reversible charge/discharge process. Potential window was adjusted by considering the pH-dependence of TiO_2 conduction band potential (*i.e.*, 0.24 V to -1.01 V at pH 3).¹⁸⁻¹⁹

In the absence of multivalent metallic ions in solution, the CVs show good overlap once expressed as electron flux density normalized to the scan rate, with intensities almost independent of the applied potential in the potential window corresponding to a conductive TiO_2 film (*i.e.*, $E < E_{CB} \sim -0.54$ V at pH 3). These characteristics are typical of the electrical double layer capacitance resulting from the high surface area of GLAD- $\text{TiO}_2/\text{TiO}_2$ film, as expected in an inert KCl electrolyte and in absence of significant amount of free protons (*i.e.*, $[\text{H}_3\text{O}^+] \leq 10^{-3}$ M). The corresponding CVAs are also nicely overlapped, demonstrating thus that the small amount of charge stored at the TiO_2 electrode is independent of the scan rate (in the scan rate range investigated here) which also signs a fast electrical double layer charging process.

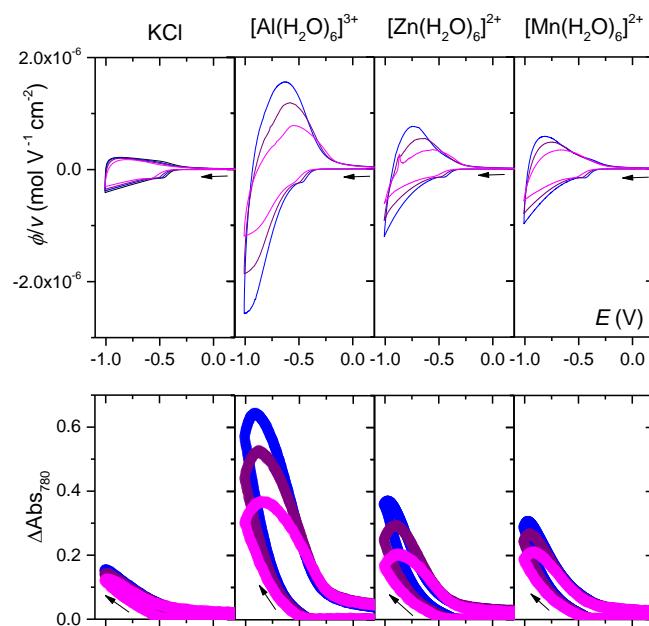


Figure 2. (Top) CVs and (Bottom) CVAs monitored at 780 nm, recorded at GLAD-TiO₂/TiO₂ (1 μm/15 nm) electrodes in aqueous solutions with either 0.3 M KCl, or 0.25 M of [Al(H₂O)₆]³⁺, [Zn(H₂O)₆]²⁺, [Mn(H₂O)₆]²⁺ (indicated on top of the graph, respectively). Currents are converted to electron flux density normalized to the scan rate, the ordinate is $\phi/v = i/FSv$ with units mol·V⁻¹cm⁻². Scan rates: 0.05 V·s⁻¹ (black), 0.1 V·s⁻¹ (blue), 0.2 V·s⁻¹ (purple) and 0.5 V·s⁻¹ (magenta). The abscissa for both CVs and CVAs are potential (V) with respect to the Ag/AgCl (3 M KCl) reference electrode. $T = 25^\circ\text{C}$. All aqueous solutions were adjusted to pH 3.

In the presence of a multivalent metallic ion in solution, once the applied potential lies within the potential window corresponding to the fully conductive state of TiO₂, the magnitudes of both CVs and CVAs are increased, however to a much larger extent for the Al³⁺-based electrolyte. This charging process is clearly related to a slow faradaic redox process occurring at the GLAD-TiO₂/TiO₂ electrode as notably evidenced by the broad reversible wave in CVs and the hysteresis in CVAs. These observations are strongly reminiscent of that observed previously at pH 7 in the presence of Hepes buffer. We thus attribute the faradaic current to the reduction/re-oxidation of Ti^{IV} ions, a process occurring with the concomitant insertion of cations from the electrolyte.

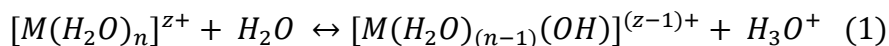
At this stage, we can make two hypotheses regarding the nature of the cation inserted at the TiO₂/electrolyte interface. The first one concerns insertion of a multivalent cation M^{Z+} resulting from desolvation of the corresponding metal-aquo-complex (*i.e.*, [M(H₂O)_n]^{Z+}). The ability of the multivalent metallic ion to insert within the bulk TiO₂ lattice is expected to be

dependent of its size (see Table 4). We notice that if the ionic radius of Al^{3+} is indeed smaller, the values reported for Zn^{2+} and Li^+ remains close, slightly lower than the value of Mn^{2+} , and much lower than the value reported for K^+ , the latter being definitely too large to be inserted in the metal oxide structure. Based on these data, insertion of all the three metallic ions used in the present study can indeed be envisioned. However, desolvation of the metal-aquo complex costs a high energy (see Table 4) to remove the solvation shell which should be a very unfavorable parameter for insertion, especially in the case of Al^{3+} .

Table 4. Ionic radii (nm) and hydration energy ($\text{kJ}\cdot\text{mol}^{-1}$) of selected cations.¹⁴⁻¹⁵

Cation	r_{ion}	$-\Delta_{\text{hyd}}G$
Al^{3+}	0.053	4525
Li^+	0.069	475
Zn^{2+}	0.075	1955
Mn^{2+}	0.083	1760
K^+	0.138	295

The second hypothesis is to envision a proton-coupled electron storage mechanism despite the absence of significant amounts of free protons in solution at pH 3.0. In that case, the proton would be provided by the $[\text{M}(\text{H}_2\text{O})_n]^{z+}$ weak acid, according to Eq. 1. It is worth to note here that $[\text{Al}(\text{H}_2\text{O})_6]^{3+}$ complex is a much stronger weak acid than $[\text{Zn}(\text{H}_2\text{O})_6]^{2+}$ and $[\text{Mn}(\text{H}_2\text{O})_6]^{2+}$ complexes, which could explain the higher amount of charge stored through ion-insertion in the Al^{3+} -based electrolyte as compared to the Mn^{2+} - and Zn^{2+} -based electrolytes (Figure 2).



In order to elucidate the exact role of Al^{3+} -based electrolytes in the ion-insertion charge storage mechanism occurring at mesoporous TiO_2 films, we decided to make a quantitative comparative study of the electrochemical charging of GLAD- $\text{TiO}_2/\text{TiO}_2$ (1 $\mu\text{m}/15$ nm) electrodes soaked in two kind of aqueous electrolytes of pH 3.0. In the following section, we thus compared the results obtained in an Al^{3+} -based electrolyte with those obtained in an acetic acid-based electrolyte, which is a weak acid ($\text{pK}_a = 4.76$) of similar strength as compared to $[\text{Al}(\text{H}_2\text{O})_6]^{3+}$ ($\text{pK}_a = 4.97$).

2.2. Mechanistic investigation of ion insertion charge storage

CVs and CVAs recorded in presence of weak acids (*i.e.*, acetic acid or $[\text{Al}(\text{H}_2\text{O})_6]^{3+}$).

The CVs and CVAs (monitored at 780 nm) simultaneously recorded at GLAD-TiO₂/TiO₂ (1 μm /15 nm) electrodes soaked in aqueous solutions with increasing amount of either acetic acid or $[\text{Al}(\text{H}_2\text{O})_6]^{3+}$ are reported in Figure 3 and 4. The range of concentration investigated was 0 to 250 mM for both weak acids, and the pH was systematically adjusted to a value of 3.0 (the value spontaneously obtained upon dissolution of 250 mM of AlCl₃ in milli-Q water). The upper limit of the concentration range was fixed by the AlCl₃ salt as dissolution of higher amount of AlCl₃ resulted into more acidic solutions and thus in a higher competitive proton insertion arising from free protons. It is worth to note here that both electrolyte solutions are not buffered at pH 3.

Once the applied potential lies within the potential window corresponding to the fully conductive state of TiO₂, shapes and magnitudes of both CVs and CVAs exhibit strong differences as a function of the weak acid concentrations (Figures 3 and 4). The onset potential at which both current and absorbance start to increase at pH 3.0 (-0.38 V is fully consistent with the reported Nernstian pH dependence of the TiO₂ conduction band edge.¹⁸⁻¹⁹

In this potential window where TiO₂ is conductive, the strong increase in current is linked to the growth of a well-defined reversible wave on top of the capacitive current. It is worth to note here that the CVs and CVAs recorded in presence of identical concentrations of acetic acid or $[\text{Al}(\text{H}_2\text{O})_6]^{3+}$ show great similarities. These similarities concern not only the quantity of charge stored during a scan (being directly linked to the variation in absorbance) but also the mechanism of the charging/discharging process on account of the identical shapes observed on the CVs in both electrolytes. The results obtained here are moreover strongly reminiscent of those presented in chapter 3 and attributed to the reversible Ti^{IV}O₂/Ti^{III}OOH redox couple.

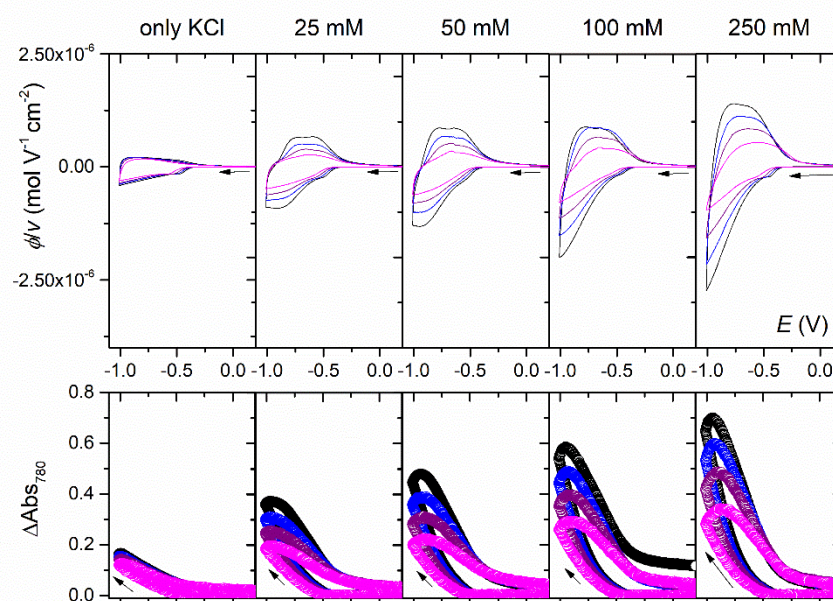


Figure 3. (Top) CVs recorded at GLAD-TiO₂/TiO₂ (1 μm/15 nm) electrodes in pH 3 aqueous solution containing 0.3 M KCl complemented with increasing concentration of **acetic acid** (reported on top of the graphs). See legend of Figure 4 for details.

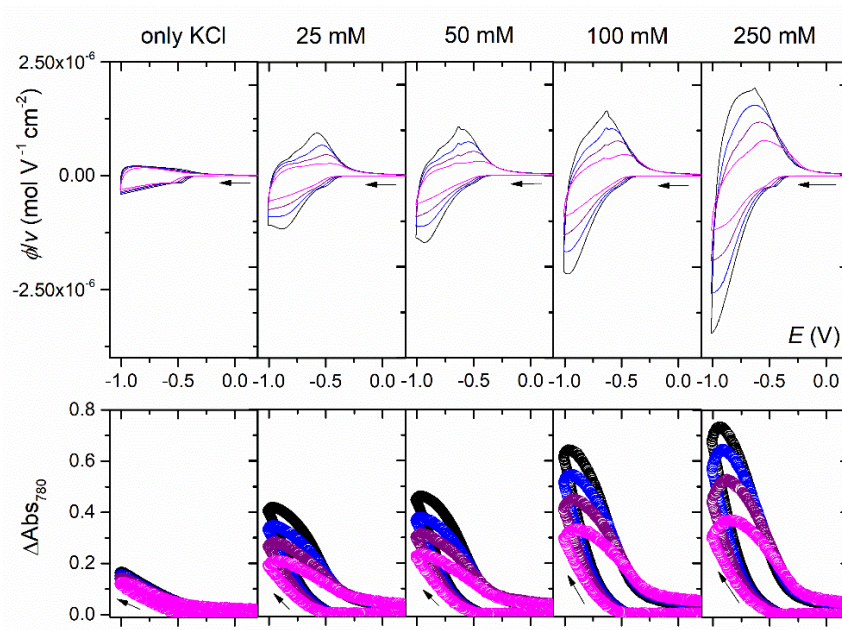


Figure 4. (Top) CVs recorded at GLAD-TiO₂/TiO₂ (1 μm/15 nm) electrodes in aqueous solutions containing 0.3 M KCl and increasing concentration of [Al(H₂O)₆]³⁺ (reported on top of the graphs) up to 100 mM or without KCl and 250 mM [Al(H₂O)₆]³⁺ to maintain similar ionic strength (pH 3). Currents are converted to electron flux density normalized to the scan rate. The ordinate $\phi/v = i/FSv$ is in mol·V⁻¹cm⁻². Scan rates: 0.05 V·s⁻¹ (black), 0.1 V·s⁻¹ (blue), 0.2 V·s⁻¹ (purple) and 0.5 V·s⁻¹ (magenta). (Bottom) corresponding CVAs monitored at 780 nm during each CV performed at different scan rates (same color code). The ordinate is in absorbance unit. The abscissa for both CVs and CVAs is the potential (V) vs. Ag/AgCl (3 M KCl). $T = 25^\circ\text{C}$.

During the charging process (forward scan), the reductive cathodic wave seems to be associated with the faradaic charging process leading to the reduction of Ti^{IV} ions within the TiO_2 lattice coupled with cation uptake for local charge compensation as demonstrated by protonation of Ti^{IV} ions in chapter 3. During the following discharging process (reverse scan), a well-defined re-oxidative peak is observed in the presence of $[\text{Al}(\text{H}_2\text{O})_6]^{3+}$, allowing to determine a formal potential of -0.82 V at $0.1 \text{ V}\cdot\text{s}^{-1}$ in presence of 0.1 M $[\text{Al}(\text{H}_2\text{O})_6]^{3+}$. In the case of acetic acid, the presence of two overlapping re-oxidative peaks attests a more complex discharging mechanism. By taking into account the second re-oxidation peak positioned at -0.62 V , a formal potential of -0.82 V is also calculated at $0.1 \text{ V}\cdot\text{s}^{-1}$ in presence of 0.1 M of acetic acid. Attribution of the faradaic process occurring here to the $\text{Ti}^{\text{IV}}\text{O}_2/\text{Ti}^{\text{III}}\text{OOH}$ redox couple is further confirmed by the formal potential value (E^0). This value is expected to shift by -60 mV per unit of pH increase, and the value obtained at pH 3.0 (*i.e.*, -0.82 V) is quite consistent with the values obtained previously at pH 7.0 and 1.85 (see Table 5).

Table 5. Main features of ion-insertion charge storage extracted from CVs and CVAs reported in chapter 3 and this chapter (Figure 3 and 4).

pH	1.85	7	3	3
Electrolyte composition	HCl + KCl	Hepes buffer + KCl	acid acid + KCl	$[\text{Al}(\text{H}_2\text{O})_6]^{3+}$
Electrode used	GLAD-TiO ₂	GLAD-TiO ₂	GLAD-TiO ₂ /TiO ₂	GLAD-TiO ₂ /TiO ₂
$[\text{H}_3\text{O}^+]$ (mM)	14	~0	~1	~1
$[\text{AH}]$ (mM)	-	77	98	98
E_{onset} (V) ^a	-0.30	-0.60	-0.38	-0.38
E^0 (V) ^b	-0.68	-1.06	-0.82	-0.82
$\Delta A_{780}^{\text{max}*}$	0.51	0.34	0.5	0.53
ϵ_{780} ($\text{M}^{-1} \text{ cm}^{-1}$)	1200	800	1000	1000
ref.	Chapter 3	Chapter 3	This work	This work

^a Potential characterizing the onset of absorbance at 780 nm.

^b Formal potential obtained from the average of cathodic and anodic peak potentials at the slowest scan rate.

* $\nu = 0.1 \text{ V}\cdot\text{s}^{-1}$.

Kinetic analysis of the ion insertion charge storage mechanism.

In this section, we used the same methodology as the one presented in chapter 3 to perform a quantitative analysis of the ion-insertion charging process based on the cyclic voltammetric data.

The electron flux density of the reversible faradaic wave is obviously not proportional to the scan rate, as evidenced in Figures 3 and 4. CVs recorded at different proton donor concentrations were thus systematically corrected from the electrochemical double-layer capacitance contribution by subtracting CVs recorded in 0.3 M KCl at the same pH and scan rate. Once corrected and normalized to $v^{1/2}$, the resulting CVs gathered in Figure 5 show good overlap, especially in terms of the magnitudes of cathodic peaks. This indicates a charging/discharging process limited by a diffusion-controlled mass transport, as previously observed for the proton-coupled electron storage mechanism described in chapter 3.

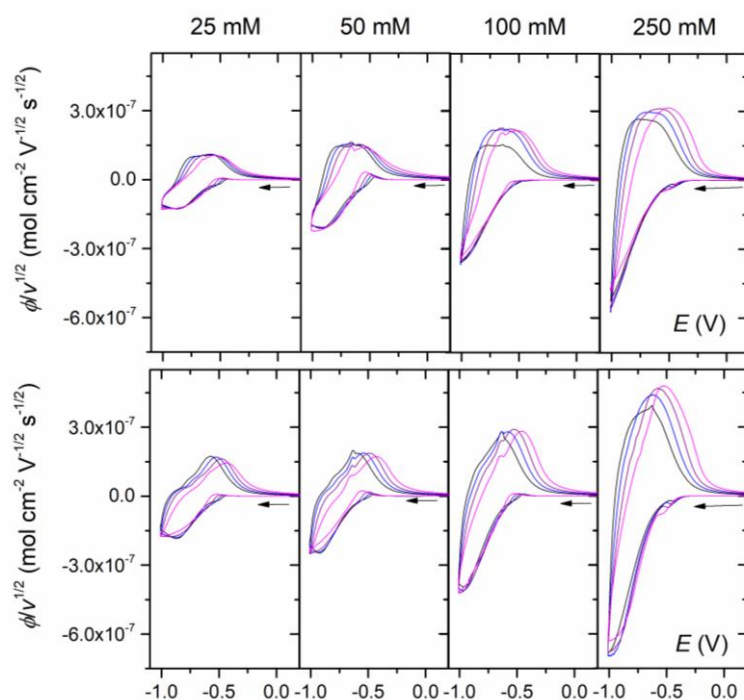


Figure 5. (Top) CVs previously presented in different concentration of **acetic acid** solution (pH 3) with correction to remove the capacitive contribution to the total current (*i.e.*, by subtracting the CVs recorded in 0.3 M KCl). (Bottom) CVs previously presented in different concentration of **[Al(H₂O)₆]³⁺** (pH 3) with correction to remove the capacitive contribution to the total current (*i.e.*, by subtracting the CVs recorded in 0.3 M KCl). Currents were all converted to electron flux density normalized to the square root of scan rate. Scan rates: 0.05 V·s⁻¹ (black), 0.1 V·s⁻¹ (blue), 0.2 V·s⁻¹ (purple) and 0.5 V·s⁻¹ (magenta). The abscissa for both the CVs and CVAs are potential (V) with respect to the Ag/AgCl (3 M KCl) reference electrode. $T = 25^{\circ}\text{C}$.

The intensity of the faradaic cathodic wave normalized to $v^{1/2}$ was plotted as a function of the weak acid concentration (Figure 6). At low weak acid concentration, *i.e.* below 100 mM, a linear dependence is observed, indicating that the reversible faradaic process is rate-limited by the solution diffusion of the weak acid in both electrolytes. At higher weak acid concentrations, the experimental data deviates from linearity, which indicates that another diffusion process becomes progressively rate-limiting. This behavior is very similar to that reported in chapter 3 for mesoporous TiO₂ electrodes soaked in a Hepes buffer solution. A progressive transition from a rate-limitation by mass transport of the proton donor in solution to a rate-limitation by the solid-state diffusion of protons within the TiO₂ lattice was indeed observed upon increasing the proton donor concentration.

At low weak acid concentration, it is thus possible to estimate the diffusion coefficient of the weak acids in solution. If we consider that the reversible cation-coupled electron transfer reaction at the TiO₂/electrolyte interface is fast (*i.e.*, a Nernstian interfacial reaction), the following Randles–Sevcik equation can be applied for both reactions:

$$\frac{\phi_{f,p}}{v^{1/2}} = \frac{i_{f,p}}{FSv^{1/2}} = 0.4463 \sqrt{\frac{F}{RT}} \sqrt{D_{AH,out}} [AH] \quad (2)$$

where $\phi_{f,p}$ and $i_{f,p}$ are the faradaic peak flux density ($C \cdot mol^{-1} \cdot cm^{-2}$) and peak current (A), v is the scan rate ($V \cdot s^{-1}$), S is the delimited geometric electrode area (or projected electrode area, cm^2); $D_{AH,out}$ ($cm^2 \cdot s^{-1}$) and $[AH]$ ($mol \cdot cm^{-3}$) are the diffusion coefficient and concentrations of acetic acid or $[Al(H_2O)_6]^{3+}$ in the bulk aqueous solution. The geometric electrode area is utilized in this equation due to the fact that the diffusion layer thickness of the soluble proton donor is much larger than the 1 μm film thickness of GLAD-TiO₂ within the range of scan rates used in the present study.

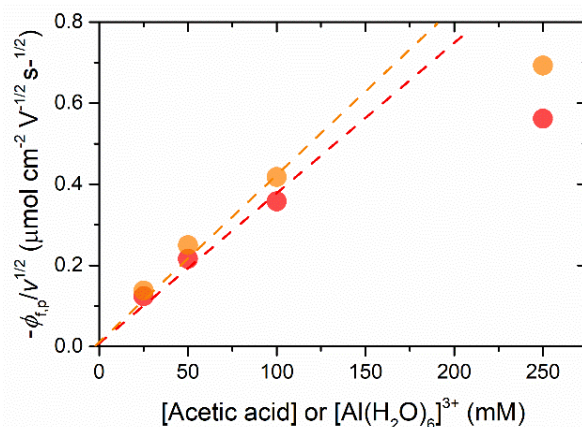


Figure 6. Cathodic peak electron flux density normalized to $v^{1/2}$ and plotted as a function of proton donor concentration: (red) acetic acid and (orange) $[\text{Al}(\text{H}_2\text{O})_6]^{3+}$ aqueous solution. Dashed lines correspond to the linear regression fits of equation 2 to the data determined at low proton donor concentration up to 100 mM.

From the linear regression fit of Eq. 2 to the linear part of experimental plots in Figure 6, it is possible to extract the diffusion coefficient $D_{AH,out}$ of either acetic acid or $[\text{Al}(\text{H}_2\text{O})_6]^{3+}$ in aqueous solution. Values of $3 \times 10^{-6} \text{ cm}^2 \cdot \text{s}^{-1}$ and $4 \times 10^{-6} \text{ cm}^2 \cdot \text{s}^{-1}$ were found for acetic acid and $[\text{Al}(\text{H}_2\text{O})_6]^{3+}$, respectively. While the value obtained for the Al^{3+} complex is very similar to the one reported in the literature (*i.e.*, $5.4 \times 10^{-6} \text{ cm}^2 \cdot \text{s}^{-1}$)²⁰, the one obtained for acetic acid is somewhat lower (*i.e.*, $1.1 \sim 1.3 \times 10^{-5} \text{ cm}^2 \cdot \text{s}^{-1}$)²⁰⁻²¹. It has however to be mentioned here that Eq. 2 is valid only at low concentrations of weak acids. According to the limited experimental data available at low weak acid concentrations, the experimental values determined here are subject to significant uncertainty. This analysis demonstrates that in both electrolytes, diffusion of the weak acid is rate-limiting at low concentrations. However, it does not allow to conclude in the case of Al^{3+} on the nature of the inserting cation.

A way to identify the nature of the inserted cation would be to determine the diffusion coefficient of the inserted cation within the bulk TiO_2 lattice. It could be achieved by increasing the weak acid concentration sufficiently in such a way to be no more controlled by the mass transport in solution but instead by the mass transport in the solid phase. Unfortunately, as discussed previously, it was not possible to increase more the AlCl_3 concentration because of pH considerations. It would have been interesting to compare the values obtained in the two electrolytes, which would have been additional evidence of proton insertion if similar values had been obtained.

Estimation of the charge storage capacity.

The total charge density Q (in $C \cdot cm^{-2}$) stored in the 1 μm thick GLAD-TiO₂ film can be easily determined either from the absorbance change monitored at 780 nm or from integration of current density using the following Eq. 3:

$$Q = F \frac{\Delta A_{780}}{1000 \varepsilon_{780}} = \int \frac{i}{S} dt \quad (3)$$

where ΔA_{780} and ε_{780} are the absorbance variation and extinction coefficient of stored electron at 780 nm, F the faradaic constant ($96500 C \cdot mol^{-1}$), i the applied current (in A), and S geometric surface area (in cm^2).

In this work, the charge storage capacity was estimated from either CVAs or galvanostatic experiments (see below). CVA has the advantage, compared to CV, of being free from the competitive faradaic contribution arising from the HER during the charging process, whereas galvanostatic experiments are commonly used in the battery research field.

From the total charge density Q , it is possible to calculate the total charge storage capacity (in $C \cdot g^{-1}$) of the electrode according to the following Eq. 4:

$$\frac{Q (C \cdot cm^{-2})}{d (g \cdot cm^{-3}) \times l (cm)} = Q (C \cdot g^{-1}) \quad (4)$$

with Q the charge density, d the film density (*i.e.*, $2.5 \cdot 10^{-3} g \cdot cm^{-3}$ for GLAD-TiO₂) and l the film thickness (*i.e.*, $10^{-4} cm$). The coulomb (C) can be also expressed by the product of current (A) and time (t), thus the charge storage capacity can be converted to $mA \cdot h \cdot g^{-1}$, which is the unit commonly used in the battery field.

It has to be mentioned here that the total charge storage capacity estimated by Eq. 4 has two contributions, one arising from the electrical double layer (*i.e.*, EDLCs, in absence of proton donor in solution) and the second one arising from the ion-insertion charge storage (*i.e.*, in the presence of a proton provider). In the present study, the charge stored by ion-insertion during the time-course of a CV recorded at $0.1 V \cdot s^{-1}$ in presence of 0.1 M of acetic acid or $[Al(H_2O)_6]^{3+}$ was estimated to be $34 mC \cdot cm^{-2}$ ($141 C \cdot g^{-1}$ or $39 mA \cdot h \cdot g^{-1}$) and $38 mC \cdot cm^{-2}$ ($150 C \cdot g^{-1}$ or $42 mA \cdot h \cdot g^{-1}$), respectively. These values are very close to each other, and slightly higher than the one obtained at the same scan rate in 0.1 M Hepes at pH 7 (*i.e.* $25 mC \cdot cm^{-2}$ or $101 C \cdot g^{-1}$ or $28 mA \cdot h \cdot g^{-1}$). Still, they remain far from the maximal value expected if one

assumes that the TiO₂ lattice can accommodate up to 50 % of Ti^{III} ions, which corresponds to a maximal ion-insertion charge storage capacity of 165 mA·h·g⁻¹. This could be due to the short time window explored during a cyclic voltammetric scan (reduction occurs within *ca.* 10 s at 0.1 V·s⁻¹), impeding to reach thermodynamic equilibrium and thus a high accumulation.

Analysis of the charge storage capacity by galvanostatic experiments.

In order to investigate charge storage on longer time scales than the one provided by cyclic voltammetry, and to get closer to battery operating conditions, we performed galvanostatic experiments to further analyze the charging/discharging process occurring at mesoporous TiO₂ films soaked in the acetic acid or Al³⁺-based electrolytes. These experiments were initially performed on the GLAD-TiO₂/TiO₂ electrodes used for the spectroelectrochemical experiments described above. However, even if these electrodes are more stable as compared to the GLAD-TiO₂ electrodes used in chapter 3, electrode failure was still observed under strong charge accumulation conditions. Accordingly, the ITO protection by a 15 nm thin film of bulk TiO₂ was not completely satisfactory. Therefore, GLAD-TiO₂/TiO₂ electrodes were also used for galvanostatic experiments, allowing us to optimize the charge storage capacity of the mesoporous TiO₂ film in the aqueous electrolytes.

Galvanostatic experiments were performed at GLAD-TiO₂/TiO₂ and GLAD-TiO₂/Ti electrodes in either 0.3 M KCl or 0.25 M acetic acid with 0.3 M KCl, or 0.25 M [Al(H₂O)₆]³⁺ at pH 3 (Figure 7). In these studies, the anodic cut off potential associated to full discharging was set to +0.24 V at pH 3, a potential at which TiO₂ is fully insulating. The cathodic cut-off potential was set to values ranging from -0.82 V, which corresponds to the formal Ti^{III}/Ti^{IV} potential determined by CVs at pH 3, to -1.12 V. The galvanostatic experiments were moreover performed at different current densities of 2, 1, 0.4, and 0.2 mA·cm⁻². These values can be expressed as charging rates (C) as commonly used in the battery field. The C-rate is a rate measurement when a battery is charged or discharged relatively to its maximum capacity. A C-rate of 1 C corresponds thus to the current value required to fully charge or discharge the electrode in one hour. By assuming a theoretically maximum proton insertion charge storage capacity of 165 mA·h·g⁻¹ (*i.e.*, 0.5 mole fraction of protonated Ti³⁺ site by analogy of the Li⁺ insertion, see chapter 3), the current range density of 2 to 0.2 mA·cm⁻² used here corresponds to C-rates values of 45 to 4.5 C. In the following section, the charge storage capacity (*i.e.*, state-

of-charge) was determined from the discharging process in such a way to avoid contribution from the hydrogen evolution reaction (HER) occurring during the charging process (see below).

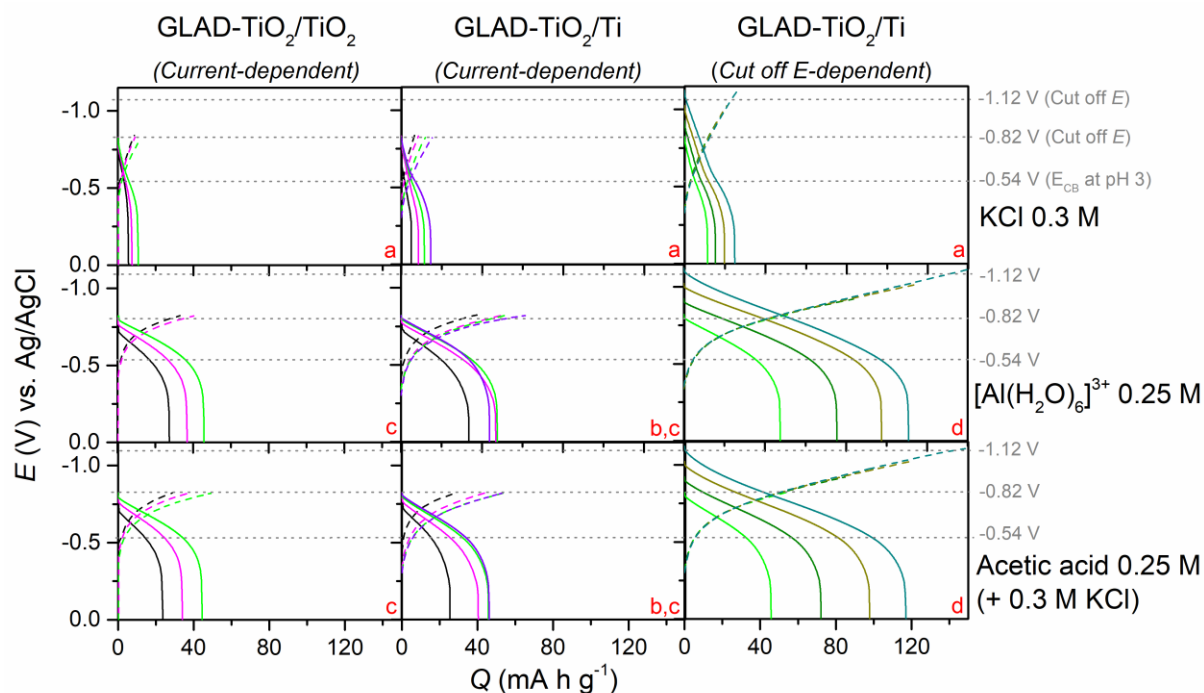


Figure 7. Galvanostatic (dashed line) charging and (solid line) discharging curves recorded at (left column) GLAD-TiO₂/TiO₂, (middle and right column) GLAD-TiO₂/Ti electrodes soaked in (top line) 0.3 M KCl, (middle line) 0.25 M [Al(H₂O)₆]³⁺, and (bottom line) 0.25 M acetic acid with 0.3 M KCl aqueous solution at pH 3. (Left and middle column) Cut off potential is fixed at **-0.82 V** and the applied current density is (black) 2 mA·cm⁻², (magenta) 1 mA·cm⁻², (green) 0.4 mA·cm⁻², and (violet) 0.2 mA·cm⁻². (Right column) The applied current density is fixed at **0.4 mA·cm⁻²** and the cathodic cut off potential is (green) -0.82 V, (olive) -0.92 V, (dark yellow) -1.02 V, and (dark cyan) -1.12 V. *T* = 25 °C. Grey dotted line indicates the position of the cut off potential values (-1.12 V and -0.82 V) and conduction band potential of TiO₂ at pH 3 (-0.54 V). *Q* indicates the charge storage capacity in mA·h·g⁻¹. Small alphabet letter relies to discussion in the main text.

Firstly, in the 0.3 M KCl electrolyte, the charge storage capacity remains low (< 25 mA·h·g⁻¹) whatever the experimental conditions. This is fully consistent with the absence of proton donor, restricting thus the charge storage to the establishment of the electrical double layer at the TiO₂/electrolyte interface. Still, the charge storage capacity (*Q*) is almost independent of the applied current density, and it increases slightly as the cathodic cut-off potential decreases (Figure 7, a), which is as expected. The data obtained at GLAD-TiO₂/TiO₂

and GLAD-TiO₂/Ti electrodes are very similar, which further confirms that the morphology of the mesoporous film is quite independent of the underlying layer of metallic Ti or bulk TiO₂.

In the presence of weak acids (*i.e.*, either acetic acid or [Al(H₂O)₆]³⁺), the charge storage capacity is significantly increased, which is attributed to the contribution of the faradaic redox process occurring at the bulk Ti^{IV}/Ti^{III} redox couple coupled to ion-insertion. Upon decreasing the current density from 2 to 0.2 mA·cm⁻² (*i.e.*, from 45 to 4.5 C) rates at a fixed cathodic cut-off potential of -0.82 V, the total charge storage capacity is increased up to a constant value of *ca.* 45 mA·h·g⁻¹ in both electrolytes below 0.4 mA·cm⁻² (Figure 7, b and Figure 8). This indicates that charge storage occurs under thermodynamic equilibrium so that proton insertion is no longer rate-limited by diffusion.

Under these conditions (current density fixed at 0.4 mA·cm⁻²), we then investigated the effect of lowering the cathodic cut-off potential down to -1.12 V. This could only be achieved with the GLAD-TiO₂/Ti electrode (Figures 7 and 8). We first notice that the time required to reach the cathodic potential value (associated to the charge passed through the electrode during the charging process) increases more rapidly than the time required to discharge the electrode (Figure 7, d). This indicates that a competitive faradaic reaction occurs at low potential, consuming electrons during the charging process. It is attributed to HER that was confirmed through the formation of small bubbles at the TiO₂ electrode under strong accumulation conditions. Consequently, the coulombic efficiency (*CE*, %) of charge storage at the mesoporous TiO₂ electrodes decreases as the cathodic cut-off potential value is downshifted. The *CE* is indeed defined as the ratio of the number of charges passed during the charging process ($Q_{charging}$) compared to the number of charges extracted from the materials during discharging process ($Q_{discharging}$) according to the following Eq. 5:

$$\text{Coulombic Efficiency (CE, \%)} = \frac{Q_{discharging}}{Q_{charging}} \times 100 \quad (5)$$

In order to get better insights into this value, which is a main parameter to envision battery applications, the total charge storage capacities as well as the corresponding coulombic efficiencies extracted from the experiments shown in Figure 7 are reported in Figure 8 at different current densities or cathodic cut-off potentials. Satisfactory *CE* values (> 90 %) are obtained under moderate accumulation conditions, *i.e.* $j > 0.4 \text{ mA cm}^{-2}$ and $E_{\text{cathodic cut-off}} > -0.92 \text{ V}$. As the current density is further lowered or the cathodic potential further downshifted, *CE*

significantly decreases which means that the competitive hydrogen evolution reaction is most likely a slow process as compared to ion-insertion.

Despite competitive HER, downshifting the cathodic cut-off potential value to -1.12 V allowed to significantly increase the charge storage capacity (Figures 7 and 8). Maximal values of 116 and 111 mA·h·g⁻¹ were obtained in acetic acid and Al³⁺-based electrolytes, respectively. By taking into account that *ca.* 25 mA·h·g⁻¹ are associated to the electrical double layer, this value indicates that *ca.* 27 % of the Ti^{IV} ions can be reversibly reduced to Ti^{III} in both electrolytes under our experimental conditions. It is again worth to note that the galvanostatic experiments achieved either in the acetic acid or Al³⁺-based electrolyte at pH 3.0 are very similar. It concerns not only the charge storage capacity and its time dependence, but also the coulombic efficiency.

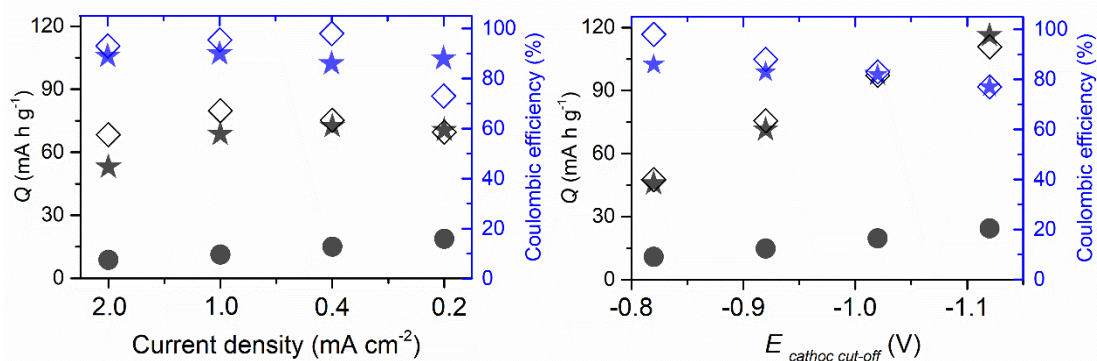
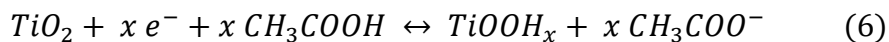


Figure 8. (Black) charges storage capacities and (blue) coulombic efficiencies obtained from galvanostatic experiments performed in (dot) 0.3 M KCl, (diamond) 0.25 M AlCl₃, and (star) 0.25 M acetic acid with 0.3 M KCl aqueous solution at pH 3.0. (Left) cut-off potential was fixed to **-0.92 V** and current densities were decreased from 2.0 to 0.2 mA·cm⁻². (Right) current density was fixed to **0.4 mA·cm⁻²** and cathodic cut off potential was progressively downshifted from -0.82 to -1.12 V. Potentials (V) are given with respect to the Ag/AgCl (3 M KCl) reference electrode. $T = 25^{\circ}\text{C}$.

2.3. Conclusion

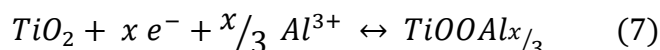
We demonstrated in the previous sections that mesoporous TiO₂ films exhibit the same charging properties in presence of either acetic acid or Al³⁺, whatever the electrochemical methodology used and the associated time window. This means that the ion-insertion mechanisms occurring in both electrolytes share common kinetic as well as thermodynamic features.

In the presence of acetic acid, it is rather clear that Ti^{IV} reduction is associated to proton uptake, as already reported for the Hepes weak acid, and that the charging/discharging equilibrium is the following:



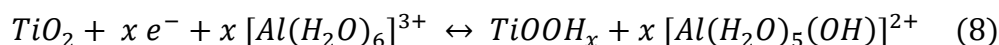
The thermodynamics of the process is governed by the $Ti^{IV}O_2/Ti^{III}OOH$ standard potential, while the kinetics is governed by mass transport of diffusion of either the weak acid in solution (at low acetic acid concentrations) or the inserted proton in the solid phase (at high acetic acid concentrations). Accordingly, the heterogeneous proton-coupled electron transfer reaction at the TiO_2 /electrolyte interface is never rate-limiting.

In the case of Al^{3+} , two different equilibria can be envisioned, depending on the insertion cation. If one assumes that Al^{3+} is capable of insertion within the metal oxide structure, then charge storage should occur through Eq. 7:



In such a case, the charge storage process would be centered on the $Ti^{IV}O_2/Ti^{III}OOAl_{0.33}$ standard potential, and consequently it would be surprising if it is located at the same value than the $Ti^{IV}O_2/Ti^{III}OOH$ couple. It would also be curious that the cation-coupled electron transfer at the TiO_2 /electrolyte interface remains fast as it would require desolvation of the $[Al(H_2O)_6]^{3+}$ complex. It would thus be rather surprising that such a charge storage mechanism will lead to similar results as the one reported in acetic acid.

We are thus quite convinced that the role of Al^{3+} is to provide protons at the TiO_2 /electrolyte interface and that all of the results we obtained thus converge toward the following charge storage mechanism in the presence of Al^{3+} in solution:



That the complex $[Al(H_2O)_6]^{3+}$ can act as a proton donor in the same way as an organic weak acid suggests that it may be a general features of multivalent metal aquo complexes, occurring thus also in presence of $[Zn(H_2O)_6]^{2+}$ and $[Mn(H_2O)_6]^{2+}$. In the case of TiO_2 , we noticed in section 2.1 that the efficiency of the process was much lower in the presence of such weak acids. We assume that this might be due to the much higher pK_a of these complexes as compared to $[Al(H_2O)_6]^{3+}$. The increase of pH on the efficiency of the process will be investigated in the following section 4.1.

The demonstration that certain inorganic salts allow rapid and massive insertion of protons in aqueous solutions sheds new light on many results published in the literature where the charging or discharging process is putatively attributed to the insertion of multivalent metal cations. This is for sure the case for a range of works in which nanostructured TiO₂ electrodes has been investigated in the presence of Al³⁺-based electrolytes.^{2-3,8} But it is also the case for other studies assuming Zn²⁺ insertion in MnO₂-based or V₂O₅-based cathode electrodes under slightly acidic aqueous conditions.²³⁻²⁴ In all of these studies, the weak acid property of the multivalent metallic aqua complex should be considered to allow for a complete picture of the charging / discharging mechanism.

3. Optimization of charge storage in acetic acid

Based on the nice results obtained at GLAD-TiO₂/Ti electrodes soaked in a 250 mM acetic acid aqueous electrolyte of pH 3, we decided to work further on optimizing the electrolyte composition in order to increase both the charge storage capacity and the coulombic efficiency. We thus decided to work in a buffered solution, in order to avoid pH-gradient at the TiO₂ interface during the charging/discharging process. All galvanostatic experiments were thus performed in an acetic acid/acetate aqueous solution at pH 5. The indicated buffered electrolyte concentration at pH 5 is thus the sum of the weak acid (*i.e.*, acetic acid, pK_a = 4.76) and conjugate base (*i.e.*, acetate) concentrations.

0.25 M acetic acid/acetate buffer at pH 5.

The cathodic cut-off potential in galvanostatic experiments (*i.e.*, potential window in CVs) was adjusted taking into account the Nernstian pH dependence of -60 mV/pH unit of both E_{CB} of TiO₂ and E^0_{TiOOH/TiO_2} .¹⁸⁻¹⁹ Thus, in order to make equivalent thermodynamic conditions for charge storage, the cathodic cut-off potential was downshifted by 120 mV between pH 3 and 5 (*i.e.*, the cathodic cut-off potential range studied at pH 3 was from -0.82 to -1.12 V, whereas it was from -0.94 to -1.24 V at pH 5). The results of the galvanostatic experiments carried out in 0.25 M acetic acid/acetate buffer in presence of 0.3 M KCl are given in Figure 9. Unfortunately, the cathodic cut off potential could not be decreased at more negative values than -1.14 V in 0.25 M acetic acid/acetate buffer with 0.3 M KCl at pH 5 due to the irreversible loss of electrode (data not shown). This might be due to some structural changes at the TiO₂ electrode due to massive HER under strong accumulation conditions.

In order to check if the cathodic cut-off potential was well adjusted to the pH shift, the charge storage capacities obtained at pH 3 and 5 in the inert 0.3 M KCl electrolyte were compared. Same charge storage capacities are indeed obtained at pH 3 (11 and 15 mA·g⁻¹ at -0.82 and -0.92 V cathodic cut off potentials) and pH 5 (12 and 14 mA·g⁻¹ at -0.94 V and -1.04 V cathodic cut off potentials) upon 120 mV downshift of the cathodic cut-off potential range (equivalent cathodic cut off potential) investigated at a current density of 0.4 mA·cm⁻².

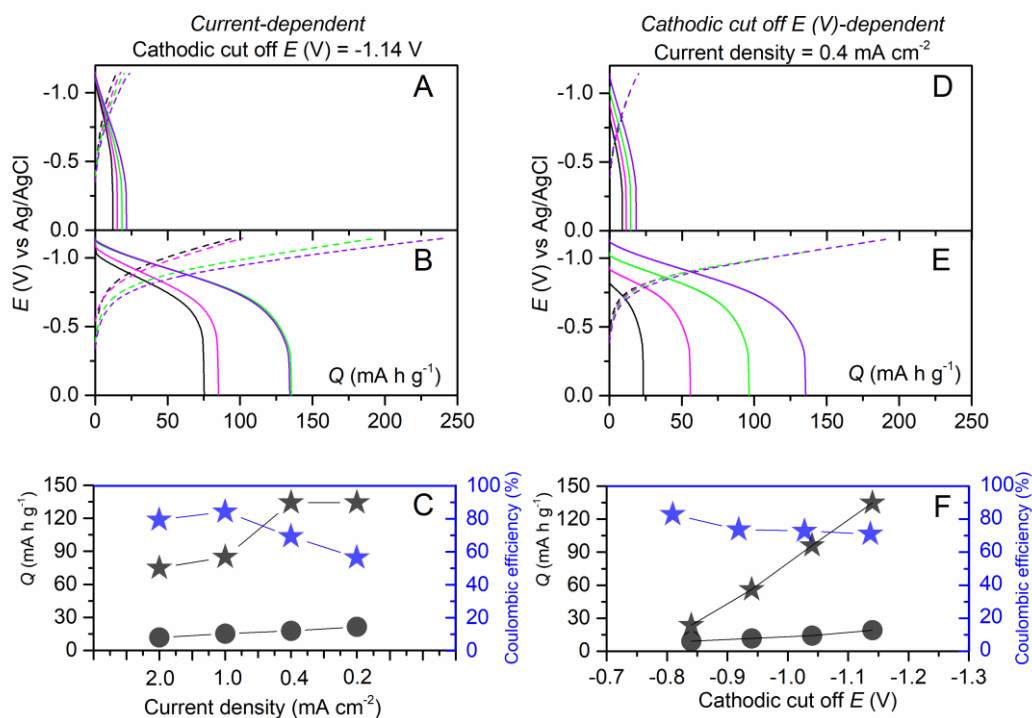


Figure 9. Galvanostatic (dashed line) charging and (solid line) discharging curves at GLAD-TiO₂/Ti in (A, D) 0.3 M KCl and (B, E) 0.25 M acetic acid/acetate buffer with 0.3 M KCl at pH 5. (A, B) Charge storage capacity (mA·g⁻¹) as a function of applied current density value of (black) 2 mA·cm⁻², (magenta) 1 mA·cm⁻², (green) 0.4 mA·cm⁻², and (violet) 0.2 mA·cm⁻² with cathodic cut-off potential of **-1.14 V**. (D, E) Charge storage capacity (mA·g⁻¹) as a function of cut-off potential value of (black) -0.84 V, (magenta) -0.94 V, (green) -1.04 V, and (violet) -1.14 V with applied current density of **0.4 mA·cm⁻²**. (C, F) (black color, left label) Charge storage capacity value and (blue color, right label) corresponding coulombic efficiency of (A and B) for (C), (D and E) for (F). Round symbol is under 0.3 M KCl at pH 5.0 and star symbol is under in 0.25 M acetic acid/acetate buffer aqueous buffer solution with 0.3 M KCl at pH 5.0.

In the presence of acetic acid and by using a fixed cathodic cut-off potential of -1.14 V, the charge storage capacity was increased up to a constant value of 135 mA·h·g⁻¹ as the current density was progressively decreased from 2 to 0.2 mA·cm⁻². Accordingly, charging occurs under thermodynamic equilibrium conditions at current densities below 0.4 mA·cm⁻². In the

same time, the coulombic efficiency is decreased from 85 to 58 % due to the increasing competitive HER (*i.e.*, proton reduction) that occurs during the charging process (Figure 9B and 9C).

With the current density fixed at $0.4 \text{ mA}\cdot\text{cm}^{-2}$, the charge storage capacity is increased up to $135 \text{ mA}\cdot\text{h}\cdot\text{g}^{-1}$ as the cut-off potential is progressively decreased from -0.84 to -1.14 V , whereas coulombic efficiency is gradually decreased down to 70 % (Figure 9E and 9F). The maximal charge storage capacity as well as the corresponding coulombic efficiency obtained in 0.25 M acetic acid/acetate at pH 3 are reported in Table 6.

Table 6. The maximal charge storage capacity features comparison between pH 3 and 5. Electrolyte composition is 0.25 M acetic acid/acetate aqueous solution with 0.3 M KCl.

pH	3	3	5
$[\text{H}_3\text{O}^+]$ (mM)	~ 1	~ 1	~ 0.01
$[\text{AH}]$ (mM)	245	245	91
applied current density ($\text{mA}\cdot\text{cm}^{-2}$)	0.4	0.4	0.4
Cathodic cut off E (V)	-1.02	-1.12	-1.14
^a Q_{EDL} ($\text{mA}\cdot\text{h}\cdot\text{g}^{-1}$)	20	25	19
^b Q_{H^+} ($\text{mA}\cdot\text{h}\cdot\text{g}^{-1}$)	78	91	116
CE (%)	83	75	70

^a Q_{EDL} indicates the charge storage capacity arising from the electrical double layer determined in 0.3 M KCl.

^b Q_{H^+} indicates the optimized charge storage capacity by proton coupled faradaic electron accumulation.

It is worth to note here that, while the cathodic cut-off potential values used are close, the results obtained at pH 3 and 5 are very similar. This is unexpected as a cut off potential of -1.14 V at pH 5 should be rather equivalent to a cut-off potential of -1.02 V at pH 3. This is not what we observed and the charging capacity obtained at pH 5 (*i.e.*, $116 \text{ mA}\cdot\text{h}\cdot\text{g}^{-1}$) is much higher than the one obtained at pH 3 (*i.e.*, $78 \text{ mA}\cdot\text{h}\cdot\text{g}^{-1}$) at an equivalent potential (*i.e.*, -1.14 V for pH 5 and -1.02 V at pH 3). This could be due to some uncertainty in the exact pH value near the electrode in the unbuffered pH 3 electrolyte. Indeed, charging is associated to proton uptake and it could thus result into a local pH increase near the electrode. Such an effect should be minimized by using the buffered electrolyte of pH 5. However, the coulombic efficiency remains quite low at pH 5.

Interestingly, there have been some studies evidencing that increasing the electrolyte concentration might help to increase the potential window by solving the problem of both HER and OER (oxygen evolution reaction) occurring in aqueous electrolytes.²⁵⁻²⁷ In a study on an aqueous potassium-ion battery, an increase of the potassium acetate concentration up to 30 molal ($\text{mol}\cdot\text{kg}^{-1}$) was shown to decrease the activity of water and as a result to reduce the competitive HER reaction at the negative TiO_2 -based electrode.²⁶

In the present study, there are two ways to increase the electrolyte concentration, by increasing either the concentration of the buffer or the concentration of the KCl supporting electrolyte. Thus, in the following study, we investigated the effect of increasing the acetic acid/acetate buffer concentration up to 8 M on the charge storage capacity and on the coulombic efficiency of the mesoporous electrodes. We systematically compared with the result obtained in 0.25 M acetic acid/acetate buffer solution (and 0.3 M KCl) or 0.25 M acetic acid/acetate buffer (and 2 M of KCl).

8 M of acetic acid/acetate buffer at pH 5.

Firstly, in order to improve the charge storage capacity, we performed galvanostatic experiments at a fixed current density of $0.2 \text{ mA}\cdot\text{cm}^{-2}$ by using a cathodic cut-off potential range of -0.74 to -1.24 V (Figure 10).

These results show a perfect overlay of the charge storage capacity obtained in the range -0.94 to -1.14 V in the different electrolyte solutions of pH 5 investigated here. This demonstrates that increasing the KCl supporting electrolyte concentration from 0.3 to 2 M in a 0.25 M acetic acid/acetate buffer has no significant influence on the charge storage capacity. In addition, increasing the buffer concentration has no effect on the charging capacity in this potential range. This further confirms that, at the current density used, charging is not rate-limited by the mass transport of weak acid in solution, as already previously mentioned.

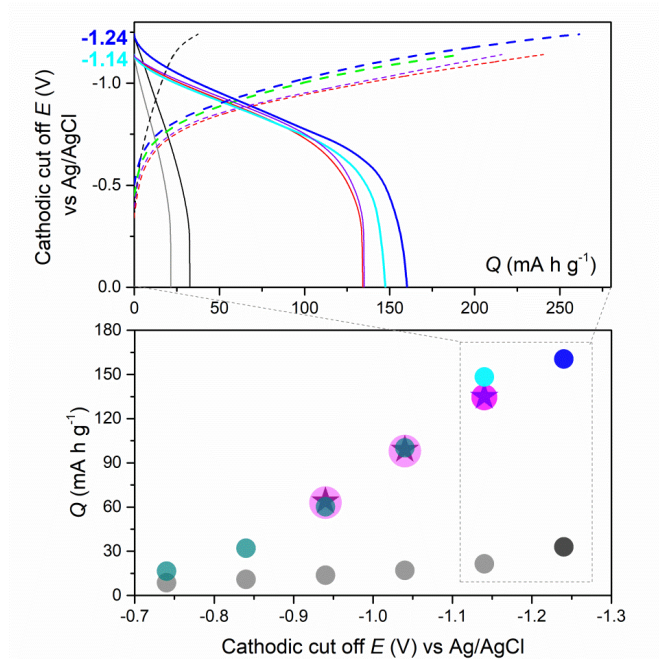


Figure 10. (top) Galvanostatic curves obtained during (dashed line) charging and (solid line) discharging and (bottom) charge storage capacities ($\text{mA}\cdot\text{g}^{-1}$) obtained at a GLAD- TiO_2/Ti as a function of cut off potential from -0.74 V to -1.24 V with applied current density of $0.2 \text{ mA}\cdot\text{cm}^{-2}$. The aqueous electrolyte solution is adjusted to pH 5 and contains (grey and black) 0.3 M KCl , (light pink and magenta) 0.25 M acetic acid/acetate buffer with 0.3 M KCl , (violet and purple, star symbol) in 0.25 M acetic acid/acetate buffer with 2 M KCl , (dark cyan, cyan, and blue) 8 M acetic acid/acetate buffer.

In 8 M acetic acid/acetate buffer it was possible to further decrease the cathodic cut-off potential down to -1.24 V without electrode failure. Under these conditions, a maximal total charge storage capacity of $161 \text{ mA}\cdot\text{h}\cdot\text{g}^{-1}$ was obtained, which is very close to the theoretical value (*i.e.* $165 \text{ mA}\cdot\text{h}\cdot\text{g}^{-1}$) calculated assuming that protons can insert into TiO_2 up to a 0.5 molar fraction (by analogy with Li^+ in anatase TiO_2). However, as already mentioned, the total charge storage capacity (Q) deduced from galvanostatic experiments corresponds not only to the ion insertion faradaic charge storage, but also to the electrical double layer surface charge storage. The charge storage capacity associated to proton insertion was thus estimated to be $128 \text{ mA}\cdot\text{h}\cdot\text{g}^{-1}$ by subtracting the charge stored in the inert KCl electrolyte under the same galvanostatic conditions (*i.e.*, $33 \text{ mA}\cdot\text{h}\cdot\text{g}^{-1}$). This implies that 20% of total stored charge results from EDLC (*i.e.*, $33 \text{ mA}\cdot\text{h}\cdot\text{g}^{-1}$) of GLAD- TiO_2/Ti film, while the remaining 80% (*i.e.*, $128 \text{ mA}\cdot\text{h}\cdot\text{g}^{-1}$) arises from the proton-coupled electron transfer reaction within the GLAD- TiO_2/Ti film. The proton insertion charge storage capacity of $128 \text{ mA}\cdot\text{h}\cdot\text{g}^{-1}$ in 8 M acid/acetate buffer

corresponds thus to the reductive protonation of $\sim 40\%$ of the total titanium ions in the lattice and is thus equivalent to x value of 0.4. According to the literature, it is possible to reach higher charge storage capacity with TiO_2 electrodes soaked in aqueous solutions,³ however, we were not able to further improve it in the present work because of the competitive HER. Further work is required to find the proper electrolyte and electrode composition in order to avoid HER and maximize proton-coupled electron storage.

In a second study, we focus on improving the coulombic efficiency of charge storage in 8 M acetic acid/acetate buffer of pH 5.0. We selected experimental conditions allowing to reach a charge storage capacity higher than $100 \text{ mA}\cdot\text{h}\cdot\text{g}^{-1}$. The experiments conducted and the results obtained are summarized in Table 7.

Table 7. Charge storage capacity ($\text{mA}\cdot\text{h}\cdot\text{g}^{-1}$) and coulombic efficiency (%) obtained from galvanostatic charging/discharging experiments conducted at GLAD- TiO_2/Ti electrodes soaked in a 8 M acetic acid/acetate buffer solution (pH 5.0) for different cathodic cut-off potential (V vs. Ag/AgCl) and applied current density ($\text{mA}\cdot\text{cm}^{-2}$).

Current density ($\text{mA}\cdot\text{cm}^{-2}$)	Cathodic cut off E (V)	Q ($\text{mA}\cdot\text{h}\cdot\text{g}^{-1}$)	CE (%)
0.2	-1.04	101	84
0.2	-1.14	147	72
0.2	-1.24	161	62
0.4	-1.14	128	82
1	-1.24	148	85

Under conditions allowing to reach the maximal charge storage capacity of $161 \text{ mA}\cdot\text{h}\cdot\text{g}^{-1}$ (*i.e.*, with an applied current density of $0.2 \text{ mA}\cdot\text{cm}^{-2}$ and a cathodic cut-off potential of -1.24 V), the coulombic efficiency is rather low (*i.e.*, 62%) due to competitive HER occurring during the charging process. We previously evidenced that CE can be increased upon increasing the current density. We confirm this tendency, and CE can be increased up to 85% upon increasing the applied current to $1 \text{ mA}\cdot\text{cm}^{-2}$. It is however at the expense of the charge storage capacity that is simultaneously decreased to $148 \text{ mA}\cdot\text{h}\cdot\text{g}^{-1}$. This last value remains however competitive, especially if one considers the very high rate used in the galvanostatic experiment (*i.e.*, 5 C).

Finally, increasing the buffer concentrations seems to be a very promising strategy to favor fast proton-coupled electron charge storage and limit the competitive HER. The 8 M concentration used in the present study lies still far from water-in-salt electrolyte conditions. Accordingly, it would be very interesting to investigate the effect of higher acetic acid/acetate buffer concentrations on the capacity and coulombic efficiency of charge storage at mesoporous TiO₂ electrodes under mild aqueous conditions.

4. Combined effect of the pH and the weak acid pK_a on the efficiency of charge storage in aqueous electrolytes

In this section, we investigated the efficiency of charge storage at mesoporous TiO₂ electrodes in aqueous solution stabilized at different pH values (from 3 to 12.7) and containing various weak acids, covering a wide range of pK_a values. Transparent GLAD-TiO₂/TiO₂ electrodes were used in this work, allowing to perform preliminary studies by spectroelectrochemistry. Especially, chronoabsorptometry (CAs) was used for easy quantification of charge storage capacity under almost thermodynamic equilibrium conditions.

In all experiments, the potential window investigated was adjusted to the pH of the aqueous solution according to the reported Nernstian pH dependence of E_{CB} of TiO₂.¹⁸⁻¹⁹ For instance, equivalent applied potential of -0.82 V at pH 3, -0.94 V at pH 5, and -1.06 V at pH 7 were used in CAs experiments, which corresponds to the formal Ti^{III}/Ti^{IV} potential determined by CVs at each pH values (see chapters 3 and 4).

4.1. Evidencing the link between pH and pK_a

In section 2.1, we evidenced electrochemical charge accumulation occurring at GLAD-TiO₂/TiO₂ electrodes in aqueous solutions of pH 3.0 containing 0.25 M of one of the following salts: AlCl₃, ZnCl₂, or MnCl₂. As a result, it was presumed that [Al(H₂O)₆]³⁺, [Zn(H₂O)₆]²⁺, and [Mn(H₂O)₆]²⁺ behave as weak acids and can thus play the role of proton providers in the proton-coupled electron charging process. Based on cyclic voltammetric experiments conducted on short time scales, we evidenced a less efficient charge storage process in the presence of Zn²⁺- and Mn²⁺-based electrolytes, which could be due to the higher pK_a value of the corresponding hexa aquo complexes, in comparison with Al³⁺.¹⁶

Based on this first observation, further experiments were carried out by CAs in different aqueous electrolytes to investigate the effect of not only the pH but also the pK_a of the weak acids on the efficiency of the charging process. We prepared aqueous electrolytes stabilized at pH 3.0, 5.0 or 7.0 containing 0.25 M of one of the following compounds: acetic acid/acetate (pK_a 4.76), $[Al(H_2O)_6]^{3+}$ (pK_a 4.97), Hepes (pK_a 7.5), $[Zn(H_2O)_6]^{2+}$ (pK_a 9.0), $B(OH)_3$ (pK_a 9.24), NH_4^+ (pK_a 9.25) or $[Mn(H_2O)_6]^{2+}$ (pK_a 10.6).¹⁶ 0.3 M of KCl is additionally contained in non-metallic aqueous electrolytes to maintain the ionic strength.

We specify here that it was however not possible to increase the pH more than 5 in 0.25 M $[Zn(H_2O)_6]^{2+}$ and 0.25 M $[Mn(H_2O)_6]^{2+}$ due to the metal ion precipitation upon addition of hydroxide ions. Figure 11 represents the stability domain of the soluble metallic ion of Al, Zn and Mn together with the $TiO_2/TiOOH$ redox potential as a function of pH. We notice that in the case of Zn^{2+} -based electrolytes, we may have competitive Zn^{2+} reduction and precipitation occurring at the TiO_2 electrode during charging at pH 5.0.

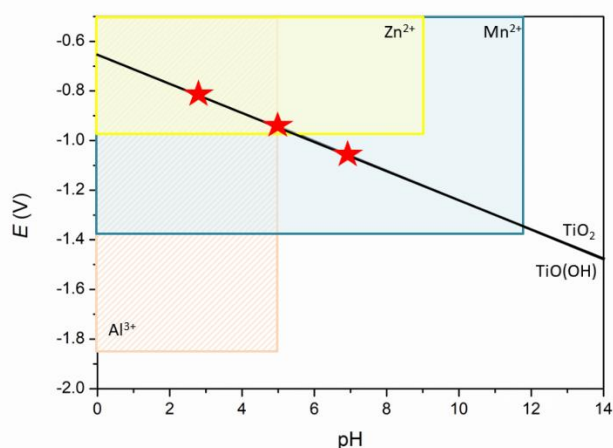


Figure 11. Schematic representation of a stable domain of the soluble metallic ion (Al, Zn and Mn) together with the $TiO_2/TiOOH$ redox potential (black line) as a function of pH, assuming a $-60 \text{ mV} / \text{pH}$ unit dependence of its formal potential, with the existence domain of the main redox-active metallic ions used in the present studies: Al^{3+} ($pK_a = 4.97$ and $E^\circ_{Al^{3+}/Al} = -1.86 \text{ V vs. Ag/AgCl}$); Zn^{2+} ($pK_a = 9$ and $E^\circ_{Zn^{2+}/Zn} = -0.96 \text{ V vs. Ag/AgCl}$) and Mn^{2+} ($pK_a = 10.8$ and $E^\circ_{Mn^{2+}/Mn} = -1.38 \text{ V vs. Ag/AgCl}$). The red stars indicate the theoretical half-charge potential of TiO_2 for the three pH values investigated in the present study.

Chronoabsorptometric experiments were performed by monitoring the absorbance variation at 780 nm, attributed to the stored electrons (or the reduced Ti^{III} ions) as a function of time. The electrodes were stabilized first during 5 seconds at an oxidizing potential (0.24, 0.12, 0 V at pH 3, 5, 7 respectively) in order to record the initial absorbance value and then

stepped to -0.82 , -0.94 , -1.06 V (at pH 3, 5, 7, respectively) during 120 seconds. The absorbance variations are given in Figure 12 (right graphs). Under such experimental conditions, thermodynamic equilibrium was almost reached as evidenced by the quite stable absorbance obtained after a few tens of seconds (indicative of an equilibrated amount of electrons injected within the material). The total charges stored after 120 s was calculated from the absorbance variation according to Eq. 3 and Eq. 4. Contribution of the amount of charges stored through the electrical double layer was systematically subtracted from the total charge storage capacity to estimate the proton-insertion charge storage capacity in each electrolyte (Figure 12, left).

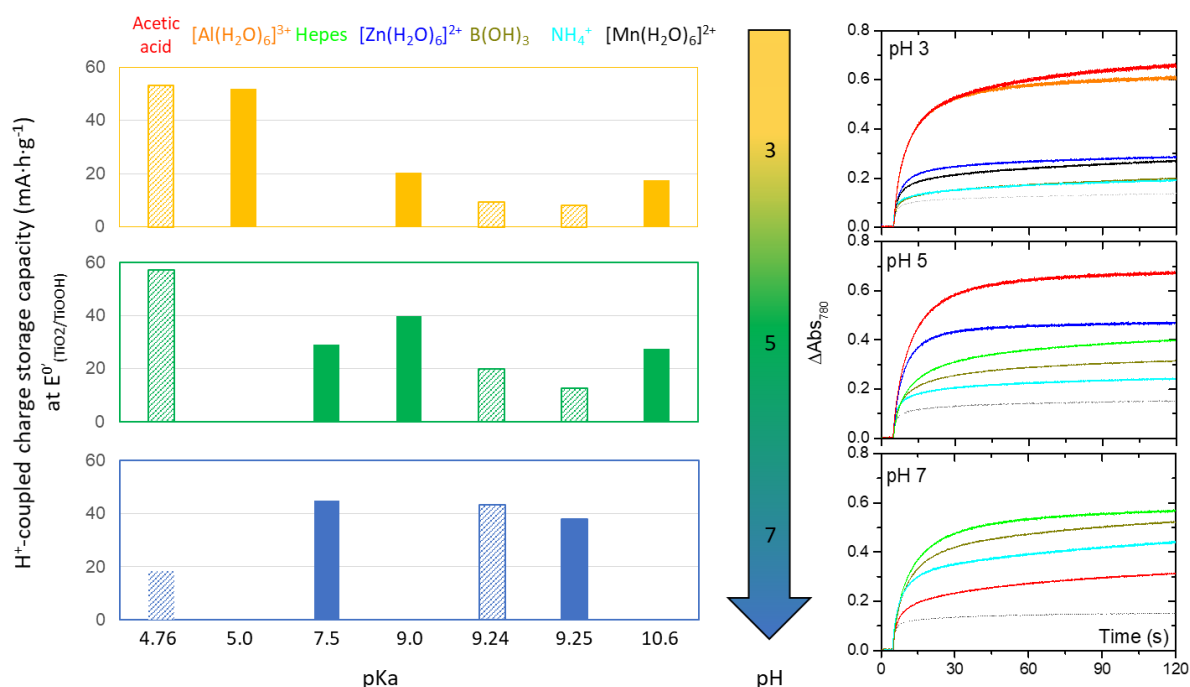


Figure 12. (left) proton coupled charge storage capacity ($\text{mA}\cdot\text{h}\cdot\text{g}^{-1}$) obtained at GLAD-TiO₂/TiO₂ electrodes deduced from (right) reductive potential step experiments plotted as a function of the pK_a of the 250 mM metallic (plain bars) non-metallic (dashed bars) weak acid/conjugate base electrolyte. CA experiments were performed from top to bottom at pH 3, 5 and 7 by applying a reductive potential of -0.82 , -0.94 , -1.06 V vs. Ag/AgCl, respectively.

From the set of data presented in Figure 12, we can make the following observations:

- Charge storage associated to proton insertion can be achieved with a wide range of weak acids characterized by different pK_a values. This was demonstrated with both

positively charged inorganic complexes as well as positively charged or neutral organic weak acids;

- For $\text{pH} < \text{pK}_a$, the amount of charge stored in presence of a weak acid increases with the pH. This can be evidenced by following the charge stored in presence of boric acid ($\text{B}(\text{OH})_3$) upon increasing the pH from 3 to 7.
- Once $\text{pH} > \text{pK}_a$, the amount of charge stored is strongly decreased (see acetic acid at pH 7.0) most likely because the weak acid is no more available.

One might notice that different amount of charge can be stored in the presence of weak acids exhibiting similar pK_a values (see the data obtained with pK_a values in the range 9 to 10.6). This is surprising because we previously demonstrated that acetic acid and $[\text{Al}(\text{H}_2\text{O})_6]^{3+}$, characterized by close pK_a values, allows to store the same amount of charge over a wide range of charging conditions. In line with these results, boric acid and ammonium ion, characterized by almost identical pK_a values, also allows to store similar amount of charge at the three pH values investigated. However, the results obtained in presence of Zn^{2+} - and Mn^{2+} -based electrolytes are not fully consistent with the pK_a values reported. This might be due to some uncertainty on the exact chemical formula of the solvated multivalent metallic ions that may partially aggregate (especially once deprotonated) and/or coordinate Cl^- ions present in the electrolyte. Moreover, in the case of Zn^{2+} , competitive reduction and precipitation of small amount of Zn at the TiO_2 electrode (especially at pH 5.0 according to Figure 11) would also affect the absorbance variation.

Still, the preliminary results obtained here unambiguously demonstrate that very weak acids characterized by pK_a values around 9 still allows for proton-coupled electron charge storage in mesoporous TiO_2 electrodes, although if this requires to adjust the potential window to more negative values. Accordingly, the next question is whether there is a limit or not in the weak acid strength, and if finally water, which is a weak acid characterized by a pK_a value of 14, could also provide protons at the TiO_2 interface under application of an appropriate potential.

4.2. Evidencing water as a proton donor

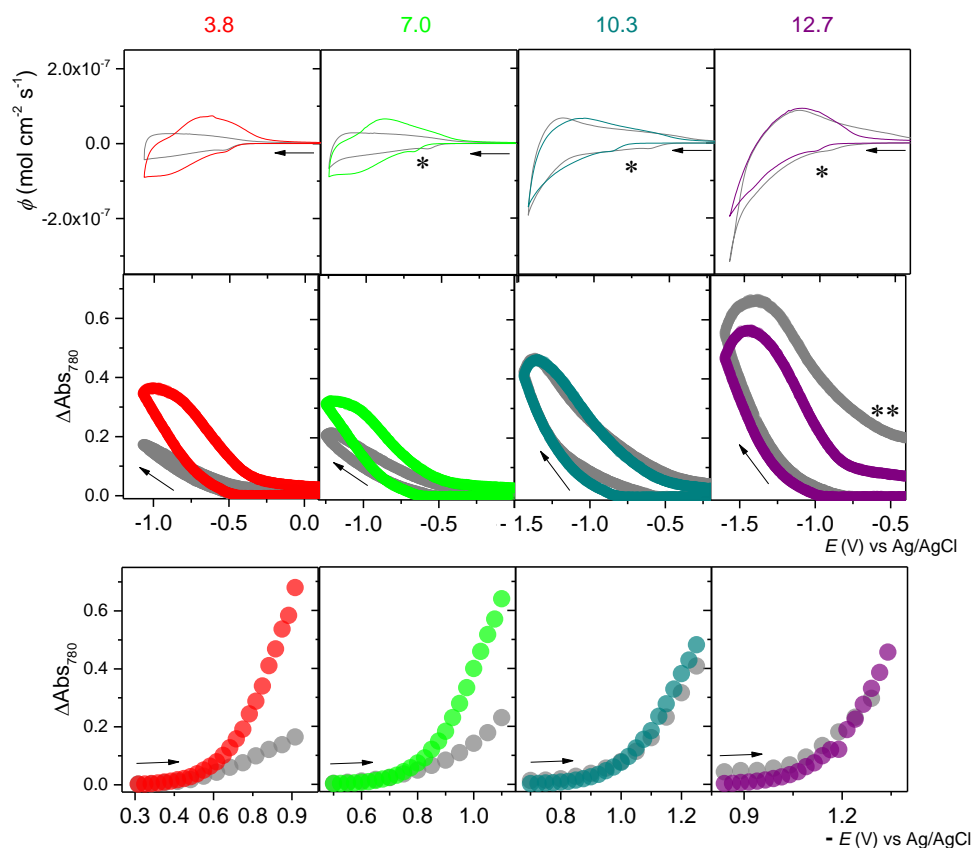
In the present study, we investigated by CVs, CVAs, and CAs the electrochemical charging of GLAD- $\text{TiO}_2/\text{TiO}_2$ electrodes soaked in various buffered solutions (Figure 13). The weak acids investigated in the present study were acetic acid at pH 3.8 (pK_a 4.76), Hepes at pH

7.0 (pK_a 7.5) and Caps at pH 10.3 (pK_a 10.4), and the total buffer concentration was adjusted in order to keep constant the weak acid concentration (~ 38 mM) at each pH. At each pH, the same experiments were conducted in the presence of 1 mM of buffer solution in order to properly define the relative contribution of the double layer electrical capacitance to the total charge stored. Unbuffered, basic KOH aqueous solutions (1 mM KOH at pH 10.7 or 38 mM KOH at pH 12.7) were also prepared to investigate the role of water as proton donor.

The spectroelectrochemical results obtained from cyclic voltammetric and chronoabsorptometric experiments are given in Figure 13. In CVs and CVAs, the potential window investigated was 0.24 to -1.01 V at pH 3.8, 0 to -1.25 V at pH 7.0, 0 to -1.43 V at pH 10.3, and 0 to -1.6 V at pH 12.7. CAs experiments were also carried out by monitoring the absorbance variation at 780 nm during successive reduction/re-oxidation steps, with a 50 mV downshift of the cathodic potential applied at each cycle within a potential windows of -0.312 to -0.912 V at pH 3.8, -0.5 to -1.1 V at pH 7.0, -0.7 to -1.3 V at pH 10.3, and -0.84 to -1.34 V at pH 12.7. The reductive charging process is fully reversible and the transparency of the electrode is fully recovered during the re-oxidation step (data not shown).

In the presence of 38 mM of either acetic acid or Hepes weak acid, well-defined faradaic waves are observed in CVs correlating with a higher absorbance increase in CVAs and CAs as compared to that observed in 1 mM of acetic acid or Hepes aqueous solution. This is characteristic of the proton-coupled electron storage mechanism already evidenced and studied in both buffer solutions. As the concentration of the weak acids remains small (*i.e.*, 38 mM), the shape of CVs and CVAs are expected to be affected by mass transport in solution. On contrary, as CAs experiments are performed on longer time scales (*i.e.*, ~ 120 s for reduction) thermodynamic equilibrium conditions are almost reached.

The results obtained at higher pH are completely different. Indeed, experiments performed in the presence of either 1 mM or 38 mM of the Caps acidic form are nicely overlapping. A small difference is observed in the onset potential of the CVs and CVAs which is due to the more acidic 1 mM Caps solution (pH 9.3) as compared to the 38 mM one (pH 10.3), but no difference is observed in the CAs as the cathodic potentials applied are adjusted to the measured pH value of each electrolyte. The lack of effect of increasing the Caps weak acid concentration on the amount of charge stored (*i.e.*, on the shape of the CV



* Potential difference of the pre-peak is observed due to the pH difference between 1 mM of weak acid (or KOH) and higher concentration of weak acid (or KOH), it is consistent with the pH dependence according to the -60 mV/pH unit increase dependence of $E_{CB}(\text{TiO}_2)$.

** Typical example of the electrode failure arising under strong accumulation conditions and attributed to the irreversible coloration of the underlying ITO substrate of GLAD-TiO₂/TiO₂ electrodes.

Figure 13. (Top row) CVs, (middle row) CVAs, and (bottom row) CAS recorded at GLAD-TiO₂/TiO₂ electrodes soaked in different aqueous electrolytes with 0.3 M of KCl and containing (red) 45 mM acetic acid/acetate buffer, (green) 50 mM Hepes buffer, (dark cyan) 50 mM Caps buffer, and (violet) 38 mM KOH solution. Grey colors corresponds to the data recorded at each pH in the presence of 1 mM of the corresponding buffer. $v = 0.1 \text{ V}\cdot\text{s}^{-1}$ for CVs and CVAs.

and on the absorbance variation of the CVAs) suggest that either there is no faradaic charge storage through proton insertion at such high pH values, or that the acidic form of the Caps buffer is not the proton donor. However, we notice that the absorbance variation of the CVAs is large, and even larger than the one observed in the presence of 38 mM acetic acid or Hepes acidic form. This demonstrates that a fast faradaic charge storage mechanism still occurs in the basic Caps buffer, despite it does not give rise to well-defined peaks in CVs.

The data recorded in presence of 1 or 38 mM of KOH are also very surprising. Under such experimental conditions, there is no weak acid except water (pKa 14). The data obtained

by CVs are hard to interpret as no clear faradaic peak is observed, but still the current intensity is much larger than that recorded in less basic aqueous solution (in absence of significant amount of weak acids). The high absorbance variations observed in CVAs again demonstrates that fast charge storage still occurs in the basic KOH solutions.

In Figure 14 are presented the results of the CAs experiments (see Figure 13) with the potentials referred no more to Ag/AgCl, which reference potential is independent of pH, but to the reversible hydrogen electrode (RHE), which reference potential is downshifted by 60 mV/pH unit as the potential window used in the present study. In the presence of only 1 mM buffer, the absorbance increase with the potential downshift remains low in most cases, which is consistent with charge storage in the electrical double layer. However, for pH values > 9.0, a slightly larger absorbance increase is observed at the lowest potential values used, which indicates a small contribution of the faradaic charge storage process. In presence of higher concentrated electrolytes, a larger absorbance increase is observed upon downshifting the potential, which attests for efficient charge storage through Ti^{IV} reduction. We notice that the data recorded at the different pH values fully overlay, even in the case where water is the only proton donor available in solution. Assuming that thermodynamic equilibrium is reached at each potential in CA experiments, it indicates that the same redox couple is involved in the faradaic charge storage process whatever the proton donor, and that its apparent standard potential exhibits a -60 mV/pH unit dependence. This is again fully consistent with its attribution to the $\text{Ti}^{\text{IV}}\text{O}_2/\text{Ti}^{\text{III}}\text{OOH}$ redox couple.

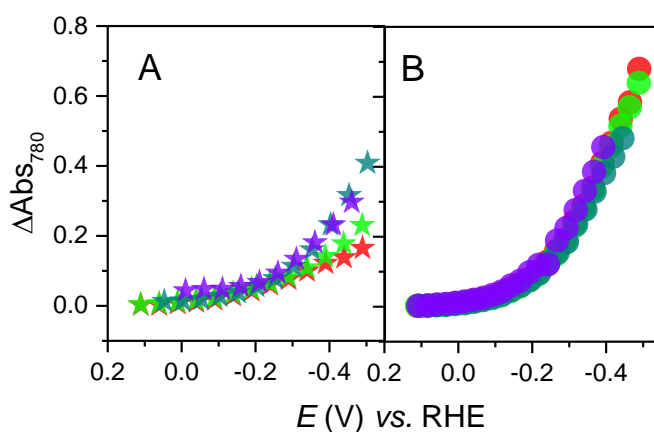


Figure 14. B: CAs recorded at GLAD- $\text{TiO}_2/\text{TiO}_2$ electrodes soaked in different aqueous electrolytes with 0.3 M of KCl and containing (red) 45 mM acetic acid/acetate buffer, (green) 50 mM Hepes buffer, (dark cyan) 50 mM Caps buffer, and (violet) 38 mM KOH solution. A: corresponds to the data recorded at each pH in the presence of 1 mM of the corresponding buffer.

In basic electrolytes ($\text{pH} > 9$), we thus evidence that a fast faradaic charge storage mechanism occurs and we assume that it involves proton insertion as no other small cation is available in the aqueous electrolyte to compensate the charge generated from reduction of Ti^{IV} ions. Accordingly, we assume that water can be the proton source, however only under strong basic pH conditions and at a correspondingly more negative potential windows. This observation is reminiscent of the previous study, where we evidenced that the proton donor efficiency of weak acids was related to the pH value relatively to their pK_a (see section 4.1). In the present case, we notice that water is almost inefficient up to pH 7.0, whereas it becomes efficient above pH 9.0. According to the high concentration of water (55 M), CVs and CVAs should not be limited by mass transport of the proton donor in basic solutions. This may explain why higher amount of charge can be stored during the time course of a CV in basic solutions as compared to what is reported in acetic acid or Hepes buffer.

5. Conclusion

In this chapter, further investigation of proton-coupled electron charge storage at mesoporous TiO_2 electrodes was achieved by modification of the electrolyte composition (*i.e.*, pH, chemical features of the weak acid).

Firstly, the resemblance of experimental results obtained by CVs, CVAs, CAs and galvanostatic experiments in the presence of acetic acid (*i.e.*, typical monoprotic acid) or $[\text{Al}(\text{H}_2\text{O})_6]^{3+}$ in the aqueous acidic electrolyte suggests that an identical charge storage mechanism occurs in both electrolytes, a mechanism based on proton insertion and wherein we attribute the proton is provided by the weak acid species in solution. This result calls into question the interpretations proposed in several studies concerning the exact mechanism of charge storage at TiO_2 electrodes soaked in Al^{3+} -based aqueous electrolytes.

Secondly, by using GLAD- TiO_2/Ti electrodes, we were able to define optimized conditions allowing to reach a total charge storage capacity as high as $161 \text{ mA}\cdot\text{h}\cdot\text{g}^{-1}$ at a quite high C rate (5 C). Under these conditions, *ca.* 80 % is due to the reductive protonation of ~ 40 % of the total titanium ions in the lattice. This value is much higher than the one previously published by us in Hepes buffer (~ 20 %), but still we were not able to reach the maximal theoretical value of 50 %. We attribute this limitation to competitive hydrogen evolution occurring under strong accumulation conditions, responsible of the low coulombic efficiencies

reported. Preliminary experiments conducted in a 8 M acetic acid/acetate buffer allows to conclude that increasing the buffer concentration is a promising strategy to favor proton insertion at the expend of proton reduction.

Finally, we demonstrate that proton-coupled electron storage in mesoporous TiO₂ electrodes is a general feature, occurring in the presence of a wide range of organic as well as inorganic weak acids. Even water can be an efficient proton donor but only under strongly basic conditions. However, the ability of the weak acid to deliver protons at the TiO₂ interface is strongly correlated to its pK_a value regarding the pH of the aqueous electrolyte, and also to the potential window investigated. Indeed, if the pH is too low as compared to the pK_a value, then the weak acid is not able to deliver protons. This is typically the case of water at pH ≤ 7.0. As the pH is further increased toward the weak acid pK_a value, the ability of the weak acid to deliver protons is increased.

References

- ¹ Posada, J. O. G.; Rennie, A. J. R.; Villar, S. R.; Martins, V. L.; Marinaccio, J.; Barnes, A.; Glover, C. F.; Worsley, D. A.; Hall, P. J. Aqueous batteries as grid scale energy storage solutions. *RENEW SUST ENERG REV.* **2017**, *68*, 1174-1182.
- ² Liu, S.; Hu, J. J.; Yan, N. F.; Pan, G. L.; Li, G. R.; Gao, X. P. Aluminium storage behavior of anatase TiO₂ nanotube arrays in aqueous solution for aluminum ion batteries. *Energy Environ. Sci.* **2012**, *5*, 9743-9746.
- ³ He, Y. J.; Peng, J. F.; Chu, W.; Li, Y. Z.; Tong, D. G. Black mesoporous anatase TiO₂ nanoleaves: a high capacity and high rate anode for aqueous Al-ion batteries. *J. Mater. Chem. A.* **2014**, *2*, 1721-1731.
- ⁴ Sun, W.; Wang, F.; Hou, S.; Yang, C.; Fan, X.; Ma, Z.; Gao, T.; Han, F.; Hu, R.; Zhu, M.; Wang, C. Zn/MnO₂ Battery Chemistry with H⁺ and Zn²⁺ Coinsertion. *J. Am. Chem. Soc.* **2017**, *139*, 9775-9778.
- ⁵ He, P.; Quan, Y.; Xu, X.; Yan, M.; Yang, W., An, Q.; He, L.; Mai, L. High-Performance Aqueous Zinc-Ion Battery Based on Layered H₂V₃O₈ Nanowire Cathode. *Small*, **2017**, *13*, 1702551, 1-7.
- ⁶ Alfaruqi, M. H.; Mathew, V.; Song, J.; Kim, S.; Islam, S.; Pham, D. T.; Jo, J.; Kim, S.; Baboo, J. P.; Xiu, Z.; Lee, K. -S.; Sun, Y. -K.; Kim, J. Electrochemical Zinc Intercalation in Lithium Vanadium Oxide: A High-Capacity Zinc-Ion Battery Cathode. *Chem. Mater.* **2017**, *29*, 1684-1694.
- ⁷ Ko, J. S.; Sassin, M. B.; Parker, J. F.; Rolison, D. R.; Long, J. W. Combining battery-like and pseudocapacitive charge storage in 3D MnO_x@carbon electrode architectures for zinc-ion cells. *Sustainable Energy & Fuels* **2018**, *2*, 626-636.
- ⁸ Sang, S.; Liu, Y.; Zhong, W.; Liu, K.; Liu, H.; Wu, Q. The electrochemical behavior of TiO₂-NTAs electrode in H⁺ and Al³⁺ coexistent aqueous solution. *Electrochim. Acta.* **2016**, *187*, 92-97.
- ⁹ Liu, S.; Pan, G. L.; Yan, N. F.; Gao, X. P. Aqueous TiO₂/Ni(OH)₂ rechargeable battery with a high voltage based on proton and lithium insertion/extraction reactions. *Energy Environ. Sci.* **2010**, *3*, 1732-1735.
- ¹⁰ Liu, S.; Ye, S. H.; Li, C. Z.; Pan, G. L.; Gao, X. P. Rechargeable Aqueous Lithium-Ion Battery of TiO₂/LiMn₂O₄ with a High Voltage. *J Electrochem Soc.* **2011**, *158*, A1490-A1497.
- ¹¹ Tang, W.; Hou, Y.; Wang, F.; Liu, L.; Wu, Y.; Zhu, K. LiMn₂O₄ Nanotube as Cathode Material of Second-Level Charge Capability of Aqueous Rechargeable Batteries. *Nano Lett.* **2013**, *13*, 2036-2040.
- ¹² Wu, M. -S.; Wang, M. -J., Jow, J. -J.; Yang, W. -D.; Hsieh, C. -Y.; Tsai, H. -M. Electrochemical fabrication of anatase TiO₂ nanostructure as an anode material for aqueous lithium-ion batteries. *J. Power Sources.* **2008**, *185*, 1420-1424.
- ¹³ Liu, J.; Wang, J.; Ku Z.; Wang, H.; Chen, S.; Zhang, L.; Lin, J.; Shen, Z. X. Aqueous Rechargeable Alkaline Co_xNi_{2-x}S₂/TiO₂ Battery. *ACS Nano.* **2016**, *10*, 1007-1016.

- ¹⁴ Marcus, Y.; Thermodynamics of Solvation of Ions. *J. Chem. Soc., Faraday Trans* **1991**, 87(18), 2995-2999.
- ¹⁵ Marcus, Y.; Ionic Radii in Aqueous Solutions. *Chem. Rev.* **1988**, 88, 1475-1498.
- ¹⁶ S.J. Hawkes. All Positive Ions Give Acid Solutions in Water. *J. Chem. Educ.* **1996**, 73, 516.
- ¹⁷ Lapidus, S. H.; Rajput, N. N.; Qu, X.; Chapman, K. W.; Persson, K. A.; Chupas, P. J. Solvation structure and energetics of electrolytes for multivalent energy storage. *Phys. Chem. Chem. Phys.*, **2014**, 16, 21941-21945.
- ¹⁸ Boschloo, G.; Fitzmaurice, D. Electron Accumulation in Nanostructured TiO₂ (Anatase) Electrodes. *J. Phys. Chem. B* **1999**, 103, 7860-7868.
- ¹⁹ Lyon, L. A.; Hupp, J. T. Energetics of the Nanocrystalline Titanium Dioxide/Aqueous Solution Interface: Approximate Conduction Band Edge Variations between H₀ = - 10 and H₋ = 26. *J. Phys. Chem. B* **1999**, 103, 4623-4628.
- ²⁰ Lide, D. R. CRC handbook of chemistry and physics, (Ed.) 82nd edition, **2001**.
- ²¹ Ribeiro, A. C. F.; Valente, A. J. M.; Sobral, A. J. F. N.; Lobo, V. M. M.; Burrow, H. D.; Estes, M. A. Diffusion coefficients of aluminium chloride in aqueous solutions at 298.15, 303.15 and 315.15 K. *Electrochim. Acta.* **2007**, 52, 6450-6455.
- ²² Krause, K. M.; Taschuk, M. T.; Harris, K. D.; Rider, D. A.; Wakefield, N. G.; Sit, J. C.; Buriak, J. M.; Thommes, M.; Brett, M. J. Surface Area Characterization of Obliquely Deposited Metal Oxide Nanostructured Thin Films. *Langmuir*, **2010**, 26, 4368-4376.
- ²³ Pan, H.; Shao, Y.; Yan, P.; Cheng, Y.; Han, K. S.; Nie, Z.; Wang, C.; Yang, J.; Li, X.; Bhattacharya, P.; Mueller, K. T.; Liu, J. Reversible aqueous zinc/manganese oxide energy storage from conversion reactions. *Nat. Energy.* **2016**, 1, 1-7.
- ²⁴ Yan, M.; He, P.; Chen, Y.; Wang, S.; Wei, Q.; Zhao, K.; Xu, X.; An, Q.; Shuang, Y.; Shao, Y.; Mueller, K. T.; Mai, L.; Liu, J.; Yang, J. Water-Lubricated Intercalation in V₂O₅·nH₂O for High-Capacity and High-Rate Aqueous Rechargeable Zinc Batteries. *Adv. Mater.* **2018**, 30, 1703725.
- ²⁵ Wu, X.; Xiang, Y.; Peng, Q.; Wu, X.; Li, Y.; Tang, F.; Song, R.; Liu, Z.; He, Z.; Wu, X. Green-low-cost rechargeable aqueous zinc-ion batteries using hollow porous spinel ZnMnO₄ as the cathode materials. *J. Mater. Chem. A.* **2017**, 5, 17990.
- ²⁶ Leonard, D. P.; Wei, Z.; Chen, G.; Du, F.; Ji, X. Water-in-Salt Electrolyte for Potassium-Ion Batteries. *ACS Energy Lett.* **2018**, 3, 373-374.
- ²⁷ Suo, L.; Borodin, O.; Gao, T.; Olguin, M.; Ho, J.; Fan, X.; Luo, C.; Wang, C.; Xu, K. "Water-in-salt" electrolyte enables high-voltage aqueous lithium-ion chemistries. *Science.* **2015**, 350, 938-943.

General conclusions

During this work, we investigated the charge transport/transfer and charge storage (*i.e.*, electron accumulation) at mesoporous TiO₂ metal oxide materials by real-time spectroelectrochemistry.

In chapter 1, we studied the interfacial electron transfer as well as the redox-mediated catalytic reduction of O₂ at GLAD-ITO and GLAD-TiO₂ electrodes functionalized by a small redox-active chromophore (Mn-ph). At Mn-ph/GLAD-ITO electrodes under non-turnover condition, the reversible Mn^{III}/Mn^{II} redox reaction at the chemisorbed Mn-ph occurs fast and under thermodynamic equilibrium until scan rate up to 1 V·s⁻¹. In presence of the O₂ substrate, a fast catalytic reaction associated to O₂ reduction was observed, but it was not possible to acquire mechanistic details as mass transport of O₂ in solution was rate-limiting under the experimental conditions tested.

On the other hand, Mn-ph/GLAD-TiO₂ electrodes exhibit contrasted behaviors in both absence and presence of the O₂ substrate, which is due to its unique semiconductive features. In degassed solutions, the irreversible reduction of Mn^{III}-ph into Mn^{II}-ph is observed at a more negative potential than the formal reduction of the chemisorbed Mn^{III}-ph/Mn^{II}-ph redox couple (*i.e.*, -0.42 V). This indicates that the interfacial electron transfer at the Mn-ph/GLAD-TiO₂ interface can only proceed in a potential window where TiO₂ is sufficiently conductive. By using a methodology previously developed in the laboratory, we successfully fitted the experimental data and extracted some key parameters such as the interfacial electron transfer rate as well as the extent of bandgap localized states involved in the heterogeneous electron transfer reaction for GLAD-TiO₂ electrodes.

This irreversible conversion of the immobilized Mn^{III}-ph, however, becomes fully reversible in the presence of O₂. This is explained by the fast re-oxidation of Mn^{II}-ph into Mn^{III}-ph through fast catalysis of O₂ reduction. Interestingly, during the forward cathodic scan, the absorbance at 432 nm was raised at a slightly more negative potential than in absence of O₂, indicating a delay in the accumulation of the reduced Mn^{II}-ph complex until O₂ depletion occurs. Simultaneously, we notice that charge accumulation within the Mn-ph/GLAD-TiO₂ electrode is also delayed, as attested by the potential shift (~ 110 mV) of the onset absorbance potential (monitored at 780 nm) under turnover conditions. This is an astonishing result as usually diffusion of electrons within the mesoporous film is assumed to be fast (*i.e.*, not rate-limiting) and thus under thermodynamic equilibrium. That the accumulation of electrons in bulk TiO₂ is indeed delayed remains not completely clarified yet and thus requires further

investigations. The possible inference can be due to the instant consumption of electrons for catalytic reduction of O₂, thus the electron accumulation within the TiO₂ is suspended. Or it can also be inferred that the apparent rate of mass transport of electrons within in the TiO₂ film can actually be a rate-limiting.

In chapter 2, we introduced an efficient and homogenous functionalization of 3D nanostructured transparent GLAD-ITO electrodes by electrochemical reduction of *in-situ* generated free-base porphyrin diazonium salts with a high degree of control over the homogeneity, surface coverage and reproducibility. The results obtained support the formation of covalently linked electroactive porphyrin oligomers grafted on the ITO surface through, most likely, an underlying metal-O-carbon bond. This leads to highly stable modified electrodes toward desorption or hydrolysis in organic as well as mild hydrolytic conditions, and allows quantitative post-metalation by zinc ions of the grafted free-base porphyrins. This resulting covalent bonding by an electrochemical grafting of dye clearly showed a much more stable functionalization onto metal oxide as compare to the chemisorption by anchoring group (and/or physical adsorption).

It is worthy to mention here that ultimate preliminary experiment concerning the electrografting of the free-base porphyrin diazonium salt was achieved with the mesoporous semiconductive GLAD-TiO₂ electrodes, but it requires more studies and was therefore not included in this manuscript. The reductive potential of free-base porphyrin diazonium salts at GLAD-ITO was located at +0.35 V, *i.e.* in a potential window where TiO₂ is totally insulating. Transposition of the procedure to the GLAD-TiO₂ film required thus to adjust the applied potential window for electrodeposition, which was shifted to more cathodic potential (*i.e.*, -0.4 to -0.9 V *vs.* SCE.). This opens new opportunities for the robust functionalization of high surface area semiconductive metal oxide electrodes by various functional molecules in order to develop sustainable photoelectrodes operating under mild aqueous solutions.

Throughout the chapters 3 and 4, we investigated the proton-coupled electron storage process (as well as the electrical double layer charge storage process) occurring at amorphous GLAD-TiO₂ electrodes in various aqueous electrolytes. This process had been so far only investigated under strongly acidic conditions (pH < 2).

In chapter 3, we demonstrate for the first time that massive, fast and proton insertion occurs in an aqueous buffered solution at neutral pH during the reductive electrochemical

charging of GLAD-TiO₂ electrodes. This diffusion controlled proton-couple charge storage upon reductive protonation of lattice Ti^{IV} ions can occur extensively at a well-defined potential not only in the presence of a unbuffered strong acid (HCl) solution but also, arrestingly, under neutral pH conditions in a buffered solution (HEPES buffer). This overall result allowed to open a potentiality of developing high rate and high power electrochemical charge storage devices based on reversible proton-ion charge/discharge processes at mesoporous metal oxide materials under mild aqueous conditions. Furthermore, a model has been developed (see annexe) to evaluate proton transport effects on charge storage in conductive materials associated with a redox process in the bulk material coupled to proton insertion from an aqueous buffered solution, a situation frequently encountered in metal oxide materials.

The preliminary studies presented in chapter 4 were initiated by questions arising from experiments reported in the literature about the exact role of multivalent metallic ions added in aqueous electrolytes and the pH range allowing for proton insertion. In order to approach these questions, we investigated charge storage in various aqueous electrolytes, in presence of organic as well as inorganic weak acids.

First, we evidenced an increased charge storage capacity in the presence of multivalent metallic ions in the aqueous electrolyte (*i.e.*, [Al(H₂O)₆]³⁺, [Zn(H₂O)₆]²⁺, and [Mn(H₂O)₆]²⁺). We made two hypotheses regarding this results; one is the insertion of a multivalent cation M^{Z+} resulting from desolvation of the aquo complex, which is energetically very unfavorable. Second hypothesis is the insertion of proton provided by the [M(H₂O)_n]^{Z+} weak acids. Following results conducted in presence of either [Al(H₂O)₆]³⁺ (pK_a = 4.97) or acetic acid (*i.e.*, typical monoprotic acid, has similar pK_a value of 4.76) at pH 3 showed great resemblances in CV, CVA, CA, and galvanostatic experiments, which strongly suggest that an identical charge storage mechanism occurs in both electrolytes. Accordingly, the second hypothesis is more reasonable.

Secondly, optimization of the charge storage capacity and the coulombic efficiency was performed in buffered acetic acid/acetate electrolyte at pH 5. Optimized conditions allowed to reach a total charge storage capacity as high as 161 mA·h·g⁻¹ at a quite high C-rate (5 C), with *ca.* 80 % due to the reductive protonation of ~40 % of the total titanium ions in the lattice. This value is much higher than the one previously obtained by us in the Hepes buffer (~20 %), but still we were not able to reach the maximal theoretical value of 50 %. This

limitation seems to have a strong connection with hydrogen evolution occurring under strong accumulation conditions, responsible of the low coulombic efficiencies reported.

Finally, we demonstrated that proton-coupled electron storage in mesoporous TiO₂ electrodes is not limited to one type of weak acid, and that even water can be an efficient proton donor although only under strongly basic conditions. The evidence that ability of the weak acid to deliver protons at the TiO₂ interface is strongly correlated to its pKa value regarding the pH of the aqueous electrolyte, and also to the potential window investigated. Indeed, as the pH is close toward the pKa value of weak acid, the ability of the weak acid to deliver protons is increased.

In fact, this proton-coupled electron charging/discharging process seems to be a general feature of porous metal oxide-based electrodes. Based on the results obtained in chapter 3 and 4, TiO₂ clearly shows a potentiality as anode electrode for an aqueous battery operating under mild and non-corrosive pH conditions. As one of the candidates for a cathode electrode, I performed some preliminary studies on manganese dioxide (MnO₂) films during my PhD. These experiments were conducted on electrochemically deposited MnO₂ film (onto ITO substrate) in presence or absence of weak acids in the aqueous electrolyte. Interestingly, we evidenced that the electrochemical reactivity of the MnO₂ film can be switched from EDLC to faradaic process depending on the presence of a proton donor in the electrolyte.

Although it certainly needs further investigations for the practical development of an aqueous-based proton insertion battery, these overall results open the possibility of a new battery concept associating two metal oxides electrodes (*e.g.*, TiO₂/MnO₂) operating under aqueous conditions by proton-coupled reversible charging/discharge process according to the following expression:



Experimental part

1. Chemicals and Materials

2. Methodology

2.1. Electrochemistry (Cyclic voltammetry, Chronoamperometry, Chronopotentiometry)

2.2. Real-time UV-visible absorption spectroelectrochemistry (Cyclic-voltabsorptometry, Chronoabsorptometry)

2.3. X-ray photoelectron spectroscopy

2.4. Resonance Raman spectroscopy

3. GLAD-Electrodes

3.1. Preparation of mesoporous GLAD-electrode

3.1.1. GLAD-ITO

3.1.2. GLAD-TiO₂

3.1.3. GLAD-TiO₂/TiO₂

3.1.4. GLAD-TiO₂/Ti

3.2. Electrode cleaning process

3.3. Surface enhancement

4. Surface modification

4.1. Chemisorption of manganese porphyrin (Mn-ph)

4.2. Electrografting of diazonium salt

1. Chemicals and Materials

HEPES, HEPES sodium salt (puriss. p.a.), Aluminum chloride hexahydrate ($\text{AlCl}_3 \cdot 6\text{H}_2\text{O}$), Zinc chloride tetrahydrate ($\text{ZnCl}_2 \cdot 4\text{H}_2\text{O}$), Zinc acetate, Tetrabutylammonium hexafluorophosphate (TBAPF_6), sodium nitrite (NaNO_2), trifluoroacetic acid (TFA) and lithium perchlorate (puriss. p.a.) were purchased from Sigma-Aldrich. Potassium hydroxide, Acetic acid (100 %, AnalaR NORMAPUR®), Hydrochloric acid (HCl, 37 %), Sodium hydroxide (NaOH) and Potassium ferricyanide ($\text{K}_3[\text{Fe}(\text{CN})_6]$) were obtained from VWR BDH Prolabo®. Acetone, ethanol, and dichloromethane for an electrode cleaning process was also purchased from VWR BDH Prolabo®. Trichloromethane was obtained from Acros Organics™. Ammonia solution (NH_3 , 28%) was provided by Prolabo RECTAPUR®. Acetonitrile purchased from Sigma-Aldrich was used for the electrografting process after distillation, and acetonitrile provided from VWR BDH Prolabo® was used for UV-visible spectrometry. Potassium chloride (Merck & Co., puriss. p.a.) were used as received. $\text{H}_2(\text{PDTP})\text{-NH}_2$ was synthesized by our collaborator in Dijon, France according to the literature.¹ Manganese porphyrin (Mn-ph) was synthesized by our collaborator (Dr. Alla Lemeune) from Université de Bourgogne.² All aqueous solutions were prepared with highly purified Milli-Q water ($18.2 \text{ M}\Omega \cdot \text{cm}$) procured by a TKA MicroPure UV purification system. Commercial planar indium tin oxide coated glass substrates (rectangular slide, $8\text{-}12 \text{ }\Omega/\square$) were purchased from Delta Technologies, and cut to $0.8 \times 3.5 \text{ cm}$.

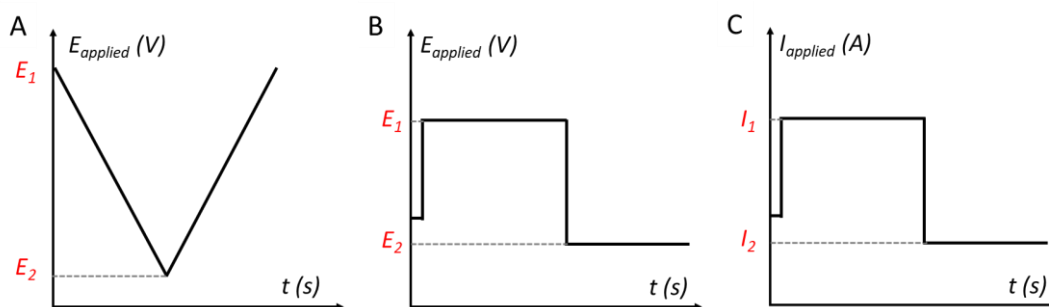
2. Methodology

Both kinetic and thermodynamic quantitative data were obtained from spectroelectrochemical or electrochemical measurements. Thus, we report on general methods for the investigation of GLAD-electrodes properties by means of electrochemistry including cyclic voltammetry, chronoamperometry, galvanostatic chronopotentiometry in section 2.1 as well as spectroelectrochemistry such as cyclic voltabsorptometry, and chronoabsorptometry in section 2.2.

2.1. Electrochemistry (Cyclic voltammetry, Chronoamperometry, Chronopotentiometry)

All electrochemical measurements were performed in a three-electrode configuration: the mesoporous GLAD working electrode (see section 3), the reference electrode (Ag/AgCl

electrode or S.C.E.) and the counter electrode (Pt wire). The potential of the working electrode is measured with respect to the reference electrode. The redox reaction takes place at the surface of the working electrode and the current flows between the working electrode and the counter electrode. All electrochemical experiments were carried out with an Autolab PGSTAT-12 potentiostat operated by GPES-4 software. Scheme 1 describes the diverse electrochemical techniques used in this work.



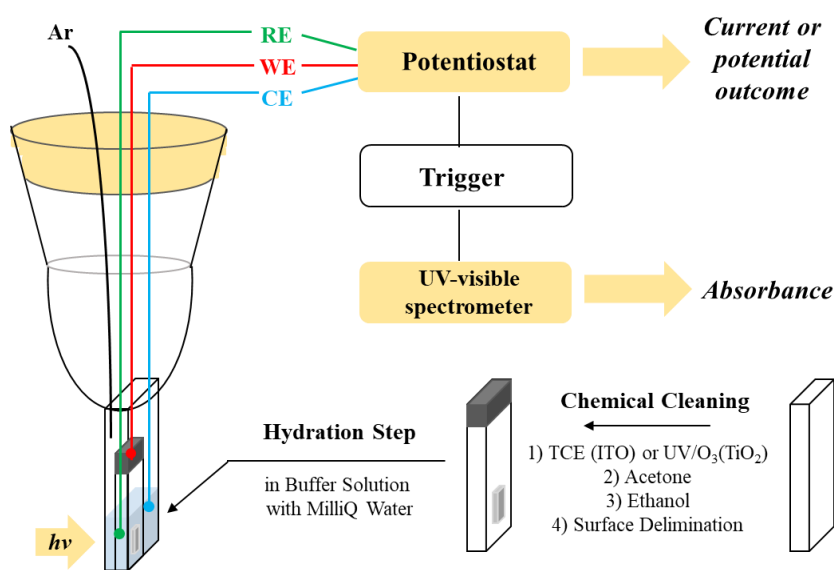
Scheme 1. Schematic representation of (A) potential sweep cyclic voltammetry, (B) chronoamperometry, and (C) Chronopotentiometry.

Voltammetry are comprised of applying an external controlled potential (or current) to the electrochemical cell and observing the measuring current flow (or potential). For instance, potential sweep techniques measure the current when the potential of the working electrode is continuously changed (*e.g.* cyclic voltammetry, scheme 1A) or stepped (*e.g.* chronoamperometry, scheme 1B). The scan rates are used from 0.05 to 2 V·s⁻¹. Ohmic drop was systematically compensated in cyclic voltammetry, with an average compensation value of 43 ± 6 Ω (N = 36) for GLAD-TiO₂ electrodes. Chronopotentiometry, on the other hand, is a technique with constant current or current steps which measures the potential of the working electrode with respect to the reference electrode (scheme 1C). This technique has the advantage to be applicable where a constant current rate is important, such as electrodeposition or battery charge/discharge studies.

2.2. Real-time UV-visible spectroelectrochemistry (Cyclic voltabsorptometry, Chronoabsorptometry)

The spectroelectrochemical experiments were performed in a one-compartment spectroelectrochemical cell using an Autolab PGSTAT-12 potentiostat controlled by GPES-4

software for electrochemical measurement and coupled to a TORUS UV–visible spectrophotometer (Ocean Optics) equipped with optical fibers and a balanced deuterium tungsten source (Micropack) for UV-visible absorption measurement. During experiments, the electrochemical cell was thermostatted at a constant temperature of 25 °C using a dedicated Peltier heater (Quantum Northwest). The potentiostat and spectrophotometer were synchronized through an input trigger signal generated by the potentiostat, thus allowing simultaneous recording of the optical absorbance and current as a function of the time-varying potential applied to the working GLAD-electrodes (scheme 2).



Scheme 2. Schematic explanation of spectroelectrochemistry.

The GLAD-electrodes were positioned perpendicular to the optical path in the quartz cell. The cell was filled with 1.2 mL of buffer solution and thoroughly deaerated by bubbling argon (for at least 20 min) ahead of each experiment and constantly flowed in the cell during experiments. An Ag/AgCl electrode in 3 M KCl (WPI, Dri-ref, + 0.2 V vs NHE at 25 °C) was used as the reference electrode, and a Pt wire was used as the counter electrode. Integration time was set to 3 ms and the number of averaged scans was typically 100 except for the spectroelectrochemical experiments where it was fixed to 2 ~ 15 depending on the scan rates. Satisfactory signal-to-noise ratios were obtained by averaging 15 scans for experiments performed at $50 \text{ mV} \cdot \text{s}^{-1}$, 6 scans for at $100 \text{ mV} \cdot \text{s}^{-1}$, 4 scans for at $200 \text{ mV} \cdot \text{s}^{-1}$ and 2 scans for at $500 \text{ mV} \cdot \text{s}^{-1}$. Experimental derivative cyclic voltabsorptograms were smoothed using a second order Savizky-Golay algorithm.

2.3. X-ray photoelectron spectroscopy

X-ray photoelectron spectroscopy (XPS) is a surface-sensitive quantitative spectroscopic technique that analyzes the elemental composition of material. XPS spectra are obtained by irradiating a material with a beam of X-rays while simultaneously measuring the kinetic energy and number of electrons that escape from the top 0 to 10 nm of the material being analyzed. In this work, X-ray photoelectron spectroscopy (XPS) measurements were performed by P. Decorse in laboratory ITODYS using a Thermo-Scientific VG ESCALAB 250 system fitted with a micro-focused, monochromatic Al K α X-ray source (1486.6 eV, 15kV) and a magnetic lens, which increases the electron acceptance angle and hence the sensitivity. The X-ray spot size diameter was 500 μ m and the pass energy was set at 100 and 40 eV for survey spectra and narrow scans, respectively. An electron flood gun was used for static charge compensation on insulating samples. Spectra were calibrated by setting the C1s component, assigned to aliphatic carbons or atmospheric contamination, to 285 eV. Measurements were carried out on samples affixed to sample holders using conductive double-sided adhesive tapes. The Avantage software (version 4.67) was used for digital acquisition and data processing. Elemental atomic concentrations were calculated from the XPS peak areas, and the corresponding Scofield sensitivity factors were corrected for the analyzer transmission work function. The O(1s) peak was fitted to 4 components by using Gaussian/Lorentzian GL(30) products.

2.4. Resonance Raman spectroscopy

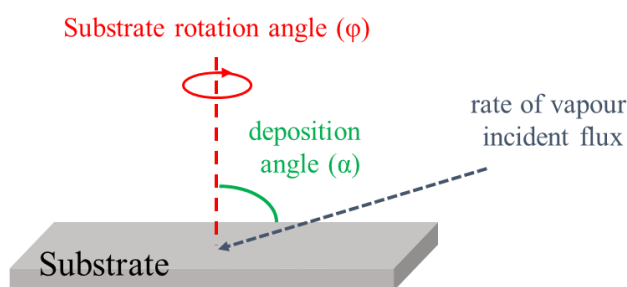
Resonance Raman spectroscopy (*i.e.*, rR spectroscopy) is a Raman spectroscopy technique with enhanced intensity to facilitate getting information about the vibrations of a chromophore. It allows to identify unknown substances with low concentration by using an incident photon energy close in energy to an electronic transition of the compound or material under examination. For this study, resonance Raman spectra were performed on GLAD-ITO electrodes functionalized with a porphyrin with excitation at 405 nm (*i.e.*, Soret band) with a single frequency collimated laser module (Ondax, Inc) and recorded with a Labram HR 800 microspectrometer (Jobin Yvon) by S. Lau-Truong in laboratory ITODYS. Spectra were recorded at room temperature (20 °C) with a power of 2 mW at the sample. For the measurements performed in solution, the microscope was equipped with a 10 \times objective

without filter, whereas for the measurements on GLAD-ITO electrodes, a 100× microscope objective was used with a D 0.3 filter. The reported spectra for solutions correspond to the average of at least 12 scans, each recorded with a 30 s (on solution) or 5s (on GLAD-ITO) acquisition time. Measurements were performed from scan to scan on different surface areas to avoid porphyrin degradation.

3. GLAD-Electrodes

3.1. Preparation of mesoporous GLAD-electrode

The working electrodes used in this thesis were prepared by glancing angle deposition (GLAD) technique from our collaborator in Canada (Dr. Kenneth Harris from the National Institute of Nanotechnology, Edmonton).⁴⁻⁵ GLAD is a one-step physical deposition technique by vaporization of precursor, for fabricating nanostructured porous thin films with engineered structured high surface area thickness, and morphological characteristics as function of the deposition angle (scheme 3). After, physically deposited films were treated by annealing process for stable optical and electrical properties. GLAD-films combines the advantages of high surface area and well-opened accessible mesoporosity allowing to investigate surface functionalization or ion insertion which is the aim of this thesis with improved consistent control and high reproducibility of film characteristics. We used GLAD-ITO and -TiO_2 electrodes prepared from deposition of 0.25- to 1- μm -thick vertical metal oxide films on the top of the various substrates (ITO, thin TiO_2 or Ti film). Deposition angle (α) from 0 to 80° were used.



Scheme 3. Schematic explanation of glancing angle deposition (GLAD) technique. The morphology of the deposited films is determined by the deposition angle (α), substrate rotation angle (φ), rate of incident flux, and rotation speed. The movement of substrate is performed by two independent motors with computer control.

Broadly, the types of GLAD-electrodes can be divided in two, GLAD-ITO and GLAD-TiO₂. Briefly, mesoporous ITO film (Cerac, 91:9 In₂O₃/SnO₂ 99.99% pure) and TiO₂ film (Cerac, 99.99% pure rutile) were deposited onto planar ITO substrate and various substrates on an electron-beam physical vapor-deposition evaporation system (Axxis, Kurt J Lesker) depending on the film thickness from 550 nm to 1 μm. Throughout the deposition, substrates were maintained at a 72° or 80° angle with respect to impinging evaporant flux while rotating as a feedback-controlled function of the deposition rate. This is a computer-controlled manipulation of two substrate-orientation motors: one to set the deposition angle (R) of the substrate chuck with respect to the impinging evaporant flux and another to rotate the substrate (φ) as a function of the deposition rate. GLAD-TiO₂ can be again classed in various types of electrode depending on the substrate, ITO (expressed to GLAD-TiO₂) or thin dense TiO₂ film (15 nm) on top of the ITO (expressed to GLAD-TiO₂/TiO₂) or dense Ti film (0.25 μm) on top of the glass (expressed to GLAD-TiO₂/Ti). Experimental reproducibility is attested by the good overlap of cyclic voltammograms recorded under identical experimental conditions for different GLAD-TiO₂ electrodes arising from different GLAD deposition batches (Figure 1, relative standard deviation RSD < 5 %, N = 7). The reproducibility of the corresponding cyclic voltabsorptograms was not as good (Savizky < 40 %), suggesting a higher sensitivity of the absorbance measurement to batch-to-batch variations in the GLAD-TiO₂ samples.

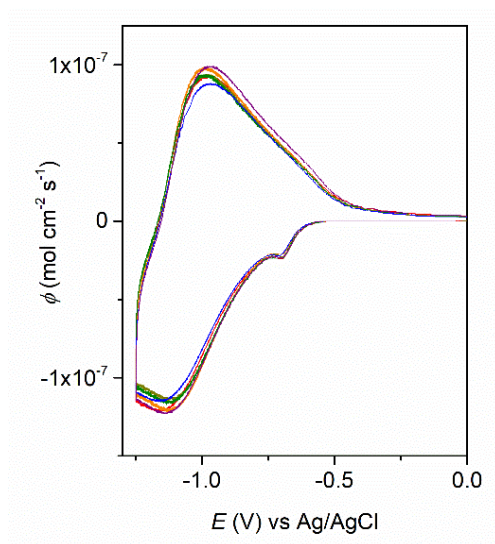


Figure 1. Cyclic voltammograms recorded at different 1 μm-thick GLAD-TiO₂ electrodes (arising from 3 different GLAD deposition batches) in 1 mM HEPES with 0.3 M KCl at pH 7. $\nu = 0.1 \text{ V s}^{-1}$, $T = 25 \text{ }^\circ\text{C}$.

3.1.1. GLAD-ITO

Mesoporous GLAD-ITO electrode was prepared with 500 nm film thickness and 80° deposition angle followed by thermal treatment. Following deposition, ITO samples were annealed at 300-350 °C for 2 to 3 h, with a 10 °C min⁻¹ temperature ramp up and down.³

3.1.2. GLAD-TiO₂

Amorphous mesoporous TiO₂ thin films on conducting tin-doped indium oxide (ITO) glass substrate (Delta Technologies, 8-12 Ω/□) were prepared by glancing angle deposition (GLAD) method followed by thermal treatment as well (only in case of using ITO substrate). Following deposition, TiO₂ was annealed at 100 °C for 24 h to ensure stoichiometric TiO₂ films and, as a result, to enhance and stabilize the optical transmission of the film.³

3.1.3. GLAD-TiO₂/TiO₂

GLAD-TiO₂/TiO₂ electrode is composed of a 15 nm dense TiO₂ underlayer prepared with a 0° deposition angle on top of the ITO substrate. Then a 1 μm-thick mesoporous TiO₂ film is deposited with a 72° deposition angle. GLAD-TiO₂/TiO₂ electrode remains transparent in the visible range which enable to perform spectroelectrochemistry. Thermal treatment was performed as same condition for GLAD-TiO₂ after deposition.

3.1.4. GLAD-TiO₂/Ti

Another type of GLAD-TiO₂/Ti electrode were prepared by first deposition of a 250 nm dense layer of Ti with 0° deposition angle on glass. Then, second deposition of 1 μm thickness TiO₂ film with 72° deposition angle was carried out on the top of the Ti dense layer (Figure 2). Thermal annealing was not treated for this type of electrode.

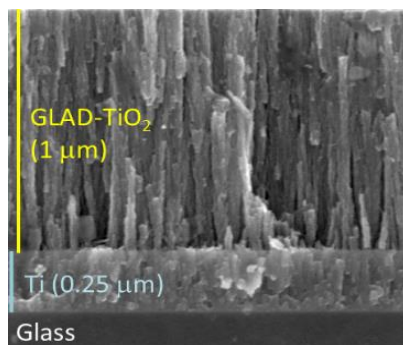


Figure 2. SEM image of 1 μm -thickness GLAD-TiO₂ with 72° deposition angle on underlying 250 nm-thickness Ti deposition layer with 0° deposition angle on top of the glass substrate.

3.2. Electrode cleaning process

Prior any experiments, planar ITO as well as GLAD-electrodes were cleaned. Planar commercial ITO electrodes were soaked in dichloromethane and acetone, 10 min in each solution under sonication. GLAD-ITO electrodes were cleaned by soaking in trichloroethylene, acetone and ethanol at 50 °C for 15, 15 and 30 min, respectively. All type of GLAD-TiO₂ electrodes were treated with UV/O₃ (UV/O₃ Procleaner plus, Bioforce nanosciences) for 15 min and further cleaned by subsequent immersion at room temperature in acetone and ethanol for 15 and 30 min, respectively. A portion of electrode surface was then delimited with an insulating layer (using nail vanish) to define rectangular working electrode areas of $0.50 \pm 0.08 \text{ cm}^2$ (evaluated from a set of $N = 35$ independent electrodes).

3.3. Surface enhancement

Surface area enhancement of $\sim 540 /\mu\text{m}$ and $\sim 70 /\mu\text{m}$ were previously obtained on GLAD-TiO₂ and -ITO with deposition angle of 72° and 80°, respectively, by BET Krypton gas adsorption isotherms method.³

From previous study carried out in our laboratory, the electrical double layer capacitance of GLAD-ITO (*i.e.*, deposited with same deposition angle of $\alpha = 80^\circ$) was recorded in a 0.3 M KCl electrolyte depending on the different film thickness.⁴ A surface area enhancement of $\sim 66 /\mu\text{m}$ was estimated which is a similar value by BET Krypton gas adsorption isotherms method (*i.e.*, $\sim 70 /\mu\text{m}$).³

Additionally, the specific surface area of GLAD-TiO₂ was also estimated by measuring the electrical double layer capacitance. In 0.3 M KCl electrolyte either at pH 7.0 or pH 5, an average electrical capacitance density of all types of GLAD-TiO₂ electrodes were measured to $22.5 \pm 1.6 \text{ mF}\cdot\text{cm}^{-2}$ once normalized to the geometric electrode area was estimated (Figure 3). Once this value is corrected from the film surface area enhancement (*i.e.*, $540/\mu\text{m}$), an intrinsic capacitance density of $41.6 \mu\text{F}\cdot\text{cm}^{-2}$ was founded. This value is close to the theoretical one ($10\text{--}20 \mu\text{F}\cdot\text{cm}^{-2}$) calculated for a flat conductive surface in an aqueous electrolyte solution, indicating that good agreement with previously reported in literature.⁵ This demonstrates that the morphology of the mesoporous GLAD-TiO₂ film is not affected by the underlying substrates (*i.e.*, Ti or TiO₂ or ITO).

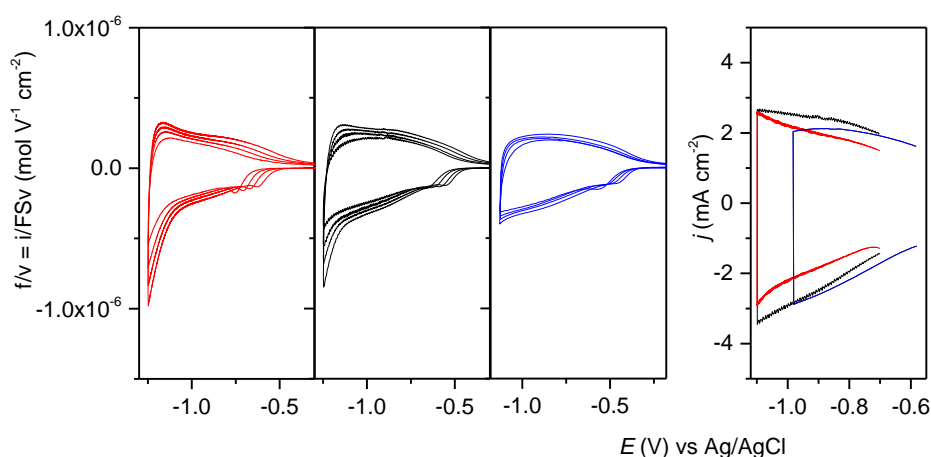


Figure 3. Electrical double layer capacitive current (converted to electron flux density and then normalized to the scan rate) recorded in 0.3 M KCl electrolyte at pH 7.0 in the potential window from -0.7 V to -1.1 V for (red) GLAD-TiO₂, (black) GLAD-TiO₂/TiO₂ electrodes and at pH 5.0 in the potential window from -0.58 V to -0.98 V for (blue) GLAD-TiO₂/Ti electrode. The applied potential window was adjusted to the 60 mV anodic shift by pH decrease according to the pH-dependence of the conduction band potential of TiO₂.

4. Surface modification

4.1. Chemisorption of manganese porphyrin (Mn-ph)

Mn-ph was chemisorbed through phosphonate group into the mesoporous GLAD-electrodes by immersing in a solution of manganese porphyrin ($25 \mu\text{M}$ in DMSO and water, 1:9, 1 ml, pH adjusted to 4~5 by HCl) during overnight. After rinsing by Milli-Q water, the Mn-ph/GLAD-electrodes were characterized by UV-visible spectroscopy.

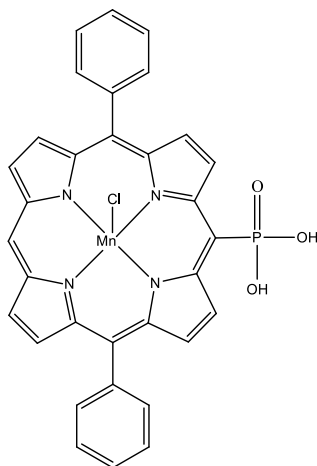
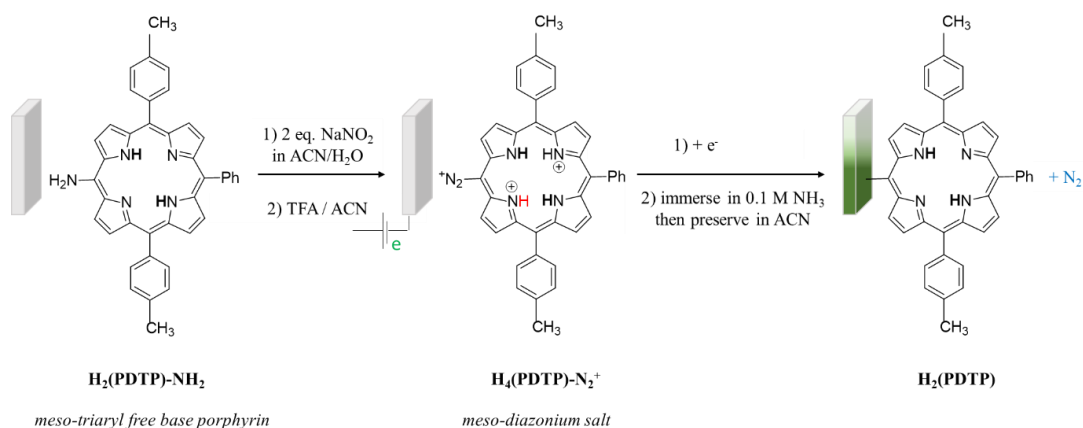


Figure 4. Chemical structure of Manganese porphyrin (Mn-ph).

4.2. Electrografting of diazonium salt

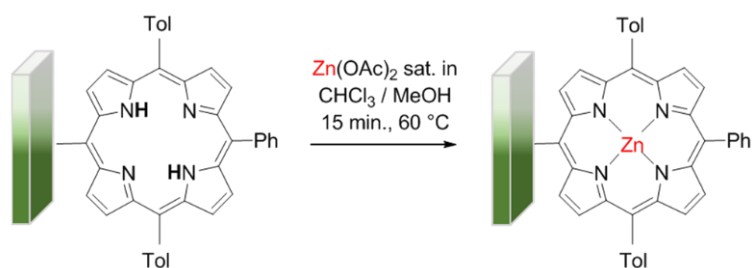
Electrode functionalization was performed in a conventional three-electrode amber glass cell under argon and at room temperature according to the literature.¹ The auxiliary electrode was a platinum wire and the reference electrode was KCl-saturated calomel (SCE). Acetonitrile (ACN) solvents were used after distillation prior to each electrografting experiment. Firstly, 1 mL of 1 mM $\text{H}_2(\text{PDTP})\text{-NH}_2$ in distilled ACN was added to the cell under argon. Afterwards, 20 μL of 1.4 mM NaNO_2 dissolved in Milli-Q water was mixed with 80 μL of distilled ACN and then added drop by drop to the porphyrin solution under argon. After 10 min, 170 μL of TFA and 830 μL of 0.11 M TBAPF_6 /distilled ACN solution were injected into the cell. Finally, the solution was diluted by adding 7.9 mL of 0.11 M TBAPF_6 /distilled ACN solution into the cell, leading to a final volume of 10 mL. The solution was further deaerated by argon bubbling for 10 min and kept under argon during the entire experiment. Multiple cyclic voltammetric scans (from 1 to 30 uninterrupted CV cycles) were continuously performed between 0.5 and 0.05 V versus SCE at $50 \text{ mV}\cdot\text{s}^{-1}$. Experiments under forced convection were achieved by bubbling argon near the working electrode surface (the bubble stream was always positioned at the same level in the cell close to the working electrode). The resulting modified electrode was thoroughly rinsed with ACN and soaked in ACN for *ca.* 30 min to allow desorption of poorly attached porphyrins, and further soaked in a 0.1 M aqueous NH_3 solution for *ca.* 10 min for deprotonation and finally rinsed again with ACN. The geometric working electrode areas of the planar ITO and GLAD-ITO electrodes

were estimated to be $0.75 \pm 0.22 \text{ cm}^2$ ($N = 10$). Current densities were obtained by normalizing the current with respect to the geometric electrode areas.



Scheme 4. Schematic representation of the *In-situ* generation of $\text{H}_4(\text{PDTP}\text{-N}_2^+)$ followed by electrochemical grafting on the electrode surface.

Porphyrin-modified planar ITO or mesoporous GLAD-ITO electrodes were converted into zinc porphyrin-modified electrodes by simply immersing the porphyrin-grafted electrodes for 15 min in a saturated zinc acetate solution of methanol/chloroform (1:9, v/v) heated to 50 °C. Afterwards, the electrodes were washed thoroughly with ACN. Zn Metallation of grafted diazonium salt on planar ITO or mesoporous GLAD-ITO electrodes were carried out by simply immersing the modified electrodes in a saturated zinc acetate solution of methanol/chloroform (1:9, v/v) heated to 50 °C during 15 min. Afterwards, the electrodes were washed thoroughly with ACN.



Scheme 5. Schematic representation of metallation process of the $\text{H}_2(\text{PDTP})$ -functionalized electrode.

References

- ¹ Hebié, S.; Devillers, C.H.; Sophie Fournier, S. ; Lucas, D. Direct Grafting of Free-Base meso-Triarylporphyrins on Electrode Materials through Diazonium Reduction: Reversible Zinc(II) Metallation of the Resulting Materials. *ChemElectroChem*. **2016**, 3, 45-50.
- ² Enakieva, Y. Y.; Michalak, J.; Absulaeva, I. A.; Volostnykh, M. V.; Stern, C.; Guillard, R.; Gessmertnykh-Lemeune, A. G.; Gorbunova, Y. G.; Tsivadze, A. Y.; Kadish, K. M. General and Scalable Approach to A2B- and A2BC-Type Porphyrin Phosphonate Diesters. *Eur. J. Org. Chem*. **2016**, 4881-4892.
- ³ Krause, K.M.; Taschuk, M.T.; Harris, K.D.; Rider, D.A.; Wakefield, N.G.; Sit, J.C.; Buriak, J.M.; Thommes, M.; Brett, M.J. Surface area characterization of obliquely deposited metal oxide nanostructured thin films. *Langmuir*. **2010**, 26, 4368-4376.
- ⁴ Renault, C.; Andrieux, C. P.; Tucker, R. T.; Brett, M. J.; Balland, V.; Limoges, B. Unraveling the Mechanism of Catalytic Reduction of O₂ by Microperoxidase-11 Adsorbed within a Transparent 3D-Nanoporous ITO film. *J. Am. Chem. Soc.* **2012**, 134, 6834-6845.
- ⁵ Kotz, R.; Carlen, M. Principles and applications of electrochemical capacitors. *Electrochim. Acta*. **2000**, 45, 2483-2498.

Annexe

Résumé :

Améliorer notre compréhension des mécanismes de transport/transfert de charges et de stockage de charges dans les films d'oxyde métallique semi-conducteur mésoporeux transparents (fonctionnalisés ou non par des chromophores redox-actifs) dans des électrolytes aqueux est d'une importance fondamentale pour le développement et l'optimisation d'une large gamme de dispositifs de production ou de stockage d'énergie éco-compatibles et/ou éco-durables (cellules solaires à colorants, batteries, photoélectrolyseurs, ...). Dans ce but, des films de TiO_2 semi-conducteur mésoporeux préparés par dépôt sous incidence rasante (GLAD- TiO_2) ont été sélectionnés pour leur grande surface spécifique, leur morphologie bien contrôlée, leur transparence élevée dans le visible et leur semiconductivité bien définie qui peut être facilement ajustée par l'application d'un potentiel externe, autorisant ainsi leur caractérisation aisée par spectroélectrochimie en temps réel.

Nous avons d'abord étudié le transfert et transport de charges dans des électrodes GLAD-ITO et GLAD- TiO_2 fonctionnalisées par une porphyrine de manganèse redox-active jouant à la fois le rôle de chromophore et de catalyseur. Nous avons démontré que la réponse électrochimique des électrodes ainsi modifiées, enregistrée en l'absence ou en présence du substrat O_2 , dépend fortement de la conductivité du film mésoporeux. En utilisant la voltamétrie cyclique couplée à la spectroscopie d'absorption UV-visible, nous avons pu extraire des informations clés telles que la vitesse du transfert d'électrons hétérogène entre le chromophore redox immobilisé et le matériau semi-conducteur, et aussi pu rationaliser le comportement électrochimique spécifique obtenu sur un film GLAD- TiO_2 modifié par la porphyrine en condition catalytique. En parallèle, nous avons développé un procédé de fonctionnalisation de ces films d'oxyde métallique mésoporeux (en l'occurrence des films GLAD-ITO) par électrogreffage de sels d'aryldiazonium générés *in situ*, permettant d'obtenir des électrodes fonctionnalisées avec un taux de recouvrement surfacique élevé et une stabilité dans le temps particulièrement bonne en conditions hydrolytiques.

Nous avons également étudié le stockage de charges au sein d'électrodes GLAD- TiO_2 dans divers électrolytes aqueux. Nous avons notamment démontré pour la première fois qu'une insertion rapide, massive et réversible de protons peut être effectuée dans des films de TiO_2 nanostructurés amorphes immergés dans un tampon aqueux neutre, le donneur de protons étant alors la forme acide faible du tampon. Nous avons également démontré que ce processus de stockage d'électrons couplé à l'insertion de protons peut se produire sur toute la gamme de pH et pour un vaste panel d'acides faibles organiques ou inorganiques, mais aussi de complexes aqueux d'ions métalliques multivalents, à condition que le potentiel appliqué et le pKa de l'acide faible soient correctement ajustés.

Mots clés: électrochimie moléculaire, stockage de charge électrochimique, électrodes d'oxyde métallique mésoporeux, spectroélectrochimie en temps réel, électrogreffage de sels d'aryldiazonium, batterie aqueuse, porphyrines immobilisées, réduction catalytique de O_2 , insertion de protons.

Abstract:

Better understanding of the mechanisms of charge transport/transfer and charge storage in transparent mesoporous semiconductive metal oxide films (either functionalized or not by redox-active chromophores) in aqueous electrolytes is of fundamental importance for the development and optimization of a wide range of safe, eco-compatible and sustainable energy producing or energy storage devices (*e.g.*, dye-sensitized solar cells, batteries, photoelectrocatalytic cells, ...). To address this question, mesoporous semiconductive TiO₂ films prepared by glancing angle deposition (GLAD-TiO₂) were selected for their unique high surface area, well-controlled morphology, high transparency in the visible, and well-defined semiconductivity that can be easily adjusted through an external bias, allowing thus their characterization by real-time spectroelectrochemistry.

We first investigated charge transfer/transport at GLAD-ITO and GLAD-TiO₂ electrodes functionalized by a redox-active manganese porphyrin that can play both the role of chromophore and catalyst. We demonstrate that the electrochemical response of the modified electrodes, recorded either in the absence or presence of O₂ as substrate, is strongly dependent on the mesoporous film conductivity. By using cyclic voltammetry coupled to UV-visible absorption spectroscopy, we were able to recover some key information such as the heterogeneous electron transfer rate between the immobilized redox-active dye and the semiconductive material, and also to rationalize the specific electrochemical behavior obtained at a porphyrin-modified GLAD TiO₂ film under catalytic turnover. In parallel, we developed a new functionalization procedure of mesoporous metal oxide films (GLAD-ITO in the present case) by electrografting of *in-situ* generated aryldiazonium salts, allowing for modified electrodes characterized by both a high surface coverage and a particularly good stability over time under hydrolytic conditions.

Also, we investigated charge storage at GLAD-TiO₂ electrodes under various aqueous electrolytic conditions. We notably evidenced for the first time that fast, massive, and reversible insertion of protons can occur in amorphous nanostructured TiO₂ films immersed in near neutral aqueous buffer, with the proton donor being the weak acid form of the buffer but not water. We also demonstrated that this proton-coupled electron charge storage process can occur over the entire range of pH and for a wide range of organic or inorganic weak acids, but also of multivalent metal ion aquo complexes, as long as the applied potential and pK_a of weak acid are properly adjusted.

Key words: molecular electrochemistry, electrochemical charge storage, Mesoporous metal-oxide electrodes, real-time spectroelectrochemistry, diazonium electrografting, aqueous battery, immobilized porphyrins, catalytic O₂ reduction, proton insertion.